Science Instrument (SI) Operations Handbook for the AXAF CCD Imaging Spectrometer (ACIS)

ACIS-PSU-SOP-01
Version 2.65 - November 20, 1997
Copy printed November 20, 1997
Post-Acceptance Review Submission

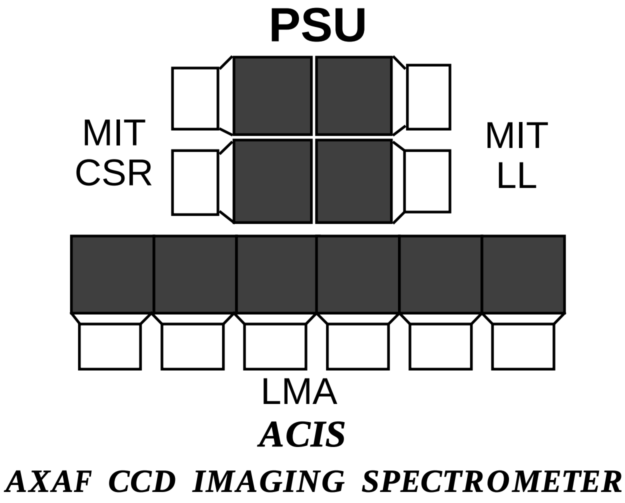

Submitted by:

John A. Nousek
SOP01 Editor, Lead PSU Co-I
Penn State University

Approved by:

Gordon P. Garmire
ACIS Instrument PI
Penn State University

Contents

List of Tables

List of Figures

Chapter 1

Introduction

1.1 Purpose

The purpose of this document is to present the information needed for the AXAF Science Center (ASC) personnel to properly operate and maintain the ACIS experiment on orbit.

1.2 Scope

This document should be perceived as an Owner's Manual for ACIS. It shall contain documentation concerning all aspects of the ACIS experiment which are needed to operate, calibrate, command, and maintain the ACIS instrument hardware, software, and data analysis tools after the conclusion of the ACIS team contract period.

1.3 Use of This Document

The document is intended to be a guide to the use and operation of the ACIS instrument. It is intended to provide a narrative introduction to the complete instrument, but it is not intended to supersede the explicit documentation provided in response to NASA DR's for the ACIS contract. In case of discrepancies between this document and other ACIS formal documentation, the other documents take precedence. Although the information in this document is correct at the time the document is released, and we anticipate future revised versions will be produced at the direction of the AXAF Project, we cannot continually update this document as knowledge of ACIS and operational procedures matures. The reader should consult the primary 'controlled' documentation for the definitive information.

Many of the important controlled documents are available from the AXAF Science Center (ASC), as well as documentation on the rest of the AXAF observatory and project. All ACIS official documents (and AXAF as well) can be obtained from the Marshall Space Flight Center (MSFC) at this address:

Document Repository
Code CN22D
George C Marshall Space Flight Center
Marshall Space Flight Center, AL 35812

Many useful documents are also available from the MIT World Wide Web site,

http://acis.mit.edu.

For the novice reader we have included a Glossary of Acronyms in Chapter 8, including brief definitions.

1.4 Version History

Version 0.1 - outline version of the document, identifying the section headings and establishing traceability to the requirements listed in MSFC DR SOP01.

Version 0.11-0.14 - text written for Sections 1,2&3 by David Lumb and John Nousek. Contributions and figures from the ASC Science Instrument Notebook (SIN) by David Huenemoerder and collaborators.

Version 0.5 - text rewritten and expanded as first draft of PDR submission (May 23, 1994). Areas submitted as outline points for later submission are indicated as follows:

Outline point *This is a sample outline point.* **TBS by:** *Nousek*

Version 1.0 - final form for initial submission at ACIS PDR (May 23, 1994). Additional inputs received from Gordon Garmire, Mark Bautz, Jim Francis, Dorothy Gordon and Steve Jones.

Version 1.1 - version containing revisions received after the ACIS PDR submission. Comments from David Burrows.

Version 1.11 - version containing revisions based on comments from PDR reviewers and RIDs. Comments from Paul Plucinsky, Joel Kastner, Allyn Tennant, and Dan Dewey. Supplemental information from Mark Bautz, Peter Ford, Jim Francis and Steve Jones. Figures made by Linda Baker, Erin Shutak and Jaime Demick.

Version 1.12 - version completely reviewed by Leisa Townsley to assure a uniform style and to clarify the narrative.

Version 1.13 - including new figures from Linda Baker and Peter Ford (MIT SRS).

Version 1.14 - major additions based on material submitted by MIT at PDR, especially the Software Requirements and On-Board Electronics design. Compiled by Leisa Townsley.

Version 1.15 - structurally revised into separate $\LaTeX$ chapters, added ACIS logo from David Lumb, inputs from Leisa Townsley, Pat Broos, and MIT Software Preliminary Design Document.

Version 1.16 - added flight CCD positions from Al Pillsbury, blur circle projections and calibration specification material from John Nousek, ground processing from Pat Broos, figures from Linda Baker.

Version 1.17 - additional material from Leisa Townsley and Pat Broos. Description of UV filter added by John Nousek

Version 1.18 - suggestions added from Eric Feigelson. Sub-pixel resolution and X-ray simulation description added from Leisa Townsley.

Version 2.00 - preliminary submission for CDR, submitted May 8, 1995.

Version 2.01, 2.02 - changes on filter and suggestions from Gordon Garmire incorporated. Material from ASC review of FI/BI chips included from Paul Plucinsky.

Version 2.10 - official CDR submission on May 31, 1995.

Version 2.11 - brought up to date calibration plan times.

Version 2.12 - included revisions based on RIDs from Joel Kastner (ASC) and Bob Wolf (TRW).

Version 2.13 - added text and figures from Niel Tice and others at Lockheed Martin Astronautics (LMA).

Version 2.14 - added ACIS sub-assembly calibration plan from Mark Bautz. Added OV plan from Mike Juda and Paul Plucinsky (ASC)

Version 2.15 - removed Spatial Histogramming bias correction per Bev Fergason (MIT).

Version 2.16 - added sub-assembly priorities from Mark Bautz; Leisa Townsley complete document review; alignment figures from Rick Foster (MIT).

Version 2.17 - revisions to software section suggested by Peter Ford (MIT). George Chartas comments incorporated. SRC data on filter measurements, bias determination description, door description and orbital bakeout from Leisa Townsley. Data reduction tools description from Pat Broos.

Version 2.18 - revisions based on Gordon Garmire review.

Version 2.19 - revisions to XRCF calibration and figure from Jiahong Juda (ASC).

Version 2.50 - start of post-XRCF release versions. Electrical description from LMA.

Version 2.51-2.53 - flight focal plane graphics from Ken Glotfelty (ASC). S array description added.

Version 2.54 - extensive revision to the calibration descriptions, filter transmission plots and figures from Leisa Townsley and George Chartas (PSU). Description of flight calibration sources from Mark Bautz (MIT). Expanded the Ground Processing description of TARA and ASC tools based on User Guide by Pat Broos and Scott Koch.

Version 2.60 - extensive revisions based on contributions from Bill Mayer (MIT).

Version 2.61 - corrections to science description by Eric Feigelson (PSU).

Version 2.62 - added list of XRCF TRW ID measurements from Leisa Townsley (PSU).

Version 2.63 - revisions based on acceptance review comments by Peter Ford (MIT).

Version 2.64 - revisions based on acceptance review comments by Bob Goeke (MIT).

1.5 Instrument Overview

The AXAF (Advanced X-ray Astrophysics Facility) promises to be the premier X-ray observatory of the 1990's. As a result of major redesigns forced by economic and political considerations, the mission of the AXAF satellite has centered on the extremely high spatial resolution of the incomparable X-ray telescope mirrors.

In order to utilize that resolution, high spatial resolution instruments are required, namely the ACIS (AXAF CCD Imaging Spectrometer) and the HRC (High Resolution Camera). ACIS offers superior high energy quantum efficiency and simultaneous imaging and spectroscopic capability, while the HRC offers low energy quantum efficiency, high time resolution and a wider field of view. The two instruments can also be used in conjunction with transmission gratings, with the ACIS primarily used with the HETG (High Energy Transmission Gratings) and METG (Medium Energy Transmission Gratings) and the HRC with the LETG (Low Energy Transmission Gratings).

The critical active element in ACIS is the CCD chip, which converts incident X-ray events into electronic signals which record the location of the event and its energy. The spatial resolution of the CCD is limited by the physical dimensions of the discrete charge collecting locations (called picture elements or pixels). These pixels are 24 μm square with essentially no spacing or dead area between pixels. Two types of chip are used in ACIS. Both are fabricated at the MIT Lincoln Laboratory in Lexington, MA. One type is used with the gate structures, on the front of the CCD, facing the X-ray beam of the AXAF mirrors (hence 'Frontside Illuminated' or FI). The other type has additional processing to remove material from the backside of the CCD, and it is deployed with the backside facing the X-ray beam (hence 'Backside Illuminated' or BI). FI chips have superior energy resolution (especially at low energy) and somewhat better high energy quantum efficiency than BI chips. BI chips have far superior low energy quantum efficiency, but poorer cosmetic quality. Both types contain 1024x1024 pixels.

In most operating modes, each pixel of the CCD stores the signal generated in it by an incident X-ray for a period of time of order seconds. The electric charges accumulated in each CCD pixel are then transferred in less than 41 msec into a section of the CCD shielded from incident radiation, where they can then be read out and the signals processed. In most applications, the incident X-ray flux will be low enough that only a single X-ray will be detected for every 100 or more pixels sampled. When this is true, the electronic signal is related to the energy of the X-ray with reasonably high accuracy ($E/\Delta E \sim 50$), and the instrument simultaneously functions as a high spatial resolution detector and moderate spectral resolution non-dispersive spectrometer. For higher flux sources, either special operating modes are required, or the analysis must allow for the possibility of multiple photons per pixel ("pile-up").

When a transmission grating is introduced into the light path between the X-ray mirrors and the ACIS, the image of a source becomes dispersed. In this case even higher spectral resolution is possible ($E/\Delta E \sim 1000$).

Because the optimal focal surfaces for imaging and spectroscopy are considerably different, it is necessary to include separate CCD arrays optimized for each application. The ACIS-I array (2x2) offers the largest field of view with best imaging performance across the field. The ACIS-S array (6x1) follows the Rowland Circle defined by the gratings, and gives the best spectroscopic energy resolution. The center detector of the ACIS-S array is the position locked into the focal plane at launch (representing the best compromise instrument if the SIM translation should fail), and offers reduced field imaging without field losses due to intra-chip gaps near the desired target.

As a CCD does not produce a prompt signal when it is struck by an X-ray, but instead must wait for the CCD to be commanded to be read out, the timing resolution is limited by the time between successive readouts. This results in a typical time resolution on photon arrival times of 3.3 seconds. If better time resolution is required, however, ACIS can be operated in several special modes which reduce the time between readouts but also drastically reduce the field of view. See the discussion of observing modes in Section 3.1.

A more detailed overview describing the instrument can be found in Chapter 2.

1.5.1 Performance Synopsis

Table 1.1 lists many characteristics relevant to the ACIS/AXAF performance. Those not discussed there will be addressed in the following sections.

1.5.2 Scientific Objectives

A wide variety of astronomical objects emit X-rays, from stellar atmospheres to hot interstellar gas, galactic halos, and active galaxies. ACIS will enable AXAF to obtain high-resolution images of astronomical objects with simultaneous moderate spectral resolution, high-resolution dispersed spectra of point sources, time-resolved spectra and/or images, and

Focal plane arrays:			
Imaging	4 CCDs approximating the telescope focal surface		
Spectroscopic	6 CCDs in a linear array on the grating Rowland Circle		
CCD format	1024 by 1024 pixels, frontside & backside illumination		
Pixel size	24 microns (0.49 arc-sec)		
		Frontside Ill. (FI)	Backside Ill. (BI)
Maximum energy resolution	1.0 keV	55 eV ($E/\Delta E = 18$)	100 eV ($E/\Delta E = 10$)
	5.9 keV	124 eV ($E/\Delta E = 48$)	140 eV ($E/\Delta E = 42$)
		Frontside Ill. (FI)	Backside Ill. (BI)
Quantum efficiency (including filter)	$> 80\%$	@ 4 keV	@ 4 keV
	$> 30\%$	0.8-8 keV	0.3-8 keV
	$> 5\%$	0.35-0.8 keV	0.15-0.3 keV
Detector projected area	16.9 by 16.9 arc-min imaging 8.3 by 50.6 arc-min spectroscopic		
System noise	$\lesssim 2$ electrons (rms) per pixel		
Electron production energy	3.65eV/e^-		
Fano factor	0.12		
Max readout-rate per channel	100,000 pixels/sec		
Number of parallel signal channels	4		
Pulse-height encoding	12 bits/pixel		
Max internal data-rate	6.4 Mbs ($100,000 \times 4 \times 16 \times 6$ CCD)		
Output data-rate	24 kb per sec		
CCD frame repetition times	3.3 sec (nominal full array) 0.18 sec (fastest-single CCD)		
Minimum line readout time	100 ms (full line)		
Minimum pixel readout time	100.0μs		
Nominal exposure time	0.2 to 10.0 s		
Point-source sensitivity	4×10^{-15} ergs cm^{-2} s^{-1} in 10^4 s (0.4-6.0 keV)		
Detector operating temperature	$-120°$ C		

Table 1.1: ACIS Characteristics

moderate resolution dispersed spectra of extended sources. The spatial and spectral resolution in conjunction with the detector sensitivity and collecting area will allow forefront investigation into many areas of astrophysics. Among the objectives are to:

- measure accurately the discrete X-ray source contribution to the X-ray background

- determine galaxy and galaxy cluster structure and evolution, and substructure of intracluster plasma, out to a redshift of 1-2
- map the temperature and elemental abundance distribution, especially of iron, in clusters of galaxies
- study characteristics of active galactic nuclei, starburst galaxies and quasars, particularly emission mechanisms, time-variability, jets and lenses
- detect and determine the distribution and types of X-ray sources out to the distance of the Virgo cluster
- test Compton models of quasars and active galaxies by studying time variability as a function of energy
- classify emission from normal galaxies out to 800 Mpc and beyond
- determine the abundance of iron in supernova remnants (SNR) to ascertain the composition of the precursor star and verify models of nucleosynthesis
- determine the temperature of neutron stars in SNR to test cooling theories
- detect and identify SNR and Crab-like pulsars out to M31
- measure temperature and emission measure distributions in stellar coronal X-ray sources
- conduct time-resolved spectroscopic studies of accreting compact objects to define the disk geometry
- determine the contribution of stars to the soft X-ray background
- measure the abundance of elements in the interstellar medium
- evaluate the role of X-ray ionization in regulating star formation in molecular clouds
- study the properties and structures of stellar coronae as a function of stellar ages
- determine important physical properties of interstellar dust

1.6 Instrument Heritage

ACIS was first selected for definition as a result of a proposal in response to AO-OSSA-3-83, on 5 March 1985. Prof. Gordon Garmire of Penn State University led a team of 17 scientists from MIT, JPL and Penn State, whose submission was selected as one of four proposals for definition (Phase A/B).

In 1989 Prof. Garmire submitted an expanded proposal based on the definition phase studies, backed by a revised and expanded scientific team. The MIT team was led by Deputy IPI, Dr. George Ricker and included the development of CCDs at Lincoln Lab, under the direction of Dr. Richard Savoy, and the scientific development of CCD technology by four other MIT scientists (Dr. Mark Bautz, Prof. George Clark, Dr. John Doty, and Prof. Saul Rappaport). The PSU team, lead by Lead Co-I, Dr. John Nousek, and four other PSU scientists (Dr. David Burrows, Prof. Eric Feigelson, Dr. Richard Griffiths, and Prof. Daniel Weedman), concentrated on ground software development and calibration efforts. The JPL/CalTech team was lead by Mr. S.A. Collins, assisted by four others (Dr. Alan Metzger, Dr. Steve Pravdo, Dr. Guenter Riegler, and Dr. Wallace Sargent). This team concentrated on CCD chip evaluation and scientific applications. Performing the critical role of ACIS Project Manager was Mr. Phil Gray of MIT.

As a result of the Phase C/D review, the ACIS was selected for development for launch, and deemed a 'core' instrument of the AXAF mission. Initiation of a new start for AXAF was delayed for two years, postponing the start of AXAF Phase C/D activities until 1991.

In 1992-3 major revisions to the mission plan were incorporated to respond to budgetary pressure on the program. AXAF was split into two spacecraft. The first, AXAF-I, was to be launched by the Space Shuttle and then into a high orbit ($\sim$10,000 × 140,000 km) by a solid rocket insertion motor. The second mission, AXAF-S, was to be launched by a Delta or Atlas expendable launch vehicle into a polar sun synchronous orbit. ACIS was assigned to the AXAF-I spacecraft, for which the weight had to be substantially reduced from the original design. AXAF-I contained the original glass optic design, but used only four of the planned six mirror shells. The increased observing efficiency available in high Earth orbit partially compensated for the loss of mirror collecting area.

In 1993 the AXAF program was further reduced by cancelation of the partner AXAF-S spacecraft, with a relegation of the prime instrument to flight aboard the proposed Japanese Astro-E mission.

An important precursor to the ACIS program was the launch of the Japanese-U.S. ASCA satellite (Astro-D) on February 20, 1993. This satellite carried two Silicon Imaging Spectrometers (SIS), consisting of arrays of Lincoln Lab CCD chips, operated in a very similar manner to that planned for AXAF. The SIS were built by a collaboration headed by George Ricker and included many of the members of the ACIS team (notably Mark

Bautz, Gordon Garmire and John Nousek).

Although the SIS carried X-ray CCDs similar to the ACIS chips into orbit for the first time, and has made many important discoveries, the unmatched imaging optics (more than 200 times higher angular resolution) of the AXAF HRMA will open an entirely new era of discovery. The SIS experience has also enabled us to make important improvements in ACIS to avoid, eliminate or decrease problems such as flickering pixels, dark frame errors, light leaks and radiation damage, which have reduced the SIS CCD performance.

In 1994 and 1995 the personnel working on ACIS substantially increased as detailed design and fabrication commenced. Notable additions were Dr. Peter Ford, in charge of flight software, and Mr. Jim Francis. Dr. Bill Mayer replaced Phil Gray as ACIS Project Manager.

The ACIS flight instrument passed through thermal vacuum testing at Lincoln Laboratories in March and April, 1997. The tested and fully functional flight instrument was delivered to the Marshall Space Flight Center on April 14, 1997. It underwent end-to-end calibration testing with the HRMA until April 26, 1997, and after the HRMA was removed for assembly into the AXAF spacecraft body, the ACIS instrument received additional detector level calibration at the XRCF through May 17, 1997.

Chapter 2

Instrument

2.1 Overall Description

ACIS is the AXAF CCD Imaging Spectrometer. It is comprised of two CCD arrays, one for imaging, the other for grating spectroscopy. Each CCD in each array is tipped to approximate the relevant focal surface. In conjunction with the High Resolution Mirror Assembly (HRMA), the ACIS imaging array will provide simultaneous time-resolved imaging and spectroscopy. With the High Energy Transmission Gratings (HETG) and the Low Energy Transmission Gratings (LETG), the ACIS spectroscopic array will acquire high resolution (up to $E/\Delta E = 1000$) spectra of point sources. The bare CCD arrays themselves have an intrinsic energy resolution of about $E/\Delta E = 50$ at 6 keV. The high quantum efficiency of the CCDs enables spectroscopy with much better counting statistics than can be achieved with other X-ray detectors.

Fig. 2.1 illustrates the schematic flow of X-ray signals from the incident X-radiation through to the telemetry of science data to the ground. The incident X-rays are collected by the HRMA and focused onto the CCD chips after passing through a UV/optical light blocking filter. In the CCD chip, the X-ray is converted into an analog charge signal which is processed by the DEA (Detector Electronics Assembly) signal chains, resulting in a digital number proportional to the charge induced in each pixel. These digital signals are further processed by the DPA (Digital Processing Assembly), which, depending on the mode of the instrument, selects the most important signals for telemetry to the ground. The DPA provides these science data and engineering housekeeping data to the RCTU (Remote Command and Telemetry Unit), which interfaces the experiment to the rest of the spacecraft, eventually resulting in telemetry of these data to the ground for scientific and engineering analysis.

From an organizational point of view, the ACIS experiment is divided into two parts:

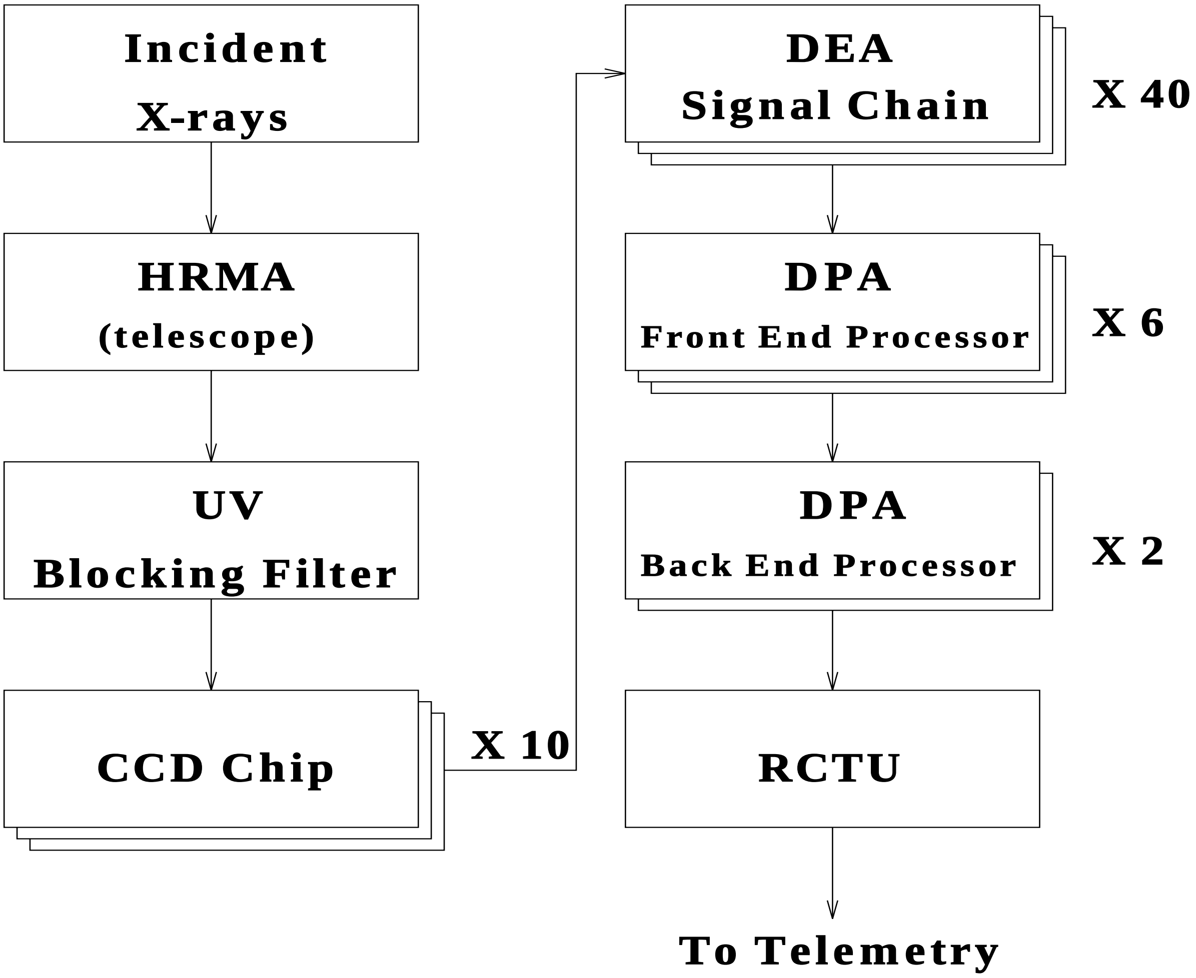

Figure 2.1: Schematic flow of information through the ACIS experiment.

the Detector & Processor Subsystem (DPS), and the Power & Thermal-Control Subsystem (PTS) developed at LMA. The DPS consists of the Detector Assembly (DA), DEA and DPA. The PTS consists of the Power Supply and Mechanism Controller (PSMC) and the Thermal Control System.

The entire ACIS experiment is mounted on the Science Instrument Module (SIM) which translates in the spacecraft Z direction to allow selection of ACIS aim point, or to allow ACIS to move to a stow position (while the HRC is collecting data). A side view of the DA is shown in Figure 2.2.

The functional duties of each DPS subassembly are as follows: The DA includes the CCD arrays, fiducial lights and an X-ray calibration source used primarily for ground

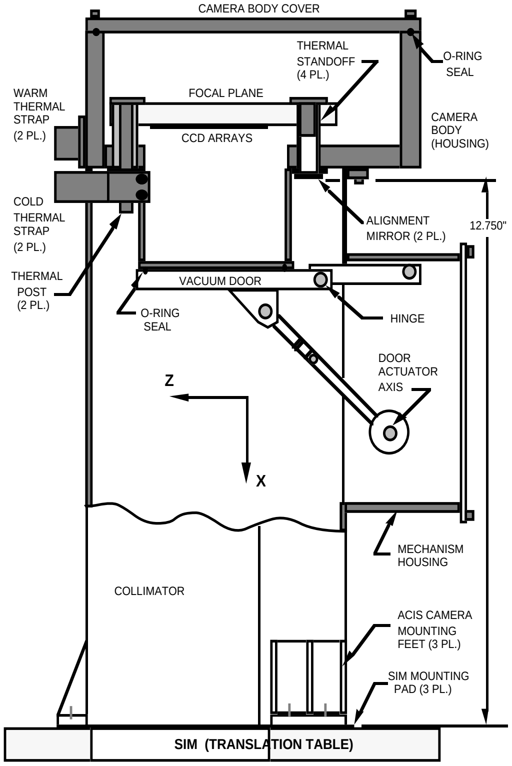

Figure 2.2: ACIS Detector Assembly Layout

test. The DA also includes the mechanical structures of the detector housings, focal plane support structures, mechanical door, radiation shielding and long collimator/stray light baffle. Signals from the CCDs are amplified and digitized in the DEA. The DPA controls instrument operation, extracts valid X-ray events and processes data for downlink. The TRW Government-furnished Remote Command & Telemetry Unit (RCTU) provides the interface between the Observatory and the ACIS experiment for transmission of commands and data.

The PTS subassembly functions are: The PSMC supplies conditioned power to all assemblies. The Thermal Control System provides thermal control for the DA (via warm and cold radiators) to allow operation of the CCD chips at a nominal temperature of -120 C. Heaters provided by the SIM will maintain minimum temperature levels on ACIS electronic assemblies.

The ACIS experiment contains two ancillary subsystems. These are the Calibration Sources installed at the SIM stow position to allow calibration activities in-flight while the ACIS is not in the focal spot of the HRMA, and the Door Assembly, which is expected to open just once, and remain in the open position for the rest of the spacecraft lifetime. (If necessary the Door Assembly can be closed and reopened.)

2.2 Systems Level Analysis

2.2.1 Optical

2.2.1.1 CCD Chip Array Layouts

The ACIS active sensors consist of two independent arrays of Lincoln Lab framestore CCD chips, one optimized for imaging performance over the entire array (ACIS-I) and the other optimized for spectral resolving power of the combined ACIS/HETG/HRMA system (ACIS-S). The center unit of the second array also serves as the optimum detector for reduced field imagery and will be the launch-lock position. A mixture of frontside illuminated and backside illuminated CCD chips is used in the ACIS-S array, each chip having an X-ray sensitive active area consisting of a planar, roughly 2.4 cm square (~ 6 cm^2).

The rationale for requiring the two arrays is as follows. The ACIS-I array provides the best imaging performance over the widest possible field allowed by the HRMA optical properties. The difference between the ACIS-I array and a flat detector or the ACIS-S spectroscopic array corresponds to a factor of up to two in the angular resolution of the instrument over the entire field of view, which leads to a factor of four in the limiting sensitivity for detecting sources under some conditions. Additionally, the three-dimensional spatial positioning of the chips in the ACIS-I array leads to nearly complete coverage of the entire HRMA focal surface for which the blur circle is 5 arc-sec or less. The ACIS-S array has less than half the coverage on the sky (field of view) at this performance.

On the other hand, ACIS-S is essential for meeting the needs of the grating readout. The grating focal surface is nearly flat, so trying to use ACIS-I as a readout for the gratings would lose the same factor of two in angular resolution, and therefore spectral resolution, which the ACIS-S array loses when used for imaging. (Note that grating spectral resolving power is directly related to angular resolution.) Additionally, a large array in one dimension is needed for wavelength coverage, so ACIS-I would only cover 1/3 of the spectral band that ACIS-S will cover. However, the flat nature of the ACIS-S array is not a drawback for reduced field imaging applications where field of view is less important. Thus in cases where the presence of the gaps between chips will be undesirable, but the size of the field of view is small, ACIS-S may be preferable for imaging applications. Another application of ACIS-S would be for observations which require the preservation of the symmetry of the point spread function for targets near the telescope axis. Finally, only ACIS-S contains BI CCD chips, so in those cases where detection or imaging of soft spectrum sources is required ACIS-S must be used.

To achieve these goals, ACIS-I consists of four CCD chips tipped in two dimensions so as to form a shallow 2x2 bowl. The center of the active area of each chip lies approximately on the tangent to a 250 mm radius sphere. (See Fig. 2.11 on page 49 for an isometric projection of this array as an aid in visualization.)

The ACIS-I CCD chips are butted as closely as possible, with gaps not exceeding 0.54 mm spacing. The framestore portions of the chips project outward from the center of the array, roughly orthogonal to both the HRMA axis and the direction of SIM translation.

The ACIS-S array consists of six chips butted so that their active areas form a single one-dimensional array of chips. The framestore areas project along the SIM translation direction, perpendicular to the HRMA axis. (See Fig. 2.12, page 50.) When focused by the SIM translation and axial focusing motion, the mechanical alignment is such that the HRMA axis intersects the array 6.25 mm in from the seam between the third and fourth chips in the row. These seams are as small as possible, but no larger than 0.431 mm. The ACIS-S array chips are very slightly, and progressively, tipped to approximate the Rowland Circle of the gratings. The center of each chip is positioned at the tangent point to a cylinder of radius of roughly 4325 mm, with the on-axis focal spot falling directly on the surface of the chip to provide optimum focus over the entire dispersed spectrum.

The spacing between the ACIS-I and S arrays is set at 8 mm, in order to allow space for filter support structures, without blocking or vignetting the field of view of either array.

The internal alignment of the ACIS experiment is determined on-orbit by knowledge to 0.1 mil of the fiducial light reference system over at least 85% of the orbit. The anticipated time interval when internal ACIS alignment will degrade is during the six hours nearest perigee passage.

The external alignment knowledge that is relevant to ACIS performance is the relation between the active areas of the CCD chips in the I and S arrays and the HRMA optical coordinate system. This alignment is maintained by co-aligning both the ACIS-I and S arrays with the system of six fiducial lights. The ACIS-I and S arrays are mechanically part of a single structure, the Focal Plane (FP), which must be correlated to the coordinate system defined by the centroid of the fiducial light system. The knowledge of the position of ACIS with respect to AXAF is determined via two reference mirrors mounted on the front of the detector housing.

Mechanical fabrication will place the ACIS focal plane at the designed location. Offsets of the focal plane from the position of alignment mark inscribed on the alignment mirrors mounted to the detector housing are then measured. Nominal locations of the mirrors and fiducial marks are shown in Figures 2.3 and 2.4. The positional tolerance on the alignment mirrors is ±0.050 inch.

The full alignment involves four steps. Each CCD chip active area is mounted into the

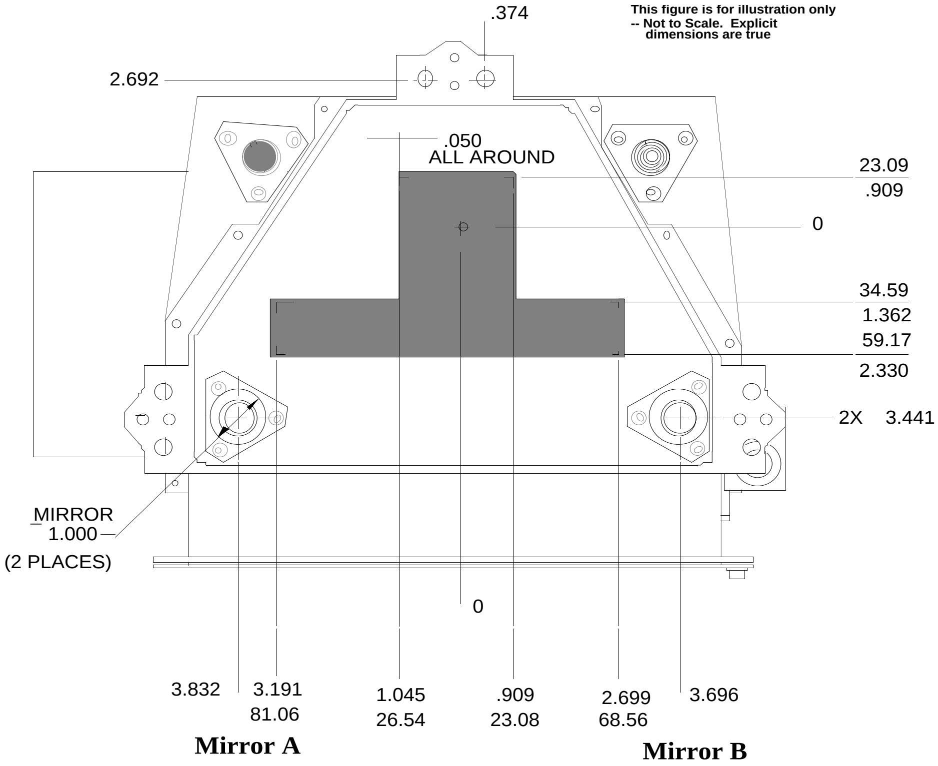

Figure 2.3: ACIS Detector Housing Alignment Mirror Locations. Dimensions given in mm and inches at room temperature.

FP structure such that the four corners are positioned as closely as possible to the focal plane coordinates specified in Figure 2.5. These positions are checked using microscopy to within 7.6 μm in Y and Z, and 25 μm in X (HRMA focus). The positions of the CCDs are used to determine the actual focal surface which is then related to an orientation mirror which is attached to the FP structure. This mirror has its normal determined within 2 arcsec.

Four thermoplastic standoffs mechanically hold the FP structure to the detector housing. The alignment between the fiducial marks on the mirrors on the exterior of the detector housing and the FP coordinate system will be better than 100 μm in X and 25 μm in Y and Z. The normals of the exterior mirrors shall be correlated to within a few arc-sec of the FP coordinate system defined by the focal plane mirror.

Positioning the ACIS is achieved by mechanical attachment of the detector housing to the SIM. Alignment is achieved by use of shims placed between the mounting feet of the collimator and the SIM.

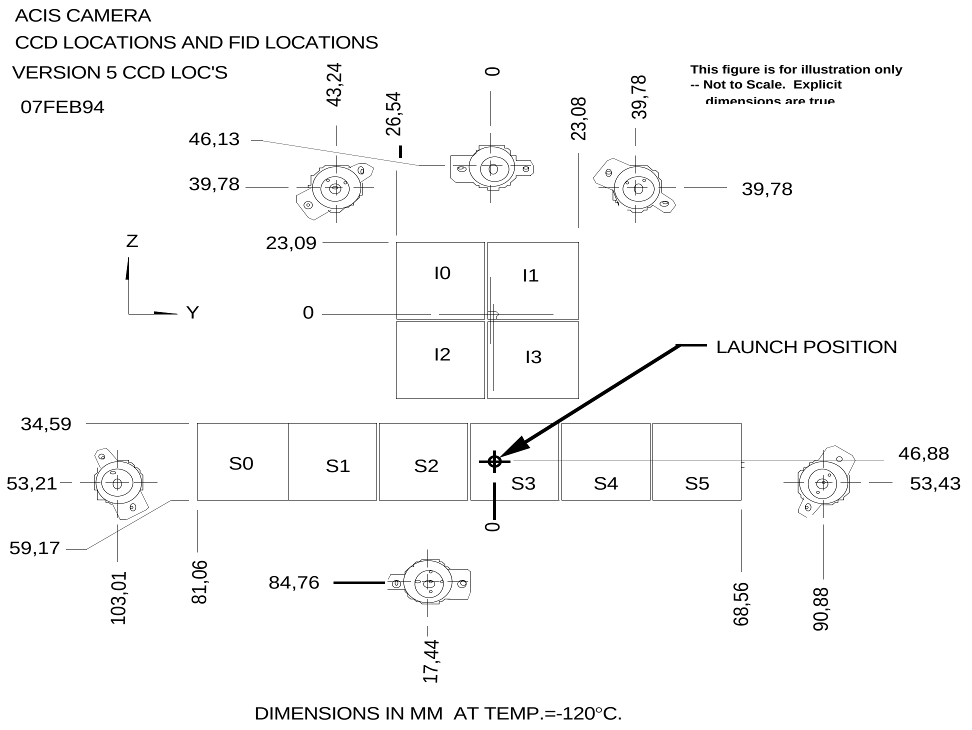

Figure 2.4: ACIS Fiducial Light Locations

Focussing of the ACIS instrument can be achieved via two complementary techniques. Shutter focus can only be done in the XRCF calibration facility. All except one quadrant of the mirrors were covered by closed shutters. The resulting out-of-focus image appears like a pie-shaped quadrant, which has a centroid displaced toward the open shutter quadrant if the detector is closer to the mirrors than the focus, and displaced away from the open quadrant if the detector is farther than the focus. The amplitude of the displacement is proportional to the distance out of focus.

The shutter focus procedure consists of collecting images from all four open quadrants sequentially, then changing the axial displacement of the detector to the opposite side of the focus point and repeating the measurement. The signs of the displacements should all flip, and by interpolating the common measurements the point of flipping can be independently determined from all four quadrants. Typically the detector is then moved to the interpolated focus point and one more shutter sequence is done, checking that no significant displacement of the image occurs, confirming the focal point.

In orbit no shutters are present. The focus determination is done by minimizing the

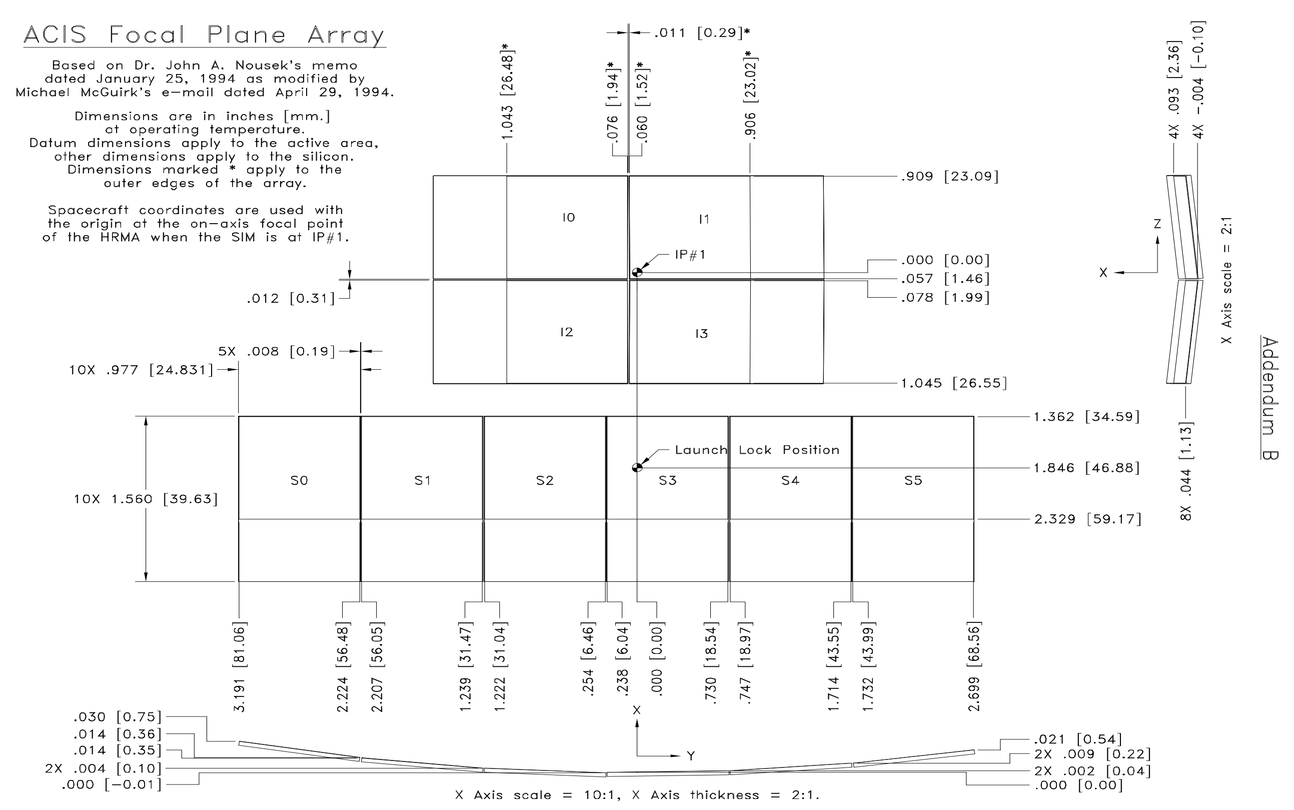
ACIS Focal Plane Array

Based on Dr. John A. Nousek's memo dated January 25, 1994 as modified by Michael McGuirk's e-mail dated April 29, 1994.

Dimensions are in inches [mm.] at operating temperature. Datum dimensions apply to the active area, other dimensions apply to the silicon. Dimensions marked * apply to the outer edges of the array.

Spacecraft coordinates are used with the origin at the on-axis focal point of the HRMA when the SIM is at IP#1.

X Axis scale = 10:1, X Axis thickness = 2:1.

Figure 2.5: ACIS CCD Chip Geometry

variance (second moment) of the image as a function of axial displacement. Several axial points are measured and a parabolic fit made to determine the minimum. Note that this approach is slower because more points must be measured and that more photons are needed to accurately measure the variance as opposed to the centroid of a distribution.

Stray light (i.e. light at any wavelength which strikes the ACIS CCD chips without being brought to a focus by the HRMA) represents a source of potential signal degradation to ACIS. Although individual photons of UV or longer wavelength cannot be individually recognized by ACIS their presence increases the effective readnoise, and hence degrades the energy resolution of the instrument.

The optical blocking filter substantially reduces the UV/optical flux, but in order to eliminate the deleterious effects of stray light it is necessary to limit the stray light striking the CCDs to less than 1 photon per pixel per readout. This level is met by an AXAF

Observatory stray light requirement to limit the maximum ACIS irradiance by stray light to less than 2×10^9 photons-cm^2-s^{-1} over the band 3000 Å to 11000 Å. In addition over the UV range (100 Å to 3000 Å) solar flux must be attenuated by at least 10^{10} and bright Earth flux must be attenuated by at least 10^7.

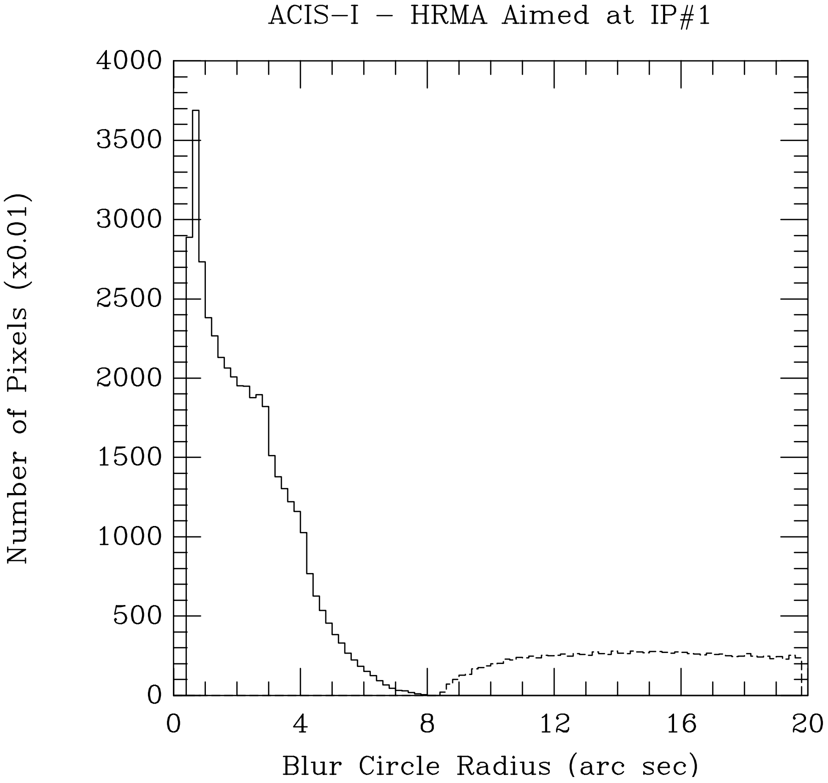

Figure 2.6: ACIS image quality. X-axis in units of arc-sec, Y-axis in units of hundreds of CCD pixels. The broken line histogram includes the S array chip contribution.

The image quality depends upon the mirror type and figure, the ACIS geometry, and detector location and orientation. The four imaging CCDs are not co-planar, but crudely tile the focal surface. A figure of merit is shown in Figure 2.6, which displays the number of pixels for which 68% of the encircled energy is within the radius specified on the horizontal axis — over 50% of the array is better than 2 arc-sec, and 90% of the array has better than 4 arc-sec imaging. (As the mirror shells have different effective area with energy, the blur performance is energy dependent. Fig. 2.6 is calculated in the low energy limit.) This figure includes the intrinsic blur of the HRMA. Other sources of blurring – misalignments (ACIS-HRMA axes; ACIS tilt; HRMA focus) and time-resolution (if the aspect changes over the exposure interval, for example) — are estimated to amount to about 0.3 arc-sec (which add in quadrature, if random, to the data in Figure 2.6).

The total field of view of each array is set by the plate scale of the optical system, which makes each pixel cover 0.49 arc-sec square regions on the sky. After allowing for the narrow gaps between the CCD chips the imaging array covers a total field of view of roughly 16.9 arc min square. Vignetting reduces the effective area of the telescope as the off-axis angle increases, and the imaging performance also degrades. For a more detailed discussion of the imaging properties of the separate arrays see Sec. 2.3.2.2, page 50.

As ACIS can operate up to six CCD chips in parallel, it is possible to include two ACIS-S chip outputs when ACIS-I is located at the HRMA focus. Although the image performance of these two chips will be worse than the ACIS-I chips because of the large off-axis angle, these chips add 50% to the total sky coverage of ACIS in this mode. The blur performance of these chips is shown by the broken line histogram in Fig. 2.6.

2.2.2 Mechanical

The following section describes the structural design of the ACIS Detector Assembly and the Thermal Control Subsystem (TCS). These assemblies are installed onto the Science Instrument Module (SIM) which is attached directly to the optical bench of the AXAF telescope.

2.2.2.1 ACIS Structural Design

ACIS Detector Assembly

The primary components of the Detector Assembly as shown in Figure 2.7 are the titanium collimator, the door and door drive mechanism, aluminum camera body, the connector back plate assembly, the CCD focal plane, and the focal plane support assembly (FSA). The Venting Subsystem, which is not shown in the diagrams, provides a low conductance vent path to the outside of the Spacecraft.

The titanium collimator is used primarily to support the camera body which is 13 inches away from the SIM interface. Titanium was chosen because of its mechanical and thermal properties. It has a high Modulus of Elasticity, low coefficient of expansion, and low thermal conductivity which makes it an ideal choice for this application. The collimator is a one-piece component machined out of a solid billet of titanium and provides for a first mode resonance of the Detector Assembly of 200 hertz. This is significantly above the 50 hertz requirement. The collimator attaches to the SIM with six 0.25" diameter bolts.

The collimator supports the door drive mechanism and includes the door, seal retainer, linkages, drive shaft, bushings and the actuator. The two-bar linkage provides an over-center locked position to hold the door closed during launch. A swing link provides for a

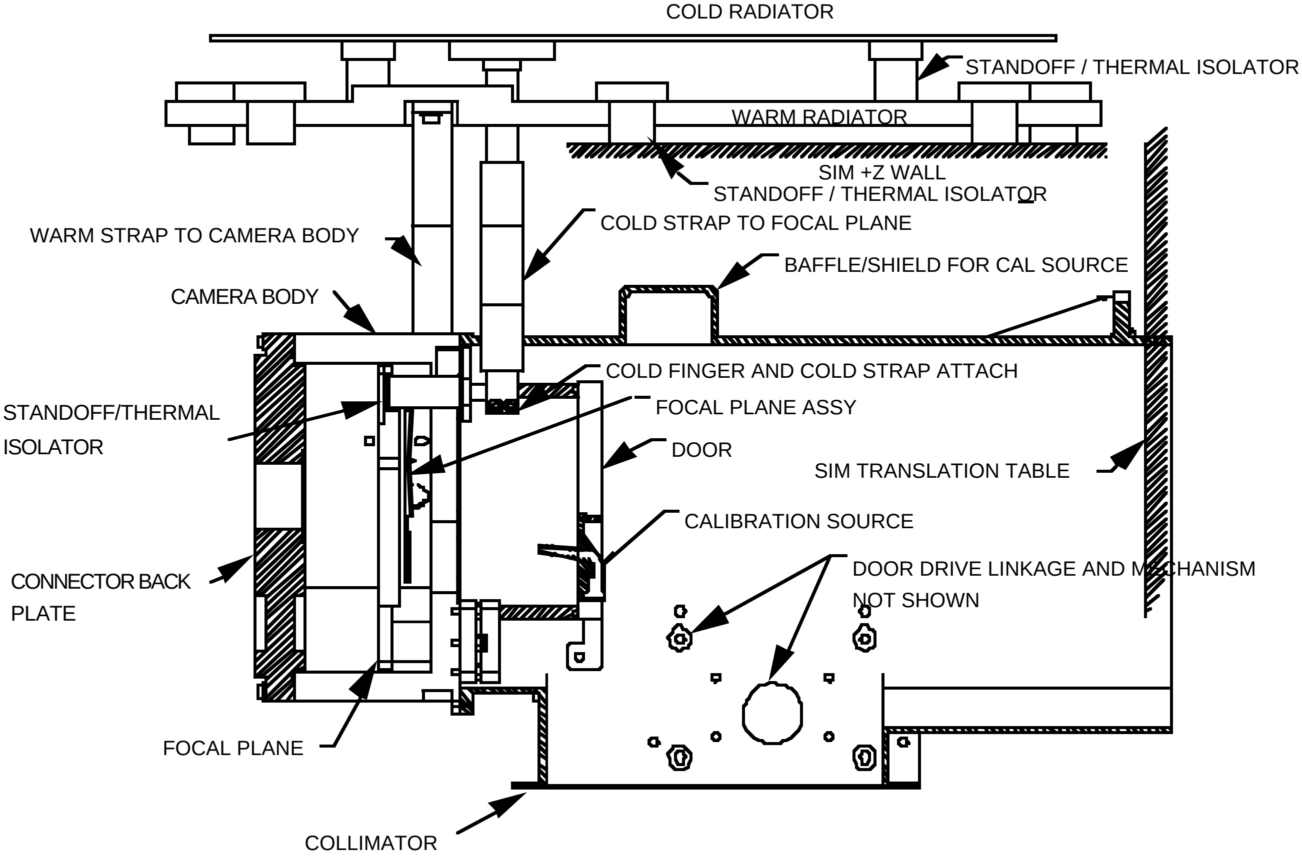

Figure 2.7: ACIS Detector Assembly Cross Section

uniform seating of the door onto the seal retainer. An access cover provides access to the mechanism components during assembly. An externally mounted paraffin actuator rotates the drive shaft and door to the open position once the AXAF is on orbit. To open the door on-orbit, a command is received from the RCTU by the PSMC which turns on an internal heater in the actuator. The PSMC monitors the limit switches and turns off the heater when the door is latched open. Actuator case temperature is also monitored and will turn the actuator heater off in the event this temperature reaches 135 C.

The camera body, which is machined from a single block of aluminum, provides a isothermal and clean environment for the focal plane and Optical Blocking Filters (OBF). Viton O-rings seal all mechanical interfaces so that a vacuum can be maintained inside the detector during ground testing. The vacuum keeps the focal plane and OBF clean and prevents acoustic energy from being transmitted to the OBF during test and at launch.

The side walls are at least 0.5 inches thick to provide radiation shielding for the CCDs. Internal surfaces of the camera body are gold plated. The top of the camera body is a precision ground surface for the FSA standoffs, Alignment Reference Mirrors, collimator top flange and the fiducial lights. The camera body attaches to the collimator with eleven #6 screws.

The camera back plate provides a vacuum feedthrough to the CCDs for the interconnect cabling from the DEA. The back plate is approximately 0.9 inches thick, is gold plated on inside surfaces, and has Viton O-ring seals. Flex cables attach the electrical feed-throughs to the CCDs. Nineteen #6 screws between the camera body and the back plate assembly provide uniform clamping pressure on the O-ring.

The collimator, camera back plate and other surfaces visible to the CCD are coated with gold. This gold coating is sufficiently thick to absorb fluorescent photons produced within the titanium (collimator) and aluminum (camera body), which would otherwise provide a non-celestial source of background when struck by high energy charged particles or gamma rays. The gold is thin enough to produce very few fluorescent emissions.

The beryllium focal plane provides a light weight, isothermal and stable environment for the CCDs. (Beryllium is particularly useful for having no characteristic X-ray lines which can be fluoresced by incident charged particles and reach the CCD sensitive regions.) It is held in place in the camera body with the focal plane support assembly consisting of thermal standoffs, cold fingers and cold stubs. The four thermal standoffs are made of a high strength plastic called Torlon. Each standoff consists of a 0.75" diameter tube which is 1.5" long with .035" walls. A flange with (3) #6 screws attaches the standoff to the camera body. A 0.5" barrel nut clamps the top of the standoff to the cold finger and cold stub flanges. Torlon has excellent mechanical properties including high modulus, low conductivity, good fatigue properties, and low mass. Each standoff also has two O-ring interfaces which seal the standoff flange to the camera body and the top of the standoff to the cold fingers and cold stubs. Two +Z standoffs provide a vacuum tight feed- through for the copper cold fingers. Each cold finger/stub flange attaches to the focal plane with three #6 screws.

A Venting Subsystem is connected to the camera body with a 5/8" ID stainless steel vent tube that attaches to the Large Vent Valve mounted to the SIM. The valve is powered open and closed using the same model Starsys actuator as is used on the door mechanism. A bellows on each side of the large vent valve provides stress relief for installation stresses and isolates the large vent valve from dynamic movement during launch. Low conductance vent valves are used to vent any remaining pressure which is in the camera once it is on orbit. A light shield mounts to the vent tube outside the spacecraft to prevent light from getting into the camera. If necessary the vent tube can be reclosed to eliminate any possibility of light reaching the CCDs through this tube.

Thermal Control Subsystem (TCS)

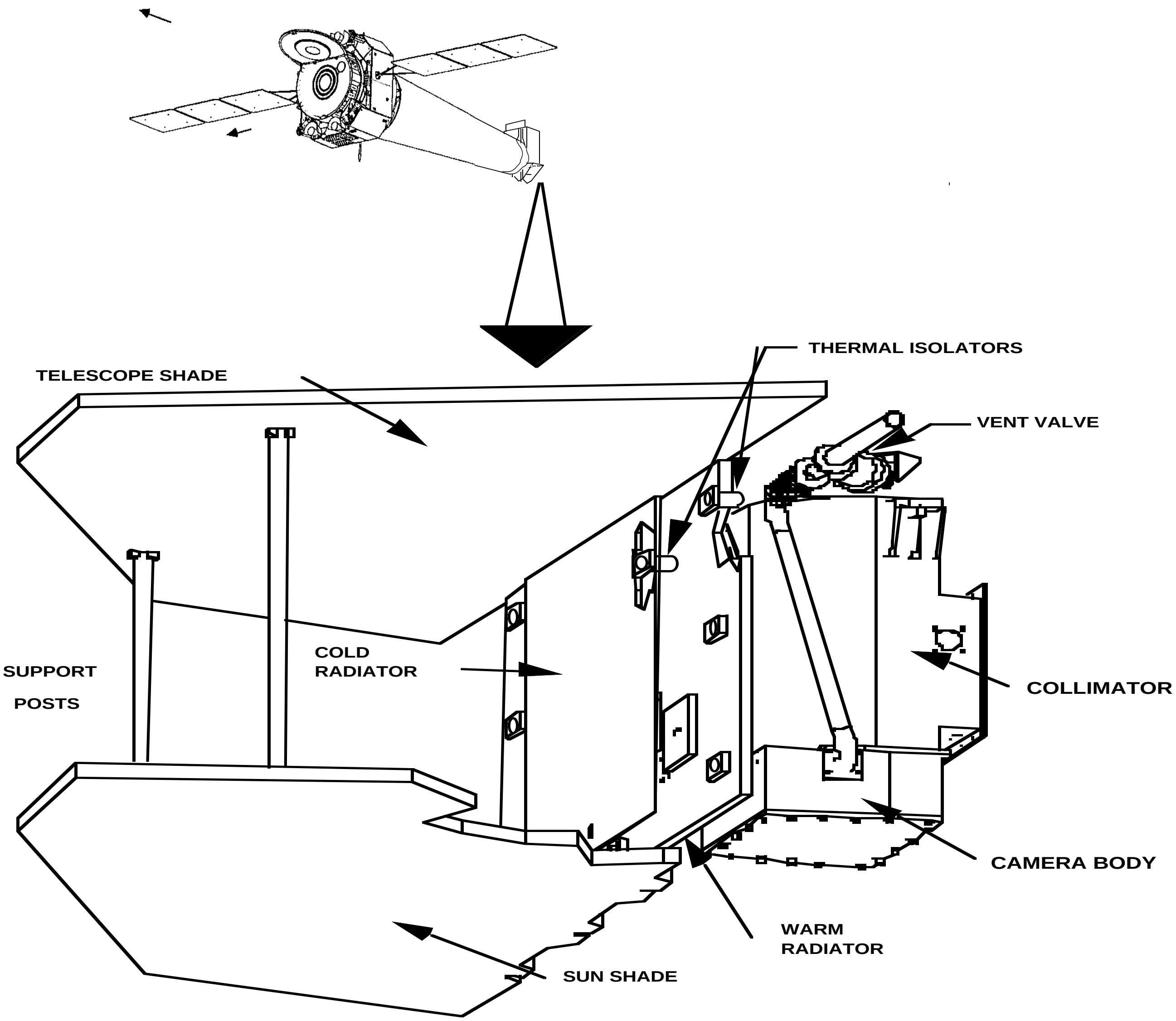

Figure 2.8: ACIS Thermal Control Subsystem (Reverse Angle)

The primary components of the Thermal Control Subsystem are the Warm and Cold Thermal Straps, the Warm and Cold Radiators, the Radiator Standoffs, the Sun and Telescope Shades, and the Shade Support Posts. Figures 2.7 and 2.8 show each of these components.

Each Warm Thermal Strap is used to conductively tie the detector housing camera body to the Warm Radiator while maintaining structural isolation from the dynamic deflections of either the radiators or the detector housing. Each strap consists of eight silver plated copper braids soldered to a copper flange at each end. Two #8 screws provide good thermal and structural interfaces at the Camera Body and the Warm Radiator. Indium foil is used at the mechanical interfaces to improve the thermal interface conductance.

The Cold Thermal Straps are similar in construction to the warm straps. However, a battery clamp is used at the interface with the cold fingers. Two #6 screws provide the clamping force between the clamp and the cold finger. Indium foil is used between the flanges at the Cold Radiator interface with (2) #8 screws providing the clamping force.

The Warm Radiator is a light weight aluminum honeycomb panel approximately four square feet in area. The outer face-sheet is .060" thick aluminum sheet and the inner is .020" thick. The honeycomb between the face-sheets is also aluminum with a 1/4" cell size. Doublers are used at each of the Warm Strap mounting locations. The radiator is held off of the +Z panel of the SIM with (8) Torlon thermal standoffs. The radiator is electrically grounded to the +Z panel of the SIM though 1750 angstroms of sputtered gold on each of the standoffs. Martin Black is used on the outside surface to provide as high an emittance as possible.

The Cold Radiator is a solid aluminum panel with a nominal thickness of 0.030". Its radiation area is 2 square feet and also has a Martin Black outer surface. The radiator has been thickened at the Cold Strap mounting locations for structural support and heat spreading. It is held off of the Warm Radiator with (6) Torlon thermal standoffs which provide a electrical ground path to the warm radiator through the sputtered gold coating.

2.2.2.2 Structural and Dynamic Testing

ACIS has undergone extensive preflight structural and dynamic testing. The ACIS team has prepared models of the mechanical and dynamic behavior of the instrument and detailed analyses of these models have been carried out to verify the models against the test data. As a full description of this testing is out of the scope of this Operations manual we refer the reader to the extensive list of ACIS provided technical documents listed in Table 2.1.

MIT Doc. #	Rev.	Name
36-01303	B	DEA, DPA & Support Structure Test Procedure
36-01501	01	Verification Test & Assessment Reports
36-01504	A	SS Stress & Vibration Analysis
36-01505	B	MIT Fracture & Fatigue Analysis
36-01510.0094		CEI Verification Report Summary - Random Vibration
36-01510.0095		" " - Design Loads
36-01510.0096		" " - Component Loads
36-01510.0097		" " - System Load Factors
36-01520.0010		ICD Verification Report Summary -Mass Properties
36-01520.0038		" " - Natural Frequency
36-01520.0039		" " - Random Vibration
36-01502	01	Technical Analysis & Models
36-01502.01	A	LMA Dynamic Analyses & Tests
36-01502.02	A	LMA Stress Analysis

Table 2.1: ACIS team provided documents concerning structural and dynamic testing, and structural modelling and analysis.

2.2.3 Thermal

The necessity to cool the CCD detector is determined by the requirement for low noise. At ambient temperatures, thermal excitations cause signal charges to be stored in every pixel. The random fluctuations of these processes impose a shot noise that is many times larger than the intrinsic on-chip amplifier noise. The actual optimum temperature is defined by a trade-off of engineering difficulty and performance. The lowest temperatures we require are actually dictated by the minimization of radiation damage effects later in the mission.

2.2.3.1 ACIS Thermal Design

This section describes the thermal design of the ACIS Detector Assembly and the Thermal Control Subsystem (TCS). Both of these assemblies are installed onto the Science Instrument Module (SIM) which is attached directly to the optical bench of the AXAF telescope. Currently, it is planned to launch the AXAF-I into a highly elliptical 10,000 by 140,000 kilometer orbit. With this high orbit, the CCDs will have a higher radiation exposure than low earth orbit. It is desirable to improve the radiation tolerance of the CCDs with increased radiation shielding and lower CCD operating temperatures made possible in this higher orbit. The current design requirement is to operate the CCDs at -120 C. The cooling approach calls for a two stage passive radiator which radiates to deep space. The details of the design are discussed in the following sections.

Detector Assembly

The Detector Assembly has several design features which help maintain the focal plane at -120 C. The titanium collimator provides thermal isolation from the SIM which is at 0 C. Titanium provides the greatest thermal isolation of any commonly used metal and provides half of the total thermal isolation from the SIM. Therefore, the camera body temperature can be maintained at -60 C. The inside of the collimator has been gold plated to provide a low emittance surface to minimize the radiative heat absorbed from the telescope which is at 10 C. (This coating also reduces Ti Kα and L fluorescence from the collimator.)

The camera body is constructed of aluminum to maximize the amount of radiation shielding close into the CCDs and to provide an isothermal environment for the focal plane. The inside of the camera is gold plated to minimize the radiated heat from the camera body which can be absorbed by the focal plane. The temperature of the camera body is maintained with heaters bonded to the -Z side of the housing. The controller for the heaters is located in the PSMC and maintains the camera body at -60±1 C except during bakeout when the housing is heated to +25 C. Thermistors mounted next to the heaters provide feedback to the PSMC to maintain temperature control. Since the camera body is constructed of 0.5” thick (min) aluminum, the temperature gradient is less than

1 C between the heaters on the -Z side of the camera and the warm straps on the +Z side. A 20 layer MLI blanket provides a thermal radiation shield between the Support Structure which is at 30 C and the detector housing which is a -60 C.

Thermal isolation is provided between the -60 C camera body and the -120 C focal plane using four Torlon standoffs. Torlon has a low conductivity and does not contribute significantly to the parasitic heat leaks between the focal plane and the camera body. External surfaces of the standoffs are gold coated (sputtered) to achieve low emittance. The top of the standoffs attach to the cold fingers and the cold stubs. Copper cold fingers provide high thermal conductivity and pass through the +Z standoffs to the outside of the camera. They provide a conductive path between the focal plane and cold straps which attach to the cold radiator.

The primary conduction path for heat from the camera body to the focal plane is through the interconnect flex cables. Copper cross sections have been minimized in these cables and the cables have been formed in a S-bend to maximize the length. They also have a low emittance surface to minimize radiation exchange between the camera body and focal plane.

The focal plane is constructed primarily of beryllium which has a very high conductivity providing an isothermal mounting surface for the CCDs. Four RTDs monitor the temperature of the focal plane. Two sets of heaters are used for controlling the temperature at -120±1 C during normal operation and +30±1 C during bakeout mode. The controller for the heaters is located in the DEA. Outside surfaces of the focal plane are gold plated to minimize the radiative heat exchange from the camera body.

Thermal Control Subsystem

The Thermal Control Subsystem (TCS) for the ACIS consists of two passive radiators, thermal standoffs, telescope shade, sun shade and the thermal control surfaces. Cut away views of the TCS can be seen in Figure 2.9. The two stage passive radiators cool the camera housing to -60 C with the first stage (warm) radiator and the focal plane to -120 C with the second stage (cold) radiator. The view to earth is small in this highly elliptical orbit. However, for the cold radiator, heating does occur at perigee when the radiators are facing the earth. The focal plane increases by 10-20 C with full earth IR and albedo, but is back to normal operating temperature within 8 hours. The radiators have no sun exposure and have a direct view of space at all other times enabling low operating temperatures.

The warm radiator is used to reject parasitic heat from the SIM (0 C) and the telescope (10 C) to deep space. The approximately 4 square feet radiator uses a high emittance Martin Black finish to reject 12 Watts to space at a temperature of -84 C for hot case conditions. Only about 2 square feet of the radiator is effective at radiating the heat due to cold radiator shadowing. A 20 layer Multi-Layer Insulation (MLI) blanket provides thermal

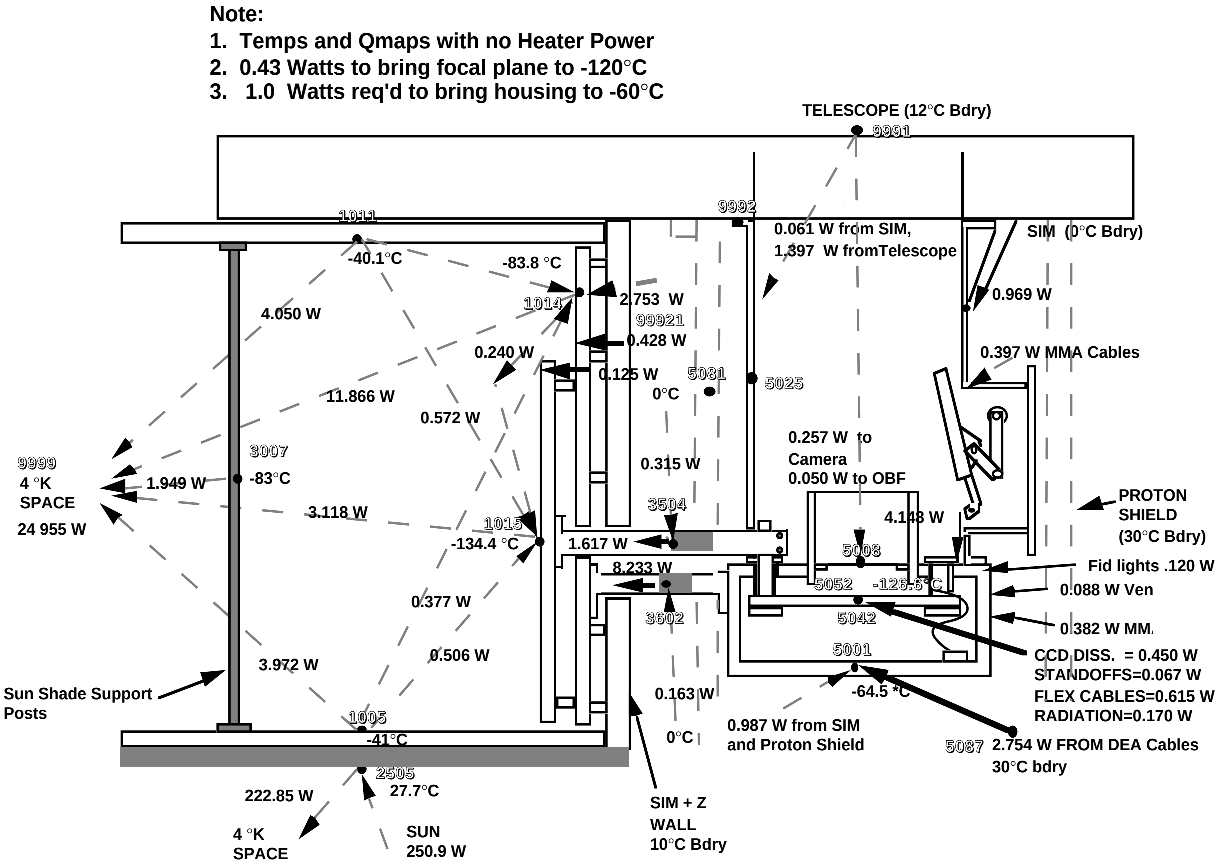

Figure 2.9: Thermal Analysis Results - Hot Case

radiation shielding from the SIM +Z panel.

The cold radiator rejects the conducted and radiated heat (parasitic) from the camera housing and the thermal dissipation of the CCDs. The total area of this radiator is 2.0 square feet and also has a Martin Black finish. This radiator rejects 3 Watts to space at a temperature of -135 C for hot case conditions. A 20 layer MLI blanket provides thermal radiation shielding from the warm radiator.

To minimize the delta T between the radiators and the detector assembly, the radiators are located as close as possible to the focal plane. When the ACIS focal plane is in the X-ray beam, a telescope shade is required to block views of the telescope and the SIM which are at around 10 C. A low emittance gold coating is required on the internal surface of the shade which views the radiators. Goldized Kapton is used for this surface and acts as a mirror to reflect the parasitic infrared radiation (heat) from the radiators to deep space.

Uncoated metallic surfaces will get very hot when exposed to the sun. Since the planned orientations of the AXAF will allow full sun on the aft end of the telescope, a sun shade is required to shield the radiators from the sun. The external surface of the sun shade uses a MLI blanket to minimize absorbed heat. As with the telescope shade, the internal surface of the sun shade will be goldized to provide a low emittance and highly reflective surface.

2.2.3.2 ACIS Thermal Configurations and Modeling

The ACIS Detector Assembly is designed to operate in a 10,000 by 140,000 kilometer elliptical orbit. Under normal operation, the focal plane will operate at -120 C. However, there are other thermal configurations for which the detector will be required to operate on-orbit.

On-Orbit in Shuttle

While the AXAF-I is in the cargo bay and on-orbit, the normal orientation is +Z nadir which orients the radiators toward the earth at an altitude of approximately 130 nautical miles. In this orientation, the focal plane and detector housing will operate at around room temperature. In contingency modes, it is possible that +Z can be oriented anti-nadir. Full sun on the radiators must be limited to less than 30 minutes, followed by a 12 hour cool-down, to prevent the focal plane from overheating.

AXAF Transfer Orbit

While the AXAF-I is being transferred to its final elliptical orbit of 10,000 by 140,000 kilometers, the radiators view of the full sun must be restricted. The limitation on hot temperature extremes are that the radiators shall be exposed to full sun no more that 30 minutes with a 12 hour cool-down. Operations at survival temperatures are also possible depending on sun orientation and survival heaters will turn on.

On-Orbit Normal Operation

During normal operations of the AXAF, the sun will never shine on the radiators. The only potential heating which can occur on the radiators is at perigee when the radiators can get full albedo and earth IR radiation when they are in the nadir direction. The focal plane can heat up during these heating pulses which occur once an orbit. However, perigee heating occurs very quickly and the focal plane temperature will come back under control within 8 hours or by the time an altitude of 60,000 kilometers has been obtained. In order to maintain control of the focal plane 0.43 Watts of heater power is required on the focal plane and 1.0 Watt on the detector housing. Figure 2.9 shows the hot case analysis results with full sun on the sun shade. Cold case conditions simply results in a higher duty cycle of the detector housing and focal plane heaters.

MIT Doc. #	Name
36-01304	Thermal Cycle Test Procedure
36-01306	ACIS Thermal Vacuum Test Procedure
36-01360	Thermal Balance Test Procedure
36-01510.0086	CEI Verification Report Summaries - Thermal Enviroments
" .0087	" " - Thermal Power Modes
" .0088	" " - Thermal Steady State Extremes
" .0089	" " - Thermal On-Orbit Extremes

Table 2.2: ACIS team provided documents concerning thermal testing.

On-Orbit Eclipse

During eclipses the ACIS will be turned off and all heater control will be lost. For extended eclipses the focal plane and detector housing can be expected to reach their survival temperature limits. Survival heaters supplied by the telescope will maintain the detector housing above -76 C which will keep the focal plane above -136 C. There are also survival heaters on the PSMC and Support Structure (to maintain survival limits for the DEA and DPA).

On-Orbit Bake-out

The last mode of operation which can be expected on-orbit is the contamination bake-out mode. Heaters mounted on the focal plane and on the detector housing are used to heat the focal plane to +30 C and the camera body to +25 C. The required steady state power on the camera body is 37 Watts and 16 Watts on the focal plane.

2.2.3.3 ACIS Thermal Testing

ACIS has undergone extensive preflight thermal testing. The ACIS team has prepared models of the thermal behavior of the instrument and detailed analyses of these models have been carried out to verify the models against the test data. As a full description of this testing is out of the scope of this Operations manual we refer the reader to the extensive list of ACIS provided technical documents listed in Table 2.2.

The detailed analysis was done via computer models and the results transferred electronically to Ball Aerospace (BASD) who is responsible for the overall ISIM thermal environment (including ACIS and the HRC). A summary of the results was included as Attachment F of 36-01510.086.

2.2.4 Power

The Power Supply and Mechanism Controller (PSMC) provides power and control to the Detector Electronics Assembly (DEA), Digitial Processor Assembly (DPA) and the Detector Assembly (DA). The major components of this unit are the DPA power supply, the DEA power supply, Vent Valve and Mechanism Control (VVMC), Detector Housing Temperature Control (DHTC), Input/Output EMI cavity (I/O EMI), and Serial Digital Telemetry (SDT).

The power system is composed of two fully redundant sides, known as side A and side B. All of the previously mentioned components are fully block redundant (i.e. A can completely replace B and vice versa), and single fault tolerant (i.e. no single point failure will cause the loss of the experiment), with one exception. The DPA power supply is not fully redundant, but each independently commandable DPA power supply (A & B) is hardwired to power a subset of three FEPs and one BEP (half of the DPA), which allows a graceful degradation of ACIS function in the event of a DPA power supply failure.

The DPA and DEA power supplies provide regulated electrical power to the DPA and DEA electronics. Telemetry monitoring of the power supply voltages and input current monitoring are provided to the RCTU. Primary power is supplied by the AXAF-I spacecraft power bus. Each DC-DC converter is synchronized to a DPA clock to assure that no operational transients occur during the time science data is being taken.

Each power supply output contains overvoltage protection to protect the load from overvoltage conditions, including turn-on transients and transients induced by load switching. Power Supply outputs also contain a current limit function such that source and load are both protected during faulty conditions.

All PSMC power supplies are designed with internal preloads to ensure stable operation with no DEA or DPA load present. Load switching of the DEA and DPA are supported on a board-by-board basis, allowing any number of DEA analog or DPA processor boards to be brought on or off-line during normal mode operations.

The VVMC controls three mechanisms: (1) the door mechanism, which is activated to open and close during ground operations, and opens once on-orbit; (2) the high-conductance vent valve mechanism, which is activated to open and close during ground operations, and opens once on-orbit; and (3) the low-conductance vent valve, which is used to equalize pressure between the DA internal volume and ambient.

Redundant actuator limit switches are employed in both the door and high-conductance valve mechanisms to report mechanism position and terminate when mechanism travel is completed. Actuator temperature is also monitored to terminate operation and preclude possible damage of the paraffin (hot wax) actuator, should mechanical fault conditions exist. Temperature measurements are also continuously reported as analog telemetry during operation of the Detector Housing (DH) door and high-conductance valve mechanisms.

ACIS Configuration	Total Power Consumption
Normal (6 CCDs on)	155W
Calibration (2 CCDs on)	100
Standby (with thermal control)	64
Memory Save (no thermal control)	20
Bake out (initial 8 hours)	168
Bake out (stable operations)	128

Table 2.3: ACIS Power Dissipation for Various Configurations in Watts.

Limit switch positions are reported as digital telemetry, with analog voltage representing the actuator temperature also reported. The VVMC also provides internal housing pressure information to ensure proper system venting during ground and on-orbit operations.

The DHTC is a Pulse Width Modulated (PWM) heater control circuit that uses redundant heaters and thermistors installed on the DA to control the Detector Housing temperature to -60^{o}C±1^{o}C over one orbit during normal mode operations, and +25^{o}C±1^{o}C for on-orbit contamination bake out mode operation. The Thermal Controller circuitry monitors the Detector Housing temperature and reports an analog voltage representing the housing temperature.

The serial digital telemetry provides status of various PTS subsystem states, and in concert with various passive and active analog measurements allows visibility into PTS operational condition. All PSMC control circuitry is commandable by RCTU High Level-Pulse Commands, requiring 'Enable and On' commands or 'Disable and Off' commands to either activate or deactivate any given PSMC function, providing single fault tolerance to inadvertant operation.

The PSMC includes under voltage protection such that PSMC outputs latch off should the spaceraft input voltage drop below specification. The PSMC output then returns to active state when the 'ON' command is reiniatiated.

ACIS normal operations power consumption (with six CCDs active, and the focal plane regulating at -120 C) is 155 W, as measured in several ACIS functional test procedures. ACIS power consumption under various configurations is listed in Table 2.3, derived from document 36-01510.218, "ACIS CEI Specification: Electrical Power Requirements". Note: If all ACIS systems are switched on together the total power consumption is 276 W; this represents a maximum possible power consumption but is neither planned nor useful.

The only known constraint on power switching is a need to prevent ACIS from operating the DEA/DPA electronics and carrying out an instrument Bake-out at the same time. (If such a condition occurred, it could draw enough power to blow the ACIS fuses on the spacecraft.)

The ability to command the focal plane array into bakeout has been removed from the current version of the DPA flight software (Rev. 1.5) stored in the flight EEPROM. A patch to the software must be uplinked before the software can command ACIS to enter a bakeout mode (but there is no hardware lock-out to prevent simultaneous DEA/DPA-Bakeout operation). The DA bakeout mode is not controlled by the DPA software (and hence is not 'safed' by Rev. 1.5). However, as is true for all PSMC commands, an "enable" and an "on" command must both be sent erroneously for a problem to develop.

2.3 Instrument Subsystems

2.3.1 CCD Chips

2.3.1.1 Description of Physical Principles

Figure 2.10 shows a simplified representation of a *frame transfer* CCD. An array of vertical electrodes is formed over the silicon surface and horizontal charge transfer columns are defined by implanted channel stop regions in the wafer surface. These orthogonally aligned elements are produced by conventional MOS fabrication procedures. Application of suitable bias voltages to the electrodes produces a matrix of potential wells which define the CCD picture elements.

The array operates as follows: when an image is focused onto the CCD, photons which penetrate the electrode structure generate electron-hole pairs in the underlying silicon substrate, and the signal charges are stored in the potential wells beneath the electrode structure (gates). After an appropriate image accumulation time, clock pulses are applied to the electrodes to shift the potential wells and their associated charges across the device. Rows of data are moved one-by-one in parallel to the output register with each parallel clock pulse cycle. Each row placed in the output register is then moved pixel-by-pixel to the output amplifier, where it passes as an analog signal to the signal processing chains. At the end of each pixel clock cycle, the charge measured at the node is uniquely identified with a pixel address. For incident light in the visible band, the charge magnitude is proportional to the illumination level at the pixel.

The electrodes are generally arranged in two groups; one group is fabricated over the top half of the array, and a second group over the bottom half. This latter half is shielded from light/X-rays, and is used to store successive image data frames previously collected in the top (labeled 'image' in Fig. 2.10) section. This mode of operation is generally used for TV imaging and is called the *framestore* mode of operation. This eliminates the requirement for a mechanical shutter to shield the array during readout, since the data transfer from

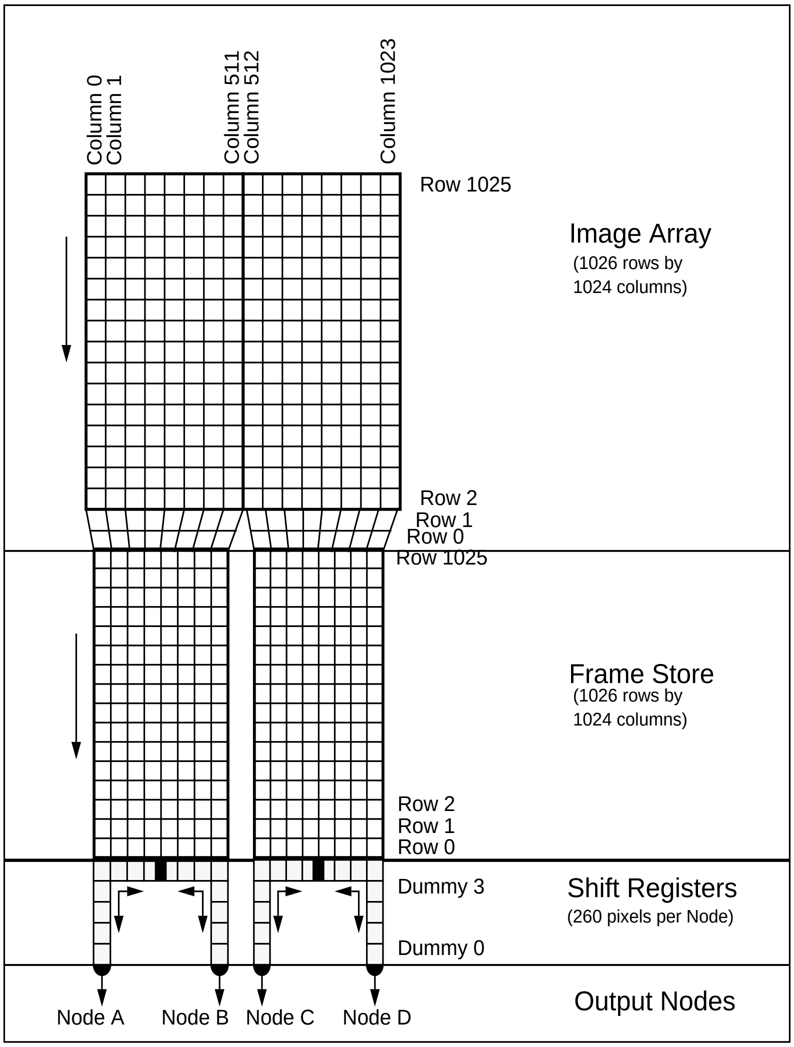

Figure 2.10: Schematic diagram of ACIS frame transfer CCD

image to store section is accomplished in a fraction of the time (msecs) taken to read out the data in the array.

A visible light photon releases only one electron-hole pair, and consequently many photons must be collected in each pixel for a measurable signal to be produced. Therefore, at visible wavelengths CCDs are used as integrating detectors, and typically the astronomical image exposures are several minutes long. Conversely, a single X-ray photon has sufficient energy to form multiple electron-hole pairs through the process of secondary ionization by the primary photo-electron. An average of one electron-hole pair is liberated for each 3.65 eV of photon energy absorbed (this figure varies slightly with temperature). The charge liberated by single X-ray photons ($\sim$100-1000 electrons) is easily detectable if the amplifier noise is low enough. Therefore, at X-ray energies, CCDs can be used as photon counting detectors, with the measured signal charges proportional to the photon energies.

This use as an imaging X-ray spectrometer requires that no more than one photon is incident on each pixel in any image frame, which imposes a requirement that image collection times be limited to $\sim$seconds for typical astronomical applications. In addition, the signal charge must ideally be completely collected within the original pixel, transported to the output node without losses due to imperfect charge transfer efficiency (CTE), and measured without degradation by device readout noise.

Each of these requirements places special demands on the detector structure, and complicates the analysis of the data produced by the device. Charge collection efficiency is a function of the electric field strength at the site of X-ray absorption and is better in devices fabricated from higher resistivity material. Charge collection efficiency also improves as the pixel size increases. Even in high resistivity devices with large pixels, however, a significant fraction of all X-ray interactions will deposit charge in more than one pixel. A crucial consequence of imperfect charge collection is that not all detectable interactions yield useful spectroscopic information. Since the distribution of charge in a group of adjacent pixels is an indicator of the efficiency of charge collection, maximum spectral resolution can only be obtained if a multiplet of pixel values (usually a 3-pixel-by-3-pixel square neighborhood) is analyzed for each event. Moreover, one can trade spectral resolution for detection efficiency by varying event analysis parameters. (Analysis of pixel multiplets also provides a means to discriminate between X-ray photon events and background events produced by high-energy particles.)

Charge transfer within a CCD is subject to inefficiencies caused by the trapping of signal charge at discrete sites in the silicon. These may be at crystalline defects or at sites with a defect introduced by a manufacturing or design error. The probability of trapping any signal depends upon many factors such as the temperature, clock rate and previous history of charge passing through the trap. In ground-based optical imaging applications there is often sufficient signal in every pixel due to photons from the night sky background that all traps remain filled, and they have a negligible effect on the image data. For X-ray photon counting applications, there is no such background, and the event arrival rate requirements noted above almost *guarantee* that traps will de-populate between the arrival of successive signal packets. Charge transfer losses therefore tend to be more severe for X-ray astronomy. The result is that, even with a charge transfer inefficiency as low as 10^{-5} per pixel, charge packets traversing 1000 pixels will lose 1% of their signal, producing an apparent spatially varying gain function. In principle this is correctable, but the variation of the transfer losses with other parameters, particularly radiation damage, hinder this correction.

A particular case of concern arises when charge transfer is not perfect, and a high photon flux strikes the CCD. In this case charge will be removed from photon induced charge packets, but when a second charge packet arrives some of the traps will still be filled. The second photon thus experiences a different charge transfer efficiency than the first. The output spectrum has poorer energy resolution and the determination of the X-ray energy to charge packet size requires a flux correction term. This problem has been termed 'sacrificial photons' by the MIT group, and detailed studies will be conducted during ACIS calibration and beyond to assess the severity of the problem. Tools to model the effect are described in Sec. 4.5.1, page 158.

The X-ray energy required to liberate a charge pair in a semiconductor is approximately an order of magnitude lower than in gas detectors, hence the potential spectroscopic advantage of CCD detectors. In a silicon device, the FWHM energy resolution in eV is given by

$$\delta E = 2.355 \times \omega\sqrt{r^2 + FE/\omega} = 8.67\sqrt{r^2 + E/32} \tag{2.1}$$

where E is the photon energy, ω=3.65 eV per electron is the charge conversion factor, r the system noise in electrons (which may include readout and dark current noise), and F the Fano factor for silicon (0.115).

Examination of equation 2.1 reveals that the CCD readout noise must be minimized in order to exploit the potential for X-ray spectroscopy offered by the silicon properties. Reducing read noise to $\sim$1 electron results in Fano noise limited performance down to energies of 0.1 keV.

The X-ray energy is inferred from the size of charge packet collected in the CCD (N_e) by assuming proportionality,

$$E = N_e \times \omega \tag{2.2}$$

Although this simple relation seems to hold at higher energies, recent work at Leicester University by G. Fraser casts doubt on the precisely linear nature of this energy response, especially at low energy. ACIS will keep abreast of work in this area and fold improved laboratory and theoretical advances into response models.

A potentially larger effect at low energy results from incomplete charge collection in backside illuminated (BI) chips. Because low energy X-rays are absorbed very near to the first surface they strike, BI low energy interactions occur very near to the back surface. This surface has been subjected to potential crystal lattice damage in the process of removing the substrate material. Preliminary lab results suggest the possibility that charge from these low energy photons may be lost to these damage sites, resulting in non-linearity of the detected charge to the incident photon energy flux below one keV.

2.3.1.2 Waveform generation

Each charge packet is shifted through the CCD by repeated cycles of clock signals applied to the electrodes of the CCD. Each pixel is covered by 3 electrodes, and the corresponding electrodes over each pixel are connected in parallel. A single row (column) shift is executed by a cycle of the 3 clock phases in the parallel (serial) registers. Operating mode changes which change the frame time or image format are simply obtained by a re-arrangement of the sequence of clock cycles.

There are only 4 basic operations:

- Image section shift
- Store section shift
- Serial readout register shift
- Pixel read cycle

Data are collected in the image section by holding the clocks in a quiescent state (the voltages and polarities of phases might be changed or optimized in flight for engineering or science reasons). While this occurs, previously collected data can be moved in the other sections at will.

After collection, data may be shifted to the store section by simultaneously clocking the image and store sections in parallel (1024 row shifts to clear the whole image into the store section).

The normal mode of readout is then to apply a store shift cycle to place one row into the serial registers, then the serial register is read out by column shifts of this register, interspersed with pixel read cycles. To read out the four amplifier nodes requires each split serial register to be fed with 256 cycles of shift and pixel reads.

The time required to readout a CCD frame, which establishes the intrinsic timing resolution of the detector, is dominated by the pixel read cycle. This requires the amplifier node to be reset to a reference voltage; then the signal charge is clocked onto this node, and the resulting voltage change off-chip must be sampled. To minimize the noise bandwidth, the sampling process must be of order 10 μs long, whereas the shift process can be much faster.

To increase the speed of image readout, unneeded pixels should not be sampled. (This might occur if the scientific motivation were to study only a single point source in the center of the image, for example.) These unneeded pixels may be ignored by repeatedly shifting the serial register without performing a pixel read cycle. Rows may be ignored by repeatedly shifting the store register without performing the row readout. Thus a combination of the correct store cycles, serial cycles and pixel read cycles can be constructed in order to read out only a fraction of the whole CCD frame.

It is expected that the basic individual clock waveforms for each cycle will be adjusted on the ground for optimum voltage swings and overlaps, and would infrequently need to be changed. The user would only have control over the observation mode image format. (See section on observation modes). The actual generation of these programmable sequences to be uploaded to the ACIS instrument is performed by the ASC.

2.3.1.3 Output Amplifiers

Each CCD chip is provided with 4 low-noise amplifier nodes. These are critical for obtaining the best energy-resolving performance of the CCD. These nodes are the limiting source of noise if the rest of the system operates ideally. Physically, the detection node is implemented as an implant within the signal transfer channel, which is connected to the gate of a MOSFET source-follower amplifier. The potential of this node is set to a high positive reference voltage by a second MOSFET switch. When the switch re-opens, signal charge is dumped from the last serial register electrode onto the node and, due to the small capacitance of the MOSFET gate, there is a measurable voltage change developed across the external load of the MOSFET source follower stage.

The off-chip circuits amplify this signal, with a general technique of comparing the samples of the reference voltage level and the signal voltage levels. The differencing process tends to reduce low frequency components that are common in MOSFET amplifiers; white noise components are minimized by proper choice of the circuit bandwidth. However this bandwidth tends to place a limit on the speed of operation of the chip ($\sim$ μseconds per pixel). The equivalent noise charge of these amplifier nodes can be of the order 2 to 3 electrons r.m.s. in this mode. A typical keV X-ray would generate an off-chip signal of $\sim$mVolts, so the noise in the off-chip circuits must be kept very low as well.

2.3.1.4 Radiation damage

CCDs generally exhibit ionizing radiation tolerance comparable with other CMOS circuits. However, various studies have shown that the charge transfer degradation is a more severe problem than conventional integrated circuit damage mechanisms. Experiments with proton irradiation showed that *displacement* damage creates measurable loss of charge transfer efficiency at doses as low as 10's of rads, which is well within the anticipated on-orbit radiation dose projected for AXAF over its lifetime. Hence ACIS will require optimized shielding and radiation resistant CCD architectures to minimize degradation of CCD performance.

To maximize the tolerance to radiation effects, the CCDs must be made with very narrow charge transfer channels to minimize the interaction with the population of traps (generated by the damaging effects of radiation). Operation at the lowest possible temperatures also helps to recover response by increasing the trap emission time constants sufficiently to ensure that the traps will tend to remain filled.

Isochronal annealing studies show that the main population of traps (but by no means all) generated by lattice displacement are Phosphorus-Vacancy centers which retain signal charge for many row cycles when the CCD temperature is $\sim$ 200 K. Cooler operating temperatures prolong the release time constants dramatically so that the traps tend to remain filled between successive readouts.

Additional means of limiting the degradation of energy resolution will be employed by directly measuring the degraded CTE values, which may allow the event pulse heights to be reconstructed by applying a pixel position dependent correction to each measured charge packet. (However energy resolution will still be degraded due to the stochastic loss of charge in the trapping centers.)

Another manifestation of radiation damage is that of dark current generation. The global increase of dark current due to the addition of extra generation sites in every pixel is not expected to be a problem, given the low operating temperatures. However individual dark current *spikes* with exceptionally high local generation rates are also apparently generated by radiation damage, and these will affect the data by adding a local offset and noise in a handful of pixels. These must be mapped, both spatially and with temporal evolution, so their effects can be minimized in data analysis.

2.3.1.5 Flickering Pixels

The feature known as ‘flickering pixels’ was first reported in 1992, but not widely known until the flight of ASCA. With the benefit of hindsight, other flight programs were also able to report on their appearance in CCDs. However the effects of flickering pixels were most dramatic in ASCA; thus an examination of the phenomenon is important for ACIS.

The manifestation is that a number of pixels show unstable states of dark current signature: sometimes the mean signal is comparable with the background level of dark current and sometimes it is at a much greater level. In the former state they do not affect the science data adversely; in the latter they appear as isolated pixel signals resembling X-ray events. If the bright state were stable, the pixels affected could be masked from the data stream through the use of a look-up table, but the instability of the defect prevents this (unless a dynamic monitoring system can be implemented).

The physical cause is poorly understood, but Hopkins and Hopkinson (IEEE Trans Nucl Sci **40**, p 1567 1993) provide the most comprehensive investigation to date. They propose that defect states can exist in different configurations, probably depending on whether the defect is charged or not. The dark current generation rate depends on which state the defect is in. It is hard to extrapolate their data to lower temperatures appropriate for ASCA and ACIS, but the general model is still probably valid.

A bulk displacement damage state may be created by a proton or ion. Depending on the precise nature of the defect type, the energy level within the bandgap, and the energy level's susceptibility to occurring in different charged states, may vary. As a result, over a period of time, any pixel may accumulate a number of dark current generation sites as the damage increases. In addition to an overall increase in background dark current, some pixels may be sites with one or more of the multi-level states. The dark charge generated in those pixels in one frame time therefore will depend on the particular configuration of states in that frame time, so that the accumulated signal may correspond to one of two (or more) generation rates.

There are a number of factors which suggest the problem may be less important for ACIS than ASCA:

1. The operating temperature will be over 50 C lower than on ASCA, and the temperature dependence is steep. Assuming the excess dark current is due to only a handful of states per pixel, the expected reduction in charge generation rate will typically be $\sim 10^{-3}$ times the rate seen with ASCA.

2. The time scale of changes between high and low states will be temperature dependent, so that for any class of defect, the defect will stay in one state longer (pixels will flicker less often).

3. The total time between successive CCD readouts on ACIS will generally be shorter, so that the charge accumulated per frame is lower; also there is less chance for the defect states to change during a frame (a more stable dark signal condition arises).

4. ACIS will be able to employ a bad pixel look-up table to veto bad pixels; also the increased data rate capabilities and event processing power will allow more local diagnostics of the data to be included for ground-based rejection of bad pixel data.

On the deficit side, it is not clear if the lower temperatures might cause a different set of states to be activated on the time scales critical to ACIS. In addition, the different orbit environment will cause a greater proportion of heavy ions to be the species creating displacement damage. It is known that these produce greater damage per particle than low-earth orbit protons, but not whether they will produce a greater proportion of the multi-energy generation states. It is expected that further investigation may reveal a more quantitative explanation of all these effects.

2.3.1.6 Other instrumental CCD effects

With operation at extremely low signal levels and the complex solid state physical phenomena that have variously been seen in CCDs, it is hard to fully model all other instrumental effects that might be present, either at beginning of life or after degradation in orbit.

Bias frame patterns can be seen whereby the absolute signal (in ADC units) measured for nominally empty pixels can change across the array. This can be due to effects such as incompletely subtracted a.c. time constants of the off-chip circuits, interaction of clock feedthroughs with the video signals, etc. Clearly any temporal changes due to thermal drift component degradation might be expected to alter these values with time.

Infrequently there may be light emitting defects which create a local background signal (usually these emanate from the amplifiers or the chip edges). Another local background signal enhancement may be spurious charge generated by an impact ionization process in high fields generated by the clocks.

These and other artifacts may be examined by regular monitoring of calibration frames telemetered to the ground in raw or histogram binned forms.

2.3.2 Focal Plane Assembly

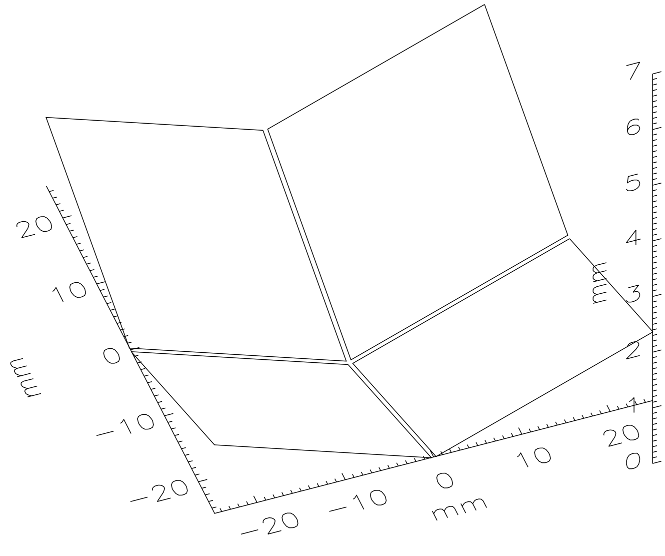

Figure 2.11: ACIS-I Array in Isometric Projection

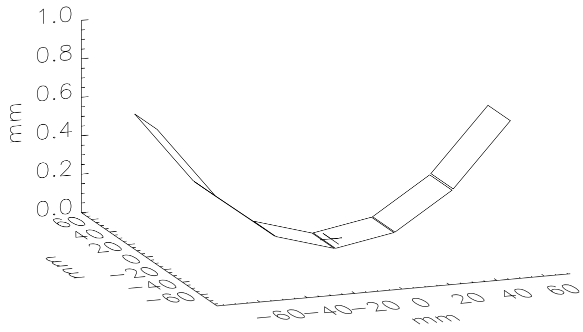

Figure 2.12: ACIS-S Array in Isometric Projection

The CCD chips are arranged into two arrays, optimized for wide field imaging (ACIS-I) and spectroscopy (ACIS-S). Please see Figs. 2.11 and 2.12 to visualize the chip layouts. Note that only the *active* area of the chips are indicated. In addition to the active area each chip has a small border of inactive silicon around the edges, and an area roughly equal to the active area which contains the framestore portion of the chip. The framestore area projects outward from each of the chip areas shown. Please note that the vertical scale on the ACIS-S figure is greatly expanded. The ACIS-S array is nearly flat (less than 0.75 mm rise from the center of the array to the outer edges).

ACIS is brought into the on-axis focus of the HRMA by a one dimensional translation carried out by the SIM. This motion is parallel to the spacecraft Z-axis. Although the SIM can move to intermediate Z translations, the operational plan is to operate ACIS for observations of the sky at three positions, called 'Aim Points'. Two aim points are chosen at symmetric points on the I array and labelled IP#1 and IP#2. IP#1 falls on the I1 chip; IP#2 on the I3 chip. The other aimpoint falls on the S3 chip, and is used for gratings observations and narrow field imaging.

Table 2.4 contains the corner coordinates of each of the ten CCD chips, given in millimeters, in the spacecraft coordinate system. The origin of the coordinate system is the on-axis focal point of the HRMA, when the SIM is located at IP#1.

2.3.2.1 I Array

2.3.2.2 I Array Imaging Performance

The optimal imaging performance of the HRMA does not lie along a plane, but instead occurs along a relatively sharply bent focal surface. This surface (intrinsic to the Wolter Type I mirror design) is different for each mirror shell pair, but each can be approximated

Table 2.4.1. ACIS-I Chip Coordinates

Chip #	X	Y	Z
	(HRMA)	(Dispersion)	(SIM)
I0	1.130	-1.939	23.088
	2.361	-26.484	23.088
	1.130	-26.546	-1.458
	-0.100	-2.001	-1.458
I1	2.361	23.024	23.088
	1.130	-1.521	23.088
	-0.100	-1.459	-1.458
	1.130	23.086	-1.458
I2	-0.100	-2.001	-1.997
	1.130	-26.546	-1.997
	2.361	-26.484	-26.543
	1.130	-1.939	-26.543
I3	1.130	23.086	-1.997
	-0.100	-1.459	-1.997
	1.130	-1.521	-26.543
	2.361	23.024	-26.543

Table 2.4.2. ACIS-S Chip Coordinates

Chip #	X	Y	Z
	(HRMA)	(Dispersion)	(SIM)
S0	0.744	-81.051	-59.17
	0.353	-56.478	-59.17
	0.353	-56.478	-34.59
	0.744	-81.051	-34.59
S1	0.348	-56.047	-59.17
	0.099	-31.473	-59.17
	0.099	-31.473	-34.59
	0.348	-56.047	-34.59
S2	0.096	-31.042	-59.17
	-0.011	-6.466	-59.17
	-0.011	-6.466	-34.59
	0.096	-31.042	-34.59
S3	-0.011	-6.035	-59.17
	0.024	18.541	-59.17
	0.024	18.541	-34.59
	-0.011	-6.035	-34.59
S4	0.026	18.972	-59.17
	0.208	43.547	-59.17
	0.208	43.547	-34.59
	0.026	18.972	-34.59
S5	0.208	43.978	-59.17
	0.528	68.552	-59.17
	0.528	68.552	-34.59
	0.208	43.978	-34.59

Table 2.4: ACIS-I & S Chip Coordinates

by a sphere which crosses the HRMA axis at the on-axis HRMA focal point. The spheres will ideally all touch at this focal point, but as they have different radii, they progressively diverge with distance off-axis.

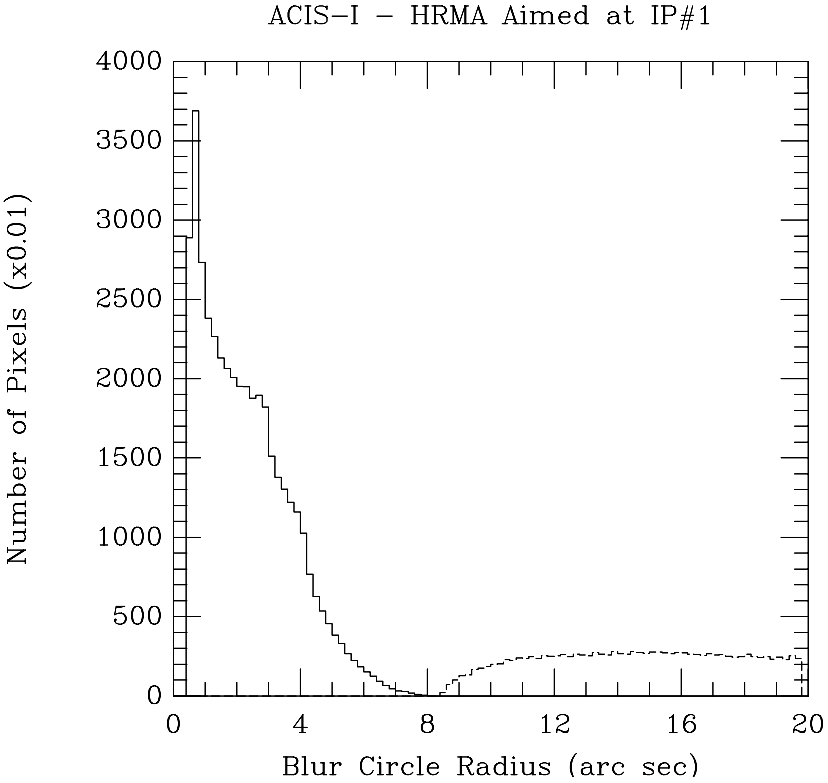

Figure 2.13: ACIS-I Blur Circle Performance: IP#1

The I array achieves better performance than a single monolithic planar detector, because the four CCD chips comprising the array have been tilted to approximate a sphere. As each single CCD is planar, and the blur performance is a function of off-axis angle, and the mirror's relative contribution is weighted by the effective area of that mirror shell (which is energy dependent), it becomes intractable to attempt any analytic prediction of the ACIS imaging response.

Instead a computer program has been developed, (available from Penn State or the ASC) which predicts the ACIS imaging properties. The prediction is based on a HRMA off-axis behavior model (SAO-AXAF-83-014) which describes the ideal rms blur performance. To this is added in quadrature an error term of $0.5''$ to account for alignment and manufacturing errors. Then the resulting blur is combined for all four shells, weighted by effective area.

This program can be iterated at each CCD pixel in the imaging array to produce a histogram of the number of pixels per blur circle increment, as shown in Fig. 2.13 & 2.14. The dotted histogram in each case arises from the use of the inner two chips of the S array to enlarge the imaging field of view. (These two chips provide degraded spatial resolution

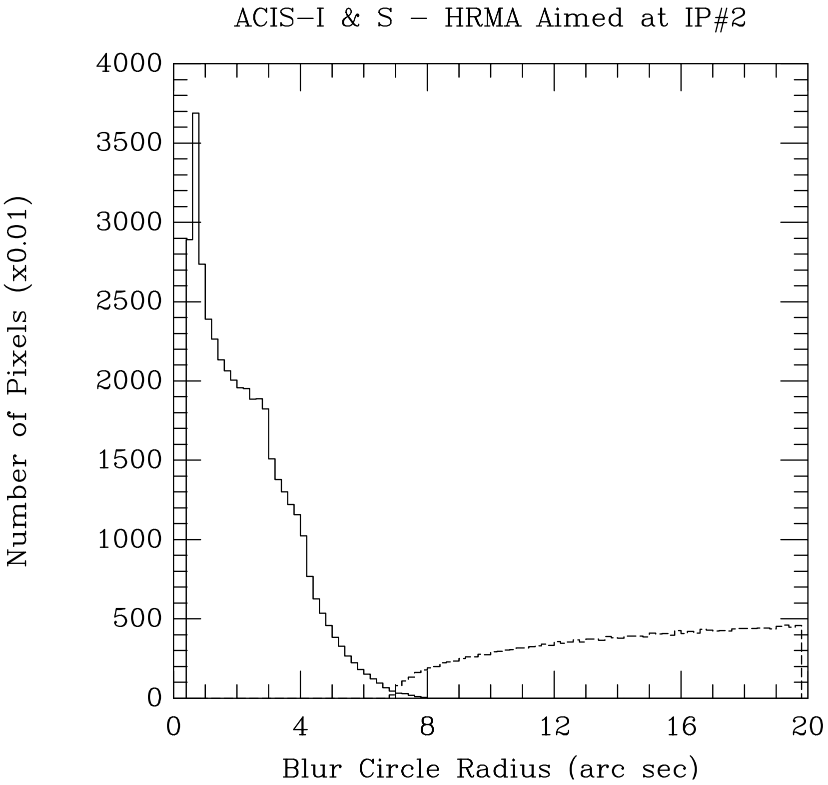

Figure 2.14: ACIS-I Blur Circle Performance: IP#2

because there are located substantially off-axis and not along the optimum imaging surface.)

Note that the S array chips provide some locations with blur performance worse than 20″ radius, but the plots have been cut off for scaling convenience. Also note that the two imaging aim points have been chosen at symmetric locations on the I array. This means that the predicted performance of the I array chips is identical for the two aim points. The sole change is that the two active chips in the S array are farther off axis at IP#1 than at IP#2, thus the broken line histogram reflects the degraded imaging performance for the S array chips active during imaging.

2.3.2.3 S Array

AXAF carries two gratings assemblies (HEG and MEG) which can be introduced into the optical path just aft of the High Resolution Mirror Assembly (HRMA). These transmission gratings disperse the X-ray light roughly along the spacecraft Y-direction. Elementary optics theory shows that the dispersed light will form focused images along a circle named the Rowland Circle which passes through the undispersed image focus and the grating assembly.

The wavelength of the X-ray light can be determined by the grating equation $2dsin(\theta) = m\lambda$, where θ is the angle of diffraction, m is the order of the image and λ is the wavelength. In the ACIS case the insertion of the gratings will make every point source in the field of view become a linearly elongated image. Undiffracted light is brought to the same focus, regardless of wavelength and forms the 'zeroth order' image. The spectral resolution is therefore given by the spatial resolution of the HRMA/ACIS combination, and not by the intrinsic energy resolution of the CCDs.

The S array configuration of CCDs is intentionally elongated in the Y direction to maximize the wavelength coverage of the CCD array.

When the Low Energy Grating (LEG) assembly is inserted into the light path, all four HRMA mirror shell light paths are covered by the same kind of grating, which are coaligned to nearly perfectly align the dispersion along the Y axis. When the High Energy Grating (HEG) assembly is inserted two different gratings each cover a pair of mirror shells. The inner two shells (P4, P6) are covered with the highest dispersion gratings, and tipped by 5° to the Y axis. These gratings are the High Energy Transmission Gratings (HETG), and are designed for use at the highest X-ray energy (which is why they cover the inner mirrors which have the best high X-ray energy response.) The outer two shells (P1, P3) are covered with different gratings with a factor of two lower dispersion. These are the Medium Energy Transmission Gratings (METG).

2.3.2.4 S Array Imaging Performance

In addition to its utility as a readout device for grating dispersed spectra, the S array has important, complementary imaging functions. As previously explained the ideal grating image resolution occurs on the Rowland Circle of the grating, which is far less steeply curved than the optimum imaging surface. Nevertheless for targets close to the HRMA on-axis image the S array has just as good imaging properties as the I array. The imaging properties of the S array are shown in Fig. 2.15.

Possible reasons to use the S array for imaging include:

- The seams between chips in the I array are closer to the on-axis target point, so if this cosmetic effect is undesired or a tight cluster of sources are observed the S array may be preferable.

- The S array chips are more nearly flat and the characterization of the PSF across the array may be simpler and more accurate than the I array. Astrometric accuracy might be better for this array for the same reason.

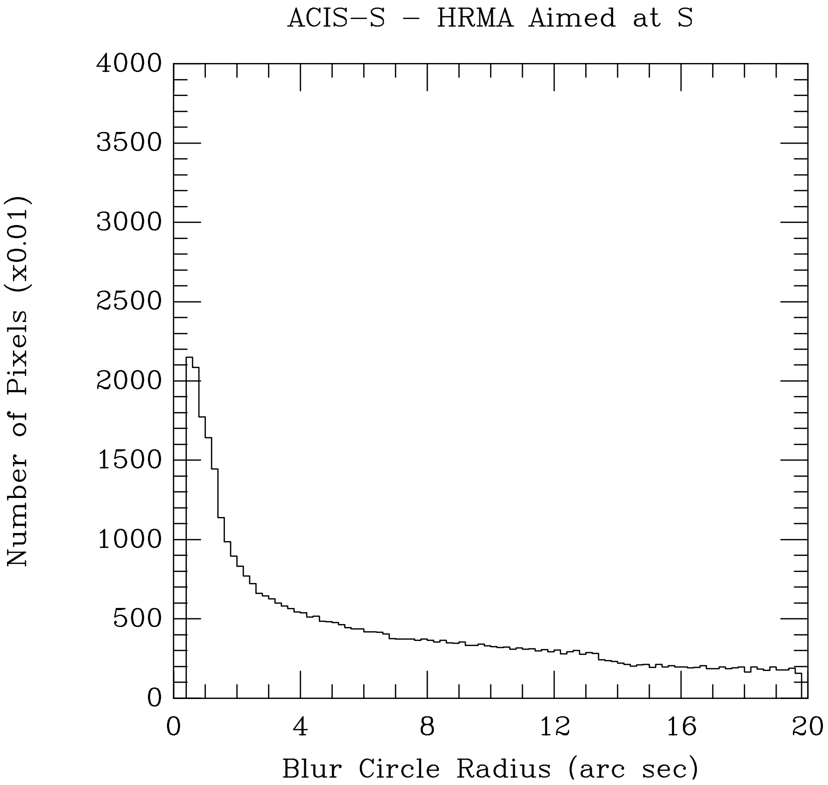

Figure 2.15: ACIS-S Blur Circle Performance with HRMA Aimed at S Aim Point

- The S array contains the only Back Illuminated (BI) CCD chips. The BI chip located at S3 provides a nearly flat (i.e. orthogonal to the incident HRMA beam) detector for imaging studies. The advantage of using a BI chip is a roughly two times higher counting rate for most sources, and even more for soft spectrum sources. The other BI chip is located at the S1 position, and is not expected to be used for direct imaging (but does provide three times higher effciciency for the important O Kα line). Note, however, that the BI chips are less uniform, have significant charge transfer inefficiency, and have worse intrinsic energy resolution than the Frontside Illuminated (FI) chips.
- The S3 chip is the AXAF Launch-Lock detector. If the SIM should fail on launch the S array may be forced to perform both roles of imaging and grating spectroscopy.

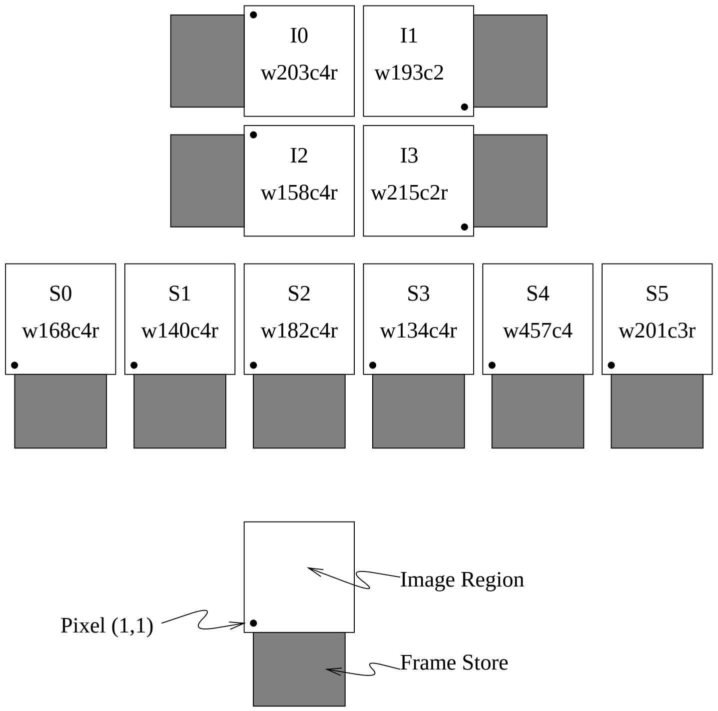

Figure 2.16: Locations and orientations of chips chosen for ACIS flight focal plane.

2.3.2.5 ACIS Flight Chip Locations

The schematic locations of the ACIS CCD chips are shown in Fig. 2.16. Note that readout orientation of the chips varies across the array due to the need to maximize use of the portion of the focal plane closest to the aimpoints.

Chips S3 (w134c4r) and S1 (w140c4r) are BI chips. The other chips are all FI. The chip naming convention is the wafer number (w134, for example), followed by the chip number on the wafer. Chips with a trailing 'r' indicate a 'reflexed' chip, i.e. one which had been bonded to an unreliable flexprint and then rebonded to a flight qualified flexprint. Ones without 'r' were only bonded once.

2.3.3 UV/Optical Filter

The ACIS-I and S arrays are covered by UV/optical blocking filters. Each array has its own filter, mounted along the line of sight from the HRMA to each array. These filters

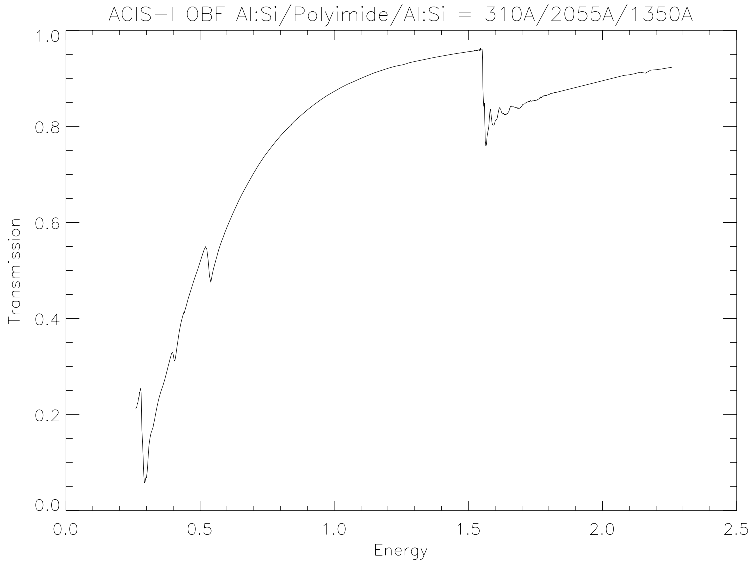

Figure 2.17: X-ray transmission of ACIS-I filter. Filter is composed of 1660 Å of aluminum on a 2055 Å thick free-standing polyimide substrate.

are necessary because CCDs are sensitive UV and optical detectors. The filters remove low energy photons with very high efficiency. The transmission of the filter is set by the requirement that less than 10^{-8} of the incident UV and optical photons are allowed to pass the filter. (However, filters meeting this requirement will pass substantially more light in the near infra-red (800-1000 nm). Unfortunately the only way to block this radiation would be to increase the filter thickness to a point where X-ray performance would deteriorate..)

The ACIS filters are constructed without mesh supporting structures to both enhance the X-ray transmission, and to remove the absolute calibration uncertainty resulting from the mesh interfering with the PSF of the converging beam of the HRMA.

The free-standing filters are relatively large (roughly 2x2 inches for the I filter, 1x6 inches for the S filter). Mechanical strength and high UV opacity is provided by Polyimide, a polycarbonate plastic with a chemical composition of $C_{22}H_{10}O_4N_2$. On each side of the Polyimide substrate a layer of aluminum is applied to provide optical light blocking. The double coat provides electrically conducting external surfaces to prevent build-up of charges.

During engineering tests, it was discovered that equal aluminum thicknesses caused Fabry-Perot interference effects leading to narrow but high spectral transmission windows. Therefore, the flight filters were fabricated with unequal aluminum thicknesses on each side. The flight filter design thicknesses (as measured by Luxel, the filter manufacturer)

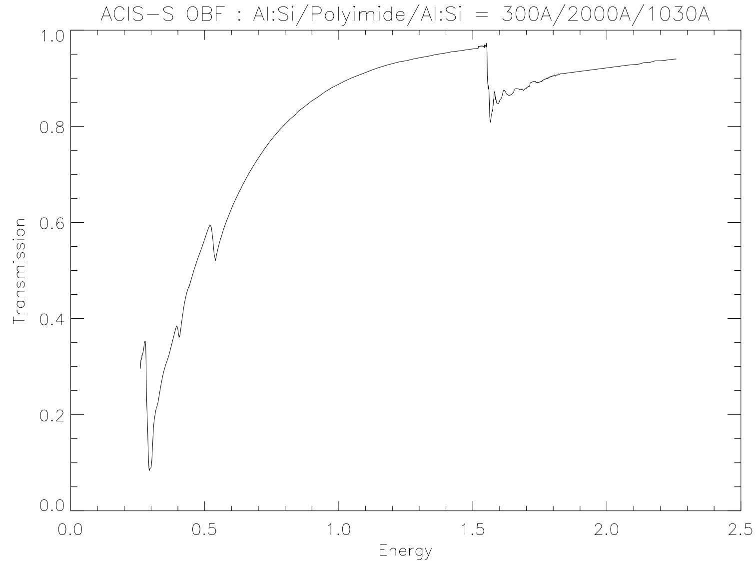

Figure 2.18: X-ray transmission of ACIS-S filter. Filter is composed of 1330 Å of aluminum on a 2000 Å thick free-standing polyimide substrate.

Filter	Al:Si Layer 1	Polyimide	Al:Si Layer 2
I array	310 ± 31 Å	2055 ± 100 Å	1350 ± 50
S array	300 ± 30 Å	2000 ± 100 Å	1030 ± 50

Table 2.5: Flight filter design thicknesses

are shown in Table 2.5.

The filter characteristics were determined by a three stage testing procedure conducted by Penn State. One suite of measurements were conducted at Penn State using Henke tube generated fluorescent X-rays and a CCDID17 CCD provided by MIT and Lincoln Lab. In this suite the filter was mounted in close proximity to the face of the CCD and measured in close approximation to flight conditions (cold temperature and CCD detectors behind them) but the length of time required and the risk of contamination prevented these measurements from being made on the finest angular scales, and limited measurement to flight prototypes only.

The need to operate the CCDs in single photon counting mode limits the brightness of the beam in the PSU measurements. To avoid this limit, synchrotron measurements were conducted; one at the Brookhaven synchrotron, and one at the Wisconsin SRC. At Brookhaven the same photo-diode detectors and beamline used by the AXAF Mission

Support Team for calibrating the HXDS filters and the HRC team for calibrating the HRC detectors were used to measure the ACIS filters. Two locations on each of two non-flight filters were measured at roughly 1000 energies to carefully determine the transmission as a function of energy. Critical to these tests is the fine energy resolution, which provides the most stringent constraints on the detailed models of the transmission as a function of energy. Especially closely sampled were the filter transmissions near the K edges of aluminum, oxygen and carbon, where XAFS (X-ray Absorption Fine Structure) effects are important.

At the SRC many more spatial locations were sampled at just four energies. These measurements were made at a very large number of points on the flight filters and on the Brookhaven filters, using a small rectangular aperture (roughly 0.76 mm x 0.76 mm), and a non-imaging, non-energy-resolving photo-diode. At least two measurements were made on every AXAF dither range sized region on the filter. The high incident flux from the synchrotron allowed high precision transmission measurements to be made in only 1.5 second.

Results of SRC testing on flight filters has shown that the relative transmission across the filter, at a single energy, can be determined to within 0.1%. Measurements of the same spatial location at five different energies produced agreement with our transmission models to within an rms of 0.34%. See Section 4.2 for a more detailed description of filter test data.

2.3.4 Door

The ACIS door mechanism is a subassembly of the Detector Housing. The Detector Housing Door is remotely activated to open and close during ground operations and open one time on-orbit, once contamination levels inside the AXAF have reached an acceptable level. The motor for the mechanism is a redundant paraffin actuator and has built-in limit switches and latches.

The door mechanism is comprised of a door, actuated through a folding linkage attached to a driveshaft. This driveshaft is rotated by two paraffin actuators with redundant heaters requiring 10 watts each over the operating range of 22 Vdc to 35 Vdc. Actuator limit switches will be monitored to report door position and terminate operation of the mechanism control circuitry. Actuator temperature will also be monitored to terminate operation to prevent rupturing of the paraffin cavity. Temperature measurements will be continuously reported as analog telemetry during operation of the Detector Housing Door. The operating temperature range for the actuator will be -65 C to +130 C. The non-operating survival temperature range will be -76 to +70 C.

The actuator causes rotation of the door, locks it in either open or closed position and indicates the end position of the door. Additionally, the actuator will indicate that it is in a mechanically acceptable state for the next door opening cycle. For the door to fully function, it must press against the door seal retainer containing a sealing o-ring. The entire mechanism is an integral part of the collimator and camera body assembly.

2.3.5 Calibration Sources

ACIS external calibration sources will consist of three radioactive sources rigidly mounted to expose the entire focal plane from a distance of roughly 18 inches (46 cm), while ACIS is out of the HRMA imaging point. ACIS will not have a direct line of sight to the sources during ACIS observations.

Suitable sources have been provided by Isotope Products in convenient packages (the A-2, a 0.5” diameter cylinder, 0.25” high). All three sources will be composed of radioactive ^{55}Fe. One source will directly illuminate the focal plane with Mn Kα and Kβ X-rays from the ^{55}Fe. In each of the other two sources, X-rays from the ^{55}Fe will illuminate a metallic target. The source geometry is such that fluorescent characteristic X-rays from the target illuminate the focal plane. Viewed from the source, each CCD subtends 2.1×10^{-3} ster. Details of the sources are shown in Table 2.6. Note that the output of each source will decay with a half-life of 2.7 years.

Serial No.	^{55}Fe Activity mCi(date) (measured)	Target Material	Principal Line (Energy)	Flux ct s^{-1} CCD^{-1} (August 1998)	Other lines (keV)
SN301	0.055 (8/96)	none	Mn K (5.9,6.4)	45	Mn L(.64-.67),Au M(2.2)
SN802	11 (5/97)	Ti	Ti K (4.5,4.9)	25(est)	Mn K(6.4)
SN702	93 (5/97)	Al	Al K (1.5)	22(est)	Mn K(6.4)

Table 2.6: ACIS External Calibration Source Characteristics

^{55}Fe is a highly compatible calibration source for the ACIS. It causes no CCD background problems and is routinely used in lab calibration. A 500 μCi source will provide 160 cts/sec over a single CCD chip. The needed collimation will reduce this slightly. Tests were conducted at the MIT CCD lab by exposing chips to this flux level to search for long term radiation damage effects on the CCD chip. The total dose at the CCD was found to be less than 10 rads for the entire mission life. The low Z material collimator (aluminum) is sufficient to ensure that little fluorescence is caused by the source. (Low Z reduces the collimator fluorescent yield.)

Two other sources of X-ray calibration lines are available only early in the mission. A contamination monitor source for the HRMA is mounted on the front cover of the mirror assembly. This source will not be visible to ACIS after the sunshade (and front mirror cover) is opened during the Orbital Verification phase, within the first 30 days of on-orbit operations. ACIS will, however, make a measurement of this source in order to measure any mirror contamination up to that point.

The HRMA contamination sources consist of 16 separate sources (one on each of four mirror shells and one on each mirror quadrant). Each source will be a combination of ^{109}Cd and ^{55}Fe, producing the characteristic L lines of Ag (near 3.0 keV), K lines of Mn (near 5.9 and 6.5 keV) and L lines of Mn (near 0.64 keV). Spectra were collected by ACIS from this source during XRCF HRMA/ACIS calibration.

The ACIS Internal Contamination Monitor source is mounted on the interior surface of the detector assembly door. The primary purpose of the source is to check for gross contamination of the ACIS blocking filter and focal plane during initial on-orbit operations. The 10 μCi ^{55}Fe source (measured in August, 1996) emits Mn L (645-670 eV) and Mn K (5.9 and 6.4 keV) X-rays in a fixed flux ratio (about 300:1, as detected with the ACIS UV optical blocking filter in place.) In order to minimize scattering of the emitted X-rays when the door is open, the ICM is equipped with a collimator. The collimator allows only a small fraction of detectors S2 and S3 to be illuminated when the door is closed. The ACIS door can in principle be closed to utilize this source, but the operational risk of failure to reopen is likely to prevent this use in any situation except for extreme emergencies.

2.3.6 DEA Hardware

2.3.6.1 Introduction

The DEA (Detector Electronics Assembly) is the direct electronic interface to the CCDs, providing all the circuitry needed for their operation and to receive their analog output. It provides the clocking information for the CCDs and digitizes the analog pixel data, sending this digitized stream to the Digital Processing Assembly (DPA) for event recognition and processing.

The DEA consists of ten independent, identical subsystems, each controlling a single CCD. A complete subsystem consists of three sections: a ‘driver’ section, a ‘video’ section, and a ‘common’ section. It requires the interaction of all three sections to service one CCD. The driver section provides signal levels, conditions the clock signals delivered to the CCD, and controls the CCD bias. The video section is responsible for amplifying, sampling, and converting analog video data from the CCD into a digital format. This section provides the Front End Processors (FEP) of the DPA with raw digital CCD pixel data for processing. The common section is responsible for receiving and dispatching commands from the Back

End Processors (BEP) of the DPA, and for managing the CCD clock sequencing.

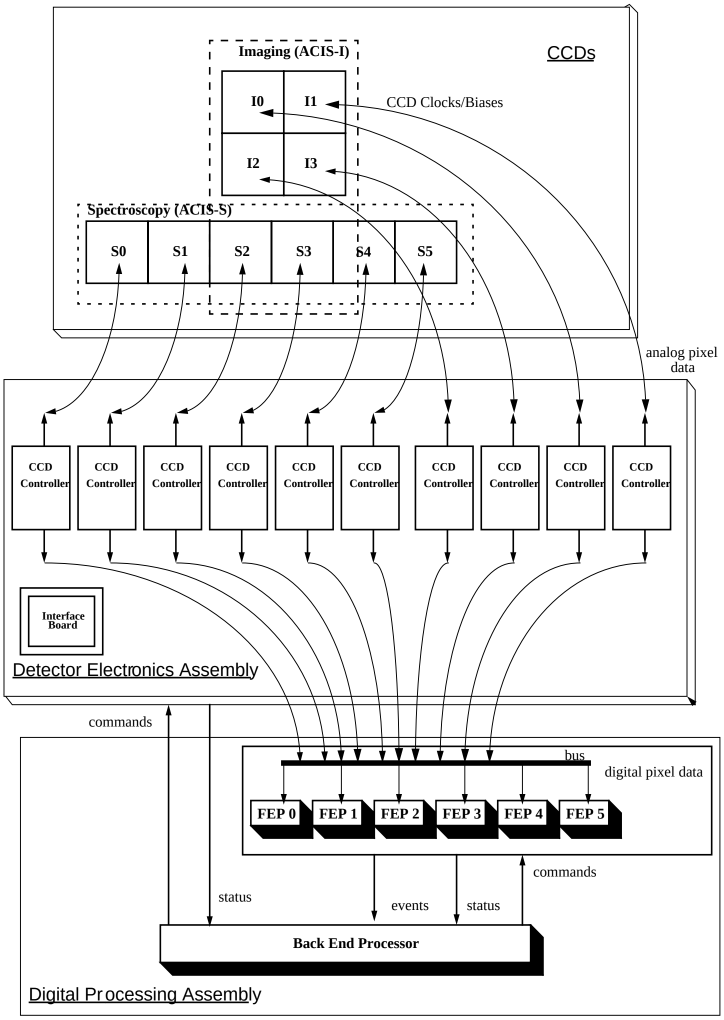

Figure 2.19: DEA Interface Overview

Figure 2.19 illustrates the main components of the DEA and how each component maps to its respective CCDs and to the components of the DPA. There are 40 analog signal chains, one for each CCD output node (with four output nodes on each chip). At any one time, at most 24 analog signal chains are in use. These in turn are multiplexed to six frontend processing chains (one for each FEP - see Section 2.3.7).

2.3.6.2 Interfaces

All ten subsystems within the DEA are identical and independent. They are each interfaced to other ACIS components in the same way. Each subsystem interfaces with the CCD it services via three groups of signals for each CCD: the clocks and the biases, which are driven from the subsystem to the CCD, and the video signals coming from the CCD to the subsystem for processing.

Each subsystem of the DEA interfaces with the DPA via four ports, two to the FEP and two to the BEP. The BEP ports allow the DEA subsystems to receive commands and to send status and housekeeping data. Both ports are identical to ensure fault tolerance and redundancy capabilities. The BEP can talk to the DEA subsystems individually or go into broadcast mode and talk to all ten subsystems simultaneously. The FEP ports allow the DEA to send digitized video data to the FEP from all CCDs simultaneously. Each FEP port can be assigned to any CCD, but at any one time it must be dedicated to a single CCD and can receive pixel data at a maximum throughput rate of 400 kilo-pixels per second.

Each DEA subsystem has a port which allows ground support equipment (GSE) to monitor the CCD video data streams, acting exactly like the FEP ports discussed above. Each port listens to the CCD that the DEA subsystem services.

2.3.6.3 DEA Sections

Driver Section

The Driver Section is responsible for controlling the CCD clock levels and biases as specified by the DPA. Figure 2.20 illustrates the major functions of the Driver Section. The BEP on the DPA sends commands to the Driver Section via the Common Section. These commands control the bias levels and clock levels sent to the CCD. The Driver drives the conditioned CCD clocks using the raw clock timing signals generated by the Common Section's Sequencer.

In more detail, the Driver decodes, executes, and communicates commands from the DPA via a resident Field Programmable Gate Array (FPGA) chip. After the command is decoded, control signals are generated and distributed throughout the driver section to execute various functions as instructed by the command for proper CCD Driver operation. This chip controls the Digital to Analog Converter (DAC) banks, which determine the CCD clock and bias amplitude voltages. These values are conditioned (i.e., amplified, filtered, and regulated) before being passed on to the CCD. Timing information is impressed upon the clock amplitudes via a switching network, which is generated by the Common Section.

The Driver Section also has the ability to monitor signals which can determine the overall functional health of the Section (housekeeping).

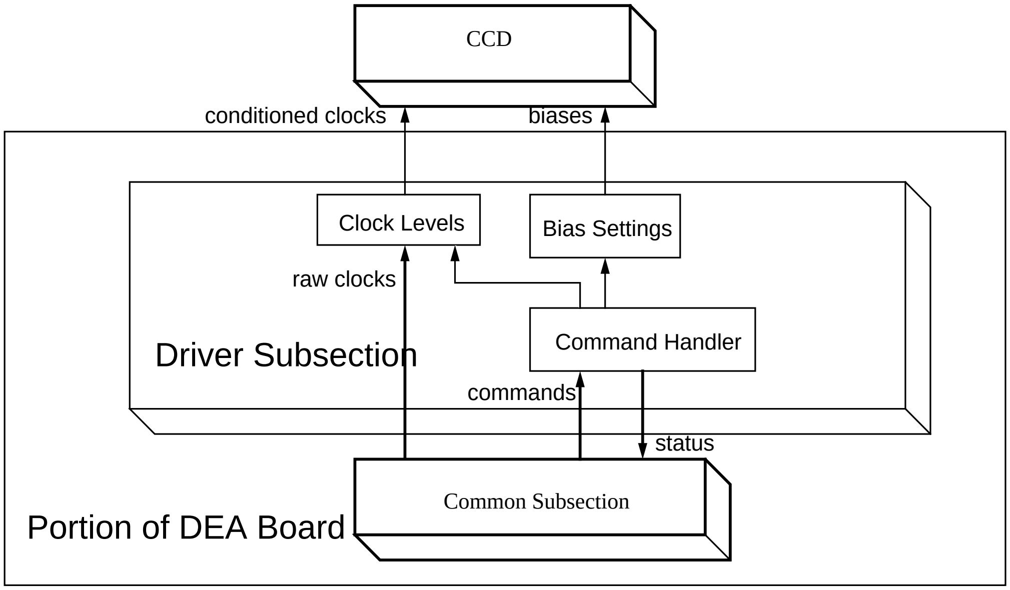

Figure 2.20: Driver Subsection Components

Video Section

The Video Section samples and digitizes the analog CCD pixel data and sends the converted data back to the DPA's Front End Processors for further processing. Figure 2.21 illustrates the major components of the Video Section. This Section integrates the signal from the CCD via the integration control signals provided by the Common Section's sequencer. The Video Section converts the integrated analog signal to a digital pixel pulse height and sends the data to one of the DPA's FEPs to be processed.

The Video Section shares a FPGA chip with the Driver Section to control all command decoding, execution and communication with the DPA. These instructions enable acquisition and digitization of the CCD video outputs.

The Video Section contains four independent video chains which process the four sections of a CCD simultaneously. All four video chains require individual offset voltage control. These offset voltages are determined by a set of DAC banks, which are set by the FPGA chip as instructed by DPA commands.

Also like the Driver Section, the Video Section provides housekeeping signals. The power conditioning network on the analog board has the ability to shut down its rail potentials when excessive current is being drawn. This provides a safety feature to prevent

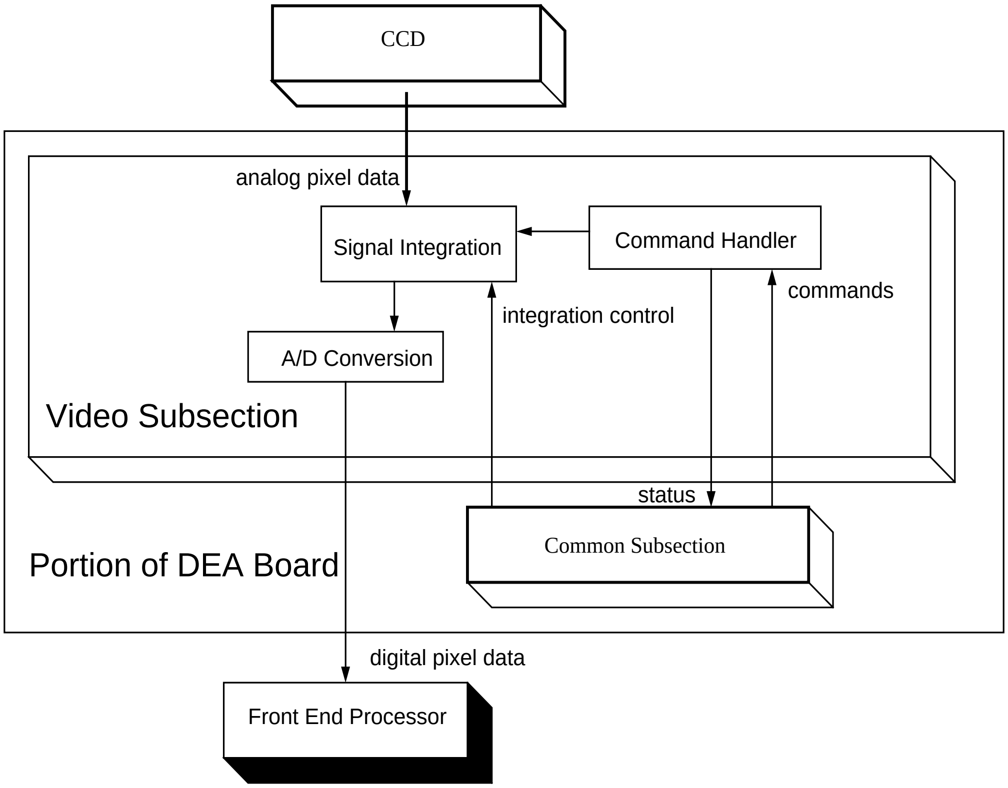

Figure 2.21: Video Subsection Components

overcurrent and failure as a result of a “latch-up”. Depending on the readout mode specified upon initialization, the power on the video chains A and C or B and D can be independently shut down to conserve power.

The Video Section acquires and digitizes four pixels in parallel, each pixel signal coming from one of four output nodes of a CCD. The acquisition process is synchronized with the CCD clocks via the Analog Sequence Bus generated by the Common Section. The X-ray-induced signals are extracted from high noise and bias voltage levels and passed on to the pre-amp before digitization. The pre-amp can introduce a programmable offset voltage to the data as well as reducing the gain from 1 ADU/e^- to 0.25 ADU/e^-. The data are then digitized, with digital conversion synchronized with the CCD clocks and controlled by timing signals sent from the Common Section. The four video channels are multiplexed into one data stream, which is then synchronized to the BEP clock.

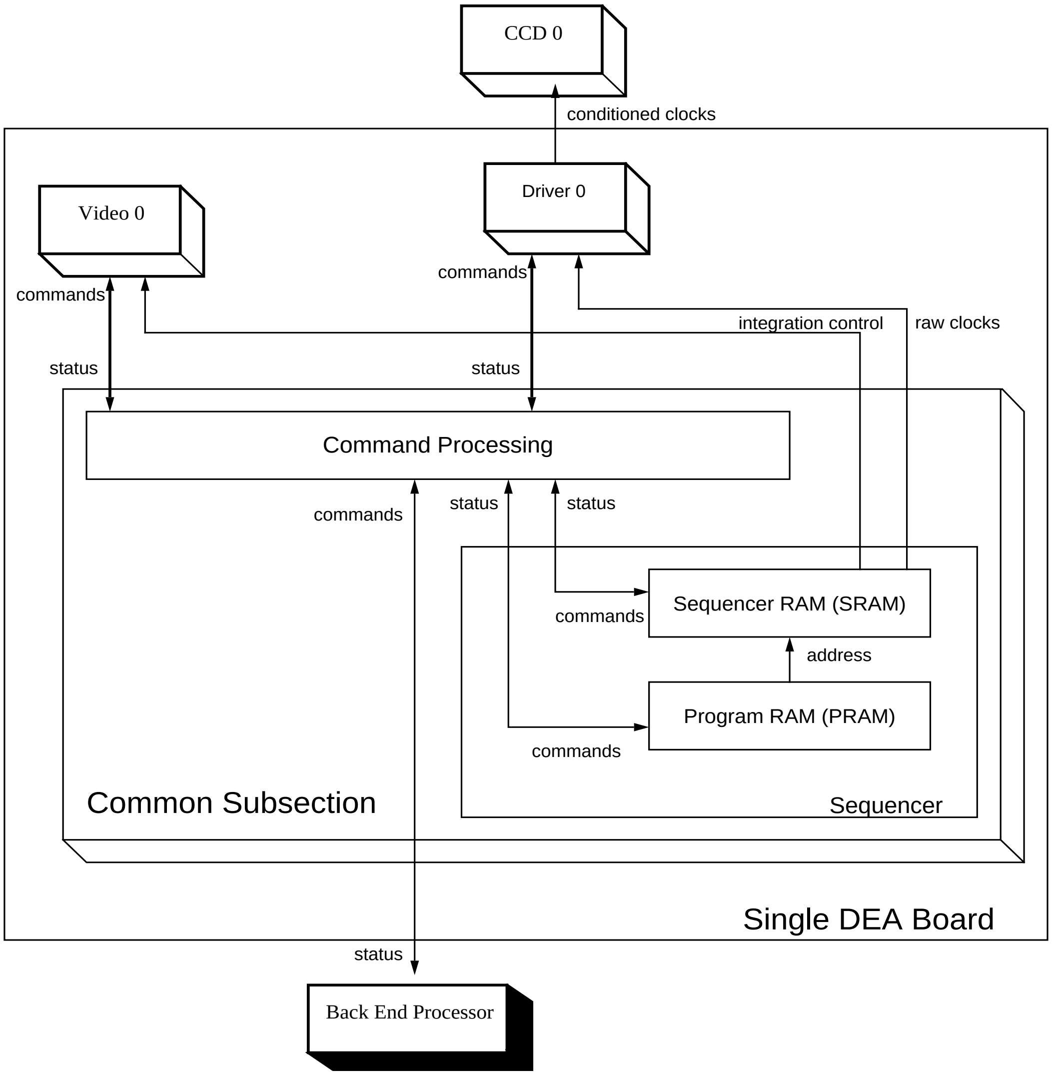

Figure 2.22: Common Subsection Components

As illustrated in Figure 2.22, each Common Section contains a command processor, which receives commands from the BEP, executes commands addressed to it, and dispatches commands to the addressed Video or Driver Section. Status from the executed command is then returned to the BEP. Each Common Section also contains a CCD Sequencer. The Sequencer contains an array of 16-bit SRAM words and an array of PRAM words. The

SRAM and PRAM control the sequencing of the corresponding CCDs.

Each bit in an SRAM word corresponds to a single CCD clock or control signal. When a word is 'executed,' each bit of the word drives its corresponding signal to either a 'high' or 'low' state. When the Sequencer runs a block of SRAM, it fetches and 'executes' each word in sequence. The time between each word is constant and is determined by the Sequencer clock. The BEP is responsible for sending commands to the Common Section to load PRAM and SRAM.

Common Section

The Common Section dictates all intersectional synchronization and sequencing of a DEA subsystem. Its main function is to generate synchronized timing signals and to distribute them via the Analog Sequencer Bus to the Driver and Video Sections. The sequencer signals going to the Driver Sections effectively transport pixel charge from the CCDs to the video processing chains in an ordered manner. The sequencer signals going to the Video Sections synchronize the acquisition and digitization of the pixel charge.

All commands to any particular subsystem go through the Common Section first and then fan out to all its associated Driver and Video Sections. The global housekeeping ADC is on an eleventh board in the DEA, whereby all the multiplexed intersectional housekeeping channels arrive and are converted as status data upon command.

A board level conditioning network on the Common Section has the ability to shut down when excessive current is being drawn. This provides a safety feature in preventing a catastrophic "latch-up".

2.3.7 DPA Hardware

2.3.7.1 Introduction

The Digital Processor Assembly (DPA) is a computer-based on-board data system which receives digitized data from the DEA and commands from the RCTU, processes data according to the commanded mode, and submits the processed data to the RCTU for eventual telemetry to the ground. The DPA is customized to meet the unique requirements of the CCD data acquisition and reduction tasks, and to achieve satisfactory compression of the incident data stream to meet the limitations of the telemetry capacity.

The DPA must be capable of receiving 28 Mbits/sec of raw pixel data, corresponding to an exposure rate of 3.3 sec for six simultaneously active CCDs, and, after post-processing by the DPA, reducing the data rate to conform with the maximum allocated telemetry bandwidth of 24 kbits/sec.

The DPA is composed of two varieties of processor boards.

BEP Backend Processor - which oversees supervisory tasks including uplink, downlink and CCD control, and also performs the X-ray event packetizing.

FEP Frontend Processor - which processes CCD data on a pixel-by-pixel basis, detects candidate X-ray events and passes them on to the BEP.

There are two BEPs in the DPA, each of which is cross-strapped to the other, but only one of which is running at any time (while the other stays in hot standby mode). The BEP tasks are relatively large timescale (i.e. on the order of seconds) and the event processing burden is comparatively low (due to the reduction in raw rate accomplished by the FEP processors). The BEP processors are redundant, and should one fail the other will be able to assume control. A non-volatile copy of the flight software resides on each BEP processor, a portion of which is downloaded to the FEP processors as they are booted.

There are six FEPs in the DPA, each listening to a selected DEA board. Control of which DEA board is active is handled by the DPA as the result of commands from the ground link. Should an FEP processor fail, then ACIS can only process data from five CCDs, but the CCDs can be *any* of the ten CCDs in the total flight array. Hence overall ACIS performance can be compensated by reassigning FEPs using software commands.

The overall functional interrelationships between the various components of the DPA, the CCDs, and RCTUs is shown in Fig. 2.23.

2.3.7.2 DPA Electronics Design

All processors in the DPA have identical cores: the MIPS3000 RISC CPU as implemented by LSI. It is commonly called the ‘Mongoose’. This is a radiation resistant (Rad-hard) version of the LSI Logic LR33000 (Self-Embedding Processor) which is adapted to the special requirements of space-systems electronics.

The ‘Mongoose’ forms the heart of the DPA processors. The chip itself includes an interrupt controller, a DMA controller, timer/counters, a serial port/debug interface, and cache control. The rest of the electronics contains processor support logic, memory, and dedicated interface circuits. The Mongoose requires little support logic. It has an internal interrupt controller with eight independent interrupt lines. An internal UART is provided. An internal DMA controller allows for autonomous memory to memory data transfer.

The BEP block diagram is shown in Fig. 2.24. There are three 32-bit busses on the BEP boards, all connected to the Mongoose. The I-bus is the Instruction Cache Bus, consisting of 32 bits of data and 20 bits of addresses, accessible via words only. The D-bus is the Data Cache Bus, consisting of 32 bits of data and 20 bits of address, again accessible only via words. The M-bus is the Memory Bus, consisting of 32 bits of data and 29 bits of address, accessible by words or bytes.

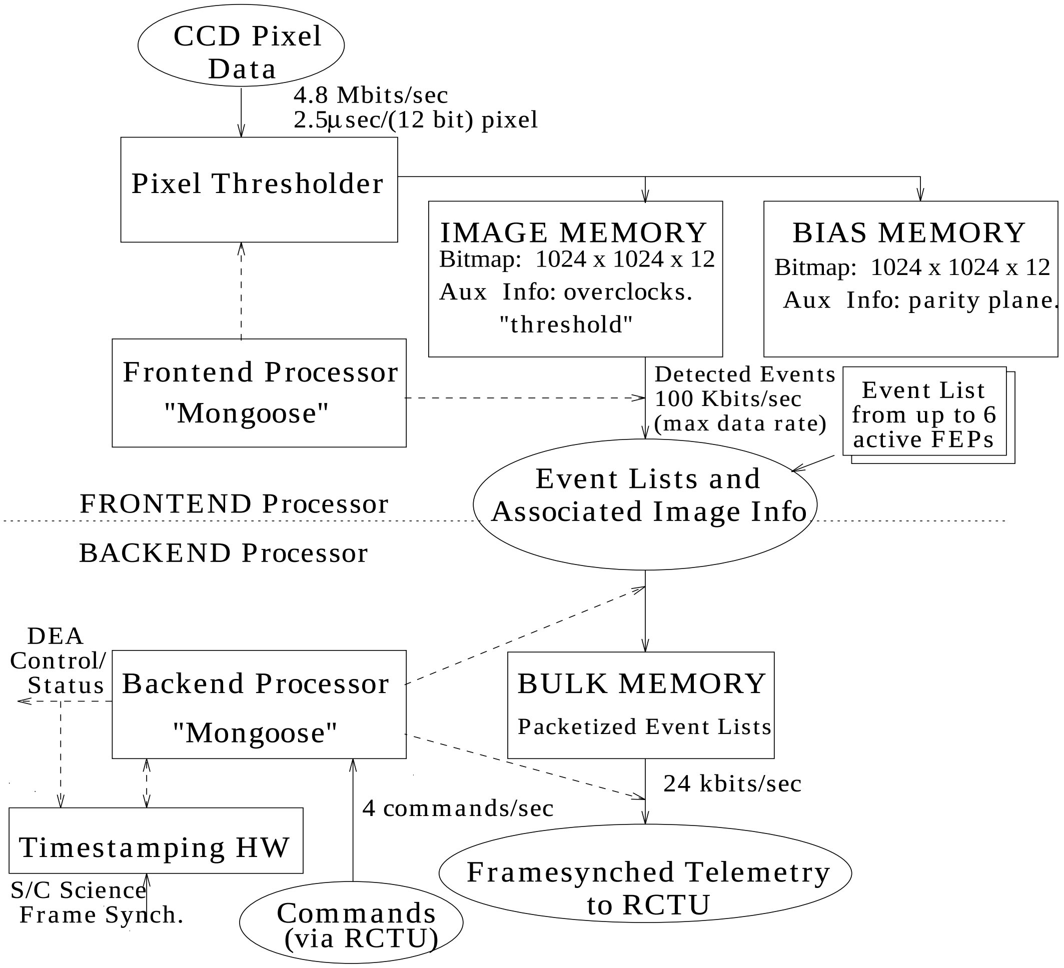

Figure 2.23: DPA Functional Block Diagram

Cached execution allows the Mongoose to take advantage of the 'Harvard Architecture' to simultaneously fetch from the data bus and the instruction bus. All Mongoose instructions are 32-bits, and will normally require one clock cycle.

The M-bus is a general purpose peripheral bus with configurable wait states. Use of the M-bus can slow processor operation due to pipeline stalls.

The BEP has a 512 kByte instruction cache in RAM. This RAM has 35 ns access time to support the 10 MHz Mongoose. The RAM is extremely Rad-hard and SEU (Single Event Upset) immune RAM. The BEP has a 256 kByte data cache. Like the instruction cache, the memory is 35 ns and Rad-hard SRAM.

Bulk memory on the BEP is used for buffering downlink packets before transmission to

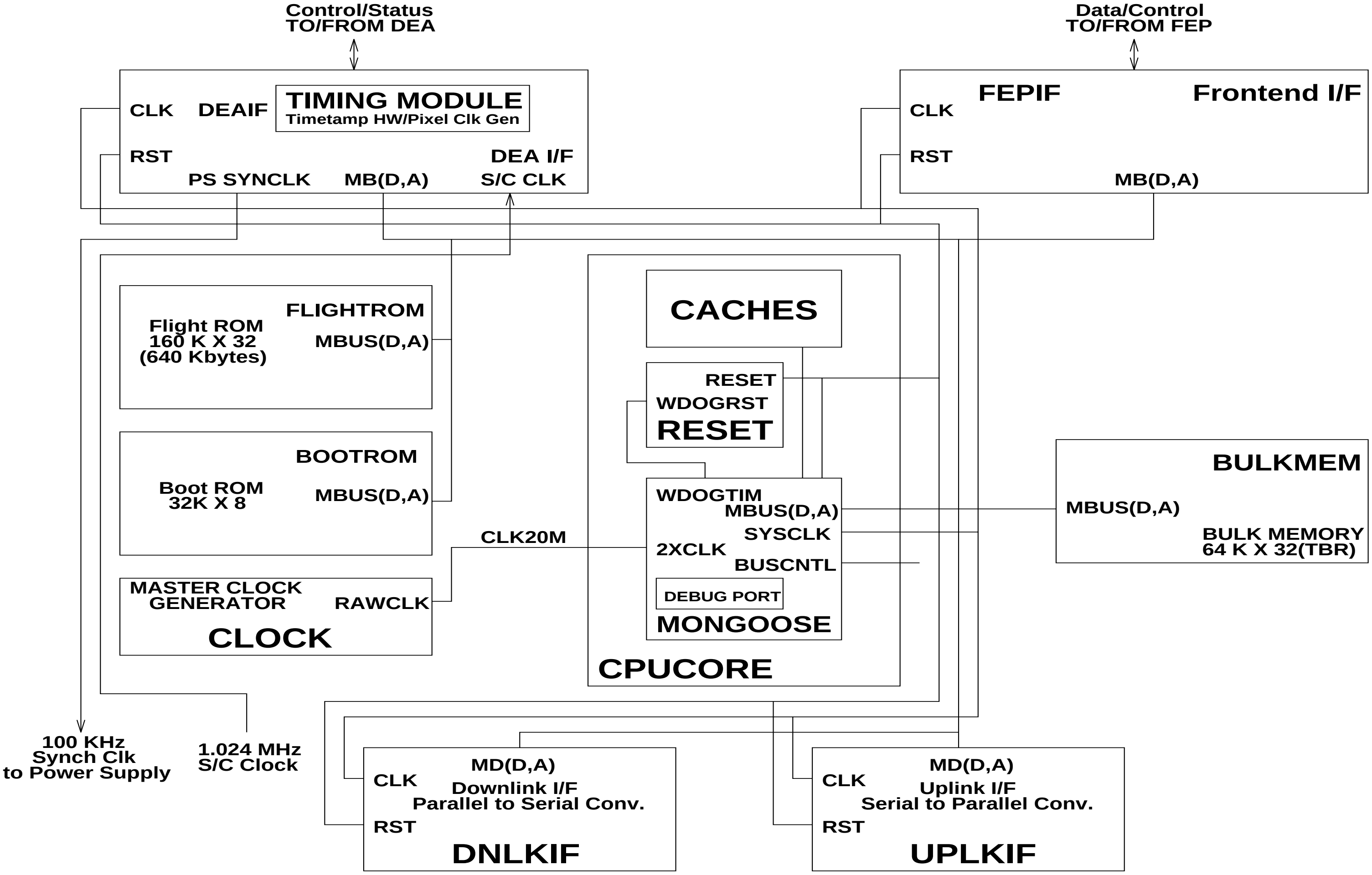

Figure 2.24: BEP Overall Block Diagram

the RCTU. The planned storage is 256 kByte. This amount of storage will buffer almost 10 exposures of event lists at the maximum data rate in faint mode.

The flight software ROM contains a non-volatile copy of both the FEP and BEP flight software. It is currently sized at 1 MByte, with 512 kByte for the BEPs and 128 kByte for the FEPs. The ROMs will be the same used for the Boot ROM.

The FEP block diagram is shown in Fig. 2.25. As with the BEP, the Mongoose forms the heart of the FEP. Because the FEP is responsible for fast processing of the CCD bit map, a dedicated image memory area has been included, which is accessible by both the Mongoose FEP and the DEA pixel processing hardware.

The FEP is a the processor which services (at any one time) a single CCD. Digitized

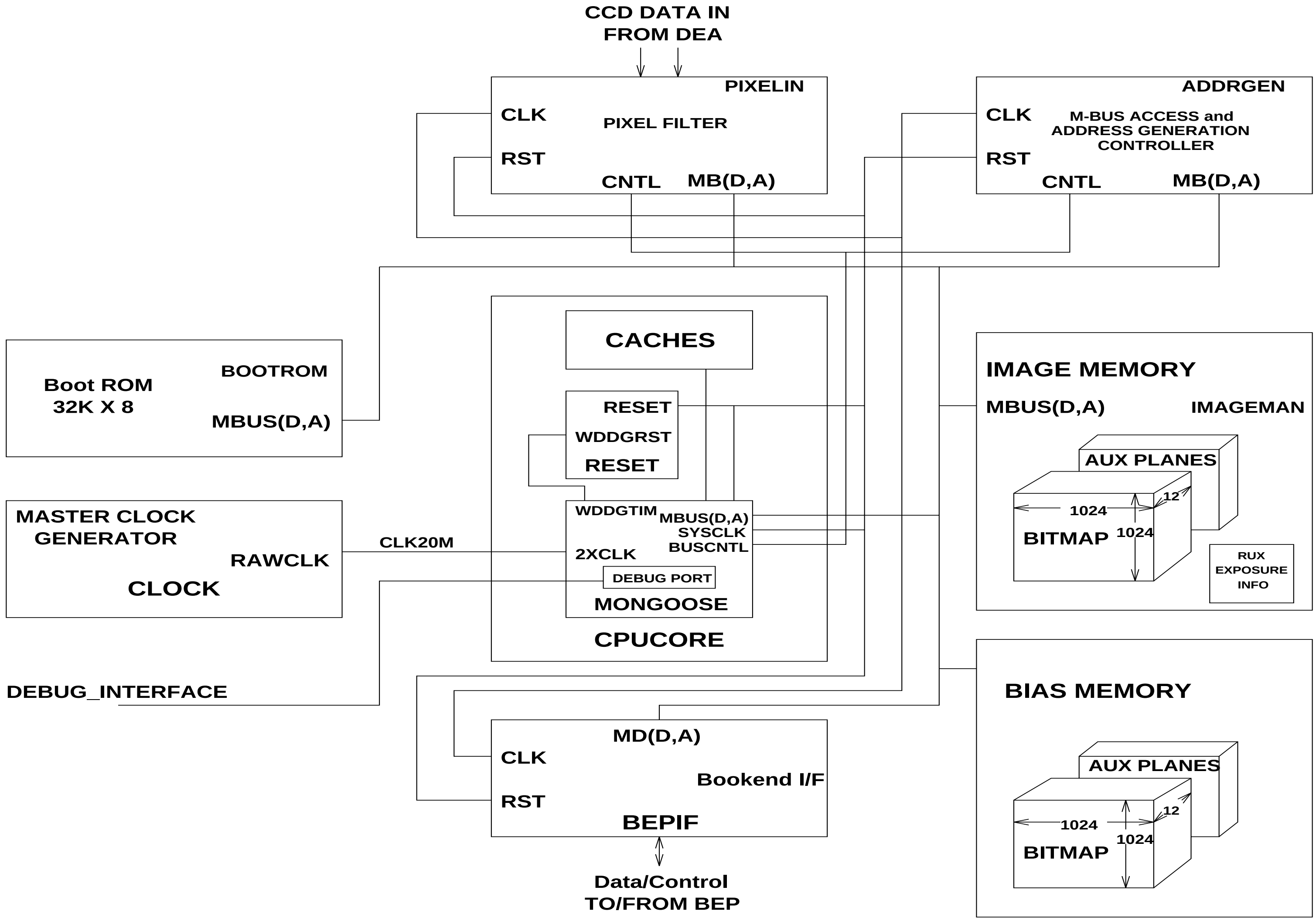

Figure 2.25: FEP Overall Block Diagram

pixel data arrives at the rate of one 12-bit word per 2.5 μsec. The FEP must process this data real-time, and reduce it to a candidate event list, which is sent to the BEP. The FEP contains dedicated hardware which works in parallel to the software, filtering pixel data in order to relieve the load on the processor, and thus meeting the speed requirements on the system.

This dedicated hardware operates on a pixel-by-pixel basis, selecting potential events based on threshold crossings. It also characterizes the dark level of the CCD by generating bias maps of the CCD pixel outputs.

The core processor and busses are identical on the FEP and BEP. Only differences will be mentioned in the following FEP description.

The processor core and bus of the FEP differs from the BEP only by the smaller instruction cache. 128 kBytes of SRAM will be used by the FEP. The pixel processing hardware detects events in the raw pixel stream of 1024x1024x12-bits in each 3.3 sec exposure. The frontend hardware performs the threshold crossing detection and relays this information to the Mongoose.

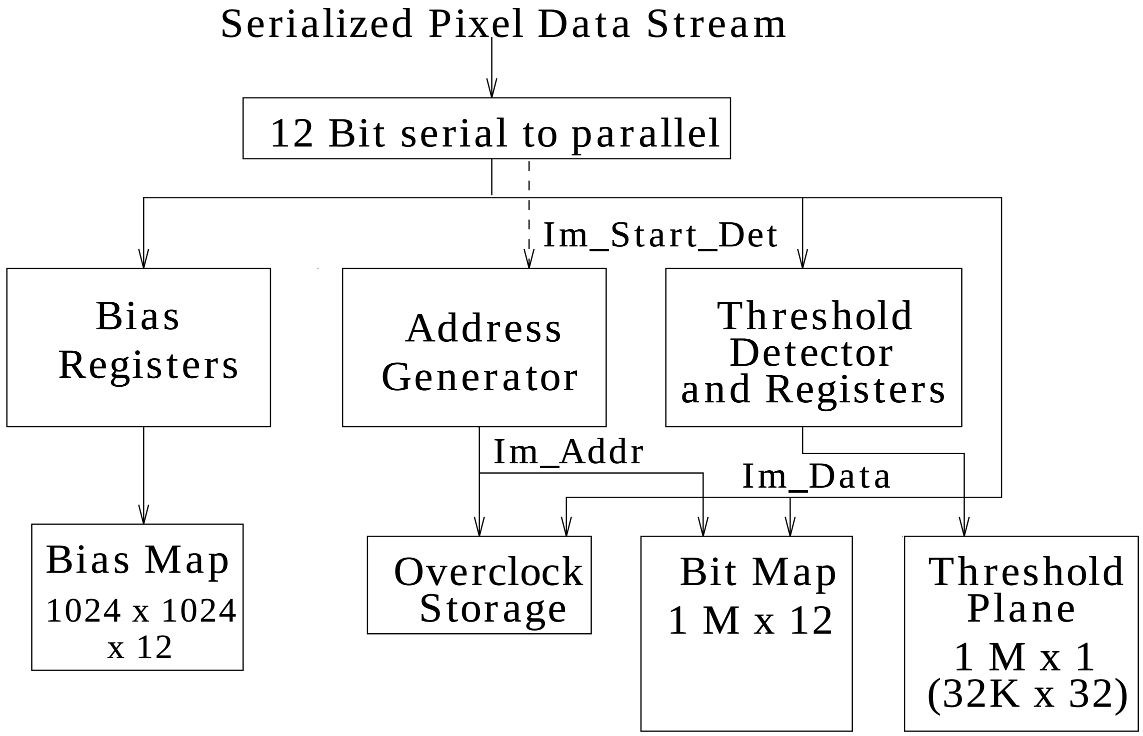

All pixel processing memory is mapped (read/write) into the Mongoose address space.

Figure 2.26: Pixel Processing Hardware Functional Block Diagram

Figure 2.26 shows the logical flow of interrelations in the pixel processing hardware.

2.3.7.3 DPA Hardware Recovery Modes

The DPA processors must be 'rugged'. The design goal was to expect and support occasional crashes and hence reboots due to single event upsets or other radiation induced crashes. The hardware supports graceful and efficient crash/reboot mechanisms.

The DPA is operable following any one single-point failure. It must be modular enough to degrade gracefully if a section of the hardware should fail. Operation following double-point failures is not guaranteed.

Due to the eccentric orbit and the long life of the AXAF mission, the total projected radiation dose on the electronics is significant. In most cases immunity to a total dose of at least 50 kRads was required. Memory devices, especially program memory, have an extremely low single-event upset rate.

The BEP reset circuitry consists of three reset sources: a power-on reset, a watchdog reset, and a discrete commanded reset. The power-on reset charges an RC network with a time constant of about 50 ms. The watchdog reset consists of a 32-bit readable and writable counter internal to the Mongoose processor. Upon reset, the counter is set to a certain value and allowed to decrement. Its end-of-count signal will directly drive the BEP reset. The discrete reset allows a 1-bit pulse command (out of a 16-bit serial digital command) to reset the BEP. This line will be directly driven by the RCTU. The watchdog reset and discrete reset have pulse widths consistent with the maximum required by any device on the board. Local status bits will be provided to the processor indicating if a reset was initiated by the watchdog timer or the command interface (for the discrete reset).

The FEP reset sources are: a power-on reset, a watchdog reset, and a BEP-controlled reset. The power-on and watchdog resets are identical to the BEP versions. The BEP-controlled reset is a dedicated wire driven by the BEP. It is controlled by a BEP read/write control register. Both BEPs will be powered at any one time.

A standby mode will be provided by the DPA, as commanded by the Spacecraft. The average and maximum current allocation for the DPA during standby mode is given in Table 2.3. One likely implementation of standby mode would be to turn off power to all the FEPs. Another might be to stop the DPA processor/logic clocks.

A signal will be sent to the DPA indicating when a Spacecraft radiation monitor has been set. Similarly, a signal will be sent to the DPA when the radiation monitor has cleared. One effect of the radiation monitor will be to cause the DPA to issue a DEA power shutdown command for the CCD components which might deteriorate if exposed during periods of high radiation activity. The spacecraft will also carry a bright object monitor which will similarly affect the DPA. (Note that the action taken when the radiation monitor signal arrives is programmable. ACIS has the capability of ignoring Spacecraft monitor signals if that is desired, by loading an appropriate software patch.)

2.3.8 Flight Software

The flight software for both the FEP and BEP is stored on ROM. This non-volatile copy will be written in erasable electronically programmable ROMs to allow a permanent, radiation hard copy of the software to be rapidly loaded or reset through the boot process.

Total flight software will require 768 kB, 512 kB for the BEP and 128 kB for the FEPs. This software resides in EEPROM on each BEP. The EEPROM can not be changed via ground commands (i.e. it is not reprogrammable on-orbit). However, the software can be "patched", with patches residing in the spacecraft memory.

2.3.9 Other

CCDs are susceptible to radiation damage. The most critical type of damage is primarily introduced by low energy protons causing lattice vacancies, which trap electrons which reduces the charge transfer efficiency of the CCD, and may produce other artifacts such as flickering and hot pixels.

The CCDs have been specially treated to implant a special 'trough' to reduce the effect of this damage, but this cannot remove it entirely.

The CCD camera includes material specifically designed to act as a shield to reduce the low energy proton flux, which has the effect of extending the lifetime of the CCD and reducing the degradation effects associated with radiation damage.

The best information on the effect of radiation damage on X-ray CCDs comes from the ASCA SIS experiment. ACIS will operate considerably colder (-120 C vs. -63 C) and have shorter frame rates (3.3 seconds vs. 4 to 16 seconds). The lower temperature 'freezes' out damage induced traps, by extending the time constant for electron escape from the traps (and hence preventing X-ray produced electrons from falling into already filled traps). The shorter frame time also helps the 'freezing out', and decreases flickering pixel effects by reducing the time for charge to flicker into the pixels, and reducing dark current.

Lab testing of radiation damaged CCDs from proton accelerators suggests these two changes will greatly improve the ACIS CCD resistance to radiation damage effects.

One important source of ionizing radiation is the focussed X-ray beam coming from the HRMA. The opinion of the Lincoln Lab CCD team is that radiation damage effects from X-rays start to be of concern at dose levels of 5 krads. The extremely sharp focus of the HRMA causes most of the flux from a point source to be focussed into a very small number of pixels, thus leading to a rapid accumulation of dose. For 1 keV X-rays the dose per photon is 0.005 rads/photon/pixel. A source like Sco X-1 can reach the dose limit (if there is no dither) in a very short time, so operations will need to exercise care to avoid placing extremely bright sources within the field of view of the CCDs for extended periods. Note that the dose accumulates even if the CCD is not turned on, and even if the radiation is absorbed in the gate (and so does not produce a detected event.)

Chapter 3

Operations

3.1 Modes

The CCD is a powerful tool for simultaneous imaging and spectral data collection. It differs from many previous X-ray detecting instruments in that it must integrate images (rather than responding promptly) and no trigger signal is generated unequivocally indicating the presence of an X-ray or other event in a pixel. Thus the pixel data stream normally requires on-board processing to recognize X-ray events and extract them, otherwise the volume of data would be too large to telemeter to the ground.

The event processing and data packetization post processing offer many parameters or choices which must be made before data can be sent to the ground. The large number makes testing and definition of each possible combination of choices impractical.

Instead we define the various processing choices which can be made under the section 'On-board Data Processing Choices' (Section 3.1.3), and a set of standard choices which we expect to be commonly employed under 'List of Routine Modes' (Section 3.1.4).

Conceptually the easiest way to understand the selection of mode switches is to consider the choices required in order to specify ACIS operation. There are four primary decisions:

- Array imaging point?
- Timed integration, or continuous readout?
- Which on-board data-processing program?
- Is a new bias frame required?

3.1.1 Imaging Point Selection

A critical decision which must be made for each observation is to choose where the on-axis HRMA image will be placed. As the ACIS instrument is located on a translating structure called the SIM, there is one degree of freedom of motion.

Five different SIM positions are planned for normal operations. Each is characterized by the intersection point of the HRMA axis on the ACIS focal plane arrays, called the imaging point. These positions are:

Spectroscopic Array: S1 This imaging point is located about 6.25 mm from the launch-lock position. It is the position which causes the grating dispersed HRMA image to fall onto the ACIS-S array. It is the position of choice for spectroscopic grating support (if the gratings are inserted) or for narrow field imaging where absence of inter-chip gaps near the center of the field of view is important, or if symmetric PSF telescope response is required.

The deliberations of the AXAF SWG concluded that the best compromise, most flexible instrument configuration would be the ACIS-S array. In case the SIM translation mechanism fails, AXAF shall be launched with the ACIS-S array at the HRMA focal point.

Imaging Array: IP1 & IP2 For wide field imaging the imaging point will be directed near the center of the ACIS-I array. Two symmetrically placed imaging points are placed on chips I1 (IP1) and I3 (IP2). The points are slightly displaced to avoid having the target image fall into the inter-chip gaps (see the description of the I Array in Section 2.3.2). IP1 and IP2 are intended to provide redundancy in case of failure of a single CCD chip or signal chain.

IP2 is slightly preferable to IP1 and was principally used as the on-axis point during XRCF calibrations. Although the I array is equally symmetric about the IP1 and IP2 points, the S array is closer to IP2 than IP1, and so serendipitous imaging on S2 and S3 will be better for IP2.

Stow Position: HI & HS When the HRC is in the focal plane ACIS will be placed in the 'stow' position. In the HS position (when the HRC is positioned for the HRC-S detector) the calibration sources (see Section 2.3.5) illuminate the ACIS-I and S arrays. During this time the ACIS will not have access to the 24 kbs science telemetry stream and will only be able to use the 0.5 kbs 'next-in-line' stream.

Depending on the HRC operations policy there may be more HRC imaging points. In this notation we call HI the HRC prime imaging point and HS the spectroscopic imaging point. The HRC position used is not expected to have any significant impact on ACIS performance.

In the HI and HS positions the specific array which is to be analyzed must be specified (see following discussion of electronic array selection).

The ACIS on-board electronics consists of ten signal chains. Each signal chain connects to one chip, but the selection of array imaging point generally determines which signal chains are active. For the S1 imaging point, chips S0-S5 are used. For the IP1 and IP2 imaging points, chips I0-I3 and S2-S3 are used. For the HI and HS points, the choice of S0-S5 or I0-I3 and S2-S3 must be made depending on which array is intended to be calibrated. (Note that the selection of a set of chips does not necessarily require that data be processed from the entire set. See Section 3.1.3.3, under Chip Readout Pattern, available options for restricting the number of CCD chips processed.)

3.1.2 Continuous or Timed Exposure

Choices selected under this section reflect decisions to select different CCD clocking waveforms. Choices selected under the next section (On-board Processing Choices) reflect decisions to select different digital event processing algorithms in the DPA.

Timed exposure readout mode Expose 0.2 to 10 seconds (typically), transfer imaging array to frame store array, then simultaneously start another exposure and read the frame store data. Note that the minimum time to readout and process every pixel in a CCD requires 3.3 seconds. Exposures shorter than this time must reduce the number of pixels processed by selecting a smaller 'sub-frame window' on the CCD. (Sec. 3.1.3.5.)

Another alternative is to collect a very short exposure (less than the 3.3 second full frame readout limit), then take the full readout time to process the complete CCD frame, but discard the incident photons while the readout is occurring. This allows short exposure times and full frame readouts, but suffers the penalty of 'dead-time', time in which the CCD is inactive for X-ray detection.

Continuous readout mode allows greater time resolution, but at the expense of angular and spectral resolution. The CCD is read continuously; each output pixel represents the integrated flux received as the charge crosses the array. The observer can 'tune' the clocking rate to accommodate the expected counting rate from a given source, but at higher rates it becomes necessary to more severely degrade the angular resolution by ignoring or combining together CCD pixels in the readout process. Two pixel

Readout Mode	Time Resolution (seconds)	Field-of-View (arc-min^2)	Spatial Resolution (pixels)	Spectral Resolution
Timed integration	0.2-10	280	$1x, 1y$	maximum
Continuous				
Normal	6×10^{-3}	2×15.2	$1x, 1024y$	maximum
Summed	54×10^{-6}	2×15.2	$1024x, 256y$	minimum

Table 3.1: ACIS Readout Modes

handling schemes are possible in continuous readout mode: Normal rate, in which each pixel of each row is read out; and Summed, which does on-chip summation of pixels; spectral resolution is degraded in this mode. Table 3.1 shows the timing and resolution of each of these modes.

3.1.3 On-board Data Processing Choices

3.1.3.1 Event Recognition

When a pixel contains data above the Event Recognition Threshold, that pixel and the surrounding 3x3 neighborhood are selected for post-processing. At that point, depending on the selected processing mode, the software must either attempt an X-ray energy reconstruction on-board the instrument, or telemeter the entire 3x3 data set to the ground. If the overall counting rate in the CCD is low enough the 'Faint' mode is used, but otherwise the 'Bright' mode must be used.

Faint Mode The recognized event is telemetered as a 3x3 local neighborhood, centered on the peak pixel. In this mode the detector x,y position and 9 CCD pixel values are processed and telemetered. The processing system is adequate to process an input event stream of up to 180 events/sec.

Very Faint Mode The recognized event is telemetered as a 5x5 local neighborhood, centered on the peak pixel. In this mode the detector x,y position and 25 CCD pixel values are processed and telemetered. The processing system is adequate to process an input event stream of up to 180 events/sec.

Bright Mode The recognized event is telemetered as a single charge value, reconstructed from the 3x3 local neighborhood by summing according to a specified split event algorithm. In this mode the x,y position, a single reconstructed CCD pixel value, and a quality flag indicating the type of event are telemetered. The processing system is adequate to process an input event stream of up to 750 events/sec.

3.1.3.2 Telemetry Saturation Limits

When planning an observation it is necessary to consider how many events will be detected. ACIS's ability to process data is a function of the number of events which are detected, and the capacity of the telemetry to send those events to the ground. ACIS has buffering capability within the instrument, but if these limits are exceeded for any significant amount of time processing of additional CCD frames is stopped and data in subsequent frames are lost until the accumulated data are readout.

Processing and telemetry saturation will occur at the following situations.

- Each FEP can handle upwards of 14,000 threshold crossings per second. A threshold crossing that is a local maximum is reported to the BEP in an event record.
- The BEP can read a total of no more than 6,000 event records per second from all FEPs.
- The BEP applies a series of filters to determine whether to accept each event: according to its CCD location, grade, and graded pulse height.
- The number of surviving events that can be written to the 24 kbaud downlink depends on the BEP mode:

Readout Mode	Bits/event	Events/sec*
CC graded	34	700
CC faint	55	432
TE graded	58	410
TE faint	128	186
TE faint+bias	236	100
TE very faint	320	74

* assumes only minimal DEA and S/W housekeeping.

Table 3.2: Telemetry Saturation Limits for each Readout Mode

- When the telemetry stream becomes saturated, a FEP will find that it is unable to write all event records from the current exposure frame to the BEP. It then skips one or more whole exposures until the BEP accepts more events. The result is that whole exposures are dropped.

3.1.3.3 Chip Telemetry Choices

The pattern of chip telemetry selection is selectable. Normal choices are 1, 2, 4, or 6 CCD chips. Telemetering to the ground data from fewer chips will give a smaller effective field of view on the sky, but may be necessary if a bright source makes telemetry saturation effects important, or if 'flickering' pixels become a problem.

3.1.3.4 Alternating Exposure Times

In some instances it is desireable to have both long and short frame times. One example would be the case of a grating spectrum of a bright source. The images of the zeroth order, and possibly bright spectral lines could be saturated or highly piled up with multiple photons, while the continuum and weak lines are not. If the exposure time is made very short the pile-up may be avoided, but the efficiency of the observation is greatly reduced by the need to wait for the full 3.3 seconds for the framestore array processing.

With Alternating Exposure Times all CCDs are clocked in unison, but have two exposure times. One short exposure is followed by n long exposures (where n is configurable up to 15). The short exposures are used to reduce photon pileup, and the long exposures are normal ones for fainter observations. A typical choice of long and short exposure times would be 3.3 seconds and 0.3 seconds. In this case, if the duty cycle of long exposures is 1:n (short:long), then the efficiency, η, is:

$$\eta \;=\; 1 - \frac{3}{3.3 \times (n+1)} \qquad (3.1)$$

3.1.3.5 Sub-Array Readout and Staggered Readout

Another way to reduce the frametime, and hence reduce photon pileup, is to use fewer rows of the CCD. There are two ways to do this, called Sub-Array Readout and Staggered Readout.

In Sub-Array Readout only a reduced number of rows of pixels are processed and pixel data from the rest of the chip discarded. The time required to readout a CCD frame in this mode depends on the number of rows of pixel data within the window selected and the location of the rows on the CCD. There is a fixed minimum overhead of 41 msec required to clock out the CCD at maximum speed. In addition the farther the region is from the output node, the more time must be allowed to move the charge to the output node for processing. Finally the frame transfers must be staggered to reduce the peak power requirements, so the frame time for Sub-Array Readout is:

$$t \;=\; 41 \times (m-1) + n \times 2.85 + (m \times q) \times 0.04 \text{ msec} \qquad (3.2)$$

Exposure Size (rows)	Exposure Time (msec)
18	59.13
38	115.33
54	160.29

Table 3.3: Exposure Times in Stagger Mode

where n is the number of rows selected for analysis, m are the number of CCDs turned on and q are the numbers of rows to be skipped between the output node and the start of the sub-array. Integration time is controlled by an entry in the command parameter block which has a resolution of 0.1 seconds, so the time given in Equation 3.2 is rounded up to the next 0.1 second. The minimum time (also given by power and thermal considerations) is a 100 row region located at the output node, which requires roughly 0.5 second. For a 100 row region located at the top of the CCD (farthest from the output node), the minimum 100 row sub-array frametime is 0.9 second.

If these frametimes are too long, then Staggered Readout is possible. In this case the integration region of the chip is not completely transfered into the framestore array. Instead only a smaller number of rows are shifted, leaving the previous imaging on the integration region but shifted to a different location. If the target field consists of a bright source with few other sources of X-rays, then the CCD chip will fill with multiple images of the target. When the frame is eventually completely readout the image will look like a multiply exposed piece of photographic film, with a series of staggered images vertically displaced from each other.

In this mode with only one CCD turned on, the exposure times in milliseconds are given in Table 3.3. Note that Stagger Mode was used during XRCF calibrations, but it required a software patch to execute. Its availability during flight operations would require the patch.

3.1.3.6 ‘Smear’ Exposure Times

Because ACIS operates without a shutter every Timed Exposure Mode observation CCD frame contains 41 milliseconds of data collected while the CCD is being clocked out. This has several implications which should be considered.

Images of bright point sources will have faint vertical trails which extend to the top and bottom of the CCD frame. This can profitably be used to extend the dynamic range of the CCD, because the effective exposure time gets as short as in Continuous Clocking Mode. So for a full frame exposure 3.3 seconds of integration time occurs while the target is stationary, and 41 milliseconds occurs with the target image smeared over 1024 vertical rows of pixels with the width of the point spread function of the telescope.

Of course any point or diffuse sources within the smear band will also be smeared and the contributions from each will be confused.

Note that the image smear may be particularly useful for gratings observations as the zeroth order image will be frequently piled-up or saturated, but the 'smear' image can be used to find the centroid of the zeroth order image in the dispersion direction which is critical for establishing the wavelength zero point.

Note also that for the shorter frametimes coming from Sub-Array readout and Stagger readout, that the smear data will be relatively stronger than in full frame mode.

Care must also be taken in calculating integration times for observations due to the smear time. For a point source the integration time per CCD frame within a PSF sized region is equal to the dwell time (for a full frame this is 3.3 seconds). The repetition rate of frames includes the smear time (for a full frame this is 3.34 seconds). For a diffuse source, or if a larger spatial region on the CCD is selected, then the integration time per frame should be changed appropriately.

3.1.3.7 Diagnostic

Several diagnostic modes are available for monitoring instrument performance or collecting more detailed information than normally available. These modes are highly consumptive of telemetry capacity and so should not be used in most normal operation.

Raw: The raw, unprocessed CCD pixel and overclock data are telemetered to the ground.

Raw Histogram: A histogram of the number of CCD pixels vs. data number value is telemetered, accompanied by overclock pixel average and variance, without any attempt at X-ray event energy reconstruction.

3.1.3.8 Bias Telemetry Choices

The means of telemetering the bias values will depend on the choice of event recognition and duration of time that a single bias calculation remains valid.

In bright mode, where telemetry bandwidth is at a premium, the events are graded and biases subtracted internal to the on-board processing. Only the total event size and event grade (as reconstructed on-board) is telemetered on an event-by-event basis; no bias information is telemetered with the events.

In faint mode, where more telemetry is available for non-event transmission, the user can elect to have the local 3x3 bias values telemetered along with the 3x3 event pixel values. If the same bias remains valid for an extended period, this method is an inefficient use of telemetry, as the same bias values get telemetered with succeeding samplings of the same locations (which occurs frequently due to the narrow point spread function of the AXAF mirrors). To avoid this inefficiency, faint mode can also select not to contain bias data for each event.

When bias is not telemetered on an event-by-event basis, then the entire bias frame must be sent to the ground. Complete bias maps are compressed using a Huffman first-difference algorithm, with re-loadable compression tables. Each row is compressed separately and interleaved in the downlink telemetry by a BEP processing task called the 'bias thief'. This interleaving allows ACIS to resume observations after a bias calculation, without having to wait for the bias telemetry to be complete. (We estimate that it will require a maximum of 24 minutes to downlink all six bias maps if the full 24 kbs science telemetry is free. At calibration the bias maps were telemetered much more quickly than these estimates due to higher than expected compression efficency resulting from the high degree of uniformity of the bias maps. In this case bias telemetry only took 11 minutes with the full telemetry stream.)

3.1.4 List of Routine Modes

The delivered instrument and software contains the ability to operate in a number of modes, selectable to optimize the scientific performance for various types of astrophysical targets and scientific objectives.

These modes include the ability to process and telemeter data from a single CCD in either array, the entire spectroscopic array, or the entire imaging array, and the ability to select a rectangular region of interest to either telemeter or exclude from telemetering. The efficiency of the processing after any of these choices is no worse than the minimum rates specified under the event processing modes.

Imaging The four ACIS-I CCD chips are read-out and the pixel data stream is processed so as to recognize events from background. These events are then processed through event recognition and packetizing software for telemetry to the ground as a list of potential X-ray photon events.

Typical auxiliary choices are Faint vs. Bright event packetization, 1, 2, 4 or 6 CCD mode readout and sub-array event selection windows. (6 CCD readout includes processing data from the closest S array chips to increase the field of view.)

PHA/Calibration The CCD data are not processed by event recognition, but simply accumulated into pulse height bins. A histogram of pixel pulse heights is telemetered to the ground (as opposed to individual X-ray events). This mode is mostly used during HRC science runs when ACIS is accumulating data from the external calibration sources.

For sources too bright to do photon-counting of dispersed spectra, data are compressed by applying a read-region mask, and only processing those data.

Diagnostic Full Frame All individual pixels are telemetered without processing in this mode. The processing will be adequate to process data up to the normal CCD clocking rate. Ordinarily this mode is not used for data collection. It is likely to only be used as part of a diagnostic investigation of camera performance or optimization.

3.1.5 Bias Determination

In general operation ACIS will produce far too much raw pixel data to allow all pixel values to be telemetered to the ground. Because of this, the on-board processing is required to filter the data by actively recognizing the pixels which contain information relevant to an X-ray detection (and hence allowing the information about other pixels to be discarded).

In practice this requires that ACIS internally maintain a set of values for each pixel in every CCD chip which corresponds to a 'dark' level, i.e. the signal level which corresponds to *no* incident X-ray produced electrical charge. This image is called a 'bias' frame, and is normally subtracted from a data image prior to any further processing.

Currently three bias algorithms are available in the flight software consideration and each has merit for some applications (see Sect. 3.1.5.1).

Bias frames will have to be recalculated after most changes of mode. In particular, changes from continuous to timed, changes in timed exposure durations, and changes to sub-frame windowing sizes will require new bias calculations. Furthermore, the size of the bias frame information precludes storing this information in radiation hard memory, but instead radiation tolerant memory is used. As a result of this we expect that the bias frame will acquire errors due to radiation induced bit errors during perigee crossings of the satellite. Thus we recommend new bias maps be routinely calculated after each perigee crossing, and after each initialization of the instrument following a radiation induced shutdown.

Because the calculated bias directly affects the inferred X-ray signal, it is important to telemeter the bias values to the ground. There are several options for this, typically involving the choice of on-board data processing program chosen (see Section 3.1.3).

3.1.5.1 Bias Computation Algorithms

Algorithms Requiring No Additional Storage

Ford and Somigliana at MIT have investigated a class of algorithms that possesses the considerable advantage that they use no additional FEP memory beyond the Image and Bias Map Buffers and a modest amount of Data Cache. At any moment during the course of the algorithm, each pixel is represented by only two quantities – the 12-bit value in the Image map which will be overwritten by each fresh exposure, and the 12-bit value in the Bias Map whose value must converge to the desired bias threshold level.

The distribution of values, p_i, of a pixel observed N times ($1 \leq i \leq N$) may be approximated by a narrow Gaussian, $\exp[-(p_i - p_0)^2/\sigma^2]$, with the addition of a few outlying values, especially those with $p_i \gg p_0$ produced by X-rays or ionizing particles. By definition, p_0 is the modal value and $\sigma(\ll p_0)$ is the width, typically a few data units. For new CCDs, not yet subjected to radiation damage, both p_0 and σ are nearly identical from pixel to pixel, except for a few pathological 'hot' or 'flickering' pixels.

When a CCD is damaged by radiation, it is anticipated that p_0 and σ will increase with time, and at rates that vary randomly from pixel to pixel. Such behavior has been reported by Andy Rasmussen from a study of the CCDs aboard the ASCA observatory. Algorithms that use no additional storage are unable to estimate σ from p_i, so they concentrate on the modal value p_0. Once this has been computed for all pixels, its variance $(\langle p_0^2 \rangle/N) - \langle p_0 \rangle^2$ serves as a good approximation to $\langle \sigma^2 \rangle$.

The algorithms start by examining a series of exposures to 'condition' the p_i values and derive b_i, an estimate of p_0. After the first exposure, the best estimate of b_1 is clearly p_1. After the i'th exposure, two possible algorithms yield improved values of b_i, *viz.*

$$b_i = \min(b_{i-1}, p_i) \tag{3.3}$$

which guarantees that, after a number of exposures, none of the b_i will retain anomalously high values from X-ray or ionizing particle events. The resulting b_i will generally, of course, be less than p_0 by a few σ, and it will be seriously compromised if even a few of the p_i possess anomalously *low* values. A rather more accurate conditioning can be achieved by the following two-step algorithm:

$$b_i = p_i \text{ if } p_i < (b_{i-1} - T_1) \tag{3.4}$$

$$b_i = Cp_i + (1 - C)b_{i-1} \text{ if } p_i < (b_{i-1} + T_2) \tag{3.5}$$

i.e. if the new value p_i is much less than the previously stored value b_i, let it replace the stored value. Otherwise, if the new value isn't much larger than the stored value, use a running average to better approximate the 'mean' pixel value, b_i. Optimum choice of the thresholds T_1 and T_2, and of the partitioning factor C, will depend on the expected pixel distribution functions themselves.

After N conditioning exposures, the Bias Map Buffer contains values b_N that are guaranteed to lie within a few σ's of the modal values p_0. These can now be used as rejection thresholds to identify X-ray and ionizing particle events in subsequent calibration exposures, and thereby improve their own values in the process. This is achieved by making a further set of M exposures, i.e. $0 < N < i < (N + M)$. The new pixel values p_i are subjected to the following two-step algorithm:

$$p_i = 4095 \text{ if } p_i > (b_{i-1} + T_3) \tag{3.6}$$

where T_3 is a threshold value. In addition, the 8 neighbors of any pixel that meets this criterion may also receive a contribution from the event that caused the central pixel to lie above the threshold. These neighboring pixels are therefore also reset to a value of 4095.

In the second step, the Image Map pixels are re-examined and those with values less than 4095 are used to refine the Bias Map values,

$$b_i = Cp_i + (1 - C)b_{i-1} \tag{3.7}$$

Although this algorithm guarantees that b_i will converge to the neighborhood of p_0 for all positive $C < 1$, b_i will eventually execute a random walk with width $\sim C\sigma$. In practice, the choice of C must be balanced against the exposure count M to optimize the width of the b_{N+M} distribution versus total calibration time $t \propto M + N$.

The principal advantage of this class of algorithms is that they are very simple to implement, requiring just a few lines of computer code. Preliminary tests show that the resulting bias maps compare favorably with those generated from 'strip-by-strip' algorithms. However, they do have some weaknesses, as follows:

- They converge on p_0, the modal pixel values. This would be satisfactory if the widths σ were identical for each pixel over the lifetime of the CCD since a bias threshold value of, say, $p_0 + 3\sigma$ would be a robust discriminator of energy deposition. However, this is not even true of undamaged CCDs – the width of flickering pixel values can be many times the average σ, and the situation is expected to deteriorate as the CCDs absorb high doses of radiation. The choice of bias threshold, $p_0 + T_b$, must be made carefully – if T_b is too low, flickering pixels will appear as events; if too high, low-energy events will go unreported.

- Since all parts of the final Bias Map are calculated after the last calibration exposure, there is no opportunity to copy the bias values to the downlink telemetry system while the bias is being calculated. The time required to compress and transmit the six Bias

Maps, ca. 12 minutes assuming 75% compressibility, must therefore be added to the bias calibration time.

- These algorithms rely on particular properties of the pixel distributions. For instance, if equation 3.3 or 3.4 + 3.5 are used to condition the bias values, the presence of anomalously *low* pixel values, $p_i \ll p_0$, will start the second phase of the algorithm in a poorly conditioned state and the number of subsequent exposures, M, may be insufficient for equation 3.7 to change b_i so that $|b_i - p_0| \leq C\sigma$, as desired. This situation can be alleviated by applying an additional 'grading' process at the end of the conditioning phase in which the anomalously low values of b_N are identified and replaced by better estimates, e.g. by the median of the b_N of the surrounding pixels.

MEAN-I2L2 This algorithm calculates the mean and σ^2 of N values of a pixel. It then rejects values that diverge from the mean by more than $2\sigma^2$, and then recalculates the mean and σ^2.

$$\text{Definition: } \overline{x} = \frac{1}{N}\sum_{j=1}^{N} x_j \tag{3.8}$$

$$\sigma^2 = \frac{1}{N-1}\left(\sum_{j=1}^{N} x^2 - N\overline{x}^2\right) \tag{3.9}$$

$$\text{Rejection rule: } (x_j - \overline{x})^2 \geq k^2\sigma^2 \tag{3.10}$$

The algorithm is executed by successive iterations. The mean and σ^2 are calculated, then the outliers are rejected and the mean and σ^2 are recalculated. The algorithm is repeated until the termination rule is satisfied. The value k can be thought of as an estimated value derived by Gaussian distributions; e.g. $k = 2$ implies a probability of 5% that good pixel values are being rejected. The termination rules are defined as any of the following:

- All pixel values are within an acceptance range.
- The maximum number of iterations was reached.
- The number of remaining pixels is less than or equal to the minimum number acceptable.

The algorithm is expected to work best with Gaussian or symmetric heavy-tailed distributions in the presence of outlier points for which the assumption of normality does not hold. These outlier points are rejected and the remaining data are treated as Gaussian.

The calculation is accelerated by saving the intermediate values $\sum x_j$ and $\sum x_j^2$. During the rejection phase, rejected values are subtracted from $\sum x_j$ and $\sum x_j^2$ and the sample number is updated.

MEDIAN The algorithm calculates the median of N pixel values. It sorts them in ascending order, and identifies the central value, thereby automatically rejecting the outliers which will be sorted to one end of the list or the other. Once the $\{x_n\}$ are sorted, the formula for the median is:

$$x_{med} = \begin{cases} x_{\frac{(N+1)}{2}} & \text{N odd} \\ \frac{1}{2}(x_{\frac{N}{2}} + x_{[\frac{N}{2}+1]}) & \text{N even} \end{cases} \tag{3.11}$$

A suitable rejection rule is based on the interquartile range (IQR), which indicates the distance between the upper and lower quartile:

$$x \leq x_{med} - k \text{ IQR and } x \geq x_{med} + k \text{ IQR} \tag{3.12}$$

A value of $k = 3$ can be considered to be a good approximation to reject severe outliers. The termination rule for the median is defined as follows:

- All pixel values are within an acceptance range.
- The maximum number of iterations was reached.

The algorithm is expected to work best with Gaussian or symmetric heavy-tailed distributions with few outlier points which have large σ, but zero mean. It fails if the area in the tails is large (Press, William H., et al., Numerical Recipes in C), and is somewhat influenced by points with very large values, but the rejection of contaminated sources is particularly simple.

MEDMEAN This algorithm calculates the median value after excluding some of the highest and lowest values, and excluding values based on the variance about a trial mean. Specifically, it takes the N values for a specific pixel p_i, $i = 0, N-1$, where N is the number of conditioning exposures, and removes the L largest values and the M smallest values. Using the remaining $N - L - M$ values, it computes the median value, $|p|$, and the variance, σ^2, of those p_i less than $|p|$:

$$\sigma^2 = \frac{2}{N-L-M-1} \sum_{i=0}^{N-L-M-1} (p_i - |p|)^2 \Big|_{p_i \leq |p|} \tag{3.13}$$

The trial set of p_i are compared to the trial $|p|$, and any values which do not fall within $m\sigma$ are removed, i.e., any p_i which do not satisfy the condition:

$$|p_i - |p|| \leq (\sigma \cdot m) \tag{3.14}$$

where m, L, and M are all adjustable parameters, which will be set by AXAF operations and the ASC, and will be infrequently changed.

Finally, the bias value is computed based on the remaining p_i, by the normal equation for the mean:

$$\bar{p} = \frac{1}{N^* - L - M} \sum_{i=0}^{N^*-L-M-1} p_i \tag{3.15}$$

where N^* is the number of p_i values remaining after the exclusion for eq. 3.14.

3.2 Commanding

3.2.1 Philosophy

Two basic roles facilitate the description of command scenarios: the "observer" determines the science operations of ACIS, controlling it using the various AXAF-I mission planning and control resources such as the AXAF Science Center, Operations Control Center, the Deep Space Network, and the Spacecraft. The "maintainer" determines the maintenance operations of ACIS, such as code patches and diagnostics. The "maintainer" also controls the instrument using the various AXAF-I mission planning and control resources.

For the purposes of this document, the term "science run" will be defined as a contiguous period of time during which ACIS is observing a source using a single set of parameters. Many science runs may be combined to form an "observation," or a time during which the instrument is pointed at a specific target and data are being taken. However, starting a science run involves some overhead, as no X-ray data can be collected during the instrument electronic settling time and during the calculation of new bias maps. More than one observation is possible during a single science run, and it will be an operational issue for the AXAF schedulers and operations staff to decide how to break up observations of targets with ACIS science runs.

To perform a science run, an observer commands ACIS to accept a set of parameters to use for the run then instructs ACIS to execute the run. The parameters and commands define the Science Mode parameter block and options to use for the run. ACIS then sets up the hardware and software elements according to the specified mode and proceeds to acquire, process, and telemeter event data from the selected CCDs. The observer allows

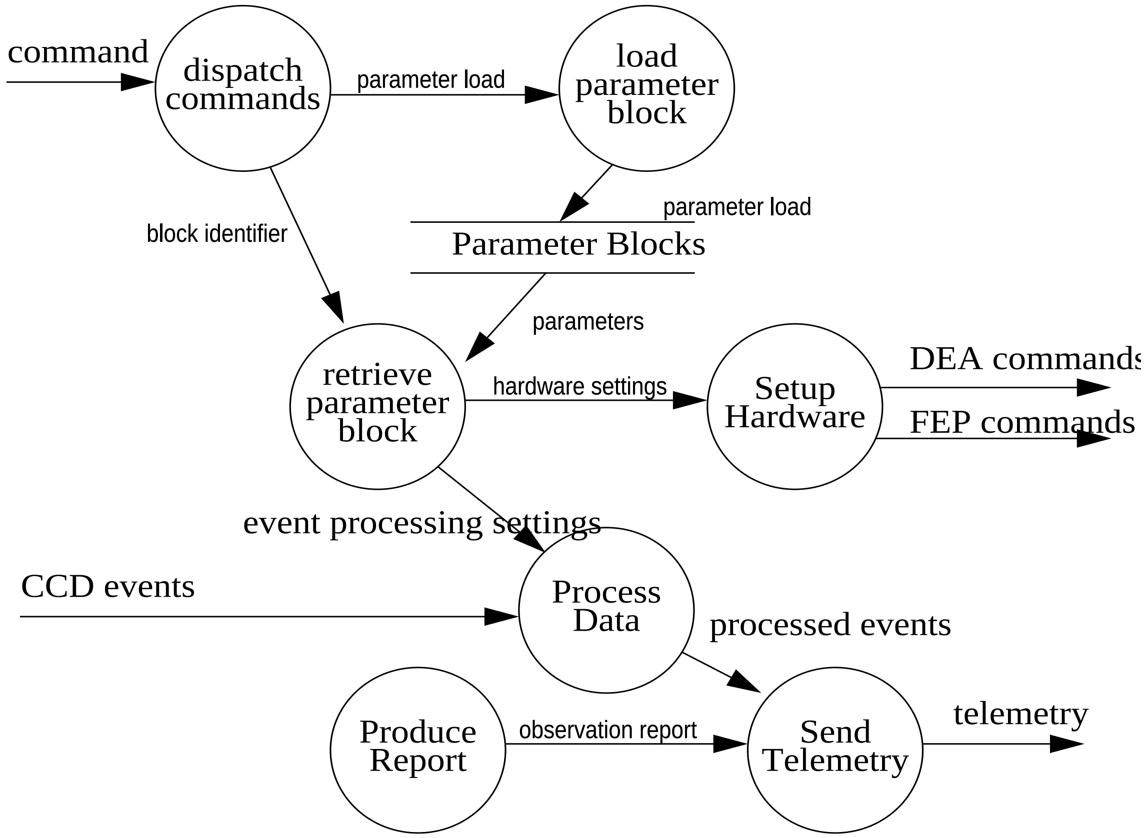

Figure 3.1: Science Run Data Flow Diagram

ACIS to continue its data acquisition for the desired period of time then commands ACIS to terminate the run. Figure 3.1 illustrates this process.

Upon receipt of a “Load Parameter Block” command, the Command Interface dispatches the command to load the specified parameter block into the list of available parameters. When it receives an “Execute Science Run” command, the Command Interface dispatches the command to a Science Mode. The Science Mode then retrieves the parameter block specified in the command. It then configures an Event Processor to prepare for events, tells the DEA Interface to set up the DEA hardware and sequencer, and instructs the FEP Interface to load code and parameters into the FEPs and to start executing. Finally, the Science Mode instructs the DEA Interface to start clocking the CCDs.

As the DEA clocks the CCDs, pixel data are produced and forwarded to the FEPs (not shown in Figure 3.1 above). The FEPs select events from the generated pixel data

Table 3.4: Generic Load Parameter Block Command Packet

Field Name	**Description**
Packet Word Length	Total number of 16-bit words in the command packet.
Packet Sequence #	Identifies the command packet in a series.
Command Opcode	"Load < *type* > Parameter Block" command opcode. This instructs the ACIS Science Instrument Software to store the "Parameter Block Data" contained within the packet.
Block ID	Block within the ACIS.
Block CRC	Checks the load for errors in transmission.
Parameter Block Data	Parameter block data to store.

and forward the event data to the BEP. The BEP's interface to the FEP then instructs the Event Processor to process the events. As the Event Processor selects, processes, and formats the events for telemetry, it instructs the Telemetry Interface to send the packaged event data.

When the observer sends the command to terminate the Science Run, the Command Interface instructs the running Science Mode to stop the run. The Science Mode, in turn, instructs the DEA Interface and FEP Interface to stop clocking the CCDs and producing events. When the FEP Interface receives an indication from the FEP that the data set is complete, it tells the Event Processor to stop. The Event Processor then completes its event processing and tells the Science Mode that it has finished. The Science Mode then forms an Observation Report and tells the Telemetry Interface to send the formed report. The detailed form of all these commands is outlined in the tables below.

Table 3.4 describes the contents of a 'generic' load parameter block command. The content of each specific type of parameter block is Science Mode dependent and is described for each Science Mode later in this chapter. ACIS will be capable of storing at least four parameter blocks in its software ROM for use during on-orbit checkout and for commonly used observational modes. This helps the maintainer to reduce the number of commands required to configure the instrument.

Tables 3.5 and 3.6 outline generic 'Start Science Run' and 'Stop Science Run' commands, respectively. There are several different telemetry formats, matched to the different ways data may be obtained with ACIS (see Section 3.3.2), but all the telemetry forms contain at least the start time of the Science Run. This allows the data to be uniquely tagged. After being commanded to stop a Science Run, the ACIS software produces a report of the complete run. Science Run Reports must contain at least the information described in Table 3.7.

Table 3.5: Generic Start Science Run Command

Field Name	**Description**
Packet Word Length	Total number of 16-bit words in the command packet.
Packet Sequence #	Identifies the command packet in a series.
Command Opcode	"Start $< ScienceMode >$ Run" command opcode. Instructs the ACIS Science Instrument Software to retrieve the parameter block indicated by the "Block ID" below, and setup and run the requested Science Mode. ACIS will continue to run the mode until commanded to stop.
Block ID	$< ScienceMode >$ block parameter block to use for the run. This block may have been loaded just prior to the Start Run command, or may be part of either the pre-loaded library, or one of the blocks provided at launch.

Table 3.6: Generic Stop Science Run Command

Item	**Description**
Packet Word Length	Total number of 16-bit words in the command packet.
Packet Sequence #	Identifies the command packet in a series.
Command Opcode	'Stop $< ScienceMode >$ Run' command opcode. Instructs the ACIS Science Instrument Software to stop the current science run.
Block ID	$< ScienceMode >$ parameter block to be used for this run.

Table 3.7: Stop Science Report Information

Field Name	**Description**
Science Run Start Time	ACIS time-stamp sampled relative to the start of the Science Run. All data produced by the run is relatable to this time-stamp.
Data Summary	Indication of how much information was produced by the run. The intent is to provide the observer with a confirmation that all the run's data have been received.
Discrepancy Summary	Summary information of any discrepancies uncovered during or after the run.

3.2.2 List of commands

Table 3.8 lists the ACIS commands according to the features called out in the Science Instrument Software Requirements Specification. Information which is sent using the discrete hardware status bits are preceded with the word "Discrete-". The remaining items are sent as command Packets, using the Serial Digital Command stream.

The definitive list of ACIS commands, including documentation and arguments, is contained in the ACIS IP&CL (Instrument Procedures and Command Language) description, MIT document number 36-53204, which is available on the Web at http://acis.mit.edu/sw.html.

3.2.3 Command Sequences

The procedure for submitting command sequences for instrument mode changes is described in the ACIS Software User's Manual, under development by Jim Francis. Please refer there for details.

The DEA has a set of hardware settings used to condition the CCD clocks, control the analog signal processing, and set the focal plane and housing temperatures. In addition, ACIS can filter bad pixels and columns from generated CCD data and provides a set of commands for a maintainer to use to manage these settings.

Over the life of the instrument, the maintainer may issue commands to ACIS to modify its settings for various DEA clock voltages, processing levels, etc. As the CCDs degrade due to radiation damage, the maintainer may also add pixels and columns for the ACIS Bad Pixel and Column Maps. The maintainer modifies settings by issuing a "Change System Configuration Settings" command to ACIS. Upon receipt of this command, ACIS updates its configuration parameter block. If a Science Run is in progress when the command is executed, the changes are held until the end of the run, after which they are loaded into the hardware. If no run is in progress, ACIS immediately loads the changes into the hardware. The maintainer edits the Bad Pixel and Column Maps using "Add" and "Reset" commands. Upon receipt of these commands, ACIS modifies the appropriate map. Any changes to the Bad Pixel or Column Map will not take effect until the start of the next Science Run.

The details of these configuration commands are described in the tables below. ACIS contains a set of System Configuration Parameters, described in Table 3.9. Each parameter is identifiable using a 16-bit setting code. To change one or more of these system configuration settings, the maintainer uses a Change Settings Command, described in Table 3.10. Upon receipt of this command, ACIS overwrites the System Configuration Parameter Block items as indicated by the entries in the command packet. ACIS also provides a command which allows the maintainer to dump the current contents of the System Configuration

Table 3.8: Generic ACIS Commands Grouped by System Feature

Science Modes

Timed Exposure (TE)	**Continuous Clocking (CC)**
Load TE Parameter Block	Load CC Parameter Block
Load 2-D Window List	Load 1-D Window List
Start TE Run	Start CC Run
Stop Run	Stop Run
Start TE Bias	Start CC Bias
Dump TE Blocks	Dump CC Blocks
Dump 2-D Windows	Dump 1-D Windows

Maintenance

Hardware Configuration	**Memory Commands**	**DEA Housekeeping**
Change Sys. Setting	Read BEP Memory	Load DEA Housekeeping Block
Add TE Bad Pixel	Write BEP Memory	Start DEA Housekeeping Run
Reset TE Bad Pixels	Execute BEP Memory	Stop DEA Housekeeping Run
Dump TE Bad Pixels	Write FEP Memory	Dump DEA Housekeeping Blocks
Add TE Bad Column	Read FEP Memory	
Reset TE Bad Columns	Execute FEP Memory	
Dump TE Bad Columns	Read SRAM	
Add CC Bad Column	Write SRAM	
Reset CC Bad Columns	Read PRAM	
Dump CC Bad Columns	Write PRAM	
	Dump Huffman Tables	
In-Flight S/W Changes	**Boot from Command**	**Radiation Monitoring**
Add Patch	Discrete- Set Boot Mode Flag	Discrete- Set Rad. Mon. Flag
Remove Patch	Discrete- Clear Boot Mode Flag	Discrete- Clear Rad. Mon. Flag
	Start Uplink Boot	
	Continue Uplink Boot	
	Discrete- Reset BEP	

Parameter Block. (As the System Configuration Block is at a fixed memory location, it can be dumped using the 'Read BEP Memory' command.)

The command to add a set of pixels to the Bad Pixel map is described in Table 3.11. Upon receipt of this command, the ACIS software adds the listed pixels to its Bad Pixel Map. Pixel positions already listed in the map are not stored a second time. The contents

Table 3.9: System Configuration Parameter Block Content[†]

Item	**Description**
Image Section Phase Clocks - High Levels	High Level of Image Section Phase Clocks.*
Image Section Phase Clocks - Low Levels	Low level of Image Section Phase Clocks.*
Framestore Section Phase Clocks - High Levels	High level of Framestore Section Phase Clocks.*
Framestore Section Phase Clocks - Low Levels	Low level of Framestore Section Phase Clocks.*
Serial Output Register Phase Clocks - High Levels	High level of Serial Output Register Phase Clocks.*
Serial Output Register Phase Clocks - Low Levels	Low level of Serial Output Register Phase Clocks.*
Output Node Reset Gate - High Levels	High level of Output Node Reset Gate.*
Output Node Reset Gate - Low Levels	Low level of the Output Node Reset Gate.*
Output Node Reset Diodes	Level applied to Output Node's Reset Diode
Output Node Drains	Level applied to the Output Node's Drain. One entry for each Output Node on each CCD.
Output Node Output Gates	Level applied to Output Node's Output Gates
Output Node Bias Offsets	Level applied to Output Node's Bias Offsets
Scuppers	Bias-level to the Scuppers.
Back-Junction Diodes	Levels of the Back Junction Diodes.
DEA/FEP Power	On/Off
Focal Plane Heater	Set points.
Bakeout Heater	On/Off

*The ACIS software loads these levels into the Driver board's clock conditioning Digital-to-Analog converters. There is a separately defined value for each quantity, and for each CCD.

[†] Each item in this table consists of a vector of values, with each element corresponding to an individual specification for each CCD.

of the Bad Pixel Map may be dumped into the telemetry stream via the "Dump Bad Pixels" command, described in Table 3.12. The result of this command is a telemetry packet, described in Table 3.13. Note that the bad pixel maps for all CCDs are sent in the telemetry packet.

Similarly, ACIS provides commands to add bad columns to the Bad Column Map. The Bad Column Map can be reset by the "Reset Bad Columns" command. The contents of the Bad Column Maps for all CCDs can be telemetered via the "Dump Bad Columns"

Table 3.10: Change Settings Command Packet

Item	**Description**
Packet Length	Length of command packet in 16-bit words
Sequence #	Identifies the command packet in a series.
Command Opcode	Change_Settings_Command opcode
# entries	Number of settings entries to follow in the command packet. The maximum number of entries is governed by the maximum size of a command packet.
Settings[#*entries*]	Array of setting entries with the following format: Setting Identifier: 16-bit identifier which uniquely identifies the item within the System Configuration Parameter Block Setting Value: Value to use for the specified item. A single setting value shall take no more than 16-bits.

Table 3.11: Add Bad Pixel Command Packet

Item	**Description**
Packet Length	Length of command packet in 16-bit words
Sequence #	Identifies the command packet in a series.
Command Opcode	Add_Bad_Pixel_Command opcode
# entries	Number of pixel entries to follow in the command packet. The maximum number of entries is governed by the maximum size of a command packet.
Pixels[#*entries*]	Bad pixel locations with the following format: CCD Identifier: CCD containing the bad pixel. Row & Column Addresses: Row and column of the bad pixel.

command. These commands are described in Tables 3.14, and 3.15, respectively. A separate but similar set of commands exists for adding, removing, and dumping bad columns in Timed Exposure Mode.

To perform calibration measurements, a maintainer configures and executes one of the existing science modes described above. The ground uses the standard telemetered science

Table 3.12: Dump Bad Pixels Command Packet

Item	**Description**
Packet Length	Length of command packet in 16-bit words
Sequence #	Identifies the command packet in a series.
Command Opcode	Dump_Bad_Pixels_Command opcode

Table 3.13: Dumped Bad Pixel Map Telemetry Content

Item	**Description**
Command Sequence #	Sequence number of the command causing the dump being performed. This allows the ground to associate the command and the resulting telemetry packets.
# entries	Number of bad pixel entries to follow in the telemetry. The maximum number of entries is governed by the maximum size of a telemetry packet.
Pixels[#*entries*]	Array of pixel entries with the following format: CCD Identifier CCD containing the bad pixel. Row & Column Addresses Row and column of the bad pixel.

Table 3.14: Add Bad Column Command Packet

Item	**Description**
Packet Length	Length of command packet in 16-bit words
Sequence #	Identifies the command packet in a series.
Command Opcode	Add_Bad_Column_Command opcode
# entries	Number of bad column entries to follow in the command packet. The maximum number of entries is governed by the maximum size of a command packet.
Columns[#*entries*]	Array of columns which are to be excluded, with the following format: CCD Identifier This specifies the CCD containing the pixel. Column Address This identifies the column number.

data to determine the desired calibration information.

Table 3.15: Dumped Bad Column Map Telemetry Content

Item	**Description**
Command Sequence #	Sequence number of the command causing the dump being performed. This allows the ground to associate the command and the resulting telemetry packets.
# entries	Number of bad column entries to follow in the telemetry. The maximum number of entries is governed by the maximum size of a telemetry packet.
Columns[#*entries*]	Array of column entries with the following format: CCD Identifier CCD containing the bad column. Column Address Column number of the bad column.

3.2.4 Operational Constraints

The Spacecraft contains a radiation monitor (the EPHIN). Whenever the EPHIN measured radiation exceeds a threshold which is settable via ground control (presumably at the direction of the ASC), the Spacecraft tells ACIS that the monitor's threshold has been exceeded. When the radiation level subsides, the Spacecraft will tell ACIS that the condition has subsided. This information appears to the ACIS software as a single radiation flag.

During periods of unexpectedly high radiation, the radiation monitor's level will trip, and the ACIS radiation monitor flag will be asserted. The software will then issue a command to the DEAs to disable power to the CCDs, DEAs and FEPs. When the radiation environment returns to acceptable levels, the flag will be de-asserted. ACIS will sample the flag for a configurable period of time (specified as one of the System Configuration Parameters). If the sampled flag remains de-asserted for the specified time, ACIS will issue a command to the DEAs to allow power to be restored to the CCDs.

Handling of the spacecraft radiation monitor is done by software, so if flight experience dictates, ACIS can choose to ignore this signal or provide a more sophisticated decision tree to decide whether to shut down or not.

3.2.5 SI Monitoring

There will be ground monitoring of the focal plane temperature, power consumption, and processor status. For each observation, CCD bias and noise level and rejected event counts will be monitored. Periodic checks will be made of CCD CTE and low energy response, as well as the HRMA focus. Much of the detailed housekeeping data is contained within the 'Science Data' portion of the ACIS telemetry, and so requires extraction from the various formats in the same manner as the X-ray event data. This means that some lag for extraction and analysis will be required. (Housekeeping data, which is directly relevant to health and safety issues, is more trivially extracted.)

In order to help a maintainer develop a history of the operation of ACIS, the ACIS Science Instrument Software maintains and telemeters software housekeeping information. Whenever an observer or maintainer sends a command to the ACIS Science Instrument Software, ACIS echoes the command in a telemetry packet. This allows a maintainer to verify that all commands intended for ACIS software were received and executed. In order to allow monitoring of the overall operation of ACIS without relying on its serial science telemetry, ACIS also provides some active status information using the discrete telemetry signals, read by the hardware and placed into the Engineering portion of the telemetry stream.

Table 3.16: Fatal Error Telemetry Content

Item	**Description**
Fatal Error Code	Indicates point at which fatal error was detected.
Optional Argument	Allows more information about the error to be telemetered. Meaning depends on the Fatal Error Code.

The ACIS software indicates its boot and running status using the four discrete telemetry signals provided by its hardware. During boot, these signals indicate the current mode of the boot and current state. If ACIS hangs during the boot, the boot status provides an indication of the last action performed prior to the lockup. While running after a commanded reset, the ACIS software cycles the signals between two or more values, indicating the current overall state of the software. If ACIS hangs, these signals freeze into one state until the Watchdog Timer resets the system. After a watchdog reset, ACIS cycles these signals between values which indicate that ACIS locked up at some point and was reset by the Watchdog Timer.

ACIS maintains a set of system statistics representing various operating conditions, such as the number of interrupts, context switches, etc. These statistics also contain the number of occurrences of various warning conditions, such as the number of dropped exposures. These statistics are represented as an array of counters. Periodically, ACIS telemeters and resets the contents of these statistic counters.

Both the ACIS Back End and Front End software periodically set their respective Watchdog Counters. The value written into the counter determines the time-out duration of the Watchdog Timer. In the event of a crash whereby the ACIS software hangs, the Watchdog Timers will reset the hung processor. If ACIS encounters a condition from which it cannot recover, it makes a best attempt to complete the current telemetry item being written to the RCTU, then issues a telemetry message indicating that it is about to reset. Table 3.16 illustrates the contents of this error message.

Periodically, a maintainer will wish to monitor various DEA operating values. ACIS provides commands allowing the maintainer to select which values to monitor and to start and stop the monitoring process. Some of these housekeeping values are coupled to specific CCDs. This housekeeping run can execute concurrently with an ACIS Science Run, and is similar in nature. To perform a DEA Housekeeping Run, the maintainer commands ACIS to accept a parameter block containing a list of DEA registers to sample and then instructs ACIS to execute the run. ACIS then samples specific items by issuing queries to the DEA and storing the responses. ACIS then telemeters the set of sampled values. The maintainer allows ACIS to continue its data acquisition for the desired time period, then commands ACIS to terminate the run.

Table 3.17: Load DEA Housekeeping Parameter Block Command Packet

Field Name	**Description**
Packet Word Length	Total number of 16-bit words in command packet.
Packet Sequence #	Identifies the command packet in a series.
Command Opcode	Load_DEA_Housekeeping_Parameter_Block command opcode. Instructs ACIS software to store the List Data contained within the packet.
Block ID	Block within ACIS.
Block CRC	Checks the load.
Sampling Period	Rate at which the ACIS should sample and telemeter the acquired information.
DEA Item List	List of DEA items to sample.

Table 3.18: Start DEA Housekeeping Run Command

Field Name	**Description**
Packet Word Length	Total number of 16-bit words in the command packet.
Packet Sequence #	Identifies the command packet in a series.
Command Opcode	Start_DEA_Housekeeping_Run command opcode. Instructs ACIS software to retrieve the parameter block indicated by the "Block ID" below, and run the requested DEA Housekeeping operation. ACIS will continue to run the mode until commanded to stop.
Block ID	Identifies the DEA Housekeeping Parameter block to use for the run. This block may have been loaded just prior to the Start Run command, or may be part of either the pre-loaded library, or one of the blocks provided at launch.

ACIS maintains one or more lists of DEA Housekeeping items to monitor. The maintainer installs this list by issuing a "Load DEA Housekeeping Parameter Block" command and selects which list to use for a run via the "Block Id" field of the list. Table 3.17 illustrates this command. The Start and Stop DEA Housekeeping Run commands are outlined in Tables 3.18 and 3.19, respectively. During a DEA Housekeeping Run, the ACIS software reports the acquired DEA register values. Table 3.20 illustrates the contents of this telemetry.

The only activities which require real-time or near real-time monitoring is the 'Bakeout' mode. Bakeout does not occur during normal operations, but the mode exists in case frost or condensation occurs on the ACIS instrument in sufficient quantity to impair instrument efficiency. When commanded by the ground control ACIS will enter Bakeout mode, turning on heaters to raise the instrument temperature. While the heaters are on, the DEA and

Table 3.19: Stop DEA Housekeeping Run Command

Item	**Description**
Packet Word Length	Total number of 16-bit words in the command packet.
Packet Sequence #	Identifies the command packet in a series.
Command Opcode	Stop_DEA_Housekeeping_Run command opcode. Instructs ACIS software to stop the current run.
Block ID	DEA Housekeeping Parameter block used for this run.

Table 3.20: DEA Housekeeping Telemetry Content

Item	**Description**
Block ID	DEA Housekeeping Parameter block which is being used to generate this telemetry information.
# entries	Number of DEA Housekeeping entries to follow in the command packet.
Items[#*entries*]	Array of DEA Housekeeping values with the following format: Item Identifier — DEA Housekeeping item being sent. Item Value — Value of the item.

DPA must not be turned on. The effect of erroneously turning on the DEA and DPA while the heaters are on will be to exceed the fuse rating on the ACIS power, resulting in failure of the experiment. Note that turning on DEA and DPA power requires two commands (an 'arm' and 'execute' pair), so that accidental activation is very unlikely. The ACIS team has communicated this requirement to the AXAF Operations team, who have accepted the responsibility.

3.2.6 Contingencies

There are no critical or semi-critical situations over which the ACIS Science Instrument Software has control, according to the ACIS Software Requirements Specification. Therefore, the software is not required to address these types of situations. There are, however, a number of safing and recovery procedures for ACIS. Note that, for this reason, the ability for the software to command the FP bakeout heater has been removed from the final version (1.5) of the flight software. A software patch must be uploaded from the ground to enter bakeout mode.

In order to enhance the ACIS software or work around problems discovered after delivery, the spacecraft OBC shall maintain an on-board list of ACIS software changes. These changes are applied upon each ROM reboot. The changes are specified using the equivalent of a series of "write memory" commands which are executed upon startup of the ACIS

Table 3.21: Add Patch Command Packet

Item	**Description**
Packet Length	Length of command packet in 16-bit words
Sequence #	Identifies the command packet in a series.
Command Opcode	Add_Patch opcode
Patch ID	Identifies the patch within the patch list.
Virtual Address	32-bit Back End Processor address to start writing into.
Length to Write	Number of 32-bit words to write.
Data to Write	Data values to be copied into BEP memory.

Table 3.22: Remove Patch Command Packet

Item	**Description**
Packet Length	Length of command packet in 16-bit words
Sequence #	Identifies the command packet in a series.
Command Opcode	Remove_Patch opcode
Patch ID	Identifies the patch within the patch list to remove.

software. This form of a write memory command is known as a patch.

To install a set of software changes, the maintainer issues a series of “Add Patch” commands to ACIS, described in Table 3.21. ACIS then just records the patch in its internal patch list, to be applied upon the next reboot from ROM. Once the maintainer is satisfied that all of the patches needed for the changes are installed, a command is issued to restart the ACIS software. After reloading its core image from ROM, the ACIS startup code installs each of the patches specified in the patch list.

To remove previously installed patches, the maintainer issues a series of “Remove Patch” commands to ACIS, described in Table 3.22. ACIS then removes the specified patches from its internal patch list. Once the maintainer has removed the old changes, a command is issued to restart the ACIS software. After reloading its core image from ROM (effectively undoing the selected patches), the ACIS startup code installs whatever patches are remaining.

In the event that a badly-conceived patch prevents the maintainer from removing the patch, the maintainer must edit the patch list by hand using the “Write BEP” command feature. Note that should a boot after a patch fail, then the next boot will not load any patches. This feature also helps the maintainer diagnose and work around problems which occur as a result of failures in the main software ROM. It serves as the maintainer’s “back door” into ACIS.

In the event of a hardware failure which allows ACIS to boot, but not to execute its ROM startup code, the maintainer can load and execute code directly from the ACIS serial

Table 3.23: Start Uplink Load Command Packet

Item	**Description**
Packet Length	Length of command packet in 16-bit words
Sequence #	Identifies the command packet in a series.
Command Opcode	Uplink_Load_Command opcode
Virtual Address to Write to	32-bit Back End Processor address to start writing into.
Length to Load	Number of 32-bit words to write. If the length exceeds the number of words allowed in the command packet, subsequent Continue_Uplink_Load commands must be sent.
Virtual Address to Start Execution from	Virtual address to jump to after the load is complete.
Data to Write	Values to be copied into BEP memory.

Table 3.24: Continue Uplink Load Command Packet

Item	**Description**
Packet Length	Length of command packet in 16-bit words
Sequence #	Identifies the command packet in a series.
Command Opcode	Continue_Load_Command opcode
Data to Write	Values to be copied into BEP memory. Values are appended to information copied from the last Start_Uplink_Load or Continue_Uplink_Load command.

command channel. To accomplish this, the maintainer issues a discrete command to set the ACIS "Uplink Load" flag, followed by a second discrete command to reset ACIS. The ACIS Boot ROM then detects the assertion of the flag and polls the uplink channel for a "Start Uplink Load" command (see Table 3.23 for the format of this command). The maintainer then sends this command, followed by zero or more "Continue Uplink Load" commands (see Table 3.24). Upon receipt of the Start Uplink Load command, ACIS saves the total load length specified in the command, copies the code specified in the command to the desired location, and saves the execution address specified in the command. If the total load length exceeds the length of the command, ACIS waits for one or more Continue Uplink Load commands. Once all of the code has been loaded, ACIS jumps to the execution address specified in the initial command. The ACIS software execution proceeds from there. If another Start Uplink Load command arrives before the load is complete, ACIS ignores the previous load and starts over.

3.2.7 Operation Scenarios

Attention is drawn to the ‘Software Users Manual’ being written by Jim Francis of MIT. It includes details of how to operate ACIS in the context of what hardware must be on, how to select parameters, how to issue normal configuration changes and so on. This manual should be available from the MIT ACIS Web page at http://acis.mit.edu.

3.3 On-board data processing

3.3.1 Overview

ACIS has significant on-board-processing with a multitude of operating modes. The duties may be listed as:

- Instrument control, housekeeping and communication with observatory data system
- Timing and control for CCD and analog processing chains
- Event finding in CCD output data streams
- Diagnostic histograms
- Event processing and data formatting

Figure 3.2 gives an overview of the data flow through ACIS. The key data processing tasks are divided between the two types of processor sections.

The next two sections describe the on-board data processing flow. Two fundamentally different processing schemes apply, depending upon whether the CCD data is collected as timed exposures, or as continuous clocking. First the timed exposures will be described, followed by the continuous data processing.

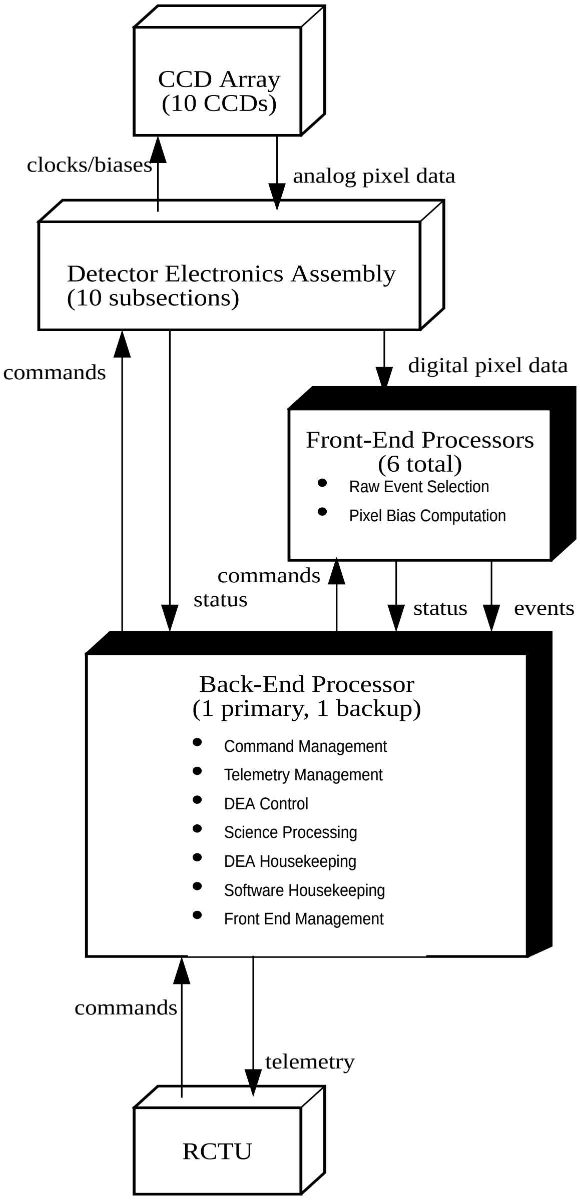

Figure 3.2: On-board data flow overview.

The basic division of responsibility between the Back and Front End Processors is as follows. The Back End Processors (BEP) must perform:

- Command Management
- Telemetry Management
- DEA Control
- Science Data Filtering and Formatting
- DEA Housekeeping Acquisition
- ACIS Software Housekeeping (including error management)
- Managing Front End Processor Code and Data Loads

The Front End Processors (FEP) must perform:

- Event Selection from Raw Pixel Data
- Pixel Bias Computation (including overclock calculations)

3.3.2 Timed Exposure Mode Data Processing

An observer uses Timed Exposure Science Mode to acquire, process and telemeter two-dimensional images from the CCD array. To execute a Timed Exposure Science Run, an observer sends a “Start Timed Exposure” command to ACIS. ACIS retrieves the parameter block referenced by the start command and proceeds to execute the science run. The observer allows ACIS to acquire, process and telemeter CCD data for a period of time, after which the observer sends a “Stop Timed-Exposure” command to ACIS. ACIS then stops the run and telemeters a Science Run Report. Figure 3.3 describes the pixel processing data flow through the DPA in Timed Exposure mode.

If the observer requires parameters not already provided by the ACIS parameter library, the observer must issue a “Load Timed Exposure Parameter Block” command to load the desired parameters for the run. If the loaded parameter block requires custom event processing windows, the observer must also issue a “Load 2-D Window List” command to place the desired window settings into the instrument. Table 3.25 describes the contents of the Timed Exposure Parameter Block, which the observer must specify to configure the Timed Exposure Mode. Since Timed Exposure Mode has the capability to select and process events in restricted 2-D windows, the selection and processing of events in specific windows must also be controlled, via a “2-D Window Parameter Block.” Table 3.26

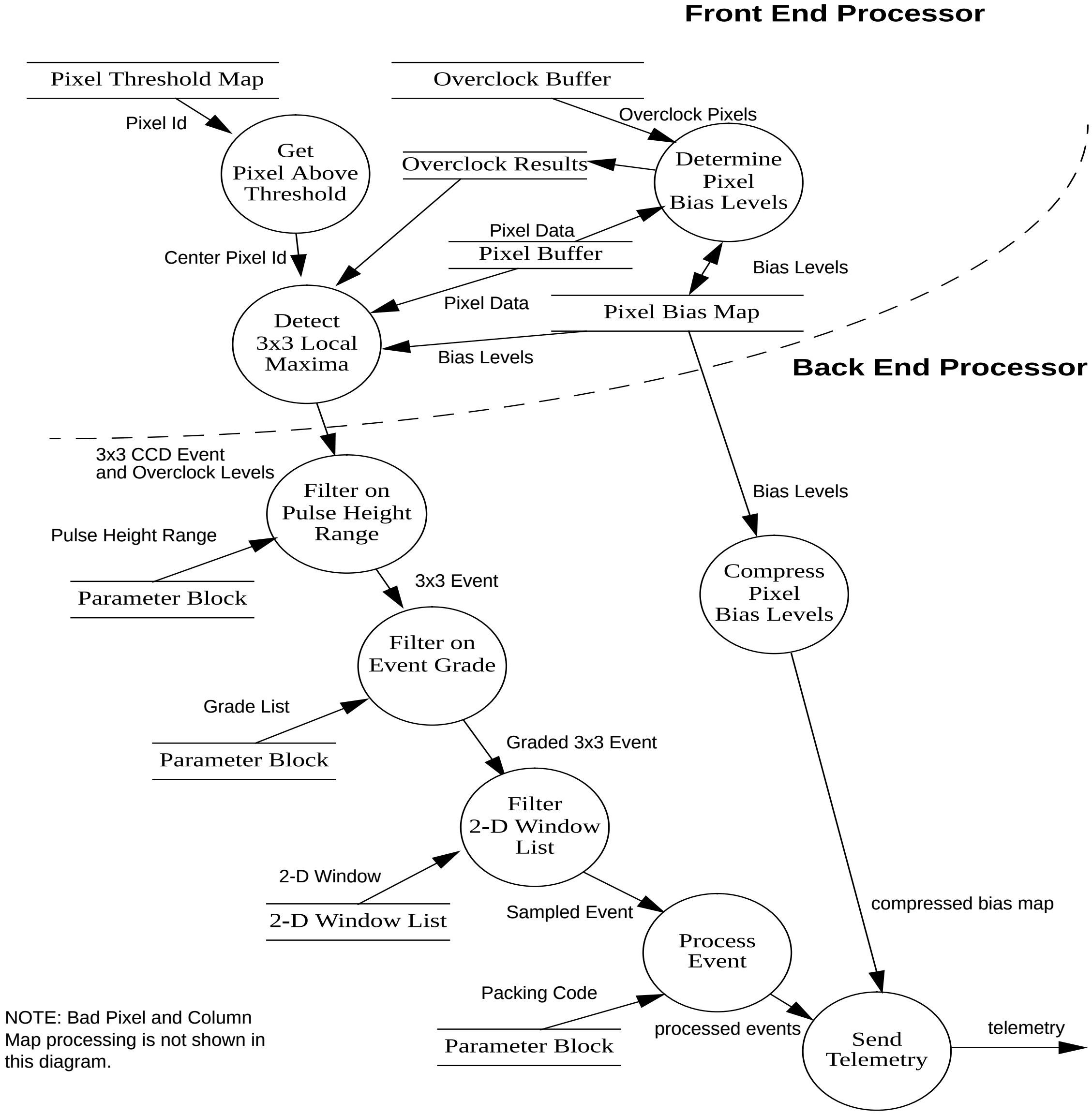

Figure 3.3: Timed Exposure Pixel Processing Data Flow

describes the contents of this block, while Table 3.27 shows the information which must be supplied to specify a list of windows.

Table 3.25: Timed Exposure Parameter Block Content

Item	**Description**
CCD Array Selection	Which CCD array to use for the Science Run: Imaging or Spectroscopy
CCD Selections	Which CCDs to use within the selected CCD Array. Capable of specifying any of the 64 possible combinations of an array's 6 CCDs.
Sub-array Readout Start and End Row	An observer uses these items to shorten the time it takes to transfer an image from the CCDs to the Front End Processors by sacrificing some of the imaging area. The start and end rows specify which contiguous horizontal swath of CCD rows are transferred from the Framestore back to the FEPs. These values are CCD-specific.
Exposure Times	Controls the amount of time that the Image Area of each CCD is integrating data. Can range from 0.2 to 10 seconds in 0.1 second increments.
Output Register Clocking Mode	Controls the clocking mode of all of the CCD's Serial Output Shift Registers. Can specify either: Full-Mode, AC-Mode, BD-Mode or Diagnostic-Mode.
Number of Overclock Pixels	Specifies the number of extra pixels to clock out all of the Serial Output Shift Registers. Timed Exposure Mode uses these pixels to determine the bias introduced to the CCD's pixel pulse height by the analog electronics. Range is 0 to 32 pixels, in 2 pixel increments.
Video Chain Response	Controls the response of the Video Subsection in the Detector Electronics Assembly. Range is 1 or 4 electrons per Analog-to-Digital Unit (ADU).
Reference to an explicit DEA Load	Optional item which allows a maintainer to by-pass the on-board SRAM/PRAM synthesizer, and load these areas directly.
Threshold Set Points	Controls minimum pulse-height above bias a pixel should have to be considered as an event candidate. Each item applies to a specific CCD. These values can range from 0 to 4095.
Front End Selection Algorithm	Specifies whether or not the Front End Processor should supply all pixels to the Back End (Raw Mode), or only those whose center is above the current threshold (Event-finding Mode) and whose pulse height is greater (or sometimes equal) to its immediate neighbors (3x3 local maxima).
Bias Exposure Count	Specifies how many exposures over which to compute the overclock level and to modify the spatial threshold levels.
Reference to Front End Processor Code	Allows a maintainer to override the standard code and data loaded into the Front End Processor, and provide a special load for the Science Run.

Table 3.25: Timed Exposure Parameter Block Content (Cont.)

Item	**Description**
Reference to a 2-D Window Collection	Specifies a set of 2-dimensional event selection and processing windows to use for the Science Run. If no windows are specified, Timed Exposure Mode shall process all events from the CCDs using the processing parameters specified in this block.
Split Threshold Set Point	Threshold used when grading events. Range from 0 to 4095.
Ignore Bad Pixel Map Flag	Controls whether or not to discard events on the basis of the CCD's list of bad pixels and columns.
Grading Selection Bit Map	Selects which event grades to accept. Accepted events whose grades are indicated in this list shall be telemetered. Consists of 256 bits, where each bit corresponds to one of the possible grade codes.
Pulse Height Lower Bound	Selects the minimum total pulse height of accepted events. Events whose total pulse height (function of the 3x3 grid around the event) is less than this value shall not be telemetered. Range is governed by the minimum and maximum corrected event pulse heights.
Pulse Height Upper Bound	Selects the maximum total pulse height of accepted events. Events whose pulse height is greater than this value shall not be telemetered. Range is governed by the minimum and maximum corrected event pulse heights.
Event List Packing Code	Selects the format to use when sending events. Currently, the following formats are supported: Raw, Raw Histogram, 3x3, 5x5, and Graded.

If configured to do so, the FEP software on ACIS will be responsible for computing, reporting, and using the overclock bias of its CCD. Overclock data are generated by clocking the Serial Output Shift Registers after all of a row's pixel data have been clocked out. As the

Table 3.26: 2-Dimensional Window Information

Item	**Description**
CCD Identifier	Selects the CCD (out of all 10) to which the window applies.
Window Position	Specifies the window position in terms of the bottom-left pixel within the CCD's Imaging Section.
Window Width	Width of the window in terms of Imaging Section columns (1-1024).
Window Height	Height of the window in terms of Imaging Section rows (1-1024).
Selection Code	Code identifying selection rules of all events whose position is within the limits of the window.
Selection Argument(s)	Any selection arguments needed by the code
Local Pulse Height Range	Sets the lower and upper pulse heights of candidate events. Events whose pulse-height is outside this range would be rejected.

Table 3.27: 2-Dimensional Window List Parameter Block

Item	**Description**
Window Count	Identifies the number of 2-D Windows contained in the Window List. Ranges from 0 to 36
Windows [Window Count]	Array of 2-D windows. The content of these windows is described in Table 3.26. The number of windows in the array is 'Window Count'.

overclock data arrive from the CCDs, the Front End hardware writes the overclock data to a set of special buffers. The FEP software then averages the data contained in these buffers to produce an overclock bias of the CCD. ACIS uses the resulting overclock bias to control the pulse height lookup table for the next exposures and the spatial threshold values for the subsequent exposures. The FEP software recomputes and applies the overclock bias every set of exposures, as specified by the "Bias Exposure Count" field of the Timed Exposure Parameter Block.

The FEP software computes the threshold for event recognition on a pixel-by-pixel basis. This threshold is used during event processing, in order to separate read noise from X-ray event candidates. The spatially varying threshold is computed for each pixel according to the following formula:

$$S_{ij} \;=\; B_{ij} + T_n + O_n, \tag{3.16}$$

where S_{ij} is the Spatial Threshold for the (*ith, jth*) pixel, B_{ij} is the predetermined bias value for that pixel, and O, Overclock Bias, and T, Threshold Set Point, are selected based on the output node, n, from which the data originate.

The FEP contains a Pixel Threshold Bitmap. This indicates which pixels in the acquired CCD image have pulse heights greater than their respective spatial threshold registers. When the "Front End Selection Mode" field of the Timed Exposure Parameter Block indicates the 3x3 or 5x5 processing mode, the FEP software scans this bitmap for each exposure. Any pixel marked as above its threshold is counted in an "above threshold" counter and is tested as an event. When the FEP is in Raw or Histogram Mode, the threshold map is ignored and all pixel data are examined.

When the "Front End Selection Mode" field of the Timed Exposure Parameter Block indicates the Event-Finding Mode, the FEP selects events from candidates indicated by the hardware Pixel Threshold Map. If a pixel is indicated in this map, the FEP software compares the uncorrected pulse height of the pixel to the eight surrounding pixels, as shown in Figure 3.4. In order to meet the criteria for an event, the center pixel (black square) must have a pulse height greater than or equal to the previous row and the pixel immediately preceding it within its row (shaded squares), and must have a pulse height greater than or equal to the pixels in the subsequent row and the pixel immediately after it in its row

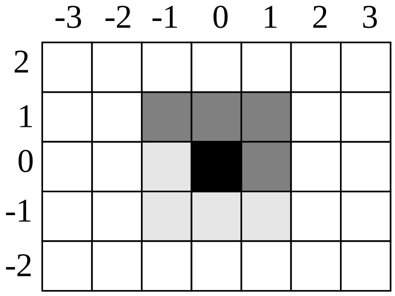

Figure 3.4: 3x3 Event-finding Mode Pixel Diagram

(hatched squares). If the pixels meet the criteria, the FEP forwards the 3x3 group of pixels to the BEP for further selection and processing.

ACIS contains a list of bad pixels and columns from each CCD. These maps are edited using maintenance commands from the ground (see Sect. 3.2). The Bad Pixel Map and Bad Column Map entries contain lists of individual pixel locations or entire columns which will be excluded from the event telemetry, when the instrument is commanded to do so. When the "Front End Selection Mode" field of the Timed Exposure Parameter Block indicates the 3x3 or 5x5 processing mode and the "Ignore Bad Pixel Map" flag is de-asserted, the software tests any events generated by the Front End to ensure that the center pixel of the 3x3 event is not listed in the Bad Pixel Map. If the center pixel is in the list, the event is counted in a "discarded event" list and no further processing on the event takes place. If the center of the event is not in the list, software accepts the event for further selection and processing. When the selection mode specifies that all pixel data shall be sent by the FEP (Raw Mode) or the "Ignore Bad Pixel Map" flag is asserted, the Bad Pixel Map is ignored and the software accepts the pixel/event data for further selection and processing.

To obtain the corrected pulse height of a pixel, the ACIS Software subtracts the overclock level and bias offset from each pixel in the 3x3 group, to obtain a bias-corrected pulse height for each pixel. The amplitude of an event is the sum of the corrected pulse heights of the appropriate pixels in the group. The pixels whose pulse heights are to be included are shown in Figure 3.5, and are as follows:

- Center Pixel (black square)
- Edge Pixels above Split Threshold (hatched squares)
  These pixels are located to the top, bottom, left, and right of the center pixel whose bias-corrected pulse height exceeds the split threshold specified by the "Split Threshold Set Point"

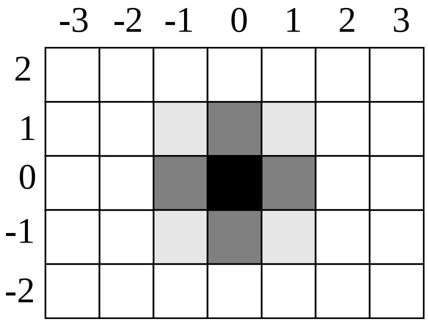

Figure 3.5: Event Amplitude Pixel Diagram

- Corner Pixels (shaded squares) above Split Threshold and adjacent to the included Edge Pixel(s)
  These pixels are located diagonally from the Center Pixel and have a corrected pulse height greater than the Split Threshold. These pixels must also be adjacent to one or more Edge Pixels whose pulse heights are above the Split Threshold.

Note that, in faint-bias mode telemetry, the bias levels are sent along with the pixel neighborhood data. In graded mode the goal is to reduce the volume of telemetry per event, so this information is not sent.

While in the 3x3 processing mode, the BEP computes the overall corrected pulse height of 3x3 events received from the FEP and compares the result with the "Pulse Height Lower Bound" and "Pulse Height Upper Bound" specified in the Timed Exposure Parameter Block. If the value is less than the lower bound or greater than the upper bound, the software increments an event rejection counter and discards the event. If the value is within range, the software accepts the event for further selection and processing. If the "Front End Selection Mode" field indicates "Raw Mode," the software will not apply a pulse-height range test and will accept all pixel data for further selection and processing.

When needed for event selection or telemetry, the BEP software computes the "grade" of a 3x3 or 5x5 pixel event. To accomplish this, the software compares the corrected pulse heights of the eight outer edge pixels of the event to the "Split Threshold" specified in the Timed Exposure Parameter Block. Each pixel corresponds to a "bit" in the grade code. If a pixel's pulse height is greater than or equal to the threshold, the corresponding bit is marked as a "1". If a pixel's pulse height is less than the threshold, the bit is marked as a "0". Since there are eight pixels on the edge of a 3x3 event, this leads to an 8-bit grade code. There are 256 possible "grades" for a 3x3 event. Figure 3.6 illustrates an example 3x3 event, with pixel pulse heights drawn as vertical bars and the split threshold drawn as a grid. The pixels whose pulse height is above the threshold are shown to the right

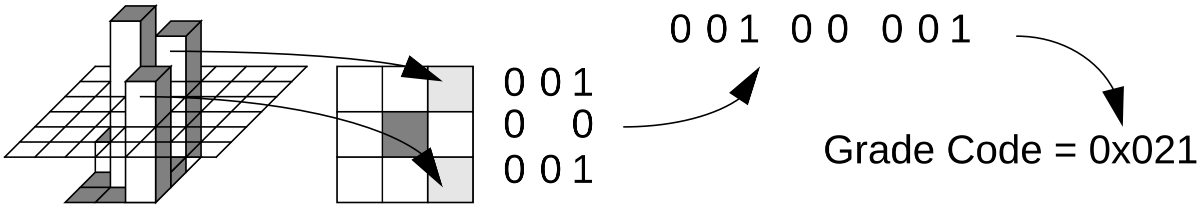

Figure 3.6: 3x3 Event Grading Illustration

as lightly shaded areas. Since the center pixel has been selected on the basis of being a local maximum, it will always be the pixel with the highest signal. (It is shown using a darker shade in the diagram.) The diagram then shows the mapping of the pixels onto grading bits, and from grading bits onto the resulting Grade Code. Note that when in 5x5 mode only the central 3x3 region is used to define the grade, and these grade definitions are identical to the 3x3 mode.

A complete list of the ACIS grades with a diagram illustrating the split event threshold crossings is given in Appendix A. Please note that ACIS grades and ASCA grades do not use the same numbering convention. ACIS grades run from 0 to 255, while ASCA grades run from 0 to 7. ACIS grade 0 is identical to ASCA grade 0 (a single, isolated event without any neighboring split threshold crossings), but all other ASCA grades are sums of many ACIS grades. Also note that when ACIS operates in “Graded Mode” only the total reconstructed energy of the X-ray event is telemetered to the ground. The total energy is computed by summing all pixels which exceed the split event threshold. On ASCA the corresponding mode (‘Bright Mode’) sums pixels regardless of whether the split threshold is crossed. The result is that some ASCA grade 5 and 7 event total energy values can not be calculated from ACIS grade and energy information alone.

When in the 3x3 or 5x5 processing mode and the “Grading Selection Bitmap” does not indicate that all possible grades are to be accepted, the BEP software computes the grade of an event and compares the computed code to the list of desired grades. If the computed grade is not in the list, the discard counter is incremented and the event is ignored. If the event’s grade is in the list, the event is accepted for further selection and processing. When in Raw Mode or if the “Grading Selection Bitmap” indicates that all possible grades are to be accepted, the software accepts the data for further selection and processing without needing to compute the grade of the event.

The BEP software can use 2-D windows to select events and pixels to report. If an event’s center pixel or an individual pixel’s position is within the bounds of a 2-D window, it is selected according to the window. For a given event or pixel, each window in the window list is checked in the order it is presented in the list. If the event/pixel position is within the boundaries of the window, the event/pixel is processed by the window. If the position is outside the bounds of the window, the next window is checked. This continues until the list is exhausted. If no window list is specified, or if the list becomes exhausted with the event/pixel not being picked up by any of the windows, the event/pixel by default is accepted for processing. This scheme acts like a default window which encompasses the entire CCD and whose property is to accept all events/pixels.

The final result of this processing is a 3x3 or 5x5 array of pixel values which are packaged into Science Data Format packets which are presented to the RCTU for telemetry to the ground. Please note that the values in the 3x3 array are telemetered in their original form (i.e. raw or non-bias subtracted). In order to properly interpret these data it is necessary to subtract the bias values on the ground. If the mode is Timed Exposure with Bias, the telemetry for each event will also contain a 3x3 array of the bias values for these same pixels.

The full expression for Bias Subtraction (in terms of packet field names as defined in the IPCL) is:

$$\mathrm{pixel} = \mathrm{pulseHeights} - \mathrm{biasValues} - \mathrm{deltaOverclocks}[\#\mathrm{node}] \tag{3.17}$$

3.3.3 Continuous Clocking Mode Data Processing

An observer uses Continuous Clocking Science Mode to acquire, process, and telemeter high time-resolution, 1-dimensional images from the CCD array. This mode provides data as a time-series of events which occurred along the columns of a CCD, acting like a strip-chart recorder, where each CCD column is analogous to a single pen.

To execute a Continuous Clocking Science Run, the observer sends a “Start Continuous Clocking Run” command to ACIS. ACIS retrieves the parameter block referenced by the start command and proceeds to execute the science run. The observer allows ACIS to acquire, process, and telemeter CCD data for a period of time, after which the observer sends a “Stop Continuous Run” command to ACIS, which then stops the run and telemeters a Science Run Report. If the observer requires parameters not already provided by the ACIS parameter library, the observer must issue a “Load Continuous Clocking Parameter Block” command to load the desired parameters for the run. Table 3.28 shows the contents of that block. If the loaded parameter block requires custom event-processing windows to select and process events based on certain column positions, the observer must also issue a “Load 1-D Window List” command to place the desired window settings into the instrument. The parameter blocks to define these 1-D window settings are described in Tables 3.29 and 3.30.

Table 3.28: Continuous Clocking Mode Parameter Block

Item	**Definition**
CCD Array Selection	Which CCD array to use for the Science Run: Imaging or Spectroscopy.
CCD Selections	Which CCDs to use within the selected CCD Array. Capable of specifying any combination of an array's 6 CCDs.
Number of Rows to Sum	Number of rows to sum prior to clocking out the output registers. Ranges from 1 to 1024.
Number of Columns to Sum	Number of pixels to sum at the Output Node prior to each transfer to the DPA. Ranges from 1 to 1024.
Output Register Clocking Mode	Controls the clocking mode of all of the CCD's Serial Output Shift Registers, either: Full-Mode, AC-Mode, BD-Mode or Diagnostic-Mode.
Number of Overclock Sums	Number of extra summed pixels to clock out of the Serial Output Shift Registers. Continuous Clocking Mode uses these pixel sums to determine the bias introduced in the CCD's pixel pulse height by the analog electronics. Ranges from 0 to 32, in 2 pixel sum increments.
Video Chain Response	Controls the response of the Video Subsection in the Detector Electronics Assembly. Range is 1 or 4 electrons per Analog-to-Digital Unit (ADU).
Reference to an explicit DEA Load	Optional item which allows a maintainer to by-pass the on-board SRAM/PRAM synthesizer, and load these areas directly.
Threshold Set Points	Control the minimum pulse-height above bias a pixel sum should have to be considered an event candidate. Each item applies to a specific CCD. Range from 0 to 4095.
Front End Selection Algorithm	Specifies whether or not the Front End Processor should supply all pixels to the Back End (Raw Mode), or only those whose center is above the current threshold and whose pulse height is greater than or equal to the (possibly summed) pixel to its left, and greater than the (possibly summed) pixel to its right (3x1 local maxima).
Bias Row Count	How many (possibly summed) rows over which to compute the overclock level and modify the threshold level. Currently, this value is in units of 1024 rows.
Threshold Overrides	Fixed threshold value to use for each CCD. Values between 0 and 4095, inclusive, specify the threshold to use. Values 4096 and greater disable the override feature for the corresponding CCD.
Reference to Front End Processor Code	Allows a maintainer to override the standard code and data loaded into the Front End Processor and provide a special load for the Science Run.
Reference to a 1-D Window Collection	Specifies a set of 1-dimensional event selection and processing windows to use for the Science Run. If no windows are specified, Continuous Clocking Mode shall process all events from the CCDs using processing parameters specified in this block.

Table 3.28: Continuous Clocking Parameter Block (Cont.)

Item	**Definition**
Split Threshold	Threshold used when grading events. Ranges from 0 to 4095.
Ignore Bad Column Map Flag	Controls whether or not to discard events on the basis of the CCDs list of bad pixels.
Grading Selection Bit Map	Selects which event grades to accept. Accepted events whose grade is in this list shall be telemetered.
Pulse Height Lower Bound	Minimum amplitude of accepted events. Events whose amplitude is less than this value shall not be telemetered. Range is governed by the minimum and maximum event amplitudes.
Pulse Height Upper Bound	Maximum amplitude of accepted events. Events whose amplitude is greater than this value shall not be telemetered. Range is governed by the minimum and maximum event amplitudes.
Event List Packing Code	Format to use when telemetering events. Currently, the following formats are supported: Raw, 3x1, Graded.

The overclock processing for this mode is almost identical to that for Timed Exposure Science Mode, except the number of clocks and exposures are specified via the Continuous Clocking Parameter Block. The FEP computes the CCD threshold according to the following formula:

$$T_n \;=\; O_n + T_n^0 + B_i, \tag{3.18}$$

where T_n is the Threshold, B_i is the column bias, O_n is the Overclock Level, and T_n^0 is the Threshold Set Point. n is the output node index.

The FEP contains a Pixel Threshold Bitmap. This bitmap indicates which pixels in the acquired CCD data have pulse heights greater than the threshold. When the "Front

Table 3.29: 1-Dimension Window Information

Item	**Description**
CCD Identifier	CCD to which the window applies.
Window Column	Position of the window in terms of the left-most column within the CCD's Image Array. Position is independent of any summing column parameters in the Continuous Clocking Parameter Block.
Window Width	Number of columns (un-summed) in the window.
Selection Code	Selection rules used for all events whose position is within the limits of the window.
Selection Argument(s)	Any selection arguments needed by the code.
Local Amplitude Range	Lower and upper amplitude range for candidate events. Events outside this range are rejected. Value is not affected by any row or column summation.

Table 3.30: 1-Dimensional Window List Parameter Block

Item	**Description**
Window Count	Number of 1-D Windows contained in the Window List. Ranges from 0 to 36
Windows [Window Count]	Array of 1-D windows. Content is described in Table 3.29. The number of windows is 'Window Count'.

End Selection Mode" field of the Continuous Clocking Parameter Block indicates the 3x1 processing mode, the FEP software will scan this bitmap for each exposure. Any pixel marked as above its threshold will be counted in an "above threshold" counter and be tested as an event. When the selection mode specifies that all pixel data should be sent by the FEP (Raw Mode), the threshold map is ignored and all pixel data are sent from the FEP to the Back End.

The 3x1 processing mode indicates that the FEP should select events from candidates indicated by the hardware Pixel Threshold Map. If a pixel is indicated in this map, the Front End software compares the uncorrected pulse height of the pixel to each pixel on either side of the candidate. If the candidate's pulse height is greater than or equal to the pixel immediately preceding it in the row, and greater than the pixel immediately following it in the row, the FEP forwards the three pixels to the BEP for further selection and processing.

To obtain the corrected pulse height of a (possibly summed) pixel, the ACIS software subtracts the scaled overclock level from the measured pulse height. The corrected pulse height of a 3x1 group of pixels is computed by summing the corrected pulse heights of all three pixels, which are greater than the "Split Threshold" as specified in the Continuous Clocking Parameter Block. The BEP compares the overall corrected pulse height of the 3x1 events with the "Pulse Height Lower Bound" and "Pulse Height Upper Bound," specified in the parameter block. If the value is less than the lower bound or greater than the upper bound, the software increments the event rejection counter and discards the event. If the value is within range, the event is accepted for further selection and processing. If the "Front End Selection Mode" field indicates "Raw Mode," the software will not apply a pulse-height range test and will accept all pixel data for further selection and processing.

When the "Front End Selection Mode" field of the Continuous Clocking Parameter Block indicates a 3x1 processing mode and the "Grading Selection Bitmap" does not indicate that all possible grades are to be accepted, the BEP software computes the grade on an event and compares the computed grade to the list of desired grades. If the computed grade is not in the list, the event is counted and discarded. If the event's grade is in the list, the event is accepted for further selection and processing. If Raw Mode is set or if the "Grading Selection Bitmap" accepts all possible grades, the software accepts the data for further selection and processing.

The BEP software uses 1-D windows to select events and pixels to telemeter. If an event's center pixel or an individual pixel's position is within the bounds of a 1-D window, it is processed according to the window's selection code. For a given event or pixel, each window in the window list is checked in the order it is presented in the list. If the event/pixel column is within the bounds of the window, the event/pixel is processed by the window. The window boundaries are expressed independently of the number of summed columns. Therefore, the pixel position, relative to a window, is really a range of positions. If this range intersects the window, it is considered a match, and the event is selected by the window. If the position is outside the bounds of the window, the next window is checked. This continues until either a match is found or the list is exhausted. If no window list is specified or if the list becomes exhausted with the event/pixel not being picked up by any of the windows, the event/pixel is, by default, accepted for processing.

As with the Timed Exposure data, the 1x3 event data are telemetered as raw, non-bias subtracted data. In Continuous Clocking the bias frames are all so small (only 1x1024 vs. 1024x1024 for Timed Exposure), that the entire Bias is always telemetered before the start of normal data collection. There is no equivalent to FaintBias mode for Continuous Clocking data.

3.3.4 Telemetry Formats

Within the science data allocation of the AXAF-I telemetry major frame, an asynchronous packetized transport protocol will be implemented for ACIS science data. ACIS engineering housekeeping will be acquired by the RCTU directly and placed in fixed locations within the AXAF-I telemetry major frames.

Table 3.31 lists the ACIS telemetry according to the features called out in the Science Instrument Software Requirements Specification. Information which is sent using the discrete hardware status bits is preceded with the word 'Discrete-'. The remaining items are sent as Telemetry Packets, using the Serial Digital Telemetry stream.

ACIS telemetry reaches the ground by being embedded within the AXAF-I telemetry stream. This stream is organized by grouping into major data frames, defined in the AXAF-I to SI Interface Document (provided by TRW). The major data frame will provide an average science data rate of 24 kbps, including headers. Aspect data will not be included with this allocation. All SI data are collected in serial 8-bit words by the RCTU.

Each 1025 byte minor frame includes a 24 word (192 bits) science data header, as listed in Table 3.32. The header is supplied by the observatory and merged with ACIS data by the CDM subsystem. Position and attitude information given in the header are defined in an Earth Centered Inertial (ECI) coordinate system with the X axis parallel to the

Table 3.31: ACIS Serial Telemetry Packets Grouped by System Feature

Science Modes

Timed Exposure (TE)	**Continuous Clocking (CC)**
TE Obs. Record	CC Obs. Record
TE Raw Exp. Record	CC Raw Exp. Record
TE Raw Pixel Record	CC Raw Pixel Record
TE Raw Hist. Data	CC Faint Record
TE Faint Record	CC Faint Data
TE Faint Data	CC Graded Record
TE Graded Record	CC Graded Data
TE Graded Data	CC Obs. Report
TE Obs. Report	CC Raw Histogram Data

Maintenance

Hardware Configuration	**Memory Commands**	**DEA Housekeeping**
Dumped TE Bad Pixel Map	BEP Memory Dump	DEA Housekeeping
Dumped TE Bad Column Map	FEP Memory Dump	
Dumped CC Bad Column Map	SRAM Memory Dump	
	PRAM Memory Dump	
	BEP Memory Exec. Reply	
	FEP Memory Exec. Reply	
	Huffman Table Dump	
SW Housekeeping		
Command Echo		
Software Statistics		
Fatal Error Message		

sky position of the vernal equinox (epoch 2000; i.e. the First Point in Aries); the Z axis parallel to the Earth rotation axis; and the Y axis defined so as to complete a right-handed coordinate system.

ACIS serial telemetry data appear in two formats. Format 1 is used when the HRC is in the focal plane, and ACIS is ‘next-in-line.’ In this configuration, ACIS telemetry is taken at 0.5 Kbps and stored in the engineering sections of the Format 1 telemetry. When ACIS is in the focal plane, Format 2 is used. In this configuration, ACIS serial telemetry is taken at 24 Kbps and is stored in the Science Data portions of the Format 2 telemetry. Table 3.33 illustrates the overall layout of Format 2’s Science Frame. Sixteen Science Frames make

Table 3.32: Science Telemetry Frame Header Contents

Code Function	**Description**
Major Frame Count	2 words
Time Code	6 words; provides Julian date to 1 μsec resolution.
AXAF Position	6 words; provides AXAF-I position in ECI coordinates. 2 words per axis with 3.0 km resolution.
Geocenter	4 words; direction of geocenter in azimuth and elevation from AXAF-I Line-of-Sight with 10^{-4} radian resolution
Attitude Code	8 words; orientation of AXAF-I in Right Ascension & Declination of the +X, +Z axes; 2 words per quantity; 10^{-4} radian resolution

Table 3.33: Science Frame Format

Frame					Repeat 7 times		
Minor Frame 0	CCSDS VCDU Header	Eng. Data	Science Header (Minor #0 only)	Science Data Sect. 0	Eng. Data	Science Data Sect. 1-7	Eng. Data
Bytes	6	26	24	72	32	96	1
Minor Frame 1	CCSDS VCDU Header	Eng. Data	Science Data Sect. 8		Eng. Data	Science Data Sect. 9-15	Eng. Data
Bytes	6	26	96		32	96	1
.	.	.	.		.	.	.
.	.	.	.		.	.	.
.	.	.	.		.	.	.
Minor Frame 7	CCSDS VCDU Header	Eng. Data	Science Data Sect. 56		Eng. Data	Science Data Sect. 57-63	Eng. Data
Bytes	6	26	96		32	96	1

up a Telemetry Major Frame. The areas labeled ‘Science Data’ contain data formatted and supplied by the ACIS software. When created by the ACIS software, the science data sections are treated as contiguous. Each section is transferred to the RCTU at 128 Kbps, with appropriate delays inserted between each non-adjacent section.

While ACIS is operated in timed exposure science mode, there are six possible telemetry formats: raw mode event telemetry, raw histogram mode telemetry, faint mode event telemetry, faint with bias mode event telemetry, very faint mode event telemetry and graded

Table 3.34: Exposure Header Content

Item	**Description**
Science Run Start Time	Start time of the science run using the ACIS time-stamp latched by the hardware at the start of the run.
Exposure Number	Identifies the clocked exposure during the run. Must allow the ground to uniquely identify over 130,000 exposures during a single run (2 second exposures for 72 hours).

Table 3.35: Raw Mode Data Telemetry Content

Item	**Description**
CCD Identifier	CCD (& node ID) from which the raw pixel data were taken.
Window Identifier	Identifies 2-D window used to select this set of pixels. (2-D windows may not be included in final version of ACIS software.)
Exposure Overclock values	Overclock values read from the CCD while the pixel data were being acquired.
Array of raw 12-bit CCD pixel data	Array of raw CCD pixel data. The bottom left position of the first pixel corresponds to the intersection of the identified window and the sub-array readout selection. The pixels are organized by row and then by column, where the number of rows and columns in the set is the intersection of the identified window and sub-array read-out parameters.

event telemetry.

In raw event mode, contiguous regions of pixels are telemetered as a set. Table 3.34 describes the exposure record telemetry and Table 3.35 describes the content of the CCD data telemetry when in this mode. This mode allows every pixel to be examined on the ground, but it is very expensive in terms of telemetry consumption. It is anticipated to be used only occasionally, and primarily as a diagnostic for study of changes in CCD behavior.

In raw histogram mode, each DEA output node has an associated histogram which counts pixels as a function of raw pulse height. Pixels produced during a single exposure whose positions are processed by a given node are counted in the corresponding histogram. After all pixels from the exposures have been processed, all the histograms are telemetered. Tables 3.34 and 3.36 describe the exposure record telemetry and the contents of the CCD data telemetry when in this mode, respectively. This mode is also primarily diagnostic, but is far less consumptive of telemetry, as only the histogram is telemetered to the ground.

In faint mode event telemetry, sets of distinct events are telemetered as 3x3 arrays of pixels. Table 3.37 illustrates the content of an exposure record, Table 3.38 shows the contents of the event lists telemetered when in this mode.

Table 3.36: Raw Histogram Mode Data Telemetry Content

Item	**Description**
CCD Identifier	CCD (& node ID) from which the raw pixel data were taken.
Node Identifier	Identifies node used to select this set of pixels.
Array of histogram counts	Array of 4096 bins. Each bin contains a count of the number of pixels within the node and whose pulse height corresponded to the bin index.

Table 3.37: Faint Mode Exposure Record Content

Item	**Description**
Science Run Start Time	Start time of the science run, as specified by the DEA latched ACIS time-stamp.
Exposure Number	Identifies the clocked exposure during the run. Allows the ground to uniquely identify over 130,000 exposures during a single run (2 second exposures for 72 hours).
Number of Events Telemetered	Number of events being telemetered in the exposure. Must accommodate at least 64K events.
Number of Pixels above threshold	Number of pixels from a CCD whose pulse heights were above their respective spatial thresholds during the exposure.
Number of Events Discarded due to Bad Pixel and Column Map	Number of events which were discarded because they were listed in the Bad Pixel and Column Map.
Number of Events Discarded by Pulse Height	Number of events which were discarded due to their pulse height. Must accommodate the total number of pixels within the CCDs.
Number of Events Discarded by Grade	Number of events which were discarded due to their 'grade.' If grade selection is not performed, these counters need not be telemetered.
Number of Events Discarded by Window	Number of events which were discarded by the processing windows.

Table 3.38: Faint Mode Event Telemetry Content

Item	**Description**
CCD Identifier	Identifies which CCD the event occurred.
Position Identifier	Row and column of the center pixel of the event.
Uncorrected Pulse Heights	Measured (uncorrected) pulse heights of the 9 pixels forming the 3x3 neighborhood of a suspected X-ray event.
Overclock Level	Overclock level used for the thresholding during the exposure which produced the event.
Spatial bias offset	Spatial bias used for thresholding for this event.

Table 3.39: Graded Event Telemetry Content

Item	**Description**
CCD Identifier	CCD the event occurred.
Position Identifier	Row and column of the center pixel of the event.
Event Amplitude	Amplitude of the event.
Grade Code	Identifies the Grade Code (see Sect. 3.3.2).
Corner Pulse Heights	Potential function of the corrected pulse-heights of the 4 corner pixels in the 3x3 event array.

Table 3.40: Continuous Raw Mode Event Data Telemetry

Item	**Description**
CCD Identifier	CCD from which the raw pixel data were taken.
Node Identifier	Node used to process this set of pixels.
Overclock values	Overclock values read from the CCD while the pixel data were being acquired.
Array of raw 12-bit CCD pixel data	Array of raw CCD pixel data.

Graded event telemetry also provides information about the 3x3 array of pixels around all suspected X-ray events. But in this mode, (as opposed to the 'Faint' mode), instead of all nine pixel values only a combined net pulse height is telemetered and an event "grade" which describes the relative distribution of pixels in the array which exceed a split event threshold (see Section 3.3.2 for the definition of event grades). The content of an exposure record in this mode is identical to that used by faint mode telemetry (see Table 3.37 above). The event data content, however, is different. Table 3.39 illustrates the content of the event lists telemetered when in this mode.

While ACIS is operated in continuous clocking science mode, a set of three possible telemetry formats exists: continuous raw mode event telemetry, continuous faint mode event telemetry, and continuous graded mode event telemetry.

In continuous raw event mode, contiguous regions of pixels are telemetered as a set. For each configurable number of rows, a "Continuous Raw Mode Record" is formed and telemetered. Table 3.34 identifies the exposure record telemetry; whereas Table 3.40 lists the elements telemetered for each pixel.

In continuous faint mode event telemetry, a series of distinct events is telemetered as 3x1 arrays of pixels. Table 3.41 illustrates the content of a continuous faint mode record, and Table 3.42 describes the contents of the event lists telemetered when in this mode.

In continuous graded mode event telemetry, sets of distinct events are telemetered using reduced pulse height information and event grade. The content of a continuous graded event

Table 3.41: Continuous Faint Mode Record Content

Item	**Description**
Science Run Start Time	Start time of the Science Run, relative to the time-stamp latched at the start of the run.
Continuous Faint Mode Record Number	Uniquely identifies a stream of data within the run. Must allow the ground to uniquely identify over 130,000 records during a single run (2 second exposures for 72 hours).
Number of Events	Number of events being telemetered as part of this event stream. Must accommodate at least 64K events.
Number of Pixels above Threshold	Number of (possibly summed) pixels whose pulse heights were above the threshold.
Number of Events Discarded due to Bad Column Map	Number of events which were discarded because they were listed in the Bad Column Map.
Number of Events Discarded by Pulse Height	Number of events which were discarded due to their pulse height. Must accommodate the total number of pixels within the CCDs.
Number of Events Discarded by Grade	Number of events which were discarded due to their "grade." If grade selection is not performed, these counters need not be telemetered.
Number of Events Discarded by Window	Number of events which were discarded by the processing windows.

Table 3.42: Continuous Faint Mode Data Telemetry

Item	**Description**
CCD Identifier	Identifies in which CCD the event occurred.
Row Identifier	Which (possibly summed) row the event was acquired. Used to obtain a high-resolution time-stamp of the event.
Column Identifier	Which (possibly summed) column the event was acquired.
Uncorrected Pulse Heights	Measured (uncorrected) pulse heights of the 3 pixels of the event's 3x1 array.
Overclock level	Overclock level used for the thresholding when the event was acquired.
Spatial Bias Offset	If computed, this identifies the spatial bias offset used for thresholding when the event was acquired.

record in this mode is identical to that used by continuous faint mode telemetry. The event data content, however, is different. Table 3.43 illustrates the content of the event lists telemetered when in this mode.

Programmability of the telemetry modes is covered by the 'Software Users Manual' by Jim Francis. Such programmability is implemented by uploading a patch to the operating software, so the capability to support required changes is nearly unlimited.

Event timing information can be related to the AXAF-I clock with an accuracy of one

Table 3.43: Continuous Graded Mode Event Data Telemetry

Item	**Description**
CCD Identifier	Identifies in which CCD the event occurred.
Row Identifier	Which (possibly summed) row the event was acquired. Used to obtain a high-resolution time-stamp of the event.
Column Identifier	Which (possibly summed) column the event was acquired.
Center Pixel Pulse Height	Corrected pulse height of the 3x1 array's center pixel.
Grade Code	Grade Code of the event.

period of the ACIS pixel. The original ICD requirement of 1 μsec was waived to allow the substition of a 100 kHz clock. As currently defined this accuracy is 15 μsec. The first 32 bits of the Science Data written following the receipt of the Science Frame Pulse is the value of a timestamp counter specially sampled and inserted into the serial output stream by ACIS hardware. Its value represents the number of pixel clock cycles since it was last reset or wrapped. This counter will wrap about once per eight hours. ACIS shall use this same counter to timestamp the start of its Science Runs. This, coupled with the Spacecraft-supplied timestamp information in the Science Header of each frame, specifies the start time of a run. All science data sent by ACIS will be indexed relative to the start of the run, using clocking-mode driven counters (such as exposure counts or data set counts).

Timing with respect to the AXAF-I central clock is received via a science frame synch signal provided by the Spacecraft Interface Unit and utilized by the BEP. The BEP acts as the ACIS Master Clock Generator and synchronizes all ACIS software functions to this signal. (Note the science header telemetry is derived from the same master oscillator [operating at 14.848 MHz] so the telemetry is also synchronous with this clock.)

ACIS provides a Master Timestamp Counter, also resident on the BEP. It is reset only on power-up of the ACIS experiment. Thereafter it is free running, incrementing with each cycle of the science frame, and thus rolling over its 32-bit capacity in 41920 seconds (roughly 700 minutes). When it rolls over it broadcasts a reset pulse to Slave Timestamp Counters running on the FEPs, thus assuring synchronization of the FEPs which generate the 'Beginning of Frame' signals at the start of every CCD frame.

The full details of how event timestamps are applied on the ground can be found in Appendix D of the Flight Software Requirements Specifications. This document (MIT Document Number 36-01103) can also be found at the MIT Web site http://acis.mit.edu/sw.html.

Microprocessor diagnostics are not currently supported in the flight software. If they are required they must be uploaded from the ground to enable true diagnostics.

Chapter 4

Calibration/Maintenance

The ultimate goal of the AXAF system calibration is to allow absolute fluxes, positions, energies, and times at the earth to be determined from the raw data telemetry from the observatory. It is impractical to calibrate all desired quantities at every detector location and every desired energy. The calibration process measures the quantities for a wide enough range of parameters to characterize and verifies the system response through detailed analytic and numerical models.

Calibration is done in three major stages: laboratory calibration of the individual components, system ground calibration at the NASA MSFC X-ray Calibration Facility (XRCF), and orbital calibration using celestial and spacecraft sources.

All stages of calibration are treated in the ACIS Science Instrument Calibration Report. This report, jointly prepared by the MIT and PSU teams, covers the description of lab and XRCF testing of the ACIS experiment and the current results and conclusions of the analysis of the testing. The following chapter is a summation of those studies. The full Calibration Report will be released in preliminary form in October, 1997. The initial formal release is planned for June, 1998. It will be available electronically from http://acis.mit.edu and via ftp from ftp.astro.psu.edu in /pub/axaf/cal_report.ps.gz.

4.1 Lab Data

The laboratory calibration of ACIS produces models based on the measurements of:

- quantum efficiency, energy resolution, and system gain and linearity as a function of incident energy and instrument parameters (such as temperature and clock voltages);
- non-X-ray light rejection efficiency, including UV/visual optical blocking filter checks;

- CCD read-noise, charge transfer efficiency, charge collection efficiency, and dark current as a function of energy and CCD parameters;
- geometric layout of CCDs relative to ACIS fiducial marks, including seam locations and sizes;
- limits to six charge transfer clock levels — high and low on each of: imaging, framestore, and serial units — for optimum CTE, noise, and dark current;
- relationship between pre-amplifier bias, reset bias, reset clock levels and read noise, amplifier responsivity, and reset performance (the time to clear the CCD, or dead time);
- verification of read-out modes.

Calibration is done by illuminating the CCDs with low energy X-rays from a monochromator or hard X-rays from a radioactive source. All CCDs have been tested, but some were tested more than others (deeper exposures, for example, which are too time-consuming to perform on all CCDs, but which can be used to characterize them). Absolute efficiency measurements have been done at the BESSY synchrotron radiation facility in Berlin on Lincoln Lab CCDs made in the same way as the flight CCDs. These chips provide transfer standards for assessing the absolute quantum efficiency of all the CCD chips flown in both the imaging and spectroscopic arrays, and the flight backup chips.

4.1.1 CCD Subassembly Calibration Measurements

This section describes the objectives, measurements, and required measurement accuracies for ACIS CCD subassembly calibration performed at the MIT Center for Space Research. These calibration measurements have been performed on each flight candidate detector before it was assembled into a flight focal plane. Only detectors which met the requirements established in the ACIS CCD Screening plan (ACIS memo PS-77) were calibrated.

4.1.1.1 CCD Subassembly Calibration Requirements

The CCD subassembly calibration measurements were selected via the following two-step process. First, scientific investigations which are most sensitive to ACIS calibration accuracy were identified. The corresponding AXAF observations were simulated using a parametric CCD response model, together with models of other components of AXAF. The parameters of the CCD response model were varied to determine the sensitivity of the scientific results to errors in the assumed CCD model parameters. The result of this first step was thus a set of constraints on the accuracy with which CCD model parameters must be determined.

The second step in the measurement selection process determined the accuracy with which various proposed laboratory measurements can constrain CCD response model parameters. This step required analysis and simulation of feasible laboratory measurements. In principle, the product of this step was a suite of laboratory measurements that calibrates ACIS CCDs with accuracy adequate to meet scientific objectives.

The parametric CCD response model clearly plays a central role in the selection of calibration measurements. The CCD response model used to derive the CCD subassembly calibration measurements specified here is described in ACIS memos PS-73 and PS-79 (Rasmussen).

Practical considerations complicate the selection of calibration measurements. Specific, readily identifiable scientific measurement requirements do not provide a complete specification of calibration accuracy requirements. More fundamentally, one could not, even in principle, anticipate all measurements that will be made with AXAF. For these reasons, it is useful to have a clear, if somewhat arbitrary, set of calibration objectives with which to guide calibration planning. The objectives adopted to plan the CCD subassembly calibration measurements described here are therefore stated, though not justified, as part of each measurement description. These objectives are consistent with the calibration goals identified in MSFC-2229; the justification of the objectives is beyond the scope of this document.

The complexities of laboratory measurements and the oversimplifications inherent in feasible simulations of those measurements must also be accounted for in calibration planning. To allow for these uncertainties, this plan called for more measurements than the absolute minimum number that simulations suggest was necessary. For example, simulations show that the required accuracy in quantum efficiency can be achieved with measurements at as few as four energies (see ACIS memo PS-72 (Isobe)); this plan called for measurements at seven energies (see section 4.1.3 below.) The additional measurements allow for the evaluation of systematic errors in both the models and the measurements.

4.1.2 Spectral Resolution Measurements (nominal conditions)

4.1.2.1 Objectives of spectral resolution measurements

1. Determine energy scale to 0.1%, FWHM to $\sim 5\%$.
2. Determine off-peak features (Si K escape, Si-K fluorescent) to 0.3% of total flux.
3. Determine magnitude of low-energy tail at level of $\sim 0.5\%$ of main peak (integrated tail area : integrated main peak area).

4.1.2.2 Assumptions for spectral resolution measurements

1. Spectral resolution is effectively independent of position on the CCD.
2. Quantum efficiency measurements provide spectral resolution data at energies different from those specified here (see next section).

System	Energy (keV)	Total Cts (/energy/CCD quad.)	No. of Frames
HIREFS Spec.	0.1-1.5	5×10^5 per band	5000
HEXS	1.489 (Al-K) 2.622 (Cl-K) 6.404 (Fe-K) 9.886 (Ge-K)	6×10^5 per energy	400×4
HEXS	4.952 (V-K) 6.930 (Co-K) 7.478 (Ni-K) 8.639 (Zn-K)	6×10^5 per energy	400×4
Si Edge Spec.	1.0-2.2	5×10^5 per band	5000

Table 4.1: Spectral Resolution Measurements

4.1.3 Quantum Efficiency Measurements (nominal conditions)

4.1.3.1 Objective

The objective of these measurements is to determine CCD detection efficiency, as a function of energy, with a statistical accuracy of 1% in each 32-pixel by 32-pixel detector cell. Details of quantum efficiency measurements are listed in Table 4.2.

4.1.3.2 Assumptions for quantum efficiency measurements

1. Tritium and HEXS were both used.
2. The nominal flux of 6400 ct/CCD/frametime was used.
3. The reference detector was illuminated by chopping.

4. "Variable voltage" measurements were made at two energies to confirm depletion depth measurements.
5. To minimize pump-down overhead, quantum efficiency measurements were made immediately after high-energy spectral resolution measurements.

System	Energy (keV)	Total Cts (/energy/CCD quad.)	No. of Frames
Tritium (BI only)	0.277 (C-K)	2.5×10^6	1600
Tritium	0.525 (O-K) 0.677 (F-K)	2.5×10^6	1600×2
HEXS	1.740 (Si-K) 2.014 (P-K) 4.511 (Ti-K) 5.899 (Mn-K) 8.048 (Cu-K)	2.5×10^6	1600×5
HEXS (var.volt.)	5.899 (Mn-K) 8.048 (Cu-K)	2×10^4/voltage	$200 \times 8 \times 2$

Table 4.2: Quantum Efficiency Measurements

4.1.4 Measurements at "Off-nominal" Conditions

4.1.4.1 Objectives

Determine the effects of temperature, clock levels and readout modes on detector performance parameters (noise, dark current, charge transfer efficiency and cosmetics), energy scale, spectral resolution and quantum efficiency.

4.1.4.2 CCD Temperature Variations

Measurements were made at the following off-nominal CCD temperatures: -130C, -125C, -115C and -110C.

4.1.4.3 Clock-level Variations

Aside from the "variable voltage" measurements described in section 5, the following "off-nominal" clock configurations were evaluated: i) minimum dark current mode (1 phase high, 2 phases low, at the standard clock levels); and ii) All phases positive.

4.1.4.4 Readout Mode Variations

Calibration data will be obtained in the following readout modes:

1. Continuous readout (no line summation).
2. Continuous readout, 2 lines summed.
3. Timed-exposure mode, 2x2 pixel summation.
4. Timed-exposure mode, XRCF window size.
5. Frame-mode, AC/BD readouts.

System	Mode Specifications			Energies (keV)	
	Temp.	Clock Levels	Readout Mode	Spectral Resolution	QE
HIREFS	-130C -110C	nom.	nom.	0.2-1.5, 5.9	5.9
HIREFS	-125C -115C	nom.	nom.	0.2-1.5, 5.9	5.9
HIREFS	-110C	4.1.4.2 i)	nom.	0.2-1.5, 5.9	5.9
IFM	nom.	nom.	4.1.4.4 iv)	0.5, 1.5, 5.9	5.9
IFM	nom.	nom.	4.1.4.4 i),ii)	0.5, 1.5, 5.9	5.9
IFM	nom.	nom.	4.1.4.4 iii)	0.5, 1.5, 5.9	5.9
IFM	nom.	4.1.4.2 ii)	nom.	0.5, 1.5, 5.9	5.9

Table 4.3: Off-nominal Calibration Measurements

4.1.4.5 Off-nominal Measurements

The various device performance, spectral resolution and quantum efficiency measurements to be made, and the associated off-nominal conditions for the measurements, are summarized in Table 4.3. The "CCD parameters" referred to in Table 4.3 will be measured according to procedures specified in the ACIS CCD Screening Plan (ACIS memo PS-77). Thus the results of these measurements will be determination of quantities such as noise, dark current, and charge transfer efficiency, for each 'off-nominal' condition listed in Table 4.3.

Name	Source Type	Energy Range (keV)	Chamber Type	Detector Translation	Reference Detector
HIREFS	Spectrometer+Fe^{55}	0.1-1.5	1 CCD	1-d Trans.	none
IFM	Monochromator+Fe^{55}	0.1-1.5	1 CCD	none	none
SES	Monochromator	0.5-2.2	1 CCD	none	none
HEXS A	photon fluorescent+H^3	0.3 - 10	2 CCD	2-d	CCD
HEXS B	photon fluorescent+H^3	0.3 - 10	2 CCD	2-d	CCD

Table 4.4: Calibration Facility Characteristics

4.1.5 Facilities and Scheduling Considerations

4.1.5.1 Facilities

The calibration was performed using 5 source/detector systems at MIT Center for Space Research. These are described in Table 4.4. The High-Resolution Erect-Field Spectrometer and its capabilities are described in ACIS memo PS-59 (Prigozhin). The High-Energy X-ray Source (HEXS) and its capabilities are described in ACIS memos PS-75 and PS-76 (Jones).

4.1.6 Sub-assembly Calibration Data Management

Both lab sub-assembly and XRCF calibration activities produced terabytes of data. Lab calibration data on the CCD chips and UV/optical blocking filters were collected by the SI team and were transferred to the ASC. Event reduced data are stored in an on-line archive at MIT, and raw CCD frames are stored on DLT tapes. The filter data are similarly stored at Penn State. The ASC has received a copy of all of these data. The ASC will assume responsibility for archiving these data and distributing them on request in an ASC defined format.

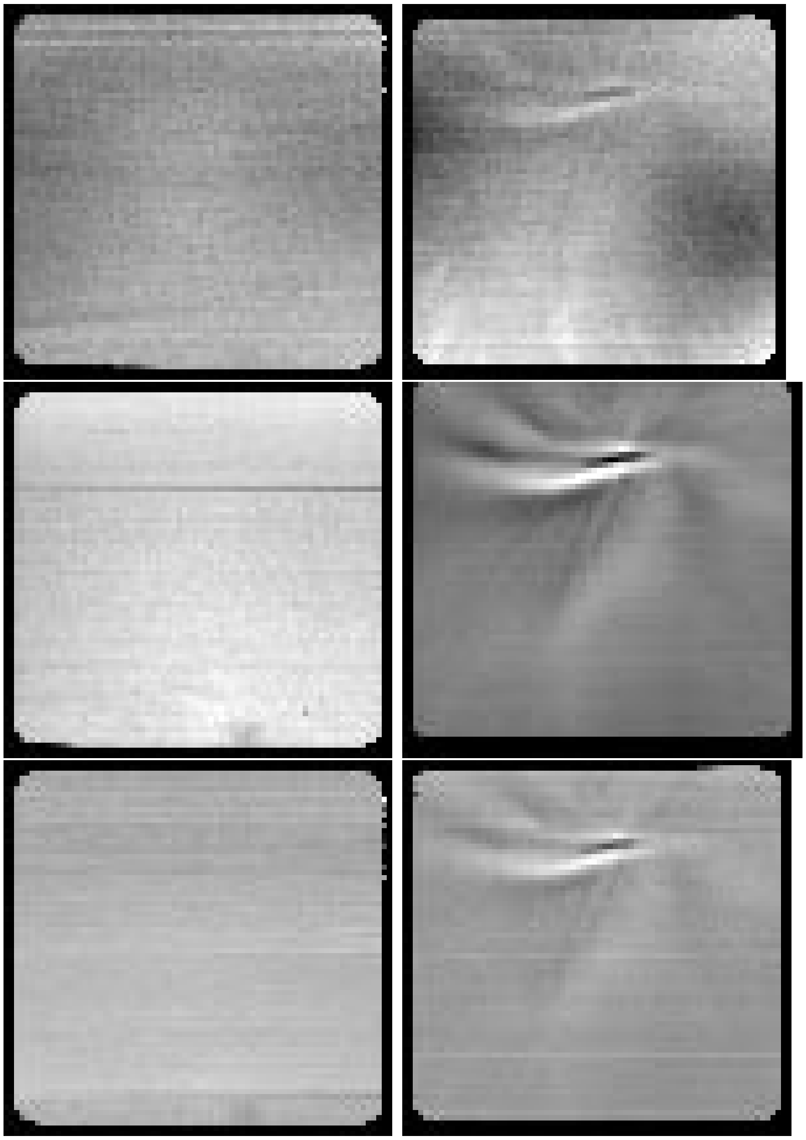

Figure 4.1: Transmission measurements of ACIS-I OBFs from the SRC. Left column is the installed flight filter (*im009*); right column is a typical backup filter (*im019*). Top row measurement made at 273 eV; middle at 522 eV; bottom at 775 eV.

4.2 Optical Blocking Filter Data

Transmissions for the ACIS pre-engineering, flight and backup OBFs have been obtained at the University of Wisconsin Synchrotron Radiation Center (SRC). The Multilayer Beamline

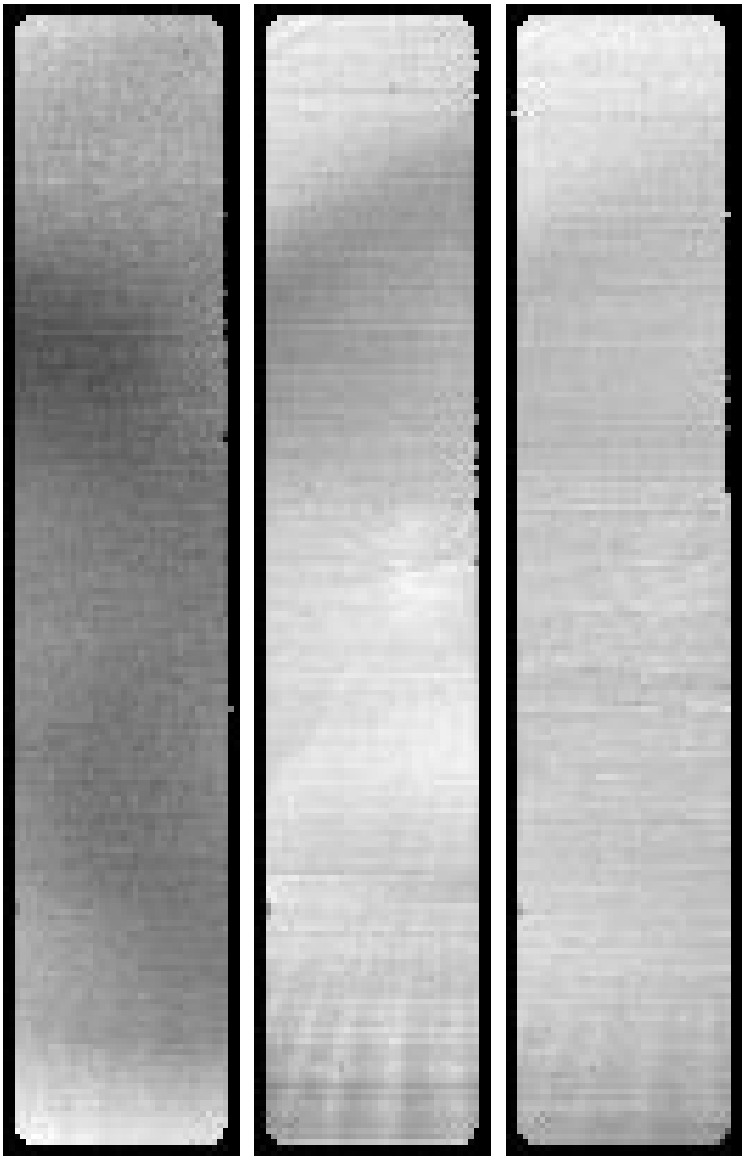

Figure 4.2: Transmission measurements of ACIS-S OBF from the SRC. Flight filter (*spec003*) - left from measurements at 273 eV; center at 522 eV; right at 775 eV.

there was ideally suited for these measurements due to its ability to access several energies in the 200-2000 eV range and its built-in, computer-controlled x-z stage, which allowed us to map the filter transmission automatically with excellent spatial resolution. See Townsley *et al.* Proc SPIE 134-145 (1996) for a description of the measurements and early results.

More than 30 filters were eventually measured at the SRC, including several which were repeatedly measured to search for contamination during testing and for ACIS camera contamination certification. (No change in transmission was ever detected during SRC tests, ruling out any significant contamination from this testing or from exposure of the filters to the ACIS camera.)

In the course of this testing it was found that the original filter substrate material (Lexan) could not be made taut enough to survive vibration testing without the formation of small pinwindows of aluminum flaking near the support structure. Accordingly the flight design was changed to use Polyimide, a similar plastic material with greater strength.

Also discovered during testing of the Lexan filters was the effect of using equal thickness alumimum coatings which induced Fabry-Perot-like interference transmission bands. These bands were narrow in wavelength, but high in transmission, so the thicknesses of the aluminum overcoats were made unequal to suppress these bands.

The final filter design consisted of a free-standing (i.e. no support mesh) membrane made of Polyimide (2000 Å thick) with an overcoat 300 Å of aluminum on one side, and 1000 Å (for the S filter) or 1300 Å (for the I filter) on the other side. The flight filters were mounted in the ACIS experiment at MIT, and were in place for the flight instrument calibration at XRCF during April and May, 1997.

Each flight filter and backup unit was measured for X-ray transmission spatial uniformity at the SRC. The resulting transmission maps (see Figures 4.1 & 4.2) show filter performance meeting or exceeding the uniformity requirements. In the figures the grayscale is set to show a full range from black to white of 2% of the median transmission at the energy displayed. Both flight filters (*im009*; left column in Fig. 4.1 and *spec003*; left column in Fig. 4.2) are outstanding, with little detectable variation above the noise level of 0.1%. (The horizontal bands are artifacts in the data and are not real.) The 273 eV data are most sensitive to variations in the aluminum overcoating; the 522 eV data are most sensitive to variations in the plastic substrate.

We obtained transmission measurements at five energies. Fitting these five points with a model of the filter transmission gave an agreement between model and data with a mean residual error of 0.34%. Each filter has been fit separately with similar results. The fit parameters for the flight filters are:

$$\text{I array}(009) = 310(\pm 31)\text{Å Al : Si} + 2055(\pm 100)\text{Å polyimide} + 1350(\pm 50)\text{Å Al : Si} \quad (4.1)$$

$$\text{S array}(003) = 300(\pm 30)\text{Å Al : Si} + 2000(\pm 100)\text{Å polyimide} + 1030(\pm 50)\text{Å Al : Si} \quad (4.2)$$

Note: the aluminum is given as Al:Si because the material is intentionally made with a 1% admixture of Si in the fabrication.

Witness sample filters and backup filters from the same batches used for the flight filters were taken to the Brookhaven National Laboratory (BNL) XC-08 synchrotron beamline for

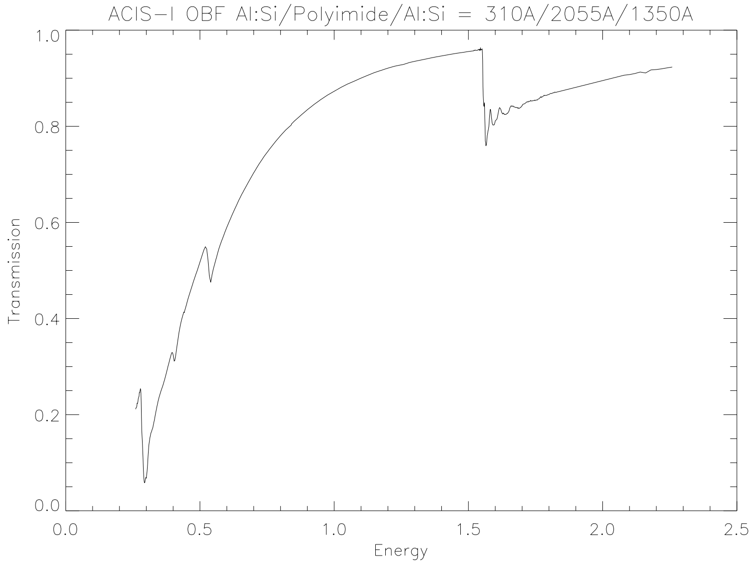

Figure 4.3: ACIS-I filter transmission as measured at BNL

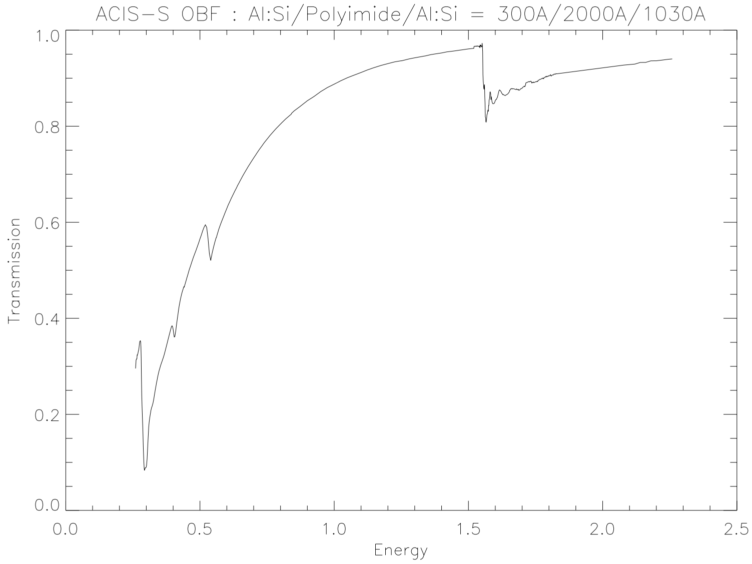

Figure 4.4: ACIS-S filter transmission as measured at BNL

further testing. On this beamline several monochromators were used to provide thousands of energy measurements of transmission at two locations on each sample. See Chartas *et* *al.* Proc. SPIE 44-54 (1996) for a description of the measurement techniques and the transmission modelling.

Plots of the transmission for the ACIS-I and ACIS-S filters are shown in figures 4.3 and 4.4. Note the presence of strong absorption edges at 1.56 keV (aluminum K) and 284 eV (carbon K), and weaker features at 525 eV (oxygen K) and 400 eV (nitrogen K). The oscillatory behavior above the aluminum and carbon edges are due to EXAFS (extended X-ray absorption fine structure), and are real effects in the transmission. Chartas *et al. ibid.* discuss methodology for fitting these structures. Analysis continues for modelling the details of the transmission curves.

In addition to the SRC and BNL measurements, flight-like and witness samples were measured at Penn State in both optical and X-ray cold tests. Flight-like filters will also be measured at the SURF II synchrotron facility in Gaithersburg, MD, to measure the UV transmission curve versus energy. White-light tests were also conducted during the Lincoln Lab thermal-vacuum testing, the XRCF testing of the flight ACIS instrument, and stray light tests will be conducted at TRW during the integration of the flight instrument with the spacecraft.

4.3 XRCF Data

In the XRCF, an ACIS/HRMA calibration was done by collecting data to compare to performance models. This will be followed by study to improve those models by changing the model parameters to best agree with the measured data. The comparison must be carried out as a function of the HRMA/ACIS geometric configuration, incident photon angle and energy, and detector temperature. Measurements did not fill parameter space, but made the best effort to span it in a minimum total integration time. Each quantity was not directly measured at every possible value within the range of every other parameter, but enough were done to scientifically characterize the detector system.

The original calibration plan could not be carried out in its entirety, due to unavoidable delays in the schedule of delivery of the flight instrument to calibration. In order to avoid wasting the calibration facility time, a proxy ACIS instrument was developed by the MIT ACIS team, which consisted of a lab CCD camera electronics and dewar and two CCD chips of the same design as used in the flight chips. This instrument, called the ACIS-2C camera, was used at the XRCF in conjunction with the HRMA to make measurements relating to the single chip relation to the HRMA response. Toward the end of the calibration period, the flight ACIS instrument arrived at XRCF, and data relating especially to the flight chip layout and the gratings dispersed spectra were collected. (Note a third calibration effort was contemplated, but never used due to the arrival of the flight ACIS. An array of non-flight quality chips was prepared (called the XRCF paddle), to enable use of the flight electronics with a CCD array in case the flight paddle was not ready. In the event the flight paddle was actually used at XRCF.)

ACIS data collection at XRCF divided into four intervals, named by the XRCF Phase notation. ACIS-2C was inserted into the XRCF chamber at the start of Phase F. During Phase F the ACIS-2C collected data for 16.86 days, resulting in 10.0 days of data requested by the ACIS team, 5.4 days for the gratings teams, and 1.1 days of problem solving when no useful data resulted. Data collection lasted from 22 Feb 1997 to 10 Mar 1997. When the flight HRC instrument arrived at calibration, it was introduced into the XRCF tank with the ACIS-2C for Phase G. The HRC received priority on testing, and no ACIS-2C measurements were made until the HRC test program was completed. When the HRC program completed, additional ACIS-2C data were collected during Phase G from 10 April to 12 April 1997.

When the flight ACIS instrument arrived, Phase G was terminated and the HRC and ACIS-2C were removed from the XRCF tank. Phase H testing of the flight ACIS provided 8.25 days of test time, divided with 5.2 days for ACIS tests, 2.9 days for gratings and 0.15 days for problem solving. The Phase H testing lasted from 18 April to 26 April 1997, when the HRMA schedule demanded termination to allow the mirrors to leave for spacecraft integration.

Following the departure of the HRMA, additional testing using the XRCF sources, without the mirror, but with the flight ACIS instrument, continued at XRCF. These tests were called flat-field tests as they used the XRCF sources to fill the active CCD pixels with roughly uniform illumination. This phase, I, lasted from 8 May to 17 May 1997.

The specific types tests, which were not mutually exclusive but have different emphases, were:

- Mapping: measure the point-response-function at many locations for the I1 and I2 aimpoints and for the S array, at nominal focus, one energy (Al K).

- Effective area: check total ACIS/HRMA effective area at 14 energies, at several positions on the detector on each array, using a defocussed beam to reduce photon pileup.

- Point-response-function: check combined ACIS/HRMA to high precision, at five energies, at six off-axis angles; supplemental to mapping by employing much higher statistical precision at a smaller number of positions.

- Point-response-function wings: similar to the previous item, but beam is increased by factor of 100 to give acceptable counting statistics in wings of response (at the cost of saturation of the core). Done at 30 positions and three energies on two arrays.

- Count-rate linearity: test the effects of flux changes on point response function and effective area. Done at a range on fluxes from much higher to much lower than the standard flux used for other measurements.

- Miscellaneous: shorter tests of specific aspects of ACIS. These include a measurement of the area lost on seams of the array (i.e. spaces between chips), measurement of the effective PSF when ACIS is in high time resolution continuous clocking modes, and measurement of the ability to locate X-ray events to below single pixel resolution by using X-ray grade information.

The XRCF testing was arranged into types of test and each test was assigned a unique identifier based on a system suggested by TRW. These identifiers are known as TRW IDs. We present the list of measurements made at XRCF in thematic blocks. This structure corresponds to the basic philosophy behind the ACIS XRCF calibration. Because we cannot directly measure all possible observing situations (and because we will need to correct the XRCF results to zero-gravity and infinite source distance) the actual calibration results are models which acceptably reproduce the XRCF results collected during calibration. Because XRCF time was so critically short, we tried to be as efficient as possible in testing the models.

Hence the strategy was to explore the response of the instrument/HRMA to variation of single parameters, concentrating largely on the values expected during flight. In every way possible, we wish to minimize uncontrolled variation, and hence we choose to group measurements into blocks, which should be executed in a systematic manner, minimizing the chance of unforeseen variations in the other parameters or behavior of the instrument or facility.

4.4 ACIS XRCF Measurement List

4.4.1 Introduction

This is the entire ACIS XRCF Measurement List, including ACIS-2C data from Phase F and Phase G as well as ACIS flight camera data from Phase H. Each class of tests is mentioned, with a brief narrative description of the intent of the set of measurements. We also present tables summarized from the “as-requested” CMDB (Calibration Measurement DataBase) for each type of test; these tables represent our best current record of the data obtained at XRCF, grouped according to the calibration goal that they satisfy.

As we describe the types of tests we list the descriptions for each test according to the TRW ID, and supplementary descriptive entries from the CMDB. The columns for all

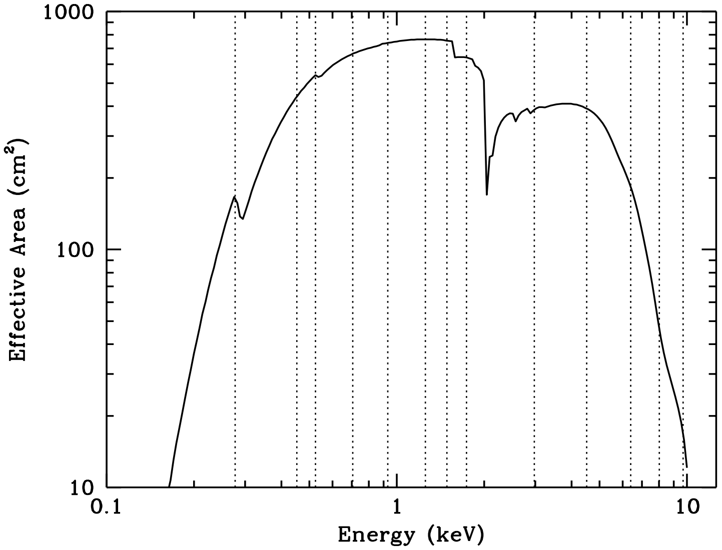

Figure 4.5: Location of ACIS calibration energies for effective area determination, superposed on plot of expected next ACIS/HRMA effective area

tables are defined below. These definitions were taken from the CMDB Web page; please refer there for more complete definitions.

- **TRW ID** – A string uniquely identifying an XRCF measurement.
- **source** – The source used to generate X-rays for this test.
- **energy** – The specific energy you wish to be using, in keV.
- **FP_Rate, Total_Cts** – The estimated rate of detected counts in the focal plane, per second; the total number of counts expected for the whole test.
- **Int_time** – The integration time for this test, in seconds.
- **mult** – Multiplicity, the number of distinct XRCF configurations sampled in this test (e.g. the number of monochromator settings for each DCM test).
- **pitch** – The angular rotation of the HRMA about the XRCF Z axis, with positive numbers increasing "down," in arcminutes.
- **yaw** – The angular rotation of the HRMA about the XRCF Y axis, with positive numbers increasing "left" (also known as "south"), in arcminutes.

- **yoff** – The linear offset of the FAM in the XRCF Y direction (+Y is "south"), in units of mm.
- **zoff** – The linear offset of the FAM in the XRCF Z direction (+Z is "up"), in units of mm.
- **Defocus** – The linear offset of the FAM in the XRCF X direction (+X is towards the X-ray source), in units of mm.
- **Focal** – Focal plane choice, the detector in the focal plane for this test.
- **HST** – The ACIS chip monitored by the high-speed tap.
- **frametime** – The amount of time in each ACIS exposure (the integration time, between CCD readouts), in seconds.
- **proc_mode** – The mode of ACIS processing.
- **rows** – The number of rows in the ACIS readout window.
- **frames** – The number of ACIS data frames taken during the measurement integration.

The DCM tests were designed to step across the Si K edge and the Ir M edges to measure the effective area and the point response function in 10 eV steps at energies avoiding the W M line contamination, using both FI and BI chips. The test plan included a HIREFS Oxygen K edge test, using HIREFS to obtain points spanning the O K edge to measure the effective area and the point response function, using both FI and BI chips. However, at O K the HIREFS beam is faint and nonuniform. Because of this, these tests were given low priority and were not accomplished due to time constraints at XRCF.

4.4.2 Shutter Focus

Shutter Focus tests are designed to find rapidly the focal spot of the HRMA and to develop estimates of where to move the ACIS or ACIS-2C by FAM motions to find the prime focal spot and place it at the desired pixel location. This test is iterated, changing X until the minimum diameter 10% power level is found. Note: due to gravitational distortion effects on telescope blur it is expected that the blur will be deformed in Y and Z. The actual criterion will be minimum image width in the Y (grating dispersion) direction.

TRW_ID	source	energy	FP_Rate,Total_Cts	Int_time	mult	pitch	yaw	yoff	zoff	Defocus	Focal	HST	frametime	proc_mode	rows	frames
F–I2C–SF–1.003	Al–Ka	1.486	164.7,20000	485.73	4	0	0	0	0	0	2C1	–	0.66	INTEG	114	21
F–I2C–SF–1.004	Al–Ka	1.486	191.62,20000	417.49	4	0	0	0	0	0	2C0	–	0.66	INTEG	114	18
F–I2C–SF–3.001	Al–Ka	1.486	260,15600	240	4	0	0	0	0	0	2C0	–	0.66	INTEG	114	11
F–I2C–SF–3.002	Al–Ka	1.486	260,15600	240	4	0	0	–8.04	–11.112	0	2C0	–	0.66	INTEG	114	11
F–I2C–SF–3.003	Al–Ka	1.486	260,15600	240	4	0	0	–8.04	11.088	0	2C0	–	0.66	INTEG	114	11
F–I2C–SF–3.004	Al–Ka	1.486	260,15600	240	4	0	0	14.16	11.088	0	2C0	–	0.66	INTEG	114	11
F–I2C–SF–3.005	Al–Ka	1.486	260,15600	240	4	0	0	14.16	–11.112	0	2C0	–	0.66	INTEG	114	11
F–I2C–SF–3.006	Al–Ka	1.486	223.47,13408.2	240	4	0	0	0	0	0	2C1	–	0.66	INTEG	114	11
F–I2C–SF–3.007	Al–Ka	1.486	223.47,13408.2	240	4	0	0	12	–4.8	0	2C1	–	0.66	INTEG	114	11
F–I2C–SF–3.008	Al–Ka	1.486	223.47,13408.2	240	4	0	0	12	15.53	0	2C1	–	0.66	INTEG	114	11
F–I2C–SF–3.009	Al–Ka	1.486	223.47,13408.2	240	4	0	0	–8.4	15.53	0	2C1	–	0.66	INTEG	114	11
F–I2C–SF–3.010	Al–Ka	1.486	223.47,13408.2	240	4	0	0	–8.4	–4.8	0	2C1	–	0.66	INTEG	114	11
H–IAS–SF–3.002	Al–Ka	1.486	9.9790,598.74	240	4	0	0	0	0	1	S3	S3	3.3	INTEG	1024	19
H–IAI–SF–2.001	DCM	2.5	9.0588,2500	1103.9	4	0	0	0	0	0	I3	I3	0.5	INTEG	100	552
H–IAS–SF–2.002	DCM	2.5	9.9194,2500	1008.13	4	0	0	0	0	0	S3	S3	3.3	INTEG	1024	77
G–I2C–SF–31.008	Mg–Ka	1.254	397.2818,10000	100.68	4	0	0	0	0	0	2C1	–	0.11	INTEG	18	5

Table 4.5: Shutter Focus Tests

4.4.3 Plate Focus

Plate Focus tests are designed to measure precisely the focus of the HRMA on the ACIS or ACIS-2C, and to relate the integration mode data to single photon counting data and to the in-flight focus data.

TRW_ID	source	energy	FP_Rate,Total_Cts	Int_time	mult	pitch	yaw	yoff	zoff	Defocus	Focal	HST	frametime	proc_mode	rows	frames
F–I2C–dF–2.003	Al–Ka	1.486	9.69,29070	3000	1	0	0	0	0	–0.25	2C1	–	0.113	PH_CNT	18	521
F–I2C–dF–2.004	Al–Ka	1.486	9.69,29070	3000	1	0	0	0	0	0	2C1	–	0.113	PH_CNT	18	521
F–I2C–dF–2.005A	Al–Ka	1.486	9.69,29070	3000	1	0	0	0	0	0.25	2C1	–	0.113	PH_CNT	18	521
F–I2C–dF–2.008	Al–Ka	1.486	9.42,28260	3000	1	0	0	0	0	–1	2C0	–	0.113	PH_CNT	18	521
F–I2C–dF–2.009	Al–Ka	1.486	9.42,28260	3000	1	0	0	0	0	–0.5	2C0	–	0.113	PH_CNT	18	521
F–I2C–dF–2.010	Al–Ka	1.486	9.42,28260	3000	1	0	0	0	0	–0.25	2C0	–	0.113	PH_CNT	18	521
F–I2C–dF–2.011	Al–Ka	1.486	9.42,28260	3000	1	0	0	0	0	0	2C0	–	0.113	PH_CNT	18	521
F–I2C–dF–2.012	Al–Ka	1.486	9.42,28260	3000	1	0	0	0	0	0.25	2C0	–	0.113	PH_CNT	18	521
F–I2C–dF–2.013	Al–Ka	1.486	9.42,28260	3000	1	0	0	0	0	0.5	2C0	–	0.113	PH_CNT	18	521
F–I2C–dF–2.014	Al–Ka	1.486	9.42,28260	3000	1	0	0	0	0	1	2C0	–	0.113	PH_CNT	18	521
F–I2C–dF–99.024	Al–Ka	1.486	9.69,29070	3000	1	0	0	0	0	–0.5	2C1	–	0.113	PH_CNT	18	521
F–I2C–dF–99.027	C–Ka	0.277	11.46,3000	261.77	1	0	0	0	0	0	2C0	–	0.113	PH_CNT	18	46
F–I2C–dF–99.028	C–Ka	0.277	11.46,3000	261.77	1	0	0	0	0	–1	2C0	–	0.113	PH_CNT	18	46
F–I2C–dF–99.029	C–Ka	0.277	11.46,3000	261.77	1	0	0	0	0	1	2C0	–	0.113	PH_CNT	18	46
F–I2C–dF–63.011	Cu–Ka	8.030	11.79,3000	254.45	1	0	0	0	0	0	2C0	–	0.113	PH_CNT	18	45
F–I2C–dF–63.012	Cu–Ka	8.030	11.79,3000	254.45	1	0	0	0	0	1	2C0	–	0.113	PH_CNT	18	45
F–I2C–dF–63.013	Cu–Ka	8.030	11.79,3000	254.45	1	0	0	0	0	–1	2C0	–	0.113	PH_CNT	18	45
F–I2C–dF–63.014	Cu–Ka	8.030	11.79,3000	254.45	1	0	0	0	0	–0.5	2C0	–	0.113	PH_CNT	18	45
F–I2C–dF–63.015	Cu–Ka	8.030	11.79,3000	254.45	1	0	0	0	0	0.5	2C0	–	0.113	PH_CNT	18	45
F–I2C–dF–64.011	Cu–Ka	8.030	11.86,3000	252.95	1	0	0	0	0	0	2C1	–	0.113	PH_CNT	18	44
F–I2C–dF–64.012	Cu–Ka	8.030	11.86,3000	252.95	1	0	0	0	0	1	2C1	–	0.113	PH_CNT	18	44
F–I2C–dF–64.012a	Cu–Ka	8.030	11.86,3000	252.95	1	0	0	0	0	1	2C1	–	0.113	PH_CNT	18	44
F–I2C–dF–64.013	Cu–Ka	8.030	11.86,3000	252.95	1	0	0	0	0	–1	2C1	–	0.113	PH_CNT	18	44
F–I2C–dF–64.014	Cu–Ka	8.030	11.86,3000	252.95	1	0	0	0	0	–0.5	2C1	–	0.113	PH_CNT	18	44
F–I2C–dF–64.015	Cu–Ka	8.030	11.86,3000	252.95	1	0	0	0	0	0.5	2C1	–	0.113	PH_CNT	18	44
F–I2C–dF–62.001	O–Ka	0.525	11.69,3000	256.63	1	0	0	0	0	0	2C0	–	0.113	PH_CNT	18	45
F–I2C–dF–62.002	O–Ka	0.525	11.69,3000	256.63	1	0	0	0	0	1	2C0	–	0.113	PH_CNT	18	45
F–I2C–dF–62.003	O–Ka	0.525	11.69,3000	256.63	1	0	0	0	0	–1	2C0	–	0.113	PH_CNT	18	45

continued on next page

continued from previous page

TRW_ID	source	energy	FP_Rate,Total_Cts	Int_time	mult	pitch	yaw	yoff	zoff	Defocus	Focal	HST	frametime	proc_mode	rows	frames
F–I2C–dF–62.004	O–Ka	0.525	11.69,3000	256.63	1	0	0	0	0	–0.5	2C0	–	0.113	PH_CNT	18	45
F–I2C–dF–62.005	O–Ka	0.525	11.69,3000	256.63	1	0	0	0	0	0.5	2C0	–	0.113	PH_CNT	18	45
F–I2C–dF–63.001	O–Ka	0.5249	10.97,3000	273.47	1	0	0	0	0	0	2C0	–	0.113	PH_CNT	18	48
F–I2C–dF–63.002	O–Ka	0.5249	10.97,3000	273.47	1	0	0	0	0	1	2C0	–	0.113	PH_CNT	18	48
F–I2C–dF–63.003	O–Ka	0.5249	10.97,3000	273.47	1	0	0	0	0	–1	2C0	–	0.113	PH_CNT	18	48
F–I2C–dF–63.004	O–Ka	0.5249	10.97,3000	273.47	1	0	0	0	0	–0.5	2C0	–	0.113	PH_CNT	18	48
F–I2C–dF–63.005	O–Ka	0.5249	10.97,3000	273.47	1	0	0	0	0	0.5	2C0	–	0.113	PH_CNT	18	48
F–I2C–dF–64.001	O–Ka	0.5249	11.8,3000	254.23	1	0	0	0	0	0	2C1	–	0.113	PH_CNT	18	45
F–I2C–dF–64.002	O–Ka	0.5249	11.8,3000	254.23	1	0	0	0	0	1	2C1	–	0.113	PH_CNT	18	45
F–I2C–dF–64.003	O–Ka	0.5249	11.8,3000	254.23	1	0	0	0	0	–1	2C1	–	0.113	PH_CNT	18	45
F–I2C–dF–64.004	O–Ka	0.5249	11.8,3000	254.23	1	0	0	0	0	–0.5	2C1	–	0.113	PH_CNT	18	45
F–I2C–dF–64.005	O–Ka	0.5249	11.8,3000	254.23	1	0	0	0	0	0.5	2C1	–	0.113	PH_CNT	18	45

Table 4.6: Plate Focus Tests

4.4.4 Point Response Function

Point Response Function (PRF) tests measure the core (PI) and wings (PW) of the PRF on-axis and at several off-axis positions, at the point of ideal focus determined by the Shutter focus/Plate focus measurements (X=0). Two types of data are collected: the core PRF is done in single photon mode in the core of the PRF; the wings PRF is done with higher fluxes, which produces photon mode in the wings but integration mode data in the core. Note that the shutter focus test data at X=0 are identical to the PRF core test for Al, so we do not repeat that test. Measurements are made at medium (Al K), high (Cu K), and low (O K) energy. We changed from the rehearsal energy of Fe to Cu because of the higher response above 6 keV of the HRMA versus the TMA. The Al K inner core test is deleted because the plate focus at X=0 provides the same data. C K is included for an ultra-low energy point for the BI chips. Tests were also made to estimate the PRF using the ACIS and ACIS-2C continuous readout mode.

Sub-pixel position measurements were also performed as part of the PRF test suite. We moved the PRF by sub-pixel amounts to sample the digitization error resulting from pixel size undersampling of the PRF and to test split X-ray event reconstruction models of sub-pixel interaction location. For FI chips, tests were performed at high (Cu K) and low (O K) energy to test for differing split event fractions. For BI chips, Cu K was also used as the high-energy test, but C K was chosen for the low-energy test for differing split event fractions.

TRW_ID	source	energy	FP_Rate,Total_Cts	Int_time	mult	pitch	yaw	yoff	zoff	Defocus	Focal	HST	frametime	proc_mode	rows	frames
F–I2C–PI–1.001	Al–Ka	1.486	283.59,28359	100	1	0	0	0	0	0	2C1	–	0.66	PH_CNT	114	17
F–I2C–PI–2.001	Al–Ka	1.486	296.95,29695	100	1	0	0	0	0	0	2C0	–	0.66	PH_CNT	114	17
F–I2C–PI–5.001	Al–Ka	1.486	98.88,148320	1500	1	0	0	0	0	90	2C1	–	6	PH_CNT	1024	251
H–IAI–PI–25.001	Al–Ka	1.486	19.5190,10000	512.32	1	0	0	0	0	0	I3	I3	0.0032	PH_CNT	1	156
H–IAI–PI–25.002	Al–Ka	1.486	19.5190,10000	512.32	1	0	0	0	0	0	I3	I3	0.0032	PH_CNT	1	156
H–IAI–PI–25.005	Al–Ka	1.486	94.8024,10000	105.48	1	0	0	0	0	0	I3	I3	0.0032	PH_CNT	1	32

continued on next page

continued from previous page

TRW_ID	source	energy	FP_Rate,Total_Cts	Int_time	mult	pitch	yaw	yoff	zoff	Defocus	Focal	HST	frametime	proc_mode	rows	frames
H–IAI–PI–25.006	Al–Ka	1.486	94.8024,10000	105.48	1	0	0	0	0	0	I3	I3	0.0032	PH_CNT	1	32
H–IAI–PI–25.009	Al–Ka	1.486	393.3634,10000	25.42	1	0	0	0	0	0	I3	I3	0.0032	PH_CNT	1	8
H–IAI–PI–25.010	Al–Ka	1.486	393.3634,10000	25.42	1	0	0	0	0	0	I3	I3	0.0032	PH_CNT	1	8
H–IAI–PI–3.001	Al–Ka	1.486	4.8569,9713.8	2000	1	0	0	0	0	0	I3	I3	0.8	PH_CNT	100	2501
H–IAI–PI–3.003	Al–Ka	1.486	4.8362,9672.4	2000	1	–7.49	0	0	–21.576	0.023	I3	I3	0.8	PH_CNT	100	2501
H–IAI–PI–3.006	Al–Ka	1.486	187.3,93673	500	1	–7.49	0	0	–21.576	0.023	I3	I3	0.8	PH_CNT	100	626
H–IAS–PI–25.003	Al–Ka	1.486	19.0917,10000	523.78	1	0	0	0	0	0	S3	S3	0.0032	PH_CNT	1	159
H–IAS–PI–25.004	Al–Ka	1.486	19.0917,10000	523.78	1	0	0	0	0	0	S3	S3	0.0032	PH_CNT	1	159
H–IAS–PI–25.007	Al–Ka	1.486	92.7270,10000	107.84	1	0	0	0	0	0	S3	S3	0.0032	PH_CNT	1	33
H–IAS–PI–25.008	Al–Ka	1.486	92.7270,10000	107.84	1	0	0	0	0	0	S3	S3	0.0032	PH_CNT	1	33
H–IAS–PI–25.011	Al–Ka	1.486	384.7521,10000	25.99	1	0	0	0	0	0	S3	S3	0.0032	PH_CNT	1	8
H–IAS–PI–25.012	Al–Ka	1.486	384.7521,10000	25.99	1	0	0	0	0	0	S3	S3	0.0032	PH_CNT	1	8
H–IAS–PI–3.008	Al–Ka	1.486	4.6749,9349.8	2000	1	3.73	1.57	–4.511	10.751	0.006	S3	S3	0.8	PH_CNT	100	2501
H–IAS–PI–3.009	Al–Ka	1.486	4.7921,9584.2	2000	1	3.73	–5.89	16.992	10.752	0.02	S3	S3	0.8	PH_CNT	100	2501
H–IAS–PI–3.013	Al–Ka	1.486	186,93076.6	500	1	3.73	1.57	–4.511	10.751	0.006	S3	S3	0.8	PH_CNT	100	626
H–IAS–PI–3.014	Al–Ka	1.486	175,87813.6	500	1	3.73	–5.89	16.992	10.752	0.02	S3	S3	0.8	PH_CNT	100	626
F–I2C–PI–2.004	C–Ka	0.277	9.44,28320	3000	1	0	0	0	0	0	2C0	–	0.113	PH_CNT	18	521
F–I2C–PI–1.004	Cu–Ka	8.030	9.63,28890	3000	1	0	0	0	0	0	2C1	–	0.113	PH_CNT	18	521
F–I2C–PI–1.005	Cu–Ka	8.030	280.54,28054	100	1	0	0	0	0	0	2C1	–	0.66	PH_CNT	114	17
F–I2C–PI–1.008	Cu–Ka	8.030	280.54,28054	100	1	0	0	0	0	0	2C1	–	6	PH_CNT	1024	17
F–I2C–PI–2.002	Cu–Ka	8.030	9.84,29520	3000	1	0	0	0	0	0	2C0	–	0.113	PH_CNT	18	521
F–I2C–PI–2.003	Cu–Ka	8.030	286.77,28677	100	1	0	0	0	0	0	2C0	–	0.66	PH_CNT	114	17
F–I2C–PI–2.008	Cu–Ka	8.030	286.77,28677	100	1	0	0	0	0	0	2C0	–	6	PH_CNT	1024	17
F–I2C–PI–3.001	Cu–Ka	8.030	4.96,1488	300	1	0	0	–0.009	0	0	2C1	–	0.113	PH_CNT	18	53
F–I2C–PI–3.002	Cu–Ka	8.030	4.96,1488	300	1	0	0	–0.006	0	0	2C1	–	0.113	PH_CNT	18	53
F–I2C–PI–3.003	Cu–Ka	8.030	4.96,1488	300	1	0	0	–0.003	0	0	2C1	–	0.113	PH_CNT	18	53
F–I2C–PI–3.004	Cu–Ka	8.030	4.96,1488	300	1	0	0	0	0	0	2C1	–	0.113	PH_CNT	18	53
F–I2C–PI–3.005	Cu–Ka	8.030	4.96,1488	300	1	0	0	0.003	0	0	2C1	–	0.113	PH_CNT	18	53
F–I2C–PI–3.006	Cu–Ka	8.030	4.96,1488	300	1	0	0	0.006	0	0	2C1	–	0.113	PH_CNT	18	53
F–I2C–PI–3.007	Cu–Ka	8.030	4.96,1488	300	1	0	0	0.009	0	0	2C1	–	0.113	PH_CNT	18	53
F–I2C–PI–3.008	Cu–Ka	8.030	4.96,1488	300	1	0	0	0.012	0	0	2C1	–	0.113	PH_CNT	18	53
F–I2C–PI–3.009	Cu–Ka	8.030	4.96,1488	300	1	0	0	0	–0.015	0	2C1	–	0.113	PH_CNT	18	53
F–I2C–PI–3.010	Cu–Ka	8.030	4.96,1488	300	1	0	0	0	–0.01	0	2C1	–	0.113	PH_CNT	18	53
F–I2C–PI–3.011	Cu–Ka	8.030	4.96,1488	300	1	0	0	0	–0.005	0	2C1	–	0.113	PH_CNT	18	53
F–I2C–PI–3.012	Cu–Ka	8.030	4.96,1488	300	1	0	0	0	0	0	2C1	–	0.113	PH_CNT	18	53
F–I2C–PI–3.013	Cu–Ka	8.030	4.96,1488	300	1	0	0	0	0.005	0	2C1	–	0.113	PH_CNT	18	53
F–I2C–PI–3.014a	Cu–Ka	8.030	4.96,1488	300	1	0	0	0	0.01	0	2C1	–	0.113	PH_CNT	18	53
F–I2C–PI–4.001	Cu–Ka	8.030	3.33,999	300	1	0	0	–0.009	0	0	2C0	–	0.113	PH_CNT	18	53
F–I2C–PI–4.002	Cu–Ka	8.030	3.33,999	300	1	0	0	–0.006	0	0	2C0	–	0.113	PH_CNT	18	53
F–I2C–PI–4.003	Cu–Ka	8.030	3.33,999	300	1	0	0	–0.003	0	0	2C0	–	0.113	PH_CNT	18	53
F–I2C–PI–4.004	Cu–Ka	8.030	3.33,999	300	1	0	0	0	0	0	2C0	–	0.113	PH_CNT	18	53
F–I2C–PI–4.005	Cu–Ka	8.030	3.33,999	300	1	0	0	0.003	0	0	2C0	–	0.113	PH_CNT	18	53
F–I2C–PI–4.005	Cu–Ka	8.030	3.42,1026	300	1	0	0	0.003	0	0	2C0	–	0.113	PH_CNT	18	53
F–I2C–PI–4.006	Cu–Ka	8.030	3.42,1026	300	1	0	0	0.006	0	0	2C0	–	0.113	PH_CNT	18	53
F–I2C–PI–4.006	Cu–Ka	8.030	3.33,999	300	1	0	0	0.006	0	0	2C0	–	0.113	PH_CNT	18	53
F–I2C–PI–4.007	Cu–Ka	8.030	3.33,999	300	1	0	0	0.009	0	0	2C0	–	0.113	PH_CNT	18	53
F–I2C–PI–4.008	Cu–Ka	8.030	3.33,999	300	1	0	0	0.012	0	0	2C0	–	0.113	PH_CNT	18	53
F–I2C–PI–4.009	Cu–Ka	8.030	3.33,999	300	1	0	0	0	–0.015	0	2C0	–	0.113	PH_CNT	18	53
F–I2C–PI–4.010	Cu–Ka	8.030	3.33,999	300	1	0	0	0	–0.01	0	2C0	–	0.113	PH_CNT	18	53
F–I2C–PI–4.011	Cu–Ka	8.030	3.33,999	300	1	0	0	0	–0.005	0	2C0	–	0.113	PH_CNT	18	53
F–I2C–PI–4.012	Cu–Ka	8.030	3.33,999	300	1	0	0	0	0	0	2C0	–	0.113	PH_CNT	18	53
F–I2C–PI–4.013	Cu–Ka	8.030	3.33,999	300	1	0	0	0	0.005	0	2C0	–	0.113	PH_CNT	18	53
F–I2C–PI–4.014	Cu–Ka	8.030	3.33,999	300	1	0	0	0	0.01	0	2C0	–	0.113	PH_CNT	18	53
G–I2C–PI–1.001	Cu–Ka	8.030	4.9674,496.74	2800	28	0	0	0	0	0	2C1	–	0.113	PH_CNT	18	486
H–IAI–PI–12.001	Cu–Ka	8.030	5.4502,8720.32	1600	1	0	0	0	0	0	I3	I3	0.1	PH_CNT	38	485
H–IAS–PI–12.002	Cu–Ka	8.030	5.4626,8740.16	1600	1	0	0	0	0	0	S3	S3	0.1	PH_CNT	38	485
H–IAI–PI–2.001	DCM	3.5	2.9769,9526.08	3200	1	1.2	1.19	–3.439	3.457	0.001	I0	I0	0.8	PH_CNT	100	4001
H–IAI–PI–2.002	DCM	3.5	2.8335,9067.2	3200	1	8.68	8.67	–24.992	25.027	0.063	I0	I0	0.5	PH_CNT	100	6401
H–IAI–PI–2.003	DCM	3.5	2.5633,8202.56	3200	1	8.68	1.19	–3.438	25.033	0.032	I0	I0	0.8	PH_CNT	100	4001
H–IAI–PI–2.007	DCM	3.5	2.9810,9539.2	3200	1	1.2	0	0	3.459	0	I1	I1	0.8	PH_CNT	100	4001
H–IAI–PI–2.008	DCM	3.5	2.8996,9278.72	3200	1	8.68	–7.47	21.522	25.022	0.054	I1	I1	0.5	PH_CNT	100	6401
H–IAI–PI–2.009	DCM	3.5	2.6413,8452.16	3200	1	1.22	–7.47	21.533	3.53	0.024	I1	I1	0.5	PH_CNT	100	6401

continued on next page

continued from previous page

TRW_ID	source	energy	FP_Rate,Total_Cts	Int_time	mult	pitch	yaw	yoff	zoff	Defocus	Focal	HST	frametime	proc_mode	rows	frames
H–IAI–PI–2.013	DCM	3.5	2.9811,9539.52	3200	1	0	1.19	–3.43	0	0	I2	I2	0.8	PH_CNT	100	4001
H–IAI–PI–2.014	DCM	3.5	2.8988,9276.16	3200	1	–7.49	8.68	–25.006	–21.585	0.055	I2	I2	0.5	PH_CNT	100	6401
H–IAI–PI–2.015	DCM	3.5	2.5696,8222.72	3200	1	–0.02	8.67	–24.991	–0.069	0.031	I2	I2	0.5	PH_CNT	100	6401
H–IAI–PI–2.019	DCM	3.5	2.9909,9570.88	3200	1	0	0	0	0	0	I3	I3	0.1	PH_CNT	38	970
H–IAI–PI–2.020	DCM	3.5	2.9706,9505.92	3200	1	–7.48	–7.47	21.522	–21.567	0.046	I3	I3	0.5	PH_CNT	100	6401
H–IAI–PI–2.021	DCM	3.5	2.6468,8469.76	3200	1	–7.49	0	0	–21.576	0.023	I3	I3	0.8	PH_CNT	100	4001
H–IAI–PI–2.022	DCM	5.2	2.8131,9001.92	3200	1	0	0	0	0	0	I3	I3	0.1	PH_CNT	38	970
H–IAI–PI–2.023	DCM	5.2	2.8172,9015.04	3200	1	–7.48	–7.47	21.522	–21.567	0.046	I3	I3	0.5	PH_CNT	100	6401
H–IAI–PI–2.024	DCM	5.2	2.8815,9220.8	3200	1	–7.49	0	0	–21.576	0.023	I3	I3	0.8	PH_CNT	100	4001
H–IAI–PI–21.001	DCM	3.5	18.0892,9044.6	500	1	–12.95	23.92	–68.939	–37.322	0.31	I	S0	3.3	PH_CNT	1024	152
H–IAI–PI–21.002	DCM	3.5	19.7738,9886.9	500	1	–12.95	15.41	–44.407	–37.322	0.169	I	S1	3.3	PH_CNT	1024	152
H–IAI–PI–21.003	DCM	3.5	2.6402,2640.2	1000	1	–12.95	6.9	–19.876	–37.321	0.09	I	S2	3.3	PH_CNT	1024	304
H–IAI–PI–21.004	DCM	3.5	2.7709,2770.9	1000	1	–12.95	–1.61	4.645	–37.32	0.071	I	S3	3.3	PH_CNT	1024	304
H–IAI–PI–21.005	DCM	3.5	18.1784,9089.2	500	1	–12.95	–10.13	29.197	–37.322	0.113	I	S4	3.3	PH_CNT	1024	152
H–IAI–PI–21.006	DCM	3.5	19.9045,9952.25	500	1	–12.95	–18.64	53.718	–37.322	0.215	I	S5	3.3	PH_CNT	1024	152
H–IAS–PI–2.031	DCM	3.5	2.9441,9421.12	3200	1	–3.73	10.24	–29.517	–10.751	0.049	S2	S2	0.5	PH_CNT	100	6401
H–IAS–PI–2.032	DCM	3.5	2.9441,9421.12	3200	1	3.73	10.24	–29.517	10.751	0.049	S2	S2	0.8	PH_CNT	100	4001
H–IAS–PI–2.035	DCM	3.5	2.6830,8585.6	3200	1	3.73	1.57	–4.511	10.751	0.006	S3	S3	0.8	PH_CNT	100	4001
H–IAS–PI–2.036	DCM	3.5	2.5128,8040.96	3200	1	3.73	–5.89	16.992	10.752	0.02	S3	S3	0.8	PH_CNT	100	4001
H–IAS–PI–2.037	DCM	3.5	2.6830,8585.6	3200	1	–3.73	1.57	–4.511	–10.751	0.006	S3	S3	0.5	PH_CNT	100	6401
H–IAS–PI–2.038	DCM	3.5	2.5128,8040.96	3200	1	–3.73	–5.89	16.992	–10.752	0.02	S3	S3	0.5	PH_CNT	100	6401
H–IAS–PI–2.043	DCM	3.5	2.8044,8974.08	3200	1	0	0	0	0	0	S3	S3	0.1	PH_CNT	38	970
H–IAS–PI–2.044	DCM	5.2	2.7940,8940.8	3200	1	0	0	0	0	0	S3	S3	0.1	PH_CNT	38	970
F–I2C–PI–1.002	Fe–Ka	6.4	9.43,28290	3000	1	0	0	0	0	0	2C1	–	0.113	PH_CNT	18	521
F–I2C–PI–1.003	Fe–Ka	6.4	285.55,28555	100	1	0	0	0	0	0	2C1	–	0.66	PH_CNT	114	17
H–IAI–PI–1.005	Fe–Ka	6.4	5.8984,9437.44	1600	1	8.68	–7.47	21.522	25.022	0.054	I1	I1	0.5	PH_CNT	100	3201
H–IAI–PI–1.014	Fe–Ka	6.4	5.7031,9124.96	1600	1	–0.02	8.67	–24.991	–0.069	0.031	I2	I2	0.5	PH_CNT	100	3201
H–IAI–PI–1.021	Fe–Ka	6.4	5.7607,9217.12	1600	1	0	0	0	0	0	I3	I3	0.1	PH_CNT	38	485
H–IAS–PI–1.029	Fe–Ka	6.4	5.4902,8784.32	1600	1	–3.73	10.24	–29.517	–10.751	0.049	S2	S2	0.5	PH_CNT	100	3201
H–IAS–PI–1.041	Fe–Ka	6.4	5.7342,9174.72	1600	1	0	0	0	0	0	S3	S3	0.1	PH_CNT	38	485
H–IAI–PI–1.023	Fe–La	0.705	5.7773,9243.68	1600	1	0	0	0	0	0	I3	I3	0.1	PH_CNT	38	485
H–IAS–PI–1.042	Fe–La	0.705	5.5768,8922.88	1600	1	0	0	0	0	0	S3	S3	0.1	PH_CNT	38	485
G–I2C–PI–1.002	Mg–Ka	1.254	4.7774,477.74	2800	28	0	0	0	0	0	2C1	–	0.113	PH_CNT	18	486
F–I2C–PI–1.006	O–Ka	0.5249	9.64,28920	3000	1	0	0	0	0	0	2C1	–	0.113	PH_CNT	18	521
F–I2C–PI–1.007	O–Ka	0.5249	298.3,29830	100	1	0	0	0	0.144	0	2C1	–	0.66	PH_CNT	114	17
F–I2C–PI–2.006	O–Ka	0.5249	9.86,29580	3000	1	0	0	0	0	0	2C0	–	0.113	PH_CNT	18	521
F–I2C–PI–2.007	O–Ka	0.5249	281.32,28132	100	1	0	0	0	0	0	2C0	–	0.66	PH_CNT	114	17
F–I2C–PI–3.015	O–Ka	0.5249	3.33,999	300	1	0	0	–0.009	0	0	2C1	–	0.113	PH_CNT	18	53
F–I2C–PI–3.016	O–Ka	0.5249	3.33,999	300	1	0	0	–0.006	0	0	2C1	–	0.113	PH_CNT	18	53
F–I2C–PI–3.017	O–Ka	0.5249	3.33,999	300	1	0	0	–0.003	0	0	2C1	–	0.113	PH_CNT	18	53
F–I2C–PI–3.018	O–Ka	0.5249	3.33,999	300	1	0	0	0	0	0	2C1	–	0.113	PH_CNT	18	53
F–I2C–PI–3.019	O–Ka	0.5249	3.33,999	300	1	0	0	0.003	0	0	2C1	–	0.113	PH_CNT	18	53
F–I2C–PI–3.020	O–Ka	0.5249	3.33,999	300	1	0	0	0.006	0	0	2C1	–	0.113	PH_CNT	18	53
F–I2C–PI–3.021	O–Ka	0.5249	3.33,999	300	1	0	0	0.009	0	0	2C1	–	0.113	PH_CNT	18	53
F–I2C–PI–3.022	O–Ka	0.5249	3.33,999	300	1	0	0	0.012	0	0	2C1	–	0.113	PH_CNT	18	53
F–I2C–PI–3.023	O–Ka	0.5249	3.33,999	300	1	0	0	0	–0.015	0	2C1	–	0.113	PH_CNT	18	53
F–I2C–PI–3.024	O–Ka	0.5249	3.33,999	300	1	0	0	0	–0.01	0	2C1	–	0.113	PH_CNT	18	53
F–I2C–PI–3.025	O–Ka	0.5249	3.33,999	300	1	0	0	0	–0.005	0	2C1	–	0.113	PH_CNT	18	53
F–I2C–PI–3.026	O–Ka	0.5249	3.33,999	300	1	0	0	0	0	0	2C1	–	0.113	PH_CNT	18	53
F–I2C–PI–3.027	O–Ka	0.5249	3.33,999	300	1	0	0	0	0.005	0	2C1	–	0.113	PH_CNT	18	53
F–I2C–PI–3.028	O–Ka	0.5249	3.33,999	300	1	0	0	0	0.01	0	2C1	–	0.113	PH_CNT	18	53
F–I2C–PI–4.015	O–Ka	0.5249	3.28,984	300	1	0	0	–0.009	0	0	2C0	–	0.113	PH_CNT	18	53
F–I2C–PI–4.016	O–Ka	0.5249	3.28,984	300	1	0	0	–0.006	0	0	2C0	–	0.113	PH_CNT	18	53
F–I2C–PI–4.017	O–Ka	0.5249	3.28,984	300	1	0	0	–0.003	0	0	2C0	–	0.113	PH_CNT	18	53
F–I2C–PI–4.018	O–Ka	0.5249	3.28,984	300	1	0	0	0	0	0	2C0	–	0.113	PH_CNT	18	53
F–I2C–PI–4.019	O–Ka	0.5249	3.28,984	300	1	0	0	0.003	0	0	2C0	–	0.113	PH_CNT	18	53
F–I2C–PI–4.020	O–Ka	0.5249	3.28,984	300	1	0	0	0.006	0	0	2C0	–	0.113	PH_CNT	18	53
F–I2C–PI–4.021	O–Ka	0.5249	3.28,984	300	1	0	0	0.009	0	0	2C0	–	0.113	PH_CNT	18	53
F–I2C–PI–4.022	O–Ka	0.5249	3.28,984	300	1	0	0	0.012	0	0	2C0	–	0.113	PH_CNT	18	53
F–I2C–PI–4.023	O–Ka	0.5249	3.28,984	300	1	0	0	0	–0.015	0	2C0	–	0.113	PH_CNT	18	53
F–I2C–PI–4.024	O–Ka	0.5249	3.28,984	300	1	0	0	0	–0.01	0	2C0	–	0.113	PH_CNT	18	53

continued on next page

continued from previous page

TRW_ID	source	energy	FP_Rate,Total_Cts	Int_time	mult	pitch	yaw	yoff	zoff	Defocus	Focal	HST	frametime	proc_mode	rows	frames
F–I2C–PI–4.025	O–Ka	0.5249	3.28,984	300	1	0	0	0	–0.005	0	2C0	–	0.113	PH_CNT	18	53
F–I2C–PI–4.026	O–Ka	0.5249	3.28,984	300	1	0	0	0	0	0	2C0	–	0.113	PH_CNT	18	53
F–I2C–PI–4.027	O–Ka	0.5249	3.28,984	300	1	0	0	0	0.005	0	2C0	–	0.113	PH_CNT	18	53
F–I2C–PI–4.028	O–Ka	0.5249	3.28,984	300	1	0	0	0	0.01	0	2C0	–	0.113	PH_CNT	18	53
F–I2C–PW–13.001	Al–Ka	1.486	9.14,27420	3000	1	–2	0	–0.96	0	0.00174	2C1	–	0.113	PH_CNT	18	521
F–I2C–PW–13.001a	Al–Ka	1.486	9.14,27420	3000	1	–2	0	–0.96	0	0.00174	2C1	–	0.113	PH_CNT	18	521
F–I2C–PW–13.002	Al–Ka	1.486	9.8,29400	3000	1	–4	0	–0.96	0	0.007	2C1	–	0.113	PH_CNT	18	521
F–I2C–PW–13.003	Al–Ka	1.486	9.43,28290	3000	1	–6	0	–0.96	0	0.0156	2C1	–	0.113	PH_CNT	18	521
F–I2C–PW–13.004	Al–Ka	1.486	9.61,28830	3000	1	–10	0	–0.96	0	5.6	2C1	–	0.23	PH_CNT	38	522
F–I2C–PW–13.005	Al–Ka	1.486	9.44,28320	3000	1	–15	0	–0.96	0	12.1	2C1	–	0.66	PH_CNT	114	506
F–I2C–PW–13.006	Al–Ka	1.486	9.11,27330	3000	1	–20	0	–0.96	0	20.7	2C1	–	6	PH_CNT	1024	501
F–I2C–PW–13.007	Al–Ka	1.486	280.8,28080	100	1	–2	0	–0.96	0	0.00174	2C1	–	0.66	PH_CNT	114	17
F–I2C–PW–13.008	Al–Ka	1.486	298.13,29813	100	1	–4	0	–0.96	0	0.007	2C1	–	0.66	PH_CNT	114	17
F–I2C–PW–13.009	Al–Ka	1.486	289.73,28973	100	1	–6	0	–0.96	0	0.0156	2C1	–	0.66	PH_CNT	114	17
F–I2C–PW–13.010	Al–Ka	1.486	295.31,29531	100	1	–10	0	–0.96	0	0.0434	2C1	–	0.66	PH_CNT	114	17
F–I2C–PW–13.011	Al–Ka	1.486	290.03,29003	100	1	–15	0	–0.96	0	0.0977	2C1	–	0.66	PH_CNT	114	17
F–I2C–PW–13.012	Al–Ka	1.486	298.78,29878	100	1	–20	0	–0.96	0	0.1736	2C1	–	0.66	PH_CNT	114	17
F–I2C–PW–13.025	Cu–Ka	8.030	9.38,28140	3000	1	–2	0	–0.96	0	0.5	2C1	–	0.113	PH_CNT	18	521
F–I2C–PW–13.026	Cu–Ka	8.030	9.53,28590	3000	1	–4	0	–0.96	0	1	2C1	–	0.113	PH_CNT	18	521
F–I2C–PW–13.027	Cu–Ka	8.030	9.46,28380	3000	1	–6	0	–0.96	0	2.2	2C1	–	0.113	PH_CNT	18	521
F–I2C–PW–13.028	Cu–Ka	8.030	9.46,28380	3000	1	–10	0	–0.96	0	5.6	2C1	–	0.23	PH_CNT	38	522
F–I2C–PW–13.029	Cu–Ka	8.030	8.51,25530	3000	1	–15	0	–0.96	0	12.1	2C1	–	0.66	PH_CNT	114	506
F–I2C–PW–13.030	Cu–Ka	8.030	9.66,28980	3000	1	–20	0	–0.96	0	20.7	2C1	–	6	PH_CNT	1024	501
F–I2C–PW–13.031	Cu–Ka	8.030	297.73,29773	100	1	–2	0	–0.96	0	0.5	2C1	–	0.66	PH_CNT	114	17
F–I2C–PW–13.032	Cu–Ka	8.030	299.53,29953	100	1	–4	0	–0.96	0	1	2C1	–	0.66	PH_CNT	114	17
F–I2C–PW–13.033	Cu–Ka	8.030	297.14,29714	100	1	–6	0	–0.96	0	2.2	2C1	–	0.66	PH_CNT	114	17
F–I2C–PW–13.034	Cu–Ka	8.030	297.13,29713	100	1	–10	0	–0.96	0	5.6	2C1	–	0.66	PH_CNT	114	17
F–I2C–PW–13.035	Cu–Ka	8.030	297.06,29706	100	1	–15	0	–0.96	0	12.1	2C1	–	0.66	PH_CNT	114	17
F–I2C–PW–13.036	Cu–Ka	8.030	298.28,29828	100	1	–20	0	–0.96	0	20.7	2C1	–	6	PH_CNT	1024	17
H–IAI–PW–12.003	Cu–Ka	8.030	181.2993,108780	600	1	0	0	0	0	0	I3	I3	0.1	PH_CNT	38	182
H–IAS–PW–12.004	Cu–Ka	8.030	181.7113,109027	600	1	0	0	0	0	0	S3	S3	0.1	PH_CNT	38	182
H–IAI–PW–2.004	DCM	3.5	175.3786,87689.3	500	1	1.2	1.19	–3.439	3.457	0.001	I0	I0	0.8	PH_CNT	100	626
H–IAI–PW–2.005	DCM	3.5	137.4065,68703.2	500	1	8.68	8.67	–24.992	25.027	0.063	I0	I0	0.5	PH_CNT	100	1001
H–IAI–PW–2.006	DCM	3.5	151.0153,75507.6	500	1	8.68	1.19	–3.438	25.033	0.032	I0	I0	0.8	PH_CNT	100	626
H–IAI–PW–2.010	DCM	3.5	175.6191,87809.6	500	1	1.2	0	0	3.459	0	I1	I1	0.8	PH_CNT	100	626
H–IAI–PW–2.011	DCM	3.5	140.6113,70305.6	500	1	8.68	–7.47	21.522	25.022	0.054	I1	I1	0.5	PH_CNT	100	1001
H–IAI–PW–2.012	DCM	3.5	155.6065,77803.2	500	1	1.22	–7.47	21.533	3.53	0.024	I1	I1	0.5	PH_CNT	100	1001
H–IAI–PW–2.016	DCM	3.5	175.6240,87812	500	1	0	1.19	–3.43	0	0	I2	I2	0.8	PH_CNT	100	626
H–IAI–PW–2.017	DCM	3.5	140.5722,70286.1	500	1	–7.49	8.68	–25.006	–21.585	0.055	I2	I2	0.5	PH_CNT	100	1001
H–IAI–PW–2.018	DCM	3.5	151.3838,75691.9	500	1	–0.02	8.67	–24.991	–0.069	0.031	I2	I2	0.5	PH_CNT	100	1001
H–IAI–PW–2.025	DCM	3.5	176.2056,88102.8	500	1	0	0	0	0	0	I3	I3	0.1	PH_CNT	38	152
H–IAI–PW–2.026	DCM	3.5	144.0505,72025.2	500	1	–7.48	–7.47	21.522	–21.567	0.046	I3	I3	0.5	PH_CNT	100	1001
H–IAI–PW–2.027	DCM	3.5	155.9328,77966.4	500	1	–7.49	0	0	–21.576	0.023	I3	I3	0.8	PH_CNT	100	626
H–IAI–PW–2.028	DCM	5.2	270.1269,135063	500	1	0	0	0	0	0	I3	I3	0.1	PH_CNT	38	152
H–IAI–PW–2.029	DCM	5.2	219.1243,109562	500	1	–7.48	–7.47	21.522	–21.567	0.046	I3	I3	0.5	PH_CNT	100	1001
H–IAI–PW–2.030	DCM	5.2	249.0239,124512	500	1	–7.49	0	0	–21.576	0.023	I3	I3	0.8	PH_CNT	100	626
H–IAS–PW–2.033	DCM	3.5	142.7686,71384.3	500	1	–3.73	10.24	–29.517	–10.751	0.049	S2	S2	0.5	PH_CNT	100	1001
H–IAS–PW–2.034	DCM	3.5	142.7686,71384.3	500	1	3.73	10.24	–29.517	10.751	0.049	S2	S2	0.8	PH_CNT	100	626
H–IAS–PW–2.039	DCM	3.5	158.0632,79031.6	500	1	3.73	1.57	–4.511	10.751	0.006	S3	S3	0.8	PH_CNT	100	626
H–IAS–PW–2.040	DCM	3.5	148.03089,74019.5	500	1	3.73	–5.89	16.992	10.752	0.02	S3	S3	0.8	PH_CNT	100	626
H–IAS–PW–2.041	DCM	3.5	158.0632,79031.6	500	1	–3.73	1.57	–4.511	–10.751	0.006	S3	S3	0.5	PH_CNT	100	1001
H–IAS–PW–2.042	DCM	3.5	148.03089,74019.5	500	1	–3.73	–5.89	16.992	–10.752	0.02	S3	S3	0.5	PH_CNT	100	1001
H–IAS–PW–2.045	DCM	3.5	165.2153,82607.7	500	1	0	0	0	0	0	S3	S3	0.1	PH_CNT	38	152
H–IAS–PW–2.046	DCM	5.2	268.2930,134146	500	1	0	0	0	0	0	S3	S3	0.1	PH_CNT	38	152
H–IAI–PW–1.009	Fe–Ka	6.4	199.1651,99582.6	500	1	8.68	–7.47	21.522	25.022	0.054	I1	I1	0.5	PH_CNT	100	1001
H–IAI–PW–1.018	Fe–Ka	6.4	192.5703,96285.2	500	1	–0.02	8.67	–24.991	–0.069	0.031	I2	I2	0.5	PH_CNT	100	1001
H–IAI–PW–1.025	Fe–Ka	6.4	141.3478,70673.9	500	1	0	0	0	0	0	I3	I3	0.1	PH_CNT	38	152
H–IAS–PW–1.031	Fe–Ka	6.4	185.3794,92689.7	500	1	–3.73	10.24	–29.517	–10.751	0.049	S2	S2	0.5	PH_CNT	100	1001
H–IAS–PW–1.043	Fe–Ka	6.4	185.2342,92617.1	500	1	0	0	0	0	0	S3	S3	0.1	PH_CNT	38	152

continued on next page

continued from previous page

TRW_ID	source	energy	FP_Rate,Total_Cts	Int_time	mult	pitch	yaw	yoff	zoff	Defocus	Focal	HST	frametime	proc_mode	rows	frames
H–IAI–PW–1.027	Fe–La	0.705	193.9209,96960.4	500	1	0	0	0	0	0	I3	I3	0.1	PH_CNT	38	152
H–IAS–PW–1.044	Fe–La	0.705	192.4921,96246.1	500	1	0	0	0	0	0	S3	S3	0.1	PH_CNT	38	152
F–I2C–PW–13.013	O–Ka	0.5249	9.59,28770	3000	1	–2	0	–0.96	0	0.5	2C1	–	0.113	PH_CNT	18	521
F–I2C–PW–13.014	O–Ka	0.5249	9.26,27780	3000	1	–4	0	–0.96	0	1	2C1	–	0.113	PH_CNT	18	521
F–I2C–PW–13.015	O–Ka	0.5249	9.9,29700	3000	1	–6	0	–0.96	0	2.2	2C1	–	0.113	PH_CNT	18	521
F–I2C–PW–13.016	O–Ka	0.5249	9.07,27210	3000	1	–10	0	–0.96	0.144	5.6	2C1	–	0.23	PH_CNT	38	522
F–I2C–PW–13.017	O–Ka	0.5249	9.93,29790	3000	1	–15	0	–0.96	0.144	12.1	2C1	–	0.66	PH_CNT	114	506
F–I2C–PW–13.018	O–Ka	0.5249	9.61,28830	3000	1	–20	0	–0.96	0	20.7	2C1	–	6	PH_CNT	1024	501
F–I2C–PW–13.019	O–Ka	0.5249	299.8,29980	100	1	–2	0	–0.96	0.144	0.5	2C1	–	0.66	PH_CNT	114	17
F–I2C–PW–13.020	O–Ka	0.5249	289.49,28949	100	1	–4	0	–0.96	0.144	1	2C1	–	0.66	PH_CNT	114	17
F–I2C–PW–13.021	O–Ka	0.5249	297.28,29728	100	1	–6	0	–0.96	0.144	2.2	2C1	–	0.66	PH_CNT	114	17
F–I2C–PW–13.022	O–Ka	0.5249	283.69,28369	100	1	–10	0	–0.96	0.144	5.6	2C1	–	0.66	PH_CNT	114	17
F–I2C–PW–13.023	O–Ka	0.5249	298.05,29805	100	1	–15	0	–0.96	0.144	12.1	2C1	–	0.66	PH_CNT	114	17
F–I2C–PW–13.024	O–Ka	0.5249	297.35,29735	100	1	–20	0	–0.96	0	20.7	2C1	–	6	PH_CNT	1024	17

Table 4.7: Point Response Function Tests

4.4.5 Effective Area

Effective Area (EA) tests measure the total effective collecting area over the PRF at many energies in photon counting mode. We performed this test at many energies due to the need for detailed sampling of energy space. The tests were done with the system substantially defocused, to minimize photon loss due to pileup. Measurements were made on-axis and at several off-axis positions.

TRW_ID	source	energy	FP_Rate,Total_Cts	Int_time	mult	pitch	yaw	yoff	zoff	Defocus	Focal	HST	frametime	proc_mode	rows	frames
F–I2C–EA–1.003	Al–Ka	1.486	49.55,20000	403.63	1	0	0	–0.96	0	40	2C1	–	6	PH_CNT	1024	68
F–I2C–EA–11.013	Al–Ka	1.486	49.33,20000	405.43	1	–2	0	–0.96	0	40	2C1	–	6	PH_CNT	1024	68
F–I2C–EA–11.014	Al–Ka	1.486	47.61,20000	420.08	1	–4	0	–0.96	0	40	2C1	–	6	PH_CNT	1024	71
F–I2C–EA–11.015	Al–Ka	1.486	45.81,20000	436.58	1	–6	0	–0.96	0	40	2C1	–	6	PH_CNT	1024	73
F–I2C–EA–11.016	Al–Ka	1.486	46.69,20000	428.35	1	–10	0	–0.96	0	40	2C1	–	6	PH_CNT	1024	72
F–I2C–EA–11.017	Al–Ka	1.486	45.86,20000	436.11	1	–15	0	–0.96	0	40	2C1	–	6	PH_CNT	1024	73
F–I2C–EA–11.018	Al–Ka	1.486	49.18,20000	406.66	1	–20	0	–0.96	0	40	2C1	–	6	PH_CNT	1024	68
F–I2C–EA–12.031	Al–Ka	1.486	46.49,20000	430.2	1	–2	0	0	0	40	2C0	–	6	PH_CNT	1024	72
F–I2C–EA–12.032	Al–Ka	1.486	49.86,20000	401.12	1	–4	0	0	0	40	2C0	–	6	PH_CNT	1024	67
F–I2C–EA–12.033	Al–Ka	1.486	47.97,20000	416.92	1	–6	0	0	0	40	2C0	–	6	PH_CNT	1024	70
F–I2C–EA–12.034	Al–Ka	1.486	48.89,20000	409.08	1	–10	0	0	0	40	2C0	–	6	PH_CNT	1024	69
F–I2C–EA–12.035	Al–Ka	1.486	48.02,20000	416.49	1	–15	0	0	0	40	2C0	–	6	PH_CNT	1024	70
F–I2C–EA–12.036	Al–Ka	1.486	46.34,20000	431.59	1	–20	0	0	0	40	2C0	–	6	PH_CNT	1024	72
F–I2C–EA–2.003	Al–Ka	1.486	46.69,20000	428.35	1	0	0	–0.96	0	40	2C0	–	6	PH_CNT	1024	72
H–IAS–EA–1.001	Al–Ka	1.486	73.1706,20000	273.33	1	0	23.86	–68.491	0	40.237	S3	S0	3.3	PH_CNT	1024	83
H–IAS–EA–1.002	Al–Ka	1.486	76.8710,20000	260.17	1	0	15.18	–43.583	0	40.096	S3	S1	3.3	PH_CNT	1024	79
H–IAS–EA–1.003	Al–Ka	1.486	77.1033,20000	259.39	1	0	–10.84	31.132	0	40.049	S3	S4	3.3	PH_CNT	1024	79
H–IAS–EA–1.004	Al–Ka	1.486	75.6216,20000	264.47	1	0	–19.52	56.051	0	40.159	S3	S5	3.3	PH_CNT	1024	81
F–I2C–EA–12.043	C–Ka	0.277	25.11,20000	796.49	1	–2	0	0	0	40	2C0	–	6	PH_CNT	1024	133
F–I2C–EA–12.044	C–Ka	0.277	26.68,20000	749.62	1	–4	0	0	0	40	2C0	–	6	PH_CNT	1024	125
F–I2C–EA–12.045	C–Ka	0.277	25.67,20000	779.12	1	–6	0	0	0	40	2C0	–	6	PH_CNT	1024	130
F–I2C–EA–12.046	C–Ka	0.277	25.89,20000	772.49	1	–10	0	0	0	45	2C0	–	6	PH_CNT	1024	129
F–I2C–EA–12.047	C–Ka	0.277	25.23,20000	792.7	1	–15	0	0	0	–30	2C0	–	6	PH_CNT	1024	133
F–I2C–EA–12.048	C–Ka	0.277	26.03,20000	768.34	1	–20	0	0	0	–20	2C0	–	6	PH_CNT	1024	129
F–I2C–EA–2.008	C–Ka	0.277	25.24,20000	792.39	1	0	0	–0.96	0	40	2C0	–	6	PH_CNT	1024	133
H–IAI–EA–23.001	C–Ka	0.277	36.6972,10000	272.5	1	4.95	4.93	–14.163	14.225	40.02	I3	I0	3.3	PH_CNT	1024	83
H–IAI–EA–23.002	C–Ka	0.277	37.3086,10000	268.030	1	4.95	–3.74	10.733	14.225	40.016	I3	I1	3.3	PH_CNT	1024	82
H–IAI–EA–23.003	C–Ka	0.277	37.3140,10000	267.99	1	–3.76	4.93	–14.163	–10.781	40.016	I3	I2	3.3	PH_CNT	1024	82

continued on next page

continued from previous page

TRW_ID	source	energy	FP_Rate,Total_Cts	Int_time	mult	pitch	yaw	yoff	zoff	Defocus	Focal	HST	frametime	proc_mode	rows	frames
H–IAI–EA–23.004	C–Ka	0.277	30.4067,10000	328.87	1	–3.76	–3.74	10.733	–10.781	40.011	I3	I3	3.3	PH_CNT	1024	100
H–IAS–EA–23.005	C–Ka	0.277	33.8649,10000	295.29	1	–13.2	7.03	–20.181	–37.895	40.093	S2	S2	3.3	PH_CNT	1024	90
H–IAS–EA–23.006	C–Ka	0.277	30.1858,10000	331.28	1	–13.2	–1.64	4.716	–37.896	40.073	S3	S3	3.3	PH_CNT	1024	101
H–IAS–EA–23.007	C–Ka	0.277	35.7706,10000	279.55	1	0	23.86	–68.491	0	40.237	S0	S0	3.3	PH_CNT	1024	85
H–IAS–EA–23.008	C–Ka	0.277	39.1692,10000	255.3	1	0	15.18	–43.583	0	40.096	S1	S1	3.3	PH_CNT	1024	78
H–IAS–EA–23.009	C–Ka	0.277	37.0765,10000	269.71	1	0	6.51	–18.675	0	40.017	S2	S2	3.3	PH_CNT	1024	82
H–IAS–EA–23.010	C–Ka	0.277	38.5090,10000	259.68	1	0	0	0	0	40	S3	S3	3.3	PH_CNT	1024	79
H–IAS–EA–23.011	C–Ka	0.277	38.2031,10000	261.75	1	0	–2.17	6.224	0	40.002	S3	S3	3.3	PH_CNT	1024	80
H–IAS–EA–23.012	C–Ka	0.277	37.4382,10000	267.1	1	0	–10.84	31.132	0	40.049	S4	S4	3.3	PH_CNT	1024	81
H–IAS–EA–23.013	C–Ka	0.277	36.8342,10000	271.48	1	0	–19.52	56.051	0	40.159	S5	S5	3.3	PH_CNT	1024	83
F–I2C–EA–1.001	Cu–Ka	8.030	28.39,20000	704.47	1	0	0	–0.96	0	40	2C1	–	6	PH_CNT	1024	118
F–I2C–EA–11.001	Cu–Ka	8.030	27.67,20000	722.8	1	–2	0	–0.96	0	40	2C1	–	6	PH_CNT	1024	121
F–I2C–EA–11.002	Cu–Ka	8.030	28.12,20000	711.23	1	–4	0	–0.96	0	40	2C1	–	6	PH_CNT	1024	119
F–I2C–EA–11.002a	Cu–Ka	8.030	28.12,20000	711.23	1	–4	0	–0.96	0	40	2C1	–	6	PH_CNT	1024	119
F–I2C–EA–11.003	Cu–Ka	8.030	27.89,20000	717.1	1	–6	0	–0.96	0	40	2C1	–	6	PH_CNT	1024	120
F–I2C–EA–11.004	Cu–Ka	8.030	27.89,20000	717.1	1	–10	0	–0.96	0	45	2C1	–	6	PH_CNT	1024	120
F–I2C–EA–11.005	Cu–Ka	8.030	27.88,20000	717.36	1	–15	0	–0.96	0	–30	2C1	–	6	PH_CNT	1024	120
F–I2C–EA–11.006	Cu–Ka	8.030	27.72,20000	721.5	1	–20	0	–0.96	0	–20	2C1	–	6	PH_CNT	1024	121
F–I2C–EA–12.001	Cu–Ka	8.030	47.9,20000	417.53	1	–2	0	0	0	40	2C0	–	6	PH_CNT	1024	70
F–I2C–EA–12.002	Cu–Ka	8.030	48.67,20000	410.93	1	–4	0	0	0	40	2C0	–	6	PH_CNT	1024	69
F–I2C–EA–12.003	Cu–Ka	8.030	48.29,20000	414.16	1	–6	0	0	0	40	2C0	–	6	PH_CNT	1024	70
F–I2C–EA–12.004	Cu–Ka	8.030	48.28,20000	414.25	1	–10	0	0	0	45	2C0	–	6	PH_CNT	1024	70
F–I2C–EA–12.005	Cu–Ka	8.030	48.27,20000	414.33	1	–15	0	0	0	–30	2C0	–	6	PH_CNT	1024	70
F–I2C–EA–12.006	Cu–Ka	8.030	46.69,20000	428.35	1	–20	0	0	0	–20	2C0	–	6	PH_CNT	1024	72
F–I2C–EA–2.001	Cu–Ka	8.030	49.15,20000	406.91	1	0	0	–0.96	0	40	2C0	–	6	PH_CNT	1024	68
H–IAI–EA–24.007	Cu–Ka	8.030	15.9156,10000	628.31	1	4.95	4.93	–14.163	14.225	40.02	I3	I0	3.3	PH_CNT	1024	191
H–IAI–EA–24.008	Cu–Ka	8.030	16.8230,10000	594.42	1	4.95	–3.74	10.733	14.225	40.016	I3	I1	3.3	PH_CNT	1024	181
H–IAI–EA–24.009	Cu–Ka	8.030	16.8311,10000	594.13	1	–3.76	4.93	–14.163	–10.781	40.016	I3	I2	3.3	PH_CNT	1024	181
H–IAI–EA–25.002	Cu–Ka	8.030	19.2976,10000	518.19	1	0	0	10.8	–2.7	40	I3	I3	3.3	PH_CNT	1024	158
H–IAS–EA–24.028	Cu–Ka	8.030	16.4785,10000	606.85	1	0	6.51	–18.675	0	40.017	S2	S2	3.3	PH_CNT	1024	184
H–IAS–EA–24.029	Cu–Ka	8.030	19.3415,10000	517.02	1	0	0	0	0	40	S3	S3	3.3	PH_CNT	1024	157
F–I2C–EA–1.007	Cu–La	0.9297	47.68,20000	419.46	1	0	0	–0.96	0	40	2C1	–	6	PH_CNT	1024	70
H–IAI–EA–25.005	Cu–La	0.9297	37.3716,10000	267.58	1	0	0	10.8	–2.7	40	I3	I3	3.3	PH_CNT	1024	82
H–IAI–EA–3.001	Cu–La	0.9297	37.5746,10000	266.13	1	4.95	4.93	–14.163	14.225	40.02	I3	I0	3.3	PH_CNT	1024	81
H–IAI–EA–3.002	Cu–La	0.9297	38.2039,10000	261.75	1	4.95	–3.74	10.733	14.225	40.016	I3	I1	3.3	PH_CNT	1024	80
H–IAI–EA–3.003	Cu–La	0.9297	38.2096,10000	261.71	1	–3.76	4.93	–14.163	–10.781	40.016	I3	I2	3.3	PH_CNT	1024	80
H–IAS–EA–18.021	Cu–La	0.9297	37.9650,10000	263.4	1	0	6.51	–18.675	0	40.017	S2	S2	3.3	PH_CNT	1024	80
H–IAS–EA–18.022	Cu–La	0.9297	36.8636,10000	271.27	1	0	0	0	0	40	S3	S3	3.3	PH_CNT	1024	83
F–I2C–EA–23.001	DCM	1.7	43.37,10000	230.57	1	–0	–0	0	0	0	2C1	–	6	INTEG	1024	39
F–I2C–EA–23.003	DCM	1.7	42.84,10000	233.42	1	–0	–0	0	0	0	2C0	–	6	INTEG	1024	39
F–I2C–EA–3.002	DCM	1.8425	40.31,20000	2976.93	6	0	0	0	0	40	2C0	–	6	PH_CNT	1024	497
F–I2C–EA–3.004	DCM	1.885	48.66,20000	2055.08	5	0	0	0	0	40	2C0	–	6	PH_CNT	1024	343
F–I2C–EA–5.001b	DCM	2.62	47.23,20000	5081.52	12	0	0	–0.96	0	40	2C1	–	6	PH_CNT	1024	847
F–I2C–EA–5.003	DCM	2.54999	46.25,20000	2162.16	5	0	0	–0.96	0	40	2C1	–	6	PH_CNT	1024	361
F–I2C–EA–5.004	DCM	2.16	45.25,20000	2209.94	5	0	0	–0.96	0	40	2C1	–	6	PH_CNT	1024	369
F–I2C–EA–5.005	DCM	2.09	47.43,20000	2108.37	5	0	0	–0.96	0	40	2C1	–	6	PH_CNT	1024	352
F–I2C–EA–6.001	DCM	1.575	48.89,20000	2454.48	6	0	0	0	0	40	2C1	–	6	PH_CNT	1024	410
F–I2C–EA–6.002	DCM	4.75	43.61,20000	4586.1	10	0	0	–0.96	0	40	2C1	–	6	PH_CNT	1024	765
F–I2C–EA–6.003	DCM	6.75	20.18,20000	9910.79	10	0	0	–0.96	0	40	2C1	–	6	PH_CNT	1024	1652
F–I2C–EA–6.004	DCM	1.575	49.53,20000	2422.77	6	0	0	0	0	40	2C0	–	6	PH_CNT	1024	404
F–I2C–EA–6.005	DCM	4.75	43.09,20000	4641.45	10	0	0	–0.96	0	40	2C0	–	6	PH_CNT	1024	774
F–I2C–EA–6.006	DCM	6.75	21.14,20000	9460.74	10	0	0	–0.96	0	40	2C0	–	6	PH_CNT	1024	1577
F–I2C–EA–72.001	DCM	3.25	46.87,10000	640.06	3	0	0	–0.96	0	23.5	2C1	–	6	PH_CNT	1024	107
G–I2C–EA–41.002	DCM	1.83	1105.0602,165759	150	1	0	0	0	0.144	23.4	2C1	–	0.66	PH_CNT	114	26
G–I2C–EA–41.008	DCM	1.88	66.3701,9955.51	900	6	0	0	0	0.144	23.4	2C1	–	0.66	PH_CNT	114	152
H–IAI–EA–2.001	DCM	6	72.4814,20000	1931.53	7	4.95	4.93	–14.666	14.731	40.021	I3	I0	3.3	PH_CNT	1024	586
H–IAI–EA–2.002	DCM	6	75.3108,20000	1858.96	7	4.95	–3.74	11.114	14.73	40.016	I3	I1	3.3	PH_CNT	1024	564
H–IAI–EA–2.003	DCM	6	75.3361,20000	1858.34	7	–3.76	4.93	–14.667	–11.164	40.016	I3	I2	3.3	PH_CNT	1024	564
H–IAI–EA–2.004	DCM	6	78.5836,20000	1781.54	7	–3.76	–3.74	11.115	–11.164	40.012	I3	I3	3.3	PH_CNT	1024	540
H–IAI–EA–2.005	DCM	6	77.7692,20000	1800.2	7	–13.2	7.03	–20.899	–39.243	40.096	I3	S2	3.3	PH_CNT	1024	546
H–IAI–EA–2.006	DCM	6	77.9840,20000	1795.24	7	–13.2	–1.64	4.884	–39.244	40.076	I3	S3	3.3	PH_CNT	1024	545
H–IAI–EA–2.020	DCM	6	73.1412,20000	1914.11	7	0	0	10.8	–2.7	40	I3	I3	3.3	PH_CNT	1024	581

continued on next page

continued from previous page

TRW_ID	source	energy	FP_Rate,Total_Cts	Int_time	mult	pitch	yaw	yoff	zoff	Defocus	Focal	HST	frametime	proc_mode	rows	frames
H–IAS–EA–2.007	DCM	6	55.8527,20000	2506.59	7	0	23.86	–70.927	0	40.246	S3	S0	3.3	PH_CNT	1024	760
H–IAS–EA–2.008	DCM	6	75.8731,20000	1845.19	7	0	15.18	–45.133	0	40.099	S3	S1	3.3	PH_CNT	1024	560
H–IAS–EA–2.009	DCM	6	73.5752,20000	1902.82	7	0	6.51	–19.339	0	40.018	S3	S2	3.3	PH_CNT	1024	577
H–IAS–EA–2.010	DCM	6	72.4895,20000	1931.31	7	0	0	0	0	40	S3	S3	3.3	PH_CNT	1024	586
H–IAS–EA–2.011	DCM	6	78.3540,20000	1786.76	7	0	–2.17	6.445	0	40.002	S3	S3	3.3	PH_CNT	1024	542
H–IAS–EA–2.012	DCM	6	72.1441,20000	1940.56	7	0	–10.84	32.239	0	40.05	S3	S4	3.3	PH_CNT	1024	589
H–IAS–EA–2.013	DCM	6	72.3609,20000	1934.75	7	0	–19.52	58.045	0	40.164	S3	S5	3.3	PH_CNT	1024	587
F–I2C–EA–1.002	Fe–Ka	6.4	27.04,20000	739.64	1	0	0	–0.96	0	40	2C1	–	6	PH_CNT	1024	124
F–I2C–EA–11.007	Fe–Ka	6.4	29.07,20000	687.99	1	–2	0	–0.96	0	40	2C1	–	6	PH_CNT	1024	115
F–I2C–EA–11.008	Fe–Ka	6.4	29.92,20000	668.44	1	–4	0	–0.96	0	40	2C1	–	6	PH_CNT	1024	112
F–I2C–EA–11.009	Fe–Ka	6.4	27.21,20000	735.02	1	–6	0	–0.96	0	40	2C1	–	6	PH_CNT	1024	123
F–I2C–EA–11.010	Fe–Ka	6.4	29.01,20000	689.41	1	–10	0	–0.96	0	45	2C1	–	6	PH_CNT	1024	115
F–I2C–EA–11.011	Fe–Ka	6.4	28.48,20000	702.24	1	–15	0	–0.96	0	–30	2C1	–	6	PH_CNT	1024	118
F–I2C–EA–11.012	Fe–Ka	6.4	27.21,20000	735.02	1	–20	0	–0.96	0	–20	2C1	–	6	PH_CNT	1024	123
F–I2C–EA–12.007	Fe–Ka	6.4	48.01,20000	416.58	1	–2	0	0	0	40	2C0	–	6	PH_CNT	1024	70
F–I2C–EA–12.008	Fe–Ka	6.4	49.41,20000	404.77	1	–4	0	0	0	40	2C0	–	6	PH_CNT	1024	68
F–I2C–EA–12.009	Fe–Ka	6.4	44.94,20000	445.03	1	–6	0	0	0	40	2C0	–	6	PH_CNT	1024	75
F–I2C–EA–12.010	Fe–Ka	6.4	49.82,20000	401.44	1	–10	0	0	0	45	2C0	–	6	PH_CNT	1024	67
F–I2C–EA–12.011	Fe–Ka	6.4	48.91,20000	408.91	1	–15	0	0	0	–30	2C0	–	6	PH_CNT	1024	69
F–I2C–EA–12.012	Fe–Ka	6.4	49.93,20000	400.56	1	–20	0	0	0	–20	2C0	–	6	PH_CNT	1024	67
F–I2C–EA–2.002	Fe–Ka	6.4	49.63,20000	402.98	1	0	0	–0.96	0	40	2C0	–	6	PH_CNT	1024	68
H–IAI–EA–25.006	Fe–Ka	6.4	18.2752,10000	547.19	1	0	0	10.8	–2.7	40	I3	I3	3.3	PH_CNT	1024	166
H–IAI–EA–3.013	Fe–Ka	6.4	19.3036,10000	518.030	1	4.95	4.93	–14.163	14.225	40.02	I3	I0	3.3	PH_CNT	1024	157
H–IAI–EA–3.014	Fe–Ka	6.4	18.1770,10000	550.14	1	4.95	–3.74	10.733	14.225	40.016	I3	I1	3.3	PH_CNT	1024	167
H–IAI–EA–3.015	Fe–Ka	6.4	18.1842,10000	549.92	1	–3.76	4.93	–14.163	–10.781	40.016	I3	I2	3.3	PH_CNT	1024	167
H–IAS–EA–18.0305	Fe–Ka	6.4	19.8577,10000	503.58	1	0	6.51	–18.675	0	40.017	S2	S2	3.3	PH_CNT	1024	153
H–IAS–EA–18.0306	Fe–Ka	6.4	19.3990,10000	515.49	1	0	0	0	0	40	S3	S3	3.3	PH_CNT	1024	157
F–I2C–EA–1.017	Fe–La	0.705	45.44,20000	440.14	1	0	0	–0.96	0	40	2C1	–	6	PH_CNT	1024	74
F–I2C–EA–11.025	Fe–La	0.705	45.21,20000	442.38	1	–2	0	–0.96	0	40	2C1	–	6	PH_CNT	1024	74
F–I2C–EA–11.026	Fe–La	0.705	48.51,20000	412.28	1	–4	0	–0.96	0	40	2C1	–	6	PH_CNT	1024	69
F–I2C–EA–11.027	Fe–La	0.705	46.67,20000	428.54	1	–6	0	–0.96	0	40	2C1	–	6	PH_CNT	1024	72
F–I2C–EA–11.028	Fe–La	0.705	47.53,20000	420.78	1	–10	0	–0.96	0	45	2C1	–	6	PH_CNT	1024	71
F–I2C–EA–11.029	Fe–La	0.705	42.1,20000	475.05	1	–15	0	–0.96	0	–30	2C1	–	6	PH_CNT	1024	80
F–I2C–EA–11.030	Fe–La	0.705	40.34,20000	495.78	1	–20	0	–0.96	0	–20	2C1	–	6	PH_CNT	1024	83
F–I2C–EA–12.013	Fe–La	0.705	27.1,20000	738	1	–2	0	0	0	40	2C0	–	6	PH_CNT	1024	124
F–I2C–EA–12.014	Fe–La	0.705	26.17,20000	764.23	1	–4	0	0	0	40	2C0	–	6	PH_CNT	1024	128
F–I2C–EA–12.015	Fe–La	0.705	25.18,20000	794.28	1	–6	0	0	0	40	2C0	–	6	PH_CNT	1024	133
F–I2C–EA–12.016	Fe–La	0.705	25.38,20000	788.02	1	–10	0	0	0	45	2C0	–	6	PH_CNT	1024	132
F–I2C–EA–12.017	Fe–La	0.705	27.21,20000	735.02	1	–15	0	0	0	–30	2C0	–	6	PH_CNT	1024	123
F–I2C–EA–12.018	Fe–La	0.705	26.07,20000	767.16	1	–20	0	0	0	–20	2C0	–	6	PH_CNT	1024	128
F–I2C–EA–2.005	Fe–La	0.705	27.24,20000	734.21	1	0	0	–0.96	0	40	2C0	–	6	PH_CNT	1024	123
H–IAI–EA–24.013	Fe–La	0.705	38.3593,10000	260.69	1	4.95	4.93	–14.163	14.225	40.02	I3	I0	3.3	PH_CNT	1024	79
H–IAI–EA–24.014	Fe–La	0.705	39.0007,10000	256.4	1	4.95	–3.74	10.733	14.225	40.016	I3	I1	3.3	PH_CNT	1024	78
H–IAI–EA–24.015	Fe–La	0.705	39.0064,10000	256.36	1	–3.76	4.93	–14.163	–10.781	40.016	I3	I2	3.3	PH_CNT	1024	78
H–IAI–EA–25.003	Fe–La	0.705	31.0882,10000	321.66	1	0	0	10.8	–2.7	40	I3	I3	3.3	PH_CNT	1024	98
H–IAS–EA–24.035	Fe–La	0.705	38.7572,10000	258.01	1	0	6.51	–18.675	0	40.017	S2	S2	3.3	PH_CNT	1024	79
H–IAS–EA–24.036	Fe–La	0.705	37.0485,10000	269.91	1	0	0	0	0	40	S3	S3	3.3	PH_CNT	1024	82
F–I2C–EA–1.009	Mg–Ka	1.254	47.21,20000	423.63	1	0	0	–0.96	0	40	2C1	–	6	PH_CNT	1024	71
F–I2C–EA–1.029	Mg–Ka	1.254	40.8,20000	490.19	1	0	0	0	0	40	2C0	–	6	PH_CNT	1024	82
G–I2C–EA–1.010	Mo–La	2.293	45.2022,20000	442.45	1	0	0	–0.96	0	40	2C1	–	6	PH_CNT	1024	74
F–I2C–EA–2.012	Ni–La	0.852	29.19,20000	685.16	1	0	0	–0.96	0	40	2C0	–	6	PH_CNT	1024	115
F–I2C–EA–2.020	Ni–La	0.852	49.53,20000	403.79	1	0	0	0	0	40	2C1	–	6	PH_CNT	1024	68
F–I2C–EA–1.005	O–Ka	0.5249	41.31,20000	484.14	1	0	0	–0.96	0	40	2C1	–	6	PH_CNT	1024	81
F–I2C–EA–11.037	O–Ka	0.5249	41.1,20000	486.61	1	–2	0	–0.96	0	40	2C1	–	6	PH_CNT	1024	82
F–I2C–EA–11.038	O–Ka	0.5249	43.66,20000	458.08	1	–4	0	–0.96	0	40	2C1	–	6	PH_CNT	1024	77
F–I2C–EA–11.039	O–Ka	0.5249	42,20000	476.19	1	–6	0	–0.96	0	40	2C1	–	6	PH_CNT	1024	80
F–I2C–EA–11.040	O–Ka	0.5249	42.36,20000	472.14	1	–10	0	–0.96	0	45	2C1	–	6	PH_CNT	1024	79
F–I2C–EA–11.041	O–Ka	0.5249	41.28,20000	484.49	1	–15	0	–0.96	0	–30	2C1	–	6	PH_CNT	1024	81
F–I2C–EA–11.042	O–Ka	0.5249	45.72,20000	437.44	1	–20	0	–0.96	0	–20	2C1	–	6	PH_CNT	1024	73

continued on next page

continued from previous page

TRW_ID	source	energy	FP_Rate,Total_Cts	Int_time	mult	pitch	yaw	yoff	zoff	Defocus	Focal	HST	frametime	proc_mode	rows	frames
F–I2C–EA–12.025	O–Ka	0.5249	28.14,20000	710.73	1	–2	0	0	0	40	2C0	–	6	PH_CNT	1024	119
F–I2C–EA–12.026	O–Ka	0.5249	27.17,20000	736.1	1	–4	0	0	0	40	2C0	–	6	PH_CNT	1024	123
F–I2C–EA–12.027	O–Ka	0.5249	29.05,20000	688.46	1	–6	0	0	0	40	2C0	–	6	PH_CNT	1024	115
F–I2C–EA–12.028	O–Ka	0.5249	29.59,20000	675.9	1	–10	0	0	0	45	2C0	–	6	PH_CNT	1024	113
F–I2C–EA–12.029	O–Ka	0.5249	29.13,20000	686.57	1	–15	0	0	0	–30	2C0	–	6	PH_CNT	1024	115
F–I2C–EA–12.030	O–Ka	0.5249	28.2,20000	709.22	1	–20	0	0	0	–20	2C0	–	6	PH_CNT	1024	119
F–I2C–EA–2.007	O–Ka	0.5249	28.29,20000	706.96	1	0	0	–0.96	0	40	2C0	–	6	PH_CNT	1024	118
H–IAI–EA–24.001	O–Ka	0.5249	37.3352,10000	267.84	1	4.95	4.93	–14.163	14.225	40.02	I3	I0	3.3	PH_CNT	1024	82
H–IAI–EA–24.002	O–Ka	0.5249	37.9586,10000	263.44	1	4.95	–3.74	10.733	14.225	40.016	I3	I1	3.3	PH_CNT	1024	80
H–IAI–EA–24.003	O–Ka	0.5249	37.9641,10000	263.4	1	–3.76	4.93	–14.163	–10.781	40.016	I3	I2	3.3	PH_CNT	1024	80
H–IAI–EA–24.004	O–Ka	0.5249	38.6796,10000	258.53	1	–3.76	–3.74	10.733	–10.781	40.011	I3	I3	3.3	PH_CNT	1024	79
H–IAI–EA–25.001	O–Ka	0.5249	30.4905,10000	327.97	1	0	0	10.8	–2.7	40	I3	I3	3.3	PH_CNT	1024	100
H–IAS–EA–24.021	O–Ka	0.5249	37.7219,10000	265.09	1	0	6.51	–18.675	0	40.017	S2	S2	3.3	PH_CNT	1024	81
H–IAS–EA–24.022	O–Ka	0.5249	36.6008,10000	273.21	1	0	0	0	0	40	S3	S3	3.3	PH_CNT	1024	83
H–IAI–EA–25.004	Si–Ka	1.739	39.6983,10000	251.9	1	0	0	10.8	–2.7	40	I3	I3	3.3	PH_CNT	1024	77
H–IAI–EA–3.007	Si–Ka	1.739	39.7868,10000	251.34	1	4.95	4.93	–14.163	14.225	40.02	I3	I0	3.3	PH_CNT	1024	77
H–IAI–EA–3.008	Si–Ka	1.739	36.4065,10000	274.67	1	4.95	–3.74	10.733	14.225	40.016	I3	I1	3.3	PH_CNT	1024	84
H–IAI–EA–3.009	Si–Ka	1.739	36.4118,10000	274.63	1	–3.76	4.93	–14.163	–10.781	40.016	I3	I2	3.3	PH_CNT	1024	84
H–IAS–EA–18.028	Si–Ka	1.739	36.1793,10000	276.4	1	0	6.51	–18.675	0	40.017	S2	S2	3.3	PH_CNT	1024	84
H–IAS–EA–18.029	Si–Ka	1.739	37.9455,10000	263.53	1	0	0	0	0	40	S3	S3	3.3	PH_CNT	1024	80
F–I2C–EA–1.004	Ti–Ka	4.51	29.13,20000	686.57	1	0	0	–0.96	0	40	2C1	–	6	PH_CNT	1024	115
F–I2C–EA–11.019	Ti–Ka	4.51	28.61,20000	699.05	1	–2	0	–0.96	0	40	2C1	–	6	PH_CNT	1024	117
F–I2C–EA–11.020	Ti–Ka	4.51	27.46,20000	728.33	1	–4	0	–0.96	0	40	2C1	–	6	PH_CNT	1024	122
F–I2C–EA–11.021	Ti–Ka	4.51	29,20000	689.65	1	–6	0	–0.96	0	40	2C1	–	6	PH_CNT	1024	115
F–I2C–EA–11.022	Ti–Ka	4.51	28.33,20000	705.96	1	–10	0	–0.96	0	45	2C1	–	6	PH_CNT	1024	118
F–I2C–EA–11.023	Ti–Ka	4.51	28.72,20000	696.37	1	–15	0	–0.96	0	–30	2C1	–	6	PH_CNT	1024	117
F–I2C–EA–11.024	Ti–Ka	4.51	27.73,20000	721.24	1	–20	0	–0.96	0	–20	2C1	–	6	PH_CNT	1024	121
F–I2C–EA–12.019	Ti–Ka	4.51	48.58,20000	411.69	1	–2	0	0	0	40	2C0	–	6	PH_CNT	1024	69
F–I2C–EA–12.020	Ti–Ka	4.51	46.63,20000	428.9	1	–4	0	0	0	40	2C0	–	6	PH_CNT	1024	72
F–I2C–EA–12.021	Ti–Ka	4.51	49.24,20000	406.17	1	–6	0	0	0	40	2C0	–	6	PH_CNT	1024	68
F–I2C–EA–12.022	Ti–Ka	4.51	48.12,20000	415.62	1	–10	0	0	0	45	2C0	–	6	PH_CNT	1024	70
F–I2C–EA–12.023	Ti–Ka	4.51	48.77,20000	410.08	1	–15	0	0	0	–30	2C0	–	6	PH_CNT	1024	69
F–I2C–EA–12.024	Ti–Ka	4.51	47.09,20000	424.71	1	–20	0	0	0	–20	2C0	–	6	PH_CNT	1024	71
F–I2C–EA–2.004	Ti–Ka	4.51	49.47,20000	404.28	1	0	0	–0.96	0	40	2C0	–	6	PH_CNT	1024	68
F–I2C–EA–12.049	Ti–La	0.4522	49.04,20000	407.83	1	–2	0	0	0	40	2C0	–	6	PH_CNT	1024	68
F–I2C–EA–12.050	Ti–La	0.4522	47.35,20000	422.38	1	–4	0	0	0	40	2C0	–	6	PH_CNT	1024	71
F–I2C–EA–12.051	Ti–La	0.4522	45.56,20000	438.98	1	–6	0	0	0	40	2C0	–	6	PH_CNT	1024	74
F–I2C–EA–12.052	Ti–La	0.4522	46.41,20000	430.94	1	–10	0	0	0	45	2C0	–	6	PH_CNT	1024	72
F–I2C–EA–12.053	Ti–La	0.4522	45.68,20000	437.82	1	–15	0	0	0	–30	2C0	–	6	PH_CNT	1024	73
F–I2C–EA–12.054	Ti–La	0.4522	49.14,20000	407	1	–20	0	0	0	–20	2C0	–	6	PH_CNT	1024	68
F–I2C–EA–2.009	Ti–La	0.4522	28.02,20000	713.77	1	0	0	–0.96	0	40	2C0	–	6	PH_CNT	1024	119

Table 4.8: Effective Area Tests

4.4.6 Count-Rate Linearity

Count-rate Linearity (Pileup) tests measure the effect of increasing the level of photons per pixel on the PRF, the EA, source centroiding, and photon detection. We used two methods to vary photon density: longer readout times for constant beam flux, and brighter beam flux at constant readout times. The data are being compared to see if the pileup is different between these two methods. For FI chips, this test was repeated at medium energy (Al K) for minimum event splitting and at high energy (Cu K) for maximum event splitting. For BI chips, it was repeated at medium energy (Al K) for minimum event splitting and high energy (Cu K) for comparison with FI; we added low energy (O K) and ultra low energy (C K) for maximum BI event splitting. It was important to repeat these tests separately for each chip because the results depend intimately on the event splitting characteristics of the chip.

TRW_ID	source	energy	FP_Rate,Total_Cts	Int_time	mult	pitch	yaw	yoff	zoff	Defocus	Focal	HST	frametime	proc_mode	rows	frames
F–I2C–CR–1.001	Al–Ka	1.486	9.04,20000	2212.39	1	0	0	0	0	0	2C1	–	0.113	PH_CNT	18	384
F–I2C–CR–1.002	Al–Ka	1.486	9.04,20000	2212.39	1	0	0	0	0	0	2C1	–	0.227	PH_CNT	38	390
F–I2C–CR–1.003	Al–Ka	1.486	9.04,20000	2212.39	1	0	0	0	0	0	2C1	–	0.318	PH_CNT	54	387
F–I2C–CR–1.004	Al–Ka	1.486	9.04,20000	2212.39	1	0	0	0	0	0	2C1	–	0.66	PH_CNT	114	373
F–I2C–CR–1.005	Al–Ka	1.486	2.74,20000	7299.27	1	0	0	0	0	0	2C1	–	0.113	PH_CNT	18	1267
F–I2C–CR–1.006	Al–Ka	1.486	28.82,20000	693.96	1	0	0	0	0	0	2C1	–	0.113	PH_CNT	18	121
F–I2C–CR–1.007	Al–Ka	1.486	54.23,20000	368.8	1	0	0	0	0	0	2C1	–	0.113	PH_CNT	18	64
F–I2C–CR–1.015a	Al–Ka	1.486	0.95,10000	21052.6	2	0	0	0	0	0	2C1	–	0.113	PH_CNT	18	3654
F–I2C–CR–2.001a	Al–Ka	1.486	9.16,20000	2183.41	1	0	0	0	0	0	2C0	–	0.113	PH_CNT	18	379
F–I2C–CR–2.002	Al–Ka	1.486	9.16,20000	2183.41	1	0	0	0	0	0	2C0	–	0.227	PH_CNT	38	385
F–I2C–CR–2.003	Al–Ka	1.486	9.16,20000	2183.41	1	0	0	0	0	0	2C0	–	0.318	PH_CNT	54	382
F–I2C–CR–2.004	Al–Ka	1.486	9.16,20000	2183.41	1	0	0	0	0	0	2C0	–	0.66	PH_CNT	114	368
F–I2C–CR–2.005	Al–Ka	1.486	2.87,20000	6968.64	1	0	0	0	0	0	2C0	–	0.113	PH_CNT	18	1210
F–I2C–CR–2.006	Al–Ka	1.486	27.16,20000	736.37	1	0	0	0	0	0	2C0	–	0.113	PH_CNT	18	128
F–I2C–CR–2.007	Al–Ka	1.486	56.79,20000	352.17	1	0	0	0	0	0	2C0	–	0.113	PH_CNT	18	62
F–I2C–CR–2.029	Al–Ka	1.486	18.32,10000	1091.7	2	0	0	0	0	0	2C0	–	0.113	PH_CNT	18	190
H–IAI–CR–1.001	Al–Ka	1.486	2.9392,20000	6804.57	1	0	0	0	0	0	I3	I3	0.1	PH_CNT	38	2062
H–IAI–CR–1.003	Al–Ka	1.486	9.3359,20000	2142.27	1	0	0	0	0	0	I3	I3	0.1	PH_CNT	38	650
H–IAI–CR–1.005	Al–Ka	1.486	29.7500,20000	672.26	1	0	0	0	0	0	I3	I3	0.1	PH_CNT	38	204
H–IAI–CR–1.007	Al–Ka	1.486	55.9798,20000	357.27	1	0	0	0	0	0	I3	I3	0.1	PH_CNT	38	109
H–IAS–CR–1.002	Al–Ka	1.486	2.9340,20000	6816.63	1	0	0	0	0	0	S3	S3	0.1	PH_CNT	38	2066
H–IAS–CR–1.004	Al–Ka	1.486	9.1315,20000	2190.21	1	0	0	0	0	0	S3	S3	0.1	PH_CNT	38	664
H–IAS–CR–1.006	Al–Ka	1.486	29.0987,20000	687.31	1	0	0	0	0	0	S3	S3	0.1	PH_CNT	38	209
H–IAS–CR–1.008	Al–Ka	1.486	54.7544,20000	365.26	1	0	0	0	0	0	S3	S3	0.1	PH_CNT	38	111
F–I2C–CR–2.022	C–Ka	0.277	9.2,20000	2173.91	1	0	0	0	0	0	2C0	–	0.113	PH_CNT	18	378
F–I2C–CR–2.023	C–Ka	0.277	9.2,20000	2173.91	1	0	0	0	0	0	2C0	–	0.227	PH_CNT	38	384
F–I2C–CR–2.024	C–Ka	0.277	9.2,20000	2173.91	1	0	0	0	0	0	2C0	–	0.318	PH_CNT	54	380
F–I2C–CR–2.025	C–Ka	0.277	9.2,20000	2173.91	1	0	0	0	0	0	2C0	–	0.66	PH_CNT	114	366
F–I2C–CR–2.026	C–Ka	0.277	2.88,20000	6944.44	1	0	0	0	0	0	2C0	–	0.113	PH_CNT	18	1206
F–I2C–CR–2.026a	C–Ka	0.277	2.88,20000	6944.44	1	0	0	0	0	0	2C0	–	0.113	PH_CNT	18	1206
F–I2C–CR–2.026b	C–Ka	0.277	2.88,20000	6944.44	1	0	0	0	0	0	2C0	–	0.113	PH_CNT	18	1206
F–I2C–CR–2.027	C–Ka	0.277	26.78,20000	746.82	1	0	0	0	0	0	2C0	–	0.113	PH_CNT	18	130
F–I2C–CR–2.027a	C–Ka	0.277	26.78,20000	746.82	1	0	0	0	0	0	2C0	–	0.113	PH_CNT	18	130
F–I2C–CR–2.027b	C–Ka	0.277	26.78,20000	746.82	1	0	0	0	0	0	2C0	–	0.113	PH_CNT	18	130
F–I2C–CR–2.027c	C–Ka	0.277	26.78,20000	746.82	1	0	0	0	0	0	2C0	–	0.113	PH_CNT	18	130
F–I2C–CR–2.028a	C–Ka	0.277	58.26,20000	343.28	1	0	0	0	0	0	2C0	–	0.113	PH_CNT	18	60
F–I2C–CR–2.028b	C–Ka	0.277	58.26,20000	343.28	1	0	0	0	0	0	2C0	–	0.113	PH_CNT	18	60
F–I2C–CR–2.028c	C–Ka	0.277	58.26,20000	343.28	1	0	0	0	0	0	2C0	–	0.113	PH_CNT	18	60
F–I2C–CR–2.028d	C–Ka	0.277	58.26,20000	343.28	1	0	0	0	0	0	2C0	–	0.113	PH_CNT	18	60
F–I2C–CR–1.008	Cu–Ka	8.030	9.33,20000	2143.62	1	0	0	0	0	0	2C1	–	0.113	PH_CNT	18	372
F–I2C–CR–1.009	Cu–Ka	8.030	9.33,20000	2143.62	1	0	0	0	0	0	2C1	–	0.227	PH_CNT	38	378
F–I2C–CR–1.010	Cu–Ka	8.030	9.33,20000	2143.62	1	0	0	0	0	0	2C1	–	0.318	PH_CNT	54	375
F–I2C–CR–1.011	Cu–Ka	8.030	9.33,20000	2143.62	1	0	0	0	0	0	2C1	–	0.66	PH_CNT	114	361
F–I2C–CR–1.012	Cu–Ka	8.030	2.93,20000	6825.94	1	0	0	0	0	0	2C1	–	0.113	PH_CNT	18	1185
F–I2C–CR–1.013	Cu–Ka	8.030	27.7,20000	722.02	1	0	0	0	0	0	2C1	–	0.113	PH_CNT	18	126
F–I2C–CR–1.014	Cu–Ka	8.030	57.91,20000	345.36	1	0	0	0	0	0	2C1	–	0.113	PH_CNT	18	60
F–I2C–CR–1.016	Cu–Ka	8.030	0.91,10000	21978	2	0	0	0	0	0	2C1	–	0.113	PH_CNT	18	3814
F–I2C–CR–2.008	Cu–Ka	8.030	9.54,20000	2096.44	1	0	0	0	0	0	2C0	–	0.113	PH_CNT	18	364
F–I2C–CR–2.009	Cu–Ka	8.030	9.54,20000	2096.44	1	0	0	0	0	0	2C0	–	0.227	PH_CNT	38	370
F–I2C–CR–2.010	Cu–Ka	8.030	9.54,20000	2096.44	1	0	0	0	0	0	2C0	–	0.318	PH_CNT	54	367
F–I2C–CR–2.011	Cu–Ka	8.030	9.54,20000	2096.44	1	0	0	0	0	0	2C0	–	0.66	PH_CNT	114	353
F–I2C–CR–2.012	Cu–Ka	8.030	2.99,20000	6688.96	1	0	0	0	0	0	2C0	–	0.113	PH_CNT	18	1161
F–I2C–CR–2.013	Cu–Ka	8.030	28.31,20000	706.46	1	0	0	0	0	0	2C0	–	0.113	PH_CNT	18	123
F–I2C–CR–2.014	Cu–Ka	8.030	59.2,20000	337.83	1	0	0	0	0	0	2C0	–	0.113	PH_CNT	18	59
F–I2C–CR–2.030	Cu–Ka	8.030	0.94,10000	21276.6	2	0	0	0	0	0	2C0	–	0.113	PH_CNT	18	3692
F–I2C–CR–2.015	O–Ka	0.5249	8.5,20000	2352.94	1	0	0	0	0	0	2C0	–	0.113	PH_CNT	18	409
F–I2C–CR–2.016	O–Ka	0.5249	8.5,20000	2352.94	1	0	0	0	0	0	2C0	–	0.227	PH_CNT	38	415

continued on next page

continued from previous page

TRW_ID	source	energy	FP_Rate,Total_Cts	Int_time	mult	pitch	yaw	yoff	zoff	Defocus	Focal	HST	frametime	proc_mode	rows	frames
F–I2C–CR–2.017	O–Ka	0.5249	8.5,20000	2352.94	1	0	0	0	0	0	2C0	–	0.318	PH_CNT	54	412
F–I2C–CR–2.018	O–Ka	0.5249	8.5,20000	2352.94	1	0	0	0	0	0	2C0	–	0.66	PH_CNT	114	397
F–I2C–CR–2.019	O–Ka	0.5249	2.72,20000	7352.94	1	0	0	0	0	0	2C0	–	0.113	PH_CNT	18	1276
F–I2C–CR–2.020	O–Ka	0.5249	27.39,20000	730.19	1	0	0	0	0	0	2C0	–	0.113	PH_CNT	18	127
F–I2C–CR–2.021	O–Ka	0.5249	56.71,20000	352.67	1	0	0	0	0	0	2C0	–	0.113	PH_CNT	18	62
H–IAI–CR–1.009	O–Ka	0.5249	2.7596,20000	7247.43	1	0	0	0	0	0	I3	I3	0.1	PH_CNT	38	2197
H–IAI–CR–1.011	O–Ka	0.5249	9.7710,20000	2046.87	1	0	0	0	0	0	I3	I3	0.1	PH_CNT	38	621
H–IAS–CR–1.010	O–Ka	0.5249	2.8086,20000	7120.99	1	0	0	0	0	0	S3	S3	0.1	PH_CNT	38	2158
H–IAS–CR–1.012	O–Ka	0.5249	9.3034,20000	2149.75	1	0	0	0	0	0	S3	S3	0.1	PH_CNT	38	652

Table 4.9: Count-rate Linearity Tests

4.4.7 Spatial Linearity

The Spatial Linearity tests consist of moving the PRF across chips to determine that the desired motion converts properly from the spatial domain to the CCD pixel domain. Also look for PRF variation indicating that the CCD chips are tilted with respect to the HRMA axis.

TRW_ID	source	energy	FP_Rate,Total_Cts	Int_time	mult	pitch	yaw	yoff	zoff	Defocus	Focal	HST	frametime	proc_mode	rows	frames
H–IAI–SL–1.001	O–Ka	0.5249	5.7696,1730.88	1900	1	0	0	0	0	0	I3	I3	3.3	PH_CNT	1024	576
H–IAS–SL–1.002	O–Ka	0.5249	5.6467,1694.01	900	1	0	0	0	0	0	S3	S3	3.3	PH_CNT	1024	273

Table 4.10: Spatial Linearity Tests

4.4.8 Flight Contamination Monitor

In the Flight Contamination Monitor tests, we position the ACIS or ACIS-2C at infinite conjugate focus and observe the Forward Contamination Cover sources (Mn K and Ag L) reflecting off the mirrors over both BI and FI chips. This allowed the facility to monitor the HRMA for contamination buildup throughout XRCF testing and baselines the radiation source spectra for on-orbit contamination monitoring.

TRW_ID	source	energy	FP_Rate,Total_Cts	Int_time	mult	pitch	yaw	yoff	zoff	Defocus	Focal	HST	frametime	proc_mode	rows	frames
F–I2C–RC–72.001	Al–Ka	1.486	9297.08,2789124	3000	10	–0	–0	–3.17	0	195	2C0	–	6	PH_CNT	1024	501
H–IAS–RC–1.001	Al–Ka	1.486	70133,1.122e+08	1600	1	0	0	0	0	200	S3	I3	3.3	PH_CNT	1024	485
H–IAS–RC–1.003	C–Ka	0.277	258.3646,775094	3000	1	0	0	0	0	200	S3	I3	3.3	PH_CNT	1024	910
F–I2C–RC–72.002	Cu–Ka	8.030	905.52,271656	3000	10	–0	–0	–3.17	0	195	2C0	–	6	PH_CNT	1024	501
F–I2C–RC–72.044	Cu–Ka	8.030	1018.72,305616	3000	10	–0	–0	–3.17	0	195	2C0	–	6	PH_CNT	1024	501
G–I2C–RC–72.044	Cu–Ka	8.030	1018.7211,305616	3000	10	0	0	–3.17	0	195	2C0	–	6	PH_CNT	1024	501
H–IAS–RC–1.005	Cu–Ka	8.030	69509,2.0853e+08	3000	1	0	0	0	0	200	S3	I3	3.3	PH_CNT	1024	910
H–IAS–RC–1.004	Fe–La	0.705	18461,5.538e+07	3000	1	0	0	0	0	200	S3	I3	3.3	PH_CNT	1024	910

continued on next page

continued from previous page

TRW_ID	source	energy	FP_Rate,Total_Cts	Int_time	mult	pitch	yaw	yoff	zoff	Defocus	Focal	HST	frametime	proc_mode	rows	frames
H–IAI–RC–8.002	HIREF–W	0.68877	88.8022,266407	3000	1	0	0	0	0	40	I	I3	3.3	PH_CNT	1024	910
H–IAS–RC–8.001	HIREF–W	0.68877	88.8022,266407	3000	1	0	0	0	0	40	S3	S3	3.3	PH_CNT	1024	910
F–I2C–RC–72.004	Mg–Ka	1.254	5299.79,1589937	3000	10	–0	–0	–3.17	0	195	2C0	–	6	PH_CNT	1024	501
G–I2C–RC–72.004	Mg–Ka	1.254	5299,1.589e+06	3000	10	0	0	–3.17	0	195	2C0	–	6	PH_CNT	1024	501
G–I2C–RC–72.046	Mo–La	2.293	2368.7061,710612	3000	10	0	0	–3.17	0	195	2C0	–	6	PH_CNT	1024	501
F–I2C–RC–72.022	Ni–La	0.852	42.22,12666	3000	10	–0	–0	–3.17	0	195	2C0	–	6	PH_CNT	1024	501
F–I2C–RC–72.008	O–Ka	0.5249	0,0	3000	10	–0	–0	–3.17	0	195	2C0	–	6	PH_CNT	1024	501
F–I2C–RC–72.042	O–Ka	0.5249	9969.84,2990952	3000	10	–0	–0	–3.17	0	195	2C0	–	6	PH_CNT	1024	501
F–I2C–RC–72.006	Si–Ka	1.739	149.44,44832	3000	10	–0	–0	–3.17	0	195	2C0	–	6	PH_CNT	1024	501
F–I2C–RC–72.016	Ti–Ka	4.51	432.76,129828	3000	10	–0	–0	–4.38	5.64	195	2C1	–	6	PH_CNT	1024	501

Table 4.11: Flight Contamination Monitor Tests

4.4.9 XRCF Calibration Data Management

Lab sub-assembly and XRCF calibration activities have produced Terabytes of data. Data from the XRCF and on-orbit data arrive in telemetry format and will be converted by the ASC into its standard archival format for archiving. Ancillary data from the XRCF environmental instrumentation and the test data from the HRMA X-ray Data System (HXDS) will also be archived by the ASC. They intend to archive both raw data and processed data.

At XRCF two parallel data paths were employed. Both ACIS-2C and the flight instrument had raw CCD pixel data available through a port called the High Speed Tap (HST). These data are similar to the sub-assembly calibration data, and form a direct check on the flight telemetry format data. The HST also offered a much higher bandwidth data path valuable during ground calibration. The HST will not be available during flight. All ACIS-2C data were collected through the HST, because the ACIS on-board processors were not present. HST data were collected and archived by the ACIS EGSE. Copies of the raw data were made on DLT tapes by the ACIS team, and one copy resides at PSU and one at MIT. An additional copy was made by Bruce Wyshak of the ASC, and the DLT tapes for this copy reside at the ASC. Standardly processed data were forwarded by the ACIS EGSE via ftp to a mirror site at the XRCF third floor data system. Copies of the processed data on DLT and DAT tape are also maintained at PSU and MIT.

The second data path was the normal flight telemetry, processed as science and engineering data packets and sent to the RCTUE. Data from the RCTUE were collected and archived by the MCC. Telemetry format data from the flight instrument were processed by the AQLC computer. These data have also been archived and supplied to the ASC.

4.5 Instrument Performance Models

Theoretical and measured spectral resolutions are shown in Figure 4.6. Different relations are shown for a range in system noise.

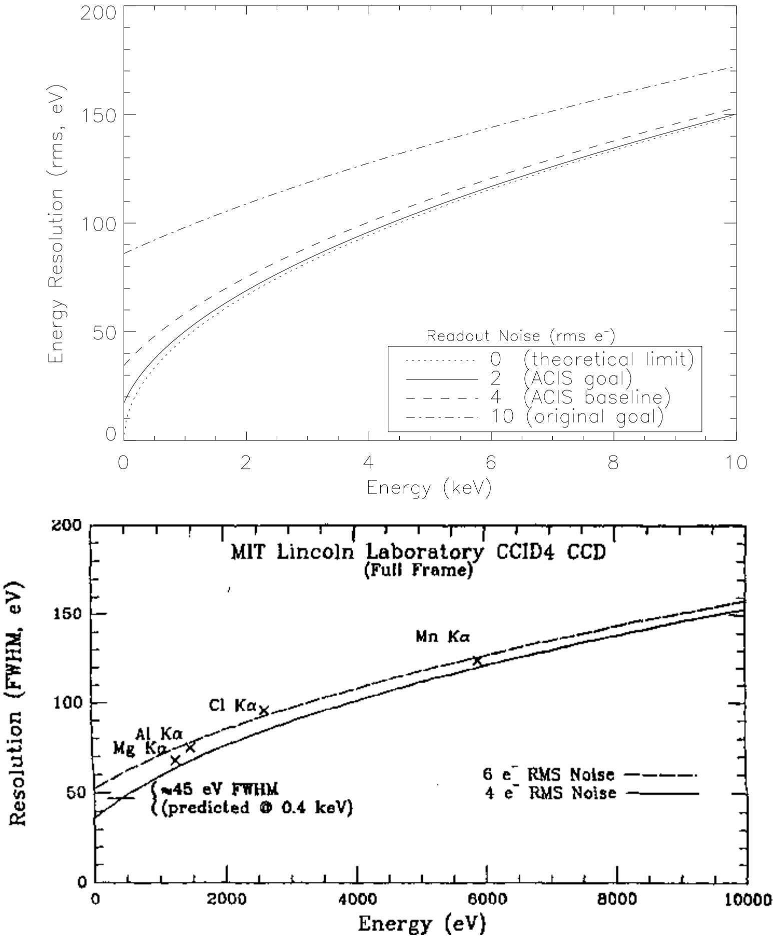

Figure 4.6: ACIS theoretical and measured spectral resolutions

The theoretical energy resolution for a single event entirely absorbed in one pixel is described by

$$\Delta E = 3.65\sqrt{8\ln 2}\sqrt{N^2 + FE/3.65}, \tag{4.3}$$

where ΔE is the FWHM of the detected peak, E is the energy, 3.65 is the energy in eV per electron released, N is the amplifier root-mean-square read noise in electrons, and F is the Fano factor.

Figure 4.7 shows minimum detectable equivalent widths, and Figure 4.8 shows model spectra. Energy resolution depends critically upon the efficiency of counting only single events (see Operating Principles [Section 2.3.1.1]), but also upon CTE, bias correction accuracy, and thermal stability.

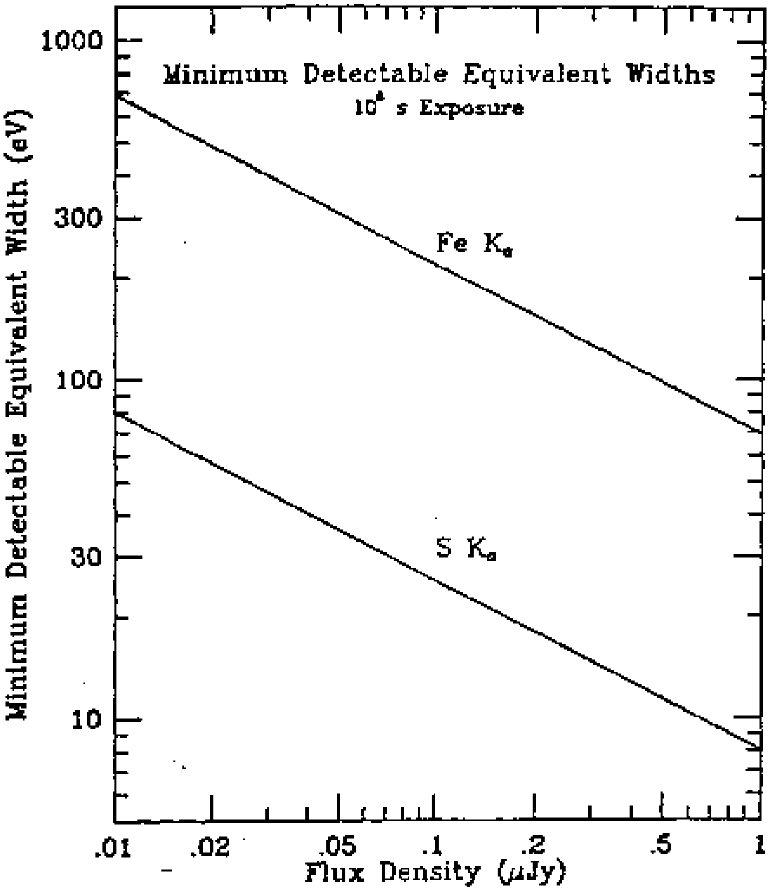

Figure 4.7: ACIS minimum detectable equivalent widths

Because of the many factors affecting instrument performance it will be necessary to provide individual response models for at least every CCD chip and possibly every CCD output node. In practical use these models will take the form of response matrices, compatible with commonly used X-ray analysis packages such as XSPEC and PROS. Unfortunately there is no simple analytic conversion to be able to transform empirical calibration data into response matrices. Instead we utilize a simulation based on physical parameters of the CCD devices, filters, HRMA and other relevant parts of AXAF, and compare the results

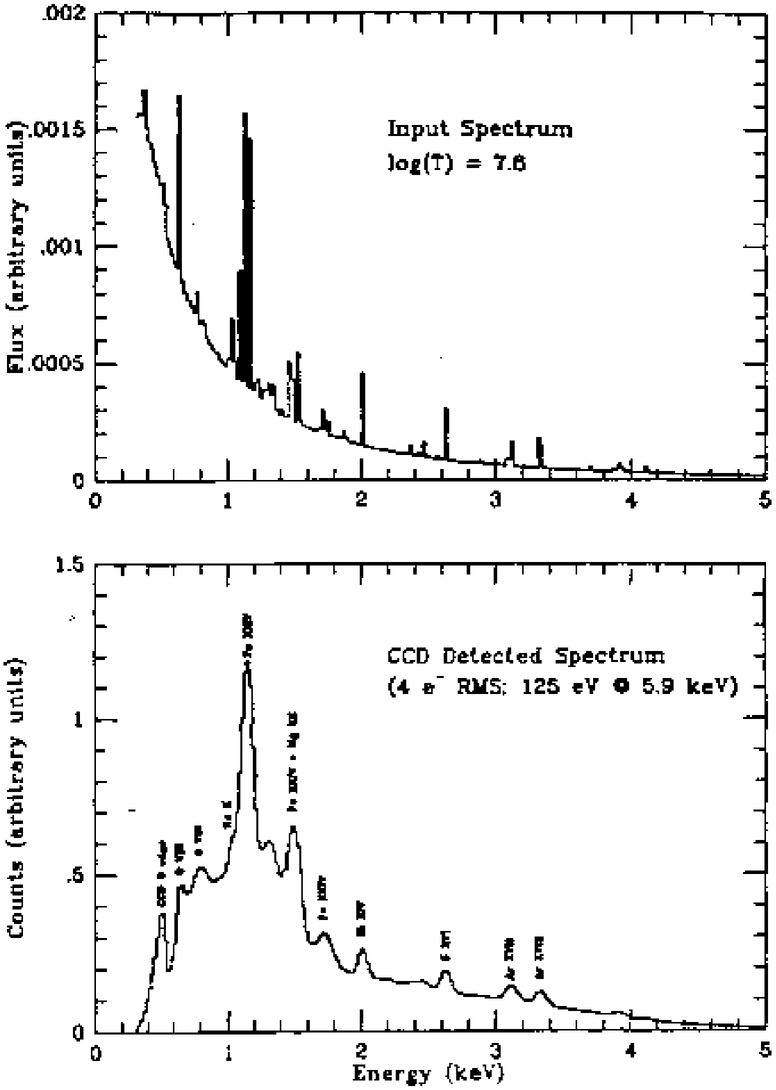

Figure 4.8: ACIS model spectra

of the simulation to the calibration measurements.

Once acceptable agreement is found between the simulation (after physical parameters have been adjusted to reasonable levels and the simulation reaches an acceptable level of detail), the simulation is used to generate response matrices and predictions of ACIS performance on scales or parameter values which are impossible to empirically measure. In the next section we describe this simulation tool.

4.5.1 CCD Interaction Simulation

The response of X-ray CCDs to photons and minimally-ionizing particles has been simulated by means of a Monte Carlo program. This algorithm draws on empirical results and predicts the response of three basic types of CCD devices: back-illuminated, epitaxial front-illuminated, and bulk front-illuminated. Each type of device is assumed to consist of a stack of slabs, each slab having different properties. The three types of CCDs are modeled by arranging these slabs in the appropriate order. The user specifies the device to be modeled by supplying the thickness of each layer.

In a back-illuminated device, the top layer is a damage or surface layer, in which liberated charge is not efficiently propagated and is largely lost to recombination. Photons which interact in this layer may only have about 20% of their charge propagated to the depletion layer. Below this damaged or "modified substrate" layer is a field-free layer, which acts as a reflecting layer and prevents charge from the depletion region from leaking out into the modified substrate and generating dark current. The surface and field-free layers sit on top of the depletion layer, which ends in the buried channel and gate structure at the bottom of the device.

An epitaxial front-illuminated device is similar to an inverted back-illuminated device. The top layer is the gate structure, modeled simply as a uniform slab of absorbing material (a "dead" layer). Beneath this is the depletion region, followed by a field-free region, then a substrate. The bulk front-illuminated device has the same dead layer on top of a depletion layer, but this is simply followed by a substrate.

In order to simulate X-ray photon detection by these devices, a random interaction depth and position on the CCD are generated for each simulated photon. The photon is allowed to interact with the device and produce a cloud of charge. This charge spreads through the layers of the device, with the spreading rate and the charge reflection and absorption dependent on the properties of each layer. Once the charge reaches the buried channel, it is "detected" by recording an appropriate number of electrons in each pixel over which the charge spread. The degree to which a given photon's charge cloud is split across pixels depends on the photon's energy, its interaction depth, and the proximity of the interaction to pixel boundaries.

The simulation accounts for the possibility of secondary fluorescent photon generation from the silicon, if the initial photon energy is high enough. Fluorescent photons from other elements in the device (such as oxygen) may occur, but with a lower probability, so they have not been included in the simulation at this time. As the charge cloud propagates through the device, some of the charge may recombine and be lost. This charge recombination has been estimated empirically and is included in the model.

The output of the simulation is a square CCD frame, with the size determined by the user. It is in units of electrons and contains photon events, readout and other noise, and minimally-ionizing particle events. These particle events were modeled similarly to photon events; the track of a particle through the detector is randomly generated, then simulated by allowing the detector to absorb energy from the particle every time it traverses one micron in depth through the device. The charge cloud generated at each interaction point is propagated just as photon charge clouds are propagated.

Figure 4.9: Example of a simulated back-illuminated CCD frame, containing 1000 1 keV photon events and 10 particle events

Figure 4.9 shows the output for a back-illuminated device with 1000 1 keV photon events and 10 particle events. Note that most of the photon events are spread among several pixels at this energy. For comparison, consider Figure 4.10, which also contains 1000 1 keV photon event and 10 particle events, but detected by a front-illuminated device. Most of

Figure 4.10: Example of a simulated front-illuminated CCD frame, containing 1000 1 keV photon events and 10 particle events

the photon events are contained in a single pixel. Note how much more the particle events have bloomed – this is a result of the thick substrate assumed for this device.

Radiation damage may also be included in the model, manifested by increased charge transfer inefficiency. This effect may have a power-law dependence with energy. The code allows the user to supply this power and the CTI.

The assumptions made in this X-ray CCD frame simulator limit its ability to reproduce actual CCD output. Several enhancements are possible. The complex geometry of the gate structure and the channel stops should be included, especially for front-illuminated devices where photons must pass through these top layers of the detector in order to be recognized.

The Fano factor (the conversion factor giving the number of eV's per electron) may be temperature and energy dependent. Once an empirical estimate of these dependencies is available, it should be incorporated into the algorithm. As mentioned above, other elements (besides silicon) present in the CCD can produce fluorescent photons. The most predominant two or three of these fluorescent lines should be included in the simulation (but note that the rates will be even lower than the 4% fluorescence rate for silicon). Currently only one dopant concentration is considered; it may be more realistic to allow different dopant concentrations for different device layers.

In spite of its limitations, the current incarnation of the frame simulator is useful for addressing timely issues in CCD characterization. The code has been used to develop an algorithm to determine sub-pixel positions of photons and to assess the problems associated with photon pile-up from bright uniform beams and bright point sources. It also should be useful in modeling flickering pixels and addressing the "sacrificial photon" problem in modeling the CTI.

The "sacrificial photon" problem occurs when the CTI is poor and a high incident flux of photons strikes the detector. The poor CTI results from traps removing electrons from the X-ray induced charge packet as it is clocked across the CCD. These traps have trapping times for electrons comparable to the row readout time. (If the trapping time were short compared to the pixel clocking time, then the trap would lose the electron and not affect the packet. If the trapping time were long, then the trap would stay filled and the CTI would disappear.)

If two photons strike the CCD row closely enough in time for the second packet to arrive before all the electrons from the first packet are re-emitted, then the trapping capacity is less for the second photon than the first (or sacrificial) photon which gave up the full charge.

The key point is that the observed charge may no longer be strictly linear with incident X-ray energy, but may have a rate dependent effect. The effects of sacrificial photons can be modeled by the full frame X-ray interaction simulator which we described, which can not be handled by any simulator which treats each X-ray interaction as independent.

4.5.2 Frontside vs. Backside CCD Performance

As previously mentioned, ACIS will employ CCDs in two fundamentally different operating configurations. Some devices will be used with the surface containing the gate structures facing the incident X-ray beam from the HRMA. This is the normal CCD operating configuration, and is called 'Frontside Illumination' (FI). Unfortunately the gate structures are required for electrical reasons to have a substantial thickness (∼4000 Å) which leads to a reduction in the low energy quantum efficiency of the device.

An alternative is to remove the substrate silicon from the back of the device, exposing

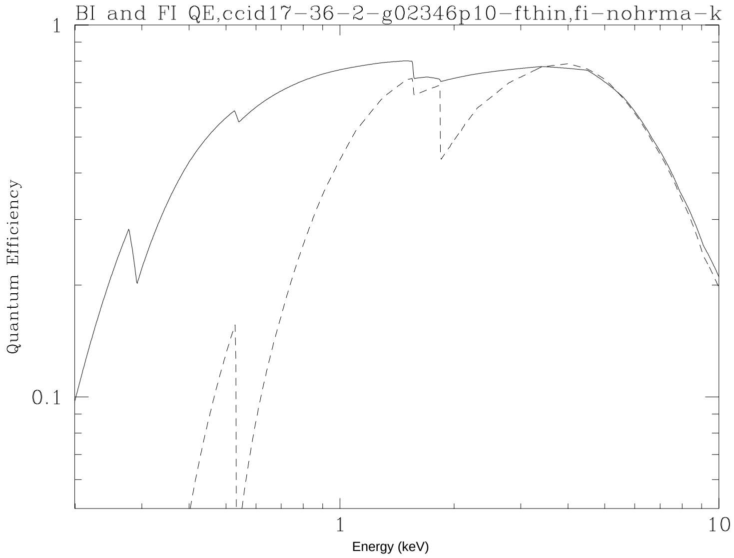

Figure 4.11: Quantum efficiency comparison between backside illuminated chip (solid line) and frontside illuminated chip (broken line)

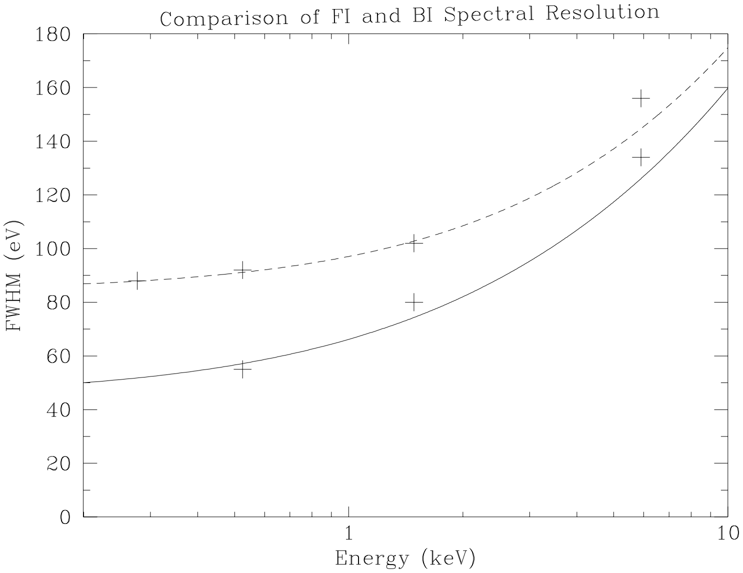

Figure 4.12: Measured and modeled FWHM of frontside illuminated CCDs (solid) and backside illuminated CCDs (broken)

the active sensing volume (the depletion layer) from the back side of the device. This configuration is called 'Backside Illumination' (BI). While BI chips have higher low energy quantum efficiency, they have somewhat lower total high energy quantum efficiency due to a lower thickness[1]. More importantly BI chips are harder to make, in that the additional processing required to make a BI chip from a potential FI parent has a loss associated with it, and lab measurements show that BI chips do not approach theoretical energy resolution as the FI chips do.

The advantages of the BI chips are particularly important for applications using the gratings, as the improved quantum efficiency at low energy is very important and the loss of energy resolution is less important because the CCD energy resolution is only used to separate orders, and not measure energy directly. Fig. 4.13 compares the quantum efficiency of BI and FI chips on a wavelength scale (which corresponds to linear spatial location along the grating dispersion direction).

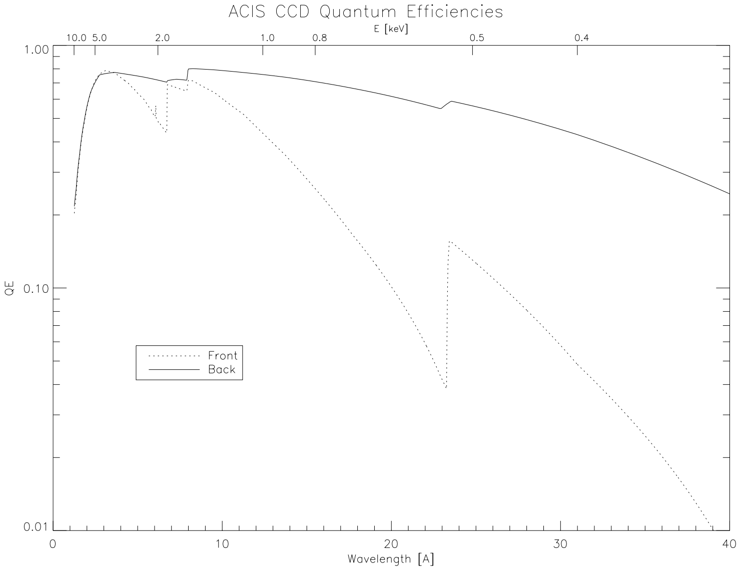

Figure 4.13: Quantum efficiency comparison between backside illuminated chip (solid line) and frontside illuminated chip (broken line)

---

[1] Data analysis choices can alter the relative quantum efficiency advantage of FI vs. BI chips. In particular low energy events in BI devices are nearly always split into more than one pixel, while the reverse is true in FI devices. Thus in routine analysis FI devices are processed using only single and singly split events, while BI devices are processed using doubly and triply split events as well. Fig. 4.11 compares quantum efficiency for these grade selections. The FI chips can be processed with the additional events as well, which would enhance the high energy quantum efficiency, at the price of degrading spectral resolution.

Fig. 4.14 shows the net effective area of ACIS-S when all CCDs are BI (broken line) and all CCDs are FI (solid line). The gain at energies below 1 keV is dramatic.

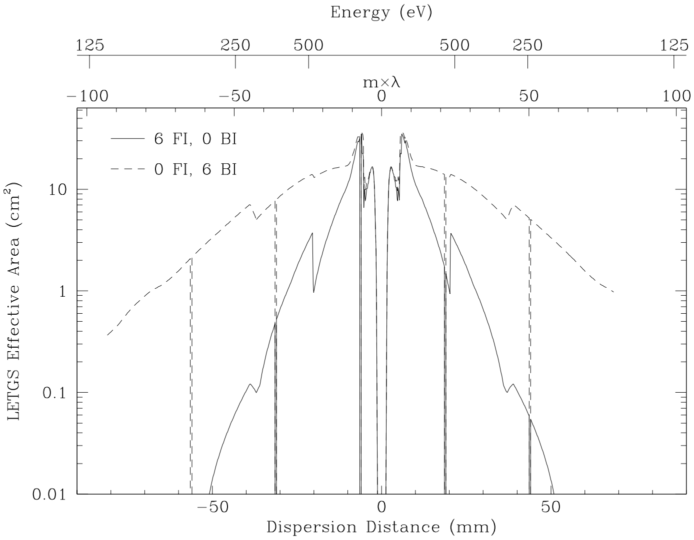

Figure 4.14: Effective area comparison for ACIS-S with backside illuminated chips (broken line) and frontside illuminated chips (solid line)

4.5.3 Sub-Pixel Position Reconstruction

The FWHM of the HRMA PSF was measured to be roughly 0.5 arc-sec, the same size as an ACIS pixel. In order to reconstruct the PSF and obtain source positions accurate to less than 0.5 arc-sec, we would like to locate individual photon interaction sites on a sub-pixel scale. We have explored this goal by using the intrinsically larger event splitting tendencies of back-illuminated (BI) CCDs at moderate (1 keV) X-ray energies.

An ACIS BI CCD was modeled using the frame simulator described above. We placed 4000 1 keV photons on a simulated ACIS BI 1024×1024 array, with the sub-pixel position fixed but the depth and array position random. This was done 121 times for 121 sub-pixel positions, mapping out a pixel in 0.1-pixel increments.

Each output image was run through an event-finding algorithm to generate a list of event energies and grades, and a histogram of the distribution of grades. Events are detected by considering a 3×3 pixel sub-array centered on a bright pixel. For clarity, the pixels in this sub-array are assigned numbers as given in the array below. Here, pixel number 4 is the brightest pixel in the sub-array.

6	7	8
3	4	5
0	1	2

Table 4.12: Pixel numbering for grade sub-arrays

The grades used are defined in Table 4.13, which refers to the pixels by the numbers given above. The cryptic grades S+, P+, and Other are equivalent to the ASCA grades of the same name and refer to the few unusual events that contain diagonal pixels or don't fit into any of the other shape categories.

event type	*constituent pixels*	*grade*	*probability maximum*
single	4	0	(0,0)
S+	4 + others	1	—
up vertical	4,7	2	(0,0.4)
down vertical	1,4	3	(0,-0.4)
left horizontal	3,4	4	(-0.4,0)
right horizontal	4,5	5	(0.4,0)
P+	4 + others	6	—
down left L	1,3,4	7	(-0.3,-0.3)
down right L	1,4,5	8	(0.3,-0.3)
up left L	3,4,7	9	(-0.3,0.3)
up right L	4,5,7	10	(0.3,0.3)
down left quad	0,1,3,4	11	(-0.4,-0.4)
down right quad	1,2,4,5	12	(0.4,-0.4)
up left quad	3,4,6,7	13	(-0.4,0.4)
up right quad	4,5,7,8	14	(0.4,0.4)
Other	4 + others	15	—

Table 4.13: Grade definitions and sub-pixel positions of probability maxima

Dividing the grade distribution histogram by the total number of detected events then gives a fractional grade distribution. One of these was generated for each sub-pixel position. Of the 16 possible grades, all but S+, P+, and Other are useful in determining event positions. These three grades were not used because there were too few events in each grade to yield a meaningful event position probability distribution (see below). Trimming these left a 13-element vector of fractional grade distribution. The normalization occurred before these grades were removed. The event-finding algorithm used an event detection threshold of 50 electrons and a split-event threshold of 20 electrons – these thresholds do affect the splitting.

We can assemble all the 13-element vectors for each sub-pixel position into a 13-plane-deep 3-D array, each plane representing the fractional grade distribution of a given grade across the pixel. Examples of these planes are given in Figures 4.15 and 4.16. The peaks of the distributions are marked in the figures and given in Table 4.13 for each plane. We can treat these planes as probability distributions for each grade, showing the likelihood that a photon impinging at a certain sub-pixel position will yield an event of the shape (grade) being considered.

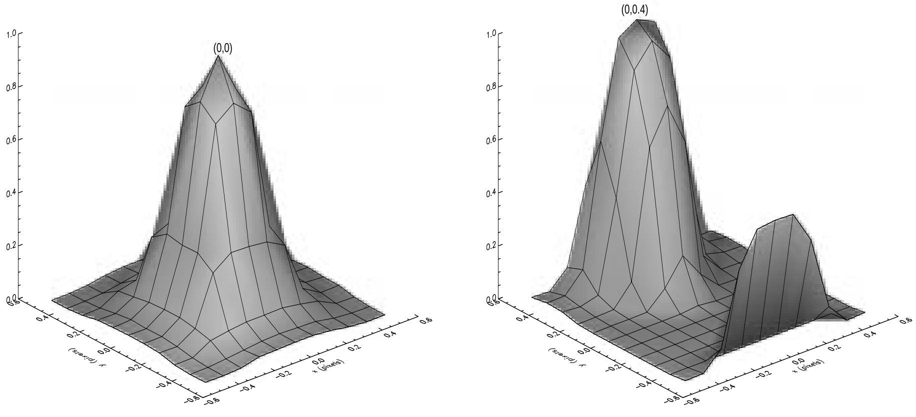

Figure 4.15: Single-pixel event position probability distribution on left; Two-pixel event position probability distribution on right.

Note the bi-modality in these distributions – the upwards single-split distribution shown in Figure 4.15 (right side), for example. Some events that occurred near the *lower* edge of the pixel were detected as *up* splits – this is because enough of the charge clouds from these events were detected in the adjacent (lower) pixel that they were detected as upward splits. This illustrates the fact that we cannot *know* in which pixel the event really occurred, we can only *assume* that it occurred in the brightest pixel, and this assumption is not always right. Note also that, by replicating these single-pixel distributions for adjacent pixels, a consistent probability distribution appears, shaped similarly to the single-pixel distribution but centered on different sub-pixel coordinates ((0.3,-0.3) for the L-shaped events shown in Figure 4.16, instead of (0,0) for the single-pixel events) and having somewhat different widths. This implies that, if we are given an event's grade, we have a distribution showing the likelihood that the event came from a certain sub-pixel position.

Returning to the simulations, we deposited 4000 photons at the same sub-pixel position

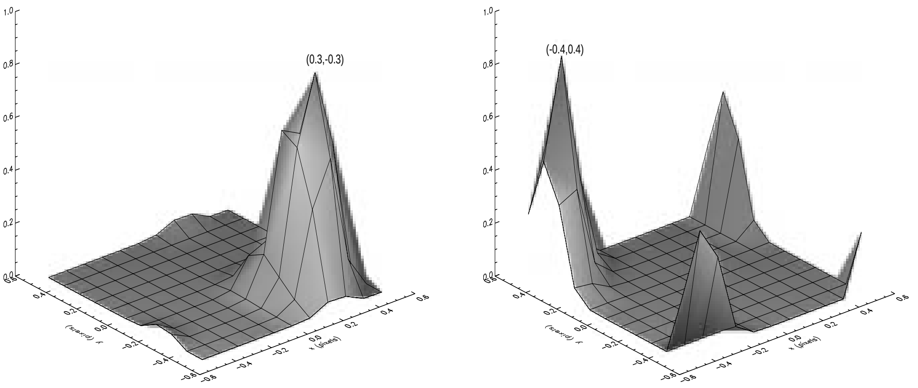

Figure 4.16: Three-pixel (L-shaped) event position probability distribution on left; Four-pixel (square-shaped) event position probability distribution on right.

and came up with a distribution of grades. We want to use that distribution of grades to estimate the position of this ensemble of events. We have probability distributions of positions for each event, but how do we combine these to yield the best-estimate position for the ensemble?

As an initial step, we chose the simplest conceivable mapping. We assumed that a given grade came from a photon which interacted at the most likely sub-pixel position for that grade, i.e. wherever the peak is in the plots mentioned above. The sub-pixel coordinates of the peak are given as the third column of Table 4.13. Then we just averaged these positions to get the most likely sub-pixel position for the ensemble.

We computed ensemble position estimates as above for each sub-pixel position. Then to test the accuracy of the method, we generated a "distortion map" by subtracting the true position from the estimated position (separately for x and y), then computing a radial distortion. Figure 4.17 shows the distortion map for the lower left pixel quadrant. This map is intended to illustrate the degree to which this simple algorithm is able to recover positions. Note that there are regions on the pixel where the algorithm works well, and regions where it does not. This leads to ambiguities in a photon's true sub-pixel position and indicates that this algorithm provides accurate sub-pixel positioning to about 1/16 pixel.

A more relevant test of the algorithm is the degree to which it can recover an accurate sub-pixel position of a point source smeared by a PSF. To simulate this, we generated photons with a two-dimensional Gaussian distribution about some pre-determined sub-

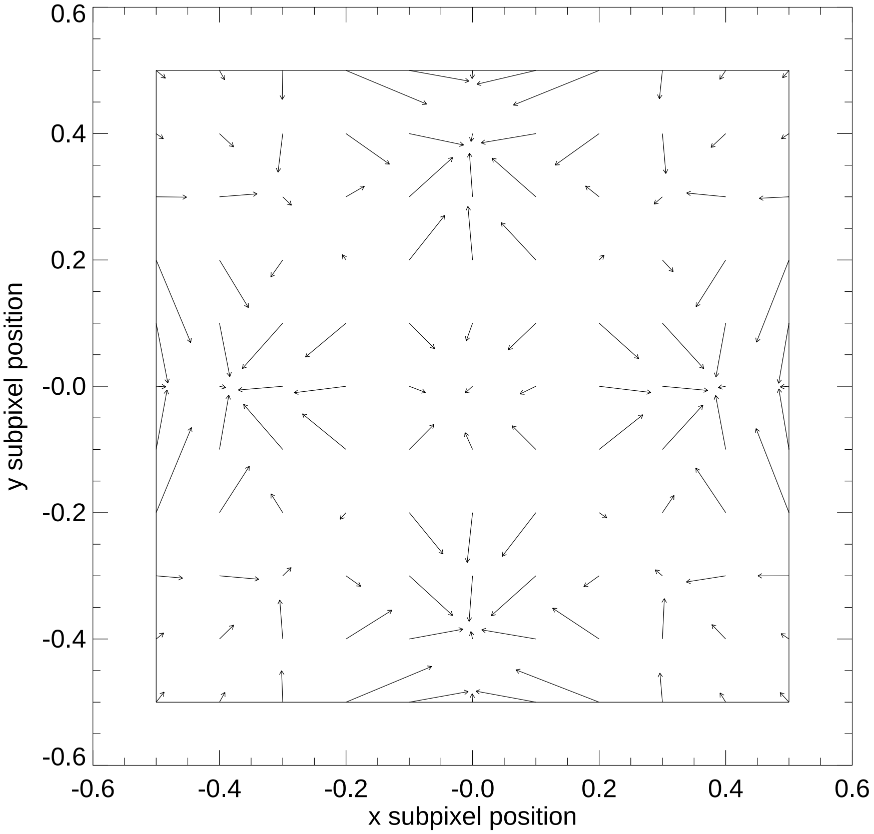

Figure 4.17: Radial distortion map for one quadrant of a pixel, showing the difference between the true (base of arrow) and reconstructed (head of arrow) positions for 36 sample positions in a pixel.

pixel position. We deposited these photons on simulated CCD frames one at a time, then simulated frame readout and event detection and grading. This rate of one photon per source per frame is consistent with the readout rate expected for modest sources with AXAF. Using each event's grade as above, and ignoring events with grades S+, P+, and Other, we assigned to the event a sub-pixel position (the most likely position for that grade). Once we had accumulated an ensemble of events, we computed the simple average and standard deviation for the x and y positions separately and compared these estimates of the source's position and the PSF widths to the input values. We also made these estimates using only integer pixel positions for each photon and using the true sub-pixel positions for each photon, for comparison. Since the positions and PSF widths obtained from the true sub-pixel positions of the photons are the best estimates we can make given the finite sample size, the fairest comparison is between these results and those for the two algorithms in question, not between the input values and the results for the two algorithms. The results are summarized in Table 4.14. Note that some source positions were deliberately located at sub-pixel positions that suffered large distortions in the earlier tests (see Figure 4.17).

Energy (eV)	# of photons	True PSF				Estimate Using Integer Pixel Pos.				Estimate Using Mapped Sub-pixel Pos.				Estimate Using Real Photon Pos.			
		x	y	σ_x	σ_y	x	y	σ_x	σ_y	x	y	σ_x	σ_y	x	y	σ_x	σ_y
1000	3000	5.30	5.00	0.85	0.85	5.30	5.00	0.90	0.89	5.30	5.00	0.85	0.86	5.30	5.00	0.85	0.85
1000	3000	5.38	5.35	0.85	0.85	5.37	5.34	0.90	0.89	5.37	5.34	0.85	0.85	5.37	5.34	0.84	0.85
1000	3000	5.20	5.50	0.85	0.85	5.18	5.48	0.90	0.91	5.18	5.49	0.85	0.87	5.18	5.49	0.84	0.86
1000	500	5.20	5.50	0.85	0.85	5.21	5.51	0.89	0.90	5.20	5.52	0.84	0.87	5.20	5.52	0.83	0.86
1000	100	5.20	5.50	0.85	0.85	5.31	5.45	0.94	0.83	5.25	5.51	0.86	0.80	5.25	5.50	0.88	0.80
1000	1000	5.05	5.35	0.85	0.85	5.03	5.30	0.88	0.90	5.07	5.30	0.84	0.86	5.06	5.30	0.84	0.86
500	1000	5.05	5.35	0.85	0.85	4.96	5.31	1.02	1.03	4.97	5.30	1.00	1.01	5.02	5.37	0.85	0.85
5000	1000	5.05	5.35	0.85	0.85	5.08	5.33	0.91	0.89	5.10	5.34	0.88	0.86	5.09	5.34	0.86	0.85
1000	1000	5.03	5.35	0.10	0.10	5.18	5.50	0.47	0.00	5.05	5.38	0.13	0.16	5.05	5.38	0.10	0.10
5000	1000	5.03	5.35	0.10	0.10	5.18	5.50	0.47	0.00	5.04	5.30	0.12	0.18	5.05	5.35	0.10	0.10
1000	1000	5.05	5.35	0.40	0.40	5.07	5.36	0.51	0.49	5.07	5.35	0.40	0.42	5.07	5.35	0.40	0.41
1000	20	5.05	5.35	0.40	0.40	5.00	5.45	0.51	0.51	5.02	5.48	0.42	0.40	5.08	5.43	0.37	0.40
1000	5	5.05	5.35	0.40	0.40	5.30	5.50	0.45	0.71	5.30	5.42	0.35	0.48	5.27	5.35	0.30	0.47

Table 4.14: Results of sub-pixel position testing using a PSF-convolved point source

These results confirm that the sub-pixel position mapping algorithm described above does a better job of recovering the source position than integer pixel positioning, when the PSF is small compared to the pixel size. Not surprisingly, the algorithms converge when the PSF is comparable to the pixel size (as we approach critical sampling). The results of the grade-based algorithm are affected by energy since the splitting is affected by energy – as fewer events are split, the sub-pixel position mapping algorithm collapses to integer pixel positioning. Sub-pixel position mapping appears to perform marginally better than integer pixel positioning for small numbers of photons.

4.5.4 Radiation Damage Modeling

Radiation damage in flight is expected to degrade the CTI performance of the CCD chips with time. Fig. 4.18-4.20 illustrate the predicted effect on a simulated astronomical spectrum with emission lines. The radiation damage estimate is based on a 95% worst case limit over five years, on data for a radiation model done by SAIC for NASA Headquarters. Fig. 4.18 shows an undamaged chip. The next two cases show the predicted spectrum for shields of 8 cm and 4 cm thicknesses.

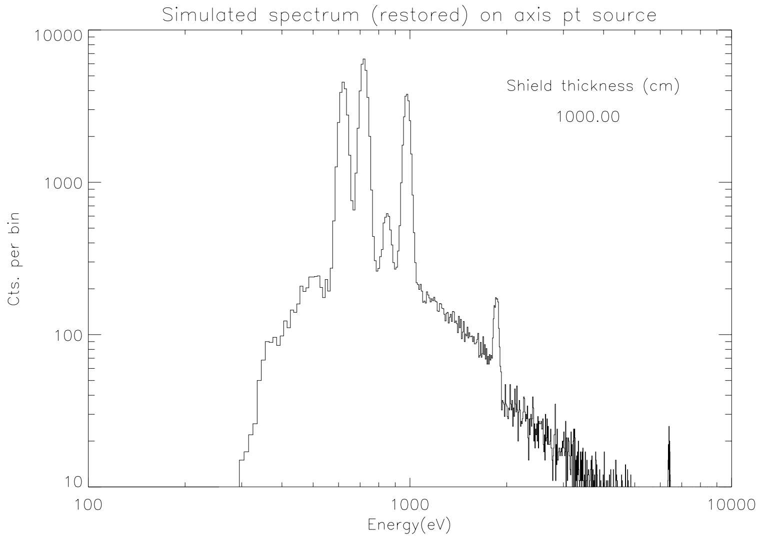

Figure 4.18: Astrophysical spectrum predicted without radiation damage

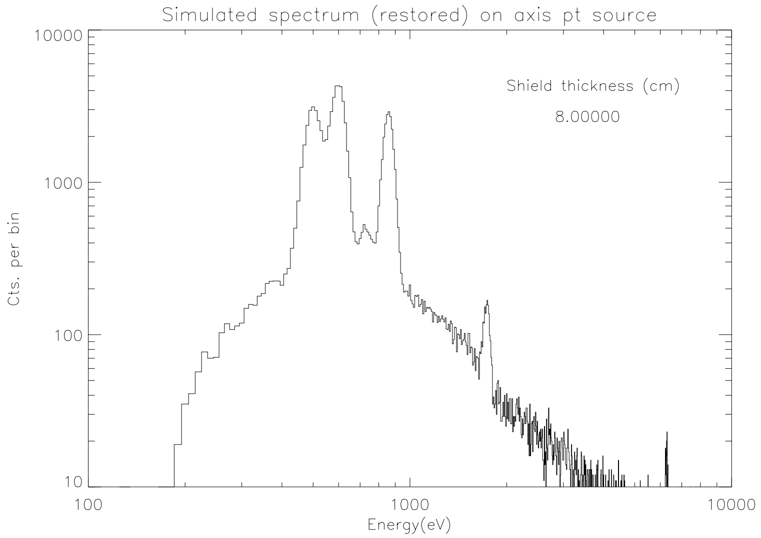

Figure 4.19: Astrophysical spectrum predicted with 8 cm of Al shielding thickness

4.6 Flight Calibration/Maintenance

Calibration on celestial sources is necessary because the XRCF cannot effectively simulate a point-source at infinity. The XRCF results must be interpreted through a model accounting

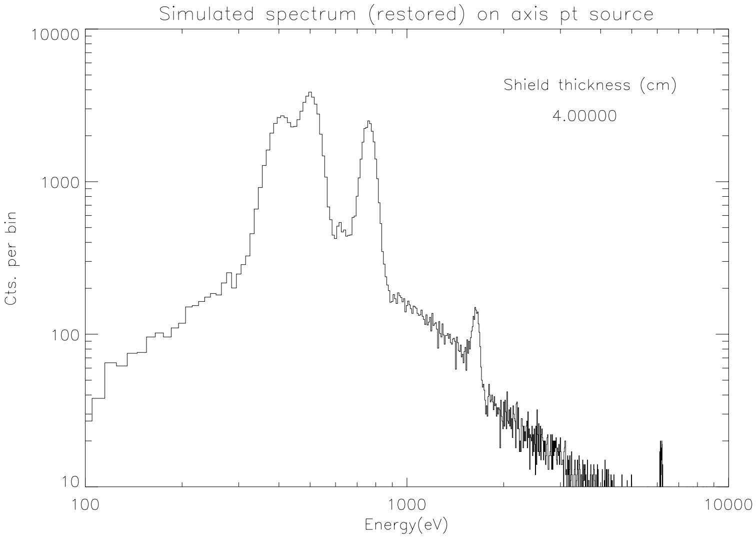

Figure 4.20: Astrophysical spectrum predicted with 4 cm of Al shielding thickness

for the decreased effective area and other effects of a finite source distance.

A subset of the ground tests will serve to link them to the pre-flight status of the instrument. The celestial tests will also determine the stability of ACIS through launch, and provide a baseline for trend analysis, anticipating possible degradation of CCDs due to particle radiation or contamination. There will be a multi-energy calibration X-ray source on board used to monitor CTE change and check the level of the chip surface contamination, which can affect the low-energy response.

4.6.1 Orbital Verification Activities

Immediately following orbital insertion AXAF will be turned on (in the sense of activating the spacecraft and science instrument systems), and will be tested to verify that it functions properly. This period is called the Orbital Verification Phase. Planning between the ASC, the spacecraft contractors and the instrument teams is currently underway to assure that the instrument is safely and efficiently brought into full operational status.

The Orbital Verification (OV) phase is very important to instrument calibration. It provides the earliest opportunity to determine the in-orbit performance of the instrument, telescope and gratings. As such, it is a crucial part of the later trend analyses, and it is very important to ensure that all the needed baseline measurements get carried out during OV.

The purpose of orbital verification is to demonstrate the overall scientific performance of

AXAF. This activity involves several aspects. We must verify science instrument operation, the ability to acquire celestial targets, the ability to position the specified science instrument at HRMA focus, the ability to acquire images and spectra, and we must determine focus and boresight.

4.6.1.1 OV Phase Constraints

There are a few constraints imposed on the activities, some of which have schedule impact. The observatory will be operated only in the expected on-orbit configuration: this means for example that systems will be powered from only the primary side, systems will not be intentionally driven to operational temperature extremes, and we expect the telemetry to be in a "science" format a majority of the time. Many of the planned activities require the telescope sunshade door to be open which limits activities prior to this event to verifying FPSI operation. Most significant among these limitations is that the science instrument module must not be translated prior to opening the sunshade door and the objective transmission grating (OTG) insert and retract mechanism must not be operated until the time of OTG verification.

The sequence of science instrument tests at the focus of the telescope is:

- ACIS-S
- ACIS-I
- ACIS-S/HETG
- HRC-I
- HRC-S
- HRC-S/LETG

In addition to operating the instruments other aspects of AXAF operations will be tested during OV. The observatory must achieve thermal stability, have its celestial location determined, be able to acquire aspect stars, and establish pointing control. We must be able to reconstruct images based on data from the science instruments and from the PCAD system. In order to operate independently, the observatory must demonstrate the ability to execute stored command loads autonomously. We must also be able to retrieve on-board recorded telemetry.

4.6.2 Science Instrument OV Phase Activities

The schedule of activities is constrained by when it is safe to perform some tasks and by time order dependencies between tasks. Many of the verification tasks require the instruments to image the sky, which in turn requires the telescope sunshade door to be open. The sunshade door cannot be opened until the ACIS camera housing door is opened and the forward contamination monitor sources are measured. The ACIS door cannot be opened until the OBA has sufficiently out-gassed and vented overboard. Thus the opening of the ACIS door provides a natural breakpoint in the schedule of activities. In what follows we will refer to the period before the opening of the ACIS door as Period 1 and that after the door is opened as Period 2.

4.6.2.1 ACIS Period 1 Activities

The period 1 ACIS activities include the initialization of the instrument, the verification of expected operating conditions, and the verification of the basic functions of the instrument. (Note that immediately after the IUS (Inertia Upper Stage: the final stage rocket motor attached to AXAF for orbital insertion) burn is completed, that valves will be opened to allow the outgassing process to start.)

The first set of activities will perform the hardware (HW) and software (SW) initializations. The very first command which must be sent to ACIS will turn on the instrument's power supplies. The Back End Processor (BEP) must then be turned on after a stable operating condition of the power supplies has been achieved. Many of the activities to be performed with ACIS will be executed by the flight SW running on the BEPs and FEPs; therefore the BEP and FEPs must be turned on before preceding with the initialization. After turn on, the BEP will be commanded to dump the flight SW to telemetry. We will verify from the outset that the flight SW has not been corrupted. The BEP will then run through a series of checks of its internal memory and its interfaces. The FEPs should be turned on during this stage. We will then establish the capability to send commands to the BEP and verify their execution.

The next stage of activities will verify the expected operating conditions of the instrument. ACIS has several temperature monitors located on the electronics boxes, the radiators, the camera housing, and the focal plane, and one pressure monitor inside the camera housing. The sequence of events will be to simply turn on the monitors and immediately start to read them out. We will then use the temperature information to confirm our preflight thermal models.

The HW and SW initialization and the verification of the physical conditions must occur as soon as possible. There may be a delay before the next stage of activities which is the CCD initialization. The first step in this stage is to apply power to the CCD analog electronics and immediately start to clock out the CCDs. The CCDs will start to produce data which must be processed by the FEPs and BEP and sent to telemetry. The first data will be produced in “diagnostic mode” which produces the most useful information for identifying problems. If everything is working, we will configure the CCDs in the timed exposure mode and start collecting data. An important test at the beginning of this data collection will be the bias computation. The events produced by the internal calibration source will provide useful diagnostic data on the state of the CCDs (specifically, has any contamination built up) but the event rate is low enough so as to not adversely effect the bias calculation. After executing in timed-exposure mode, we will load another one of the ACIS onboard parameter blocks and operate in that configuration. We will then load a parameter block from the ground and operate in that configuration. It is crucial to verify both methods of loading parameter blocks because both will be heavily used during normal operations.

The next stage is the detailed checkout of the CCD operations. The ACIS flight software will monitor the signal from the EPHIN detector and turn off power to the CCDs (by powering down the DEAs and FEPs, but not the BEPs) when the signal indicates a high radiation environment. The flight software continues to monitor the radiation signal and after a programmable number of low signals, it will turn the CCD power back on. We will verify this performance by manually setting the radiation signal high and then low and observing the flight software’s response. The detailed checkout will also include bias measurements made with different exposure times; these data are particularly useful in characterizing the CCDs’ performance. Finally, the detailed checkout will include data collected in timed exposure mode and continuous clocking mode with several configurations to verify the capability to collect useful data in these modes; these data will also be useful in characterizing the CCDs’ performance. These measurements will be conducted as normal operations commanded through parameter blocks.

The last activity of the period 1 ACIS activities is the opening of the vent valve. This is the only activity which we believe could potentially cause irreparable damage to the instrument if not executed properly. See the Functional Test Procedure for proper precautions and sequences which need to be observed to safely open the door. Key elements to this procedure include opening the low conductance valve and waiting for at least three hours to allow accumulated gas to vent prior to opening the large (hot-wax) valve.

4.6.2.2 ACIS Period 2 Activities

The period 2 ACIS activities will include some of the most dramatic in the OV phase, such as opening the ACIS door, opening the aft and forward contamination covers on the HRMA, opening the HRMA sunshade door and conducting the first astronomical observation with

AXAF.

The first activity is the opening of the ACIS door. Unfortunately, a great deal of uncertainty currently exists concerning when it is safe to open the ACIS door. The problem is that no one on the project can accurately predict the out-gassing rates of the OBA. Since ACIS is the coldest surface on the satellite (filter ≈ -60 C and CCDs ≈ -120 C), most of the contaminants will eventually freeze out on ACIS. Therefore, it is crucial that the ACIS door not be opened until the OBA has out-gassed to an acceptable level. Currently, 25 days has been proposed as the length of time required; however, this is not even an estimate, merely a number chosen on past experience and it may have little bearing on reality. Before opening the ACIS door, the ACIS internal pressure monitor and the SIM pressure monitor will be checked. If the values are significantly different, it will be necessary to wait longer. If they are the same, it may be safe to open the door but it is not guaranteed. The launch-lock position is on the ACIS-S array; therefore ACIS will be configured to collect data with the central 2 chips of the ACIS-S array and the 4 chips of the ACIS-I array. It is not clear at this time if the ACIS door should be opened first or if the HRMA aft contamination cover (ACC) should be opened first. It is possible that there will be some residual out-gassing after the ACC is opened; in this case the ACC will be opened first and some time will be allowed for this material to vent overboard. If not, the ACIS door will be opened and data will be collected on the internal background of the satellite. The ACIS door should be opened during a real-time contact since it uses a paraffin actuator which may be monitored during the process. After the ACIS door is opened, data will be collected from the Forward Contamination Monitor (FCM) sources. These data will be used to determine if a contamination layer had built up on the HRMA. The data will be collected in the ACIS timed-exposure mode which will be commanded by an on-board parameter block.

At this point, it is time to open the HRMA sunshade and collect first light with AXAF. AXAF should be positioned on the first target and the sunshade opened. ACIS will be collecting data as the door is opened and we should verify in real-time that operation has executed normally. We will use the ACIS data to verify that the door has opened completely and is not obstructing the optical path. We will also collect bias and diagnostic data to measure any increases in the background rate. Multiple observations will be conducted to find the boresight of the ACIS-S array and the ACA, this will entail changing the pointing direction many times. Multiple observations will be conducted to find the best focus of the ACIS-S array, this will entail moving the focal plane along the optical axis many times. Finally, the plate scale of the ACIS-S array will be measured in two ways. First, a point source will be moved across the field of view by changing the pointing direction and second, an observation with several objects separated by known (but small) distances will be conducted. These observations should all be conducted with normal operating modes commanded through ACIS parameter blocks.

The SIM will be moved in the Z direction for the first time in the next stage. We will first move the SIM in small steps to keep the HRMA aimpoint on the ACIS-S array. If the operations have been successfully executed and verified, we will then move the SIM so that the HRMA aimpoint falls on the ACIS-I array. We can them move the aimpoint around on the ACIS-I array and further verify the SIM performance. We will then find the boresight, focus and plate scale of the ACIS-I array using the same procedures above. All of these operations will be conducted with ACIS in a normal operating configuration.

The last activity involves inserting the High Energy Transmission Gratings (HETG) and collecting data. The SIM must be translated to place the HRMA aimpoint on the ACIS-S array. The HETG will then be inserted as ACIS is collecting data. We will collect data from several targets to verify the ability to center a target for the gratings and to verify the focus of the ACIS-S array at its outer extremes. After these operations are completed the HETG will be moved out of the way.

Finally, ACIS will be moved to the stow position. The time in the stow position is extremely useful for ACIS because there will be three X-ray calibration sources which will be used for the most detailed performance check of the CCDs. These sources will always be on and ACIS will always see them when in the stow position. ACIS will require the full 24 kbps for some of this time. ACIS will run in a normal operating mode when collecting these data.

4.6.2.3 Grating Activities

Grating verification activities cannot begin until Period 2 and each grating insert and retract mechanism must not be operated until the start of their respective grating verification. We do not anticipate the operational verification of the grating insert and retract mechanism to be more than a single insert and retract; this can be done as part of the grating verification. The HETG verification will be performed only with the ACIS-S; likewise, the LETG verification will only be performed with the HRC-S. Grating verification will consist of observing celestial targets and analyzing the data from the FPSI for the expected performance.

4.6.3 Orbital Bakeout Procedures

The ACIS focal plane and OBFs will probably be subject to non-volatile residual contamination while on-orbit. In order to mediate the detrimental effects of the buildup of these contaminants on the instrument's performance, a bakeout mode has been implemented. This involves elevating the temperature of those optical surfaces, by use of heaters on the focal plane and detector housing, and holding them at the elevated temperature for a time adequate to boil off the contaminants. The elevated temperature of the focal plane will be

+30 C, the entire bakeout cycle will take approximately two days, and it will have to be executed as frequently as deemed necessary to prevent buildup on the OBFs from degrading system performance beyond acceptable levels. Valid science data from the focal plane will not be available during bakeout and a calibration cycle will be needed at the end of the bakeout, but ACIS must be left at the focal plane location to allow a vent path for the evaporating contaminants. The composition of these contaminants has not been defined to date; the bakeout frequency assumes that the contaminants will be vented somehow during the bakeout cycle and will not immediately re-deposit themselves on the OBF surfaces, although no venting analysis has been done to trace the path of the contaminants during bakeout.

Chapter 5

Ground Processing

5.1 Ground Telemetry Processing

5.1.1 Introduction

During periods of contact between AXAF and the ground, data are telemetered to the Operations Control Center via NASA's Deep Space Network. Two distinct channels of data are sent simultaneously. One channel carries the real-time telemetry that is produced while the contact is ongoing. A second channel carries telemetry that was previously recorded onboard the satellite.

The OCC merges playback and real-time telemetry into a single, time-ordered stream which is known as Merged Telemetry. The OCC also performs operations to detect and correct (when possible) errors that were introduced by the communications channel from the satellite. The Merged Telemetry is then sent to the AXAF Science Center (ASC).

The ASC archives the telemetry and processes it to recover data from the science instruments. The ACIS science data are organized and formatted into a wide variety of data products for distribution to the scientific community and are also used in a number of calibration and operations activities within the ASC.

5.1.2 Telemetry Format

On board the ACIS experiment, a fundamental unit of data is the *science run*, which is a set of data obtained while ACIS has a fixed configuration. The design of the system for communicating science data from ACIS to the ground is organized around the science run concept. For example, changes in the configuration of ACIS are explicitly represented in the telemetry stream by the end of one science run and the beginning of another.

While transmitting science run data, the ACIS telemetry system must also transmit other sorts of data such as calibration data, command echoes, and software housekeeping information. This heterogeneous set of information is sent in an interleaved fashion using a packetized transport protocol similar to that used in computer networks. The boundaries between ACIS packets are represented by placing an ID word in the packet header at the beginning of each packet. Each packet can have a different length, which is also included in the packet header.

The packet stream produced by the ACIS computer is passed on to the satellite computer for transmission to the ground. When ACIS is in the focal plane, the ACIS packet stream is commutated into the science data fields in the AXAF major frame (see Section 2.4.4).

On the ground, the commutation and packetization steps must be inverted in order to recover each of the data streams produced by ACIS (science run data, calibration data, command logs, software housekeeping, etc.). Figure 5.1 shows a cartoon that summarizes the ACIS telemetry composition (on the satellite) and decomposition (on the ground) steps. In this simplified example, a Timed Exposure Faint Mode science run detects 9000 X-ray events. These data are formatted into three packets by the ACIS computer. These three packets are commutated into portions of two AXAF major frames by the AXAF computer. On the ground (at the ASC), a decommutation step recovers the ACIS packet stream and a de-packetization step recovers the actual science run data.

5.1.3 Level 0 Data Products

On the ground, the ASC performs a decommutation step to produce separate data streams for ACIS science data, for HRC science data, and for each of the many engineering signals that are commutated into the major frame. After this decommutation step, the ACIS science data stream is a simple byte stream since individual packets and the boundaries of science runs are not yet identified.

The ASC then performs a processing step which identifies packets in the science data stream, groups packets, and extracts data from packets in order to recover each of the data streams produced by ACIS (science run data, calibration data, command logs, software housekeeping, etc.).

These activities are known as Level 0 processing and result in Level 0 data products. Since science runs execute in one of several possible modes, Level 0 data products have formats specific to the mode of the science run. For example, a Timed Exposure Raw Mode science run produces Level 0 products that contain raw pixel data (images). A Timed Exposure Faint Mode science run produces Level 0 products that contain lists of X-ray events.

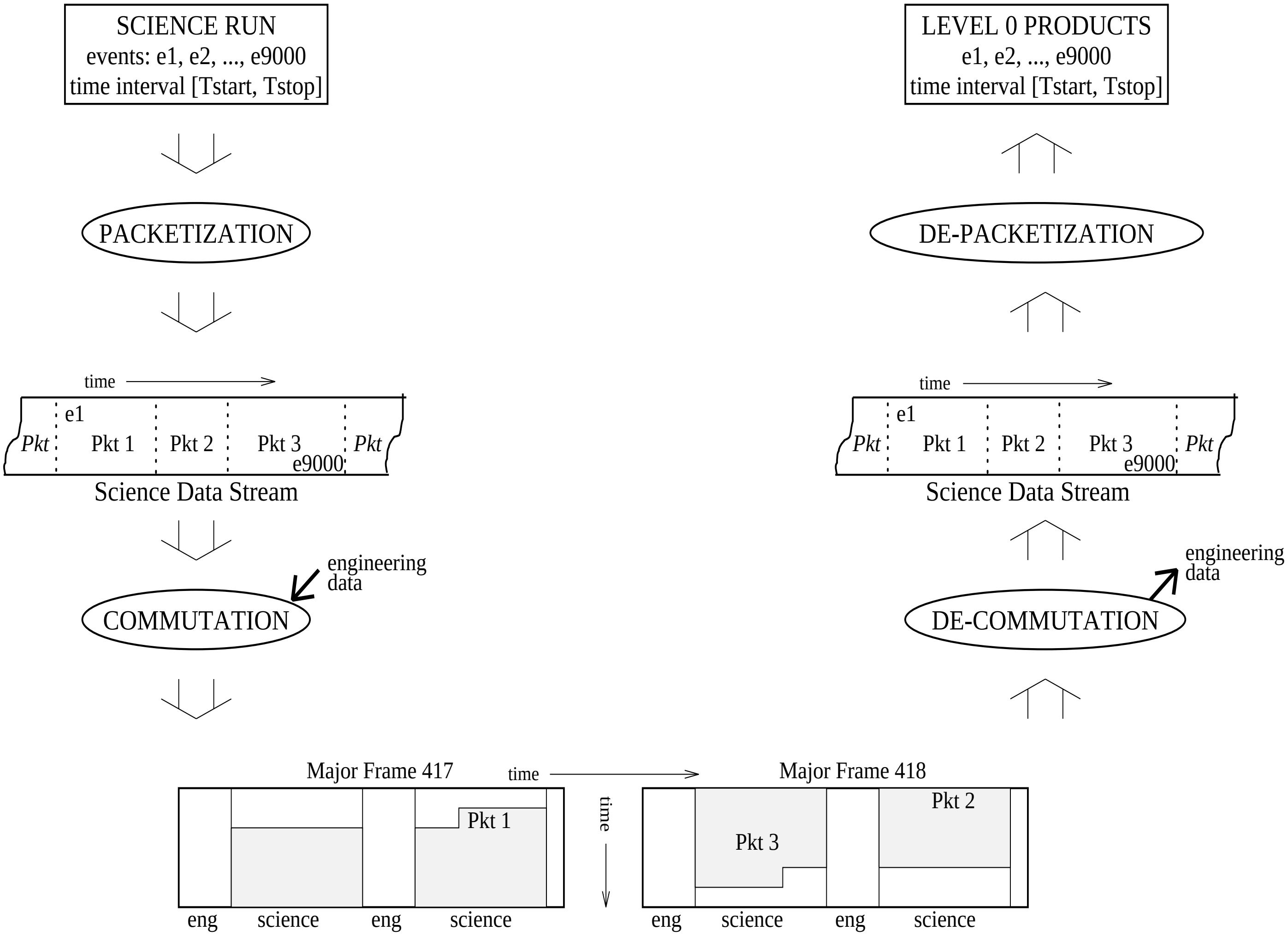

Figure 5.1: Telemetry Processing

Again as noted in the discussion of operations the event data telemetered to the ground are generally raw pixel data. The appropriate bias must be subtracted on the ground, requiring that the bias be available on an event-by-event basis (in Timed Exposure with Bias mode) or be accumulated as a complete bias map which is telemetered at the start of a Science Run.

5.1.4 Other Data Products

The ASC further processes Level 0 data products to produce other data products. For example, one Observation Request (OR) may be implemented using a number of science runs. The resulting Level 0 data products must be identified and grouped together for delivery to the guest observer. The Bias Map referred to above is another example of an ancillary data product which must be extracted and tracked for each Science Run.

5.2 Data Reduction Tools

5.2.1 ACIS-supplied Tools

During the XRCF calibration, ACIS science data were monitored by an operator on the second floor of the facility using the ACIS Quick Look Computer (AQLC), a computer workstation developed by the ACIS team. The AQLC obtains AXAF telemetry generated by the CTUE in real time, via the ACIS EGSE. The AQLC consists of two subsystems. The ACIS Telemetry Interpreter for Calibration Analysis (ATICA), converts the AXAF telemetry stream into a sequence of FITS files containing the ACIS science data. The telemetry processing performed by ATICA is essentially the same as that described in Section 5.1.

The second subsystem, Tools for ACIS Real-time Analysis (TARA), provides the human operator with a suite of tools for analyzing in real time the science data contained in the FITS files produced by ATICA as well as full-frame CCD data obtained directly from the ACIS hardware by the EGSE's 'High Speed Tap'. (As the HST data does not pass through the telemetry it is not available during the flight.) TARA includes a variety of tools – some written specifically for TARA and some incorporated from other data analysis packages – for visualizing, reducing, and analyzing ACIS data. Some examples of these tools include:

- image showing detected events within energy thresholds
- summed image (integrated event detections)
- fit of summed image to a point spread function model
- spectrum from user-selected regions of focal plane
- fit of spectra to models
- light curve from user-selected regions of focal plane
- display of single raw frames

eb (Event Browser)	manager	domain_dataset	event_database
ccd_filter	grade_filter	rowcolumn_filter	bias_error_map
diffraction_display	focal_plane_display	pixel_hist_display	property_hist_display
two_property_plot	fits_viewer	ccd_viewer	image_viewer
image_viewer_roi	plot_viewer	plot_viewer_roi	

Table 5.1: IDL Tools Produced by ACIS Team

- display of bias maps

TARA is a collection of computer programs which scientists use to analyze ACIS calibration data. Some of these are standard tools which have been in use for years in the astronomy community; others were written by the ACIS team specifically to analyze ACIS data. In the same way, some of the programs are stand-alone, and others are functions which have been integrated into a convenient GUI (Graphical User Interface) for use in an interactive mode during Analyst activity at XRCF or data reduction in a home site. The GUI interface form is known as Event Browser. Important stand-alone programs are CCD_viewer and fits_viewer, which allow direct display of raw CCD images and FITS files made by the ACIS software.

External packages which are heavily used in ACIS processing include the commercial IDL (Interactive Data Language), supported by RSI; the XANADU package (including FTOOLS, XSPEC and XRONOS), supported by Goddard Space Flight Center; and SAOimage, supported by the Center for Astrophysics. The ACIS team does not supply support or documentation for these packages, and refers users to the appropriate institution.

TARA is available for public distribution through the Penn State Web site at:

http://www.astro.psu.edu/xray/software/

Table 5.1 lists the IDL tools written by the ACIS team. Documentation for each of these tools is available by using the *xdl* command from within IDL.

5.2.1.1 Event Browser

Event Browser (EB) is an IDL widget application which is used to manipulate x-ray event lists. EB provides users with a graphical user interface for doing such things as selecting data files, filtering event lists in numerous ways, and displaying and printing results.

A particular strength of Event Browser is the ability to see the effect of changing selection criteria immediately. The selection criteria possible are many, and are very oriented to the physically important characteristics of the CCD and the AXAF HRMA imaging. Event Browser enables selection of events based on position, event energy, event grade, CCD chip, CCD amplifier and time.

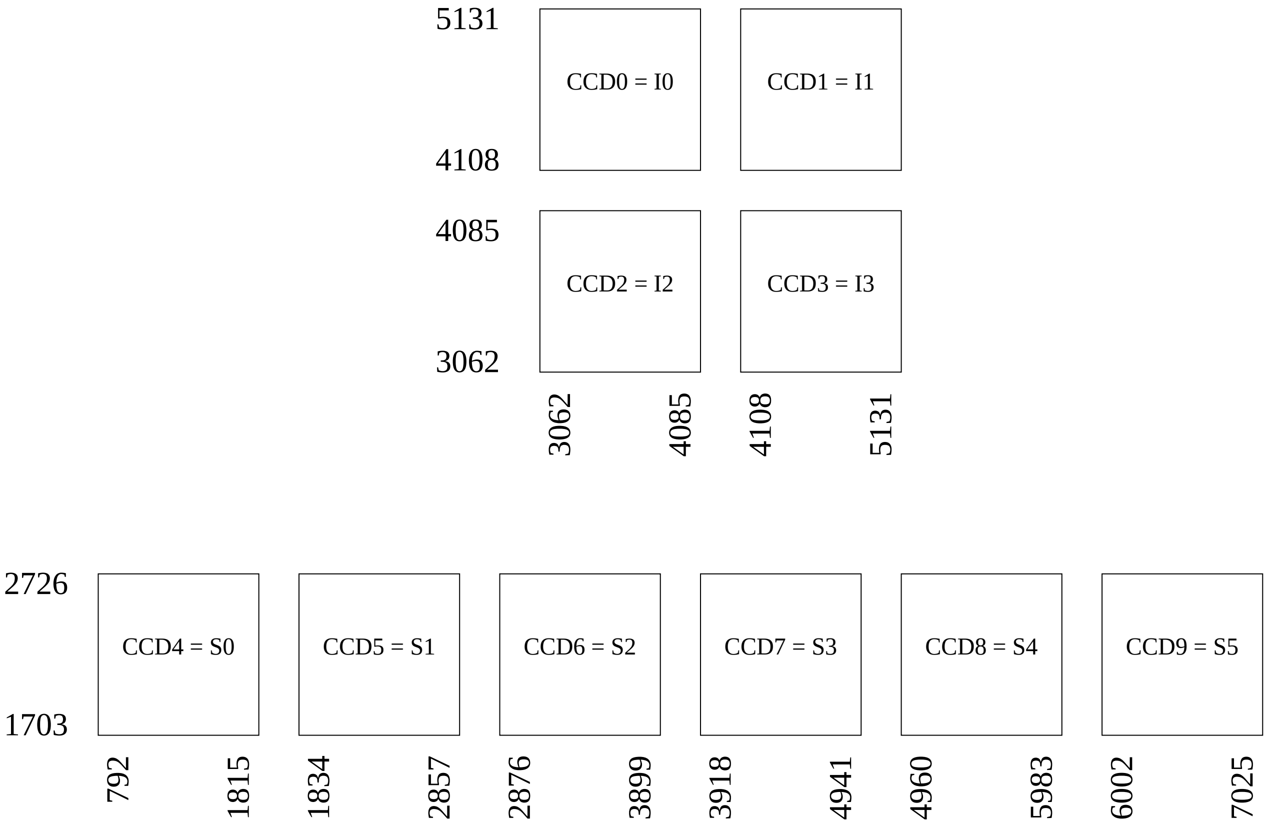

Figure 5.2: ACIS Chips in ASC DETX/DETY Coordinate System

Event Browser also offers a range of display capabilities to reveal characteristics of the dataset being examined. These include images of the spatial distribution in two dimensions, spectra (histograms of number of events vs. energy), light curves (histograms of number of events vs. time), and general two property comparisions (any two characteristics of an event [energy, time, x, y, grade] as a scatter plot).

Spectra can be converted from detector Data Number (DN) values into X-ray energy in eV to facilitate combination of data from different CCD amplifiers.

Images can be formed from data from multiple CCDs by combining them into the detector focal plane coordinate system "AXAF-ACIS-2.2", as defined by Jonathon McDowell's (ASC) "ASC Coordinates, Rev 4.0". This allows images to be produced which look like panoramic views of the sky, and to facilite reduction of dispersed spectra made by the gratings, which may fall on up to six CCD chips. Figure 5.2 shows the locations of the ACIS CCD chips in the ASC DETX/DETY focal plane coordinate system.

Regions of interest in the spatial, spectral and temporal domains can be selected interactively based on the image, spectral and light curve displays to further apply improved filtering to the data products.

Some data analysis capabilities such as simple model fitting, centroiding and plots of radial surface brightness are built into Event Browser. For more extensive analysis capability, spectra, light curves, images and other Event Browser results can be saved in the form of FITS files for export to other advanced analysis programs.

5.2.1.2 Analyst's Guide

In order to prepare ACIS personnel for work at the XRCF in examining quick look data product, an Analyst's Guide was prepared. This Guide may also be useful to anyone starting off on ACIS data analysis. The Guide is available via ftp and through the World Wide Web. See the section 'Web Resources'.

5.2.2 ASC-supplied Tools

The AXAF Science Center is charged with the task of external science user support. They have already assembled a useful set of support tools, especially in the area of AXAF performance prediction for proposal preparation. Of particular interest are PIMMS, a tool for estimating AXAF/ACIS counting rates based on rates from previous missions and assumed spectral shapes; MARX, a simplified ray-tracing program for simulating proposed observations, including grating effects; and SAO-SAC, the detailed mirror ray tracing program for detailed evaluation and prediction of HRMA performance.

These and other useful tools and user hotline support are available through the SAO/ASC web page at:

http://asc.harvard.edu

5.2.3 Web Analysis Resources

A variety of useful ACIS and AXAF related World Wide Web resources are available. Here is a listing of some of the more important:

- MIT ACIS home page -
  http://acis.mit.edu
- MIT SPIE 1996 page (description of lab calib.) -
  http://acis.mit.edu/acis/spie96
- MIT X-ray CCD group (lab CCD calibration results) -
  http://space.mit.edu/ACIS

- MIT Center for Space Research ACIS X-ray CCD Group -
  http://space.mit.edu/ACIS/ccd_acis.html
- ACIS-XRCF Performance Modeling Webpage -
  http://hea-www.harvard.edu/asc/asc/cal/simulations/acis_sim.html
- PSU ACIS Calibration page (Sci. Instrument Handbook) -
  http://www.astro.psu.edu/xray/axaf/axaf.html
- PSU Software page (AQLC requirements, ATICA design) -
  http://www.astro.psu.edu/xray/software/

5.3 Science Data

The science data will be output at a rate of 24 kbs while ACIS is at the focus of the HRMA. While the HRC is in the focus, 0.5 kbs of data will be telemetered.

There are 17 possible modes, but the most commonly used scientific mode will be the Timed Exposure, Faint Mode. In this mode, an event will be transmitted as a 9-pixel neighborhood of 12 bits/pixel to fully describe the pulse-height spectrum and allow the ground-processing system to balance the trade between resolution and quantum-efficiency. Positions are given to 18 bits. Each frame additionally contains its identification, time designation and rejected counts. Occasionally, there will be diagnostic histograms from the calibration mode.

Chapter 6

Test Procedures and Quality Assurance

The issues of Test Procedures and Quality Assurance are addressed by other ACIS documentation. We do not repeat this material here.

Operational constraints are discussed in the AXAF Constraints and Restrictions Document (CARD) OP05, which is maintained by TRW, with inputs from the ACIS team. Please refer to that document for more detail.

Chapter 7

Traceability Matrix

In order to verify that the Data Requirements specified in DR-726 have been satisfied by this document the following traceability matrix is provided. DR-726 lists specified contents required in SOP01 under section 13.3. The following table cross-references the applicable section of SOP01 (this document) against the relevant 13.3 subsection number, with a brief identifying phrase.

Table 7.1. DR-726 Traceability to SOP01		
DR-726 Req't	SOP01 Section	Description
1.	1.4	Introduction
2.	2.1, 3.1	Instrument description
3.	2.	Function descriptions at subsystem level
3.a	2.2.1	Optical Systems Design
3.b	2.2.2	Mechanical Systems Design
3.c	2.2.3	Thermal Systems Design
3.d	2.2.4	Power Design
3.e.1	2.3.1	Detector Description
3.e.2	2.3.2	Camera Design
3.e.3	2.3.6-7	Camera Signal Processing
3.e.4	”	Camera Electronics
3.e.5	4.1	Camera Sensitivity
3.e.6	2.3.2	Camera Parameters
3.e.7	4.4	Camera Trend Analysis
3.e.8	4.4	Detector Calibrations
3.e.9	-	Miscellaneous
3.f	3.2	Commanding
3.g	3.2	Data & Telemetry Processing
3.h	2.3.6-7	On-board Processors
3.i	2.3.3-5	Other Systems
4.a	4.3	Instrument Sensitivity Models
4.a	4.4	Flight Calibrations
4.b	3.2.3	Routine Command Sequences for Mode Changes
4.c	3.2.3	Routine Command Sequences for Observations
4.d	3.2.1	Good Practices
5.	4.4	Calibration Philosophy
6.	3.2.5	Near Real Time Monitoring
7.	3.2.6	Contingencies
8.	5.	Ground Processing Algorithms
9.	3.2.4	Operational Constraints
10.	5.2	Ground Processing Science Data

Table 7.1: DR-726 Traceability to SOP01

Chapter 8

Glossary of Acronyms

ACIS AXAF CCD Imaging Spectrometer, one of two focal plane instruments aboard AXAF, consisting of two arrays of CCD chips supporting imaging and transmission spectroscopy. It provides simultaneous imaging and non-dispersive moderate resolution spectroscopy.

ACIS-I Term referring to Imaging CCD array.

ACIS-S Term referring to Spectroscopic CCD array, which supports the use of the AXAF transmission gratings.

ADC Analog-to-Digital Converter, provides digital equivalent to analog signals.

ADU Analog-to-Digital Unit, unit defining integer values resulting from an analog to digital conversion.

AQLC ACIS Quick Look Computer, one of two computers used at the X-ray Calibration Facility to assess ACIS data. The AQLC reduces and displays data in near real time to evaluate the scientific validity of the data.

ASC AXAF Science Center, center for the analysis of AXAF data and general scientific support and analysis in the post-launch AXAF phase.

ADS Two meanings based on context:

1. Aspect Determination System, AXAF system determining the satellite pointing and orientation,
2. Astrophysics Data System, NASA Astrophysics Division supported system for the access, dissemination and utilization of archival astrophysical data.

AXAF Advanced X-ray Astrophysical Facility, the spacecraft carrying the ACIS experiment and the high resolution X-ray telescopes.

BESSY The Berlin synchrotron light source used to establish the reference calibration of CCDs used during the MIT pre-assembly calibration measurements to achieve an absolute quantum efficiency calibration.

BEP Backend Processor, digital signal processor and control processor which packetizes data for downlink and controls the CCDs.

BI Backside Illuminated, term applied to a type of CCD chip, in which the normal thick silicon substrate is removed and X-rays illuminate the back of the device. BI chips have good low energy quantum efficiency.

BND Beam Normalization Detector, an X-ray counter used at the XRCF to measure the intensity of the incident X-ray beam, and hence allow normalization of any measurements made at the XRCF.

BNL Brookhaven National Laboratory, site of a synchrotron used as an X-ray source during ACIS filter calibration.

CCD Charged Coupled Device, the active detector elements in ACIS.

CDR Critical Design Review, formal meeting certifying the start of full production of the overall hardware and software design.

CEI Contract End Item, item specified in the NASA contract which must be delivered by the ACIS team.

CIT Calibration Implementation Team, a group combining the CTT, MSFC Project and support staff, and TRW, which will implement the XRCF calibration of AXAF.

CTE Charge Transfer Efficiency, ratio of charge remaining after one pixel clocking to the charge before clocking.

CTI Charge Transfer Inefficiency, deviation of CTE from unity. Convenient because CTE is often very close to one.

CTT Calibration Task Team, a scientifically orientation group drawn from the Project and SI teams, charged with the responsibility of planning AXAF calibration.

DA Detector Assembly, houses CCD arrays, fiducial lights and an X-ray calibration source. Functionally equivalent to term 'CCD Camera'.

DEA Digital Electronics Assembly, ACIS digital signal processing section.

DPA Digital Processing Assembly, ACIS analog signal processing section.

DPS Detector & Processor Subsystem, subsystem dedicated to the detection and processing of X-rays, consisting of the DA, DEA and DPA.

DR Data Requirement, a formal NASA specification for required documentation format, content and delivery dates.

EGSE Electronic Ground Support Equipment, one of two computers used at the X-ray Calibration Facility to assess ACIS data. The EGSE generates commands and monitors housekeeping data to assure the health and safety of the instrument.

EMI Electro-Magnetic Interference, electro-magnetically induced noise appearing on electrical signal wires. Usually referred to in the context of eliminating or shielding to prevent EMI.

FEP Frontend Processor, digital signal processor, part of the DPA which does initial processing on raw CCD pixel data.

FI Frontside Illuminated, a traditional CCD chip design where the chip is illuminated from the front layer, which requires the X-rays to traverse the electronic gate structures. The low energy quantum efficiency of FI chips is low, but the energy resolution is superior to BI chips.

FP Focal Plane, the sub-assembly portion of the ACIS experiment which holds the CCD chips.

FWHM Full Width at Half Maximum, a measure of the width of a distribution, frequently used to describe the resolving power of the CCD for spectral emission lines.

GSE Ground Support Equipment, auxiliary equipment needed to operate the ACIS experiment during assembly and ground testing.

HETG High Energy Transmission Gratings, used to provide dispersed X-ray spectra appropriate to the higher energy X-rays collected by the HRMA. The HETG uses the ACIS as its prime detector system.

HRC High Resolution Camera, the other focal plane instrument on AXAF, based on a micro-channel plate X-ray detector.

HRMA High Resolution Mirror Assembly, the AXAF X-ray telescope mirror assembly, consisting of four nested confocal Wolter I optical systems.

HST High Speed Tap, a high speed data path providing raw CCD pixel data into the ACIS EGSE computers. These data are similar to the sub-assembly calibration data, and form a direct check on the flight telemetry format data. The HST also offers a much higher bandwidth data path valuable during ground calibration. The HST will not be available during flight.

ICD Interface Control Document, documents defining the observatory interfaces.

IPI Instrument Principal Investigator, scientist in charge of the development of the instrument and leader of the team submitting the proposal and executing the task. For ACIS the IPI is Prof. Gordon Garmire.

kbs kilobit per second, a data transfer rate measured in thousands of bits per second.

LMA Lockheed Martin Astronautics, sub-contractor providing some of the fabrication of the ACIS instrument, formerly named MMAG.

LETG Low Energy Transmission Gratings, disperse X-ray spectra appropriate to the lower energy X-rays collected by the HRMA. The LETG uses the HRC as its prime detector system.

MCC Master Control Computer, central coordinating computer at the XRCF facilty during AXAF calibration.

MMAG Martin Marietta Aerospace Group, sub-contractor providing the fabrication of the ACIS instrument, name now changed to LMA.

MIT Massachusetts Institute of Technology, home institution of ACIS CCD development work and camera design.

MSFC Marshall Space Flight Center, the home institution for the AXAF Project.

OBC On-Board Computer, the AXAF spacecraft computer which transmits commands to ACIS and which receives telemetry data for transmission to the ground.

OBDS On-Board Data System, the computing system for ACIS on-board the satellite.

OBF Optical Blocking Filter, a thin free-standing polyimide plastic film with aluminum overcoats on both sides which is placed between the telescope mirrors and the CCD detectors. This filter blocks out optical, UV and infrared light which would otherwise interfere with X-ray detection by the CCDs, but is thin enough to allow X-rays to pass through.

OV Orbital Verification, the first period of orbital operations, in which the instruments and spacecraft are turned on and proper operations are verified.

PDR Preliminary Design Review, formal meeting reviewing the overall hardware and software design.

PRAM Program Random-Access Memory, radiation resistant on-board non-volatile memory which is used to store instructions for CCD readout.

PSMC Power Supply and Mechanism Controller, supplies power and mechanism control to ACIS.

PSU Penn State University, home institution for the ACIS Principal Investigator and ground software development.

PTS Power & Thermal control Subsystem, ACIS subsystem which delivers power and maintains thermal control of the experiment.

RCTU Remote Command and Telemetry Unit, TRW supplied interface box supplying connection to spacecraft data and power busses.

SDS Software Design Specification, document specifying the software design for each build of the ground software.

SEU Single Event Upset, single bit errors introduced into memory or processors, resistance to which reflects more robust processor performance in a space environment.

SIM Science Interface Module, a translational mechanical structure which moves to allow insertion of either the HRC and ACIS into the telescope focal plane, and to shift between the ACIS-I and S arrays.

SIN Science Instrument Notebook, ASC reference document on all AXAF Science Instruments.

SOP01 Science Instrument Operations Manual [this document], required deliverable for the ACIS team, presenting the information needed to properly operate the ACIS experiment.

SRAM Sequencer Random-Access Memory, highly radiation resistant memory used to store instructions for the ACIS CCD readout.

SRR Software Requirements Review, formal meeting reviewing the adequacy and accuracy of the Software Requirements.

SRS Software Requirements Specification, document specifying the ACIS software requirements.

SRC Synchrotron Radiation Center, a synchrotron facility run by the University of Wisconsin, Madison, used for ACIS flight filter calibration.

ST STatus information, information ancillary to the scientific data which is appended to the science analysis data.

SWG Science Working Group, the team of scientists, consisting of the Instrument PIs, the Telescope Scientist, the Interdisciplinary Scientists and the Project Scientist, who work as a top-level advisory team to assure the AXAF Project remains faithful to the scientific goals of the program.

TBS, TBR, TBD To Be Supplied, Revised, Determined, terms holding space for specific numbers or text which are to be supplied, revised or determined at a later time.

VVA Vent Valve Assembly, provides a commandable opening and closing path to vent the inside of ACIS.

WBS Work Breakdown Structure, management document and numbering scheme for formalizing and categorizing the various tasks associated with this project into a tiered hierarchy with associated dependencies to enable the efficient identification and tracking of progress on the assigned goals.

XRCF X-ray Calibration Facility, the X-ray facility built at Marshall Space Flight Center to support AXAF calibration of the joint HRMA-Science Instrument system.

Appendix A

ACIS Grades

As described in Section 3.3.2, ACIS candidate X-ray events are assigned to grades based on the number and orientation of the pixels neighboring the central candidate pixel which exceed the split event threshold. In order to better visualize the patterns corresponding to a particular grade the following figure has been prepared.

– – – – X – – – – 0	– – – – X – X – – 1	– – – – X – – X – 2	– – – – X – X X – 3	– – – – X – – – X 4	– – – – X – X – X 5	– – – – X – – X X 6	– – – – X – X X X 7	– – – X X – – – – 8	– – – X X – X – – 9	– – – X X – – X – 10	– – – X X – X X – 11	– – – X X – – – X 12	– – – X X – X – X 13	– – – X X – – X X 14	– – – X X – X X X 15
– – – – X X – – – 16	– – – – X X X – – 17	– – – – X X – X – 18	– – – – X X X X – 19	– – – – X X – – X 20	– – – – X X X – X 21	– – – – X X – X X 22	– – – – X X X X X 23	– – – X X X – – – 24	– – – X X X X – – 25	– – – X X X – X – 26	– – – X X X X X – 27	– – – X X X – – X 28	– – – X X X X – X 29	– – – X X X – X X 30	– – – X X X X X X 31
X – – – X – – – – 32	X – – – X – X – – 33	X – – – X – – X – 34	X – – – X – X X – 35	X – – – X – – – X 36	X – – – X – X – X 37	X – – – X – – X X 38	X – – – X – X X X 39	X – – X X – – – – 40	X – – X X – X – – 41	X – – X X – – X – 42	X – – X X – X X – 43	X – – X X – – – X 44	X – – X X – X – X 45	X – – X X – – X X 46	X – – X X – X X X 47
X – – – X X – – – 48	X – – – X X X – – 49	X – – – X X – X – 50	X – – – X X X X – 51	X – – – X X – – X 52	X – – – X X X – X 53	X – – – X X – X X 54	X – – – X X X X X 55	X – – X X X – – – 56	X – – X X X X – – 57	X – – X X X – X – 58	X – – X X X X X – 59	X – – X X X – – X 60	X – – X X X X – X 61	X – – X X X – X X 62	X – – X X X X X X 63
– X – – X – – – – 64	– X – – X – X – – 65	– X – – X – – X – 66	– X – – X – X X – 67	– X – – X – – – X 68	– X – – X – X – X 69	– X – – X – – X X 70	– X – – X – X X X 71	– X – X X – – – – 72	– X – X X – X – – 73	– X – X X – – X – 74	– X – X X – X X – 75	– X – X X – – – X 76	– X – X X – X – X 77	– X – X X – – X X 78	– X – X X – X X X 79
– X – – X X – – – 80	– X – – X X X – – 81	– X – – X X – X – 82	– X – – X X X X – 83	– X – – X X – – X 84	– X – – X X X – X 85	– X – – X X – X X 86	– X – – X X X X X 87	– X – X X X – – – 88	– X – X X X X – – 89	– X – X X X – X – 90	– X – X X X X X – 91	– X – X X X – – X 92	– X – X X X X – X 93	– X – X X X – X X 94	– X – X X X X X X 95
X X – – X – – – – 96	X X – – X – X – – 97	X X – – X – – X – 98	X X – – X – X X – 99	X X – – X – – – X 100	X X – – X – X – X 101	X X – – X – – X X 102	X X – – X – X X X 103	X X – X X – – – – 104	X X – X X – X – – 105	X X – X X – – X – 106	X X – X X – X X – 107	X X – X X – – – X 108	X X – X X – X – X 109	X X – X X – – X X 110	X X – X X – X X X 111
X X – – X X – – – 112	X X – – X X X – – 113	X X – – X X – X – 114	X X – – X X X X – 115	X X – – X X – – X 116	X X – – X X X – X 117	X X – – X X – X X 118	X X – – X X X X X 119	X X – X X X – – – 120	X X – X X X X – – 121	X X – X X X – X – 122	X X – X X X X X – 123	X X – X X X – – X 124	X X – X X X X – X 125	X X – X X X – X X 126	X X – X X X X X X 127
– – X – X – – – – 128	– – X – X – X – – 129	– – X – X – – X – 130	– – X – X – X X – 131	– – X – X – – – X 132	– – X – X – X – X 133	– – X – X – – X X 134	– – X – X – X X X 135	– – X X X – – – – 136	– – X X X – X – – 137	– – X X X – – X – 138	– – X X X – X X – 139	– – X X X – – – X 140	– – X X X – X – X 141	– – X X X – – X X 142	– – X X X – X X X 143
– – X – X X – – – 144	– – X – X X X – – 145	– – X – X X – X – 146	– – X – X X X X – 147	– – X – X X – – X 148	– – X – X X X – X 149	– – X – X X – X X 150	– – X – X X X X X 151	– – X X X X – – – 152	– – X X X X X – – 153	– – X X X X – X – 154	– – X X X X X X – 155	– – X X X X – – X 156	– – X X X X X – X 157	– – X X X X – X X 158	– – X X X X X X X 159
X – X – X – – – – 160	X – X – X – X – – 161	X – X – X – – X – 162	X – X – X – X X – 163	X – X – X – – – X 164	X – X – X – X – X 165	X – X – X – – X X 166	X – X – X – X X X 167	X – X X X – – – – 168	X – X X X – X – – 169	X – X X X – – X – 170	X – X X X – X X – 171	X – X X X – – – X 172	X – X X X – X – X 173	X – X X X – – X X 174	X – X X X – X X X 175
X – X – X X – – – 176	X – X – X X X – – 177	X – X – X X – X – 178	X – X – X X X X – 179	X – X – X X – – X 180	X – X – X X X – X 181	X – X – X X – X X 182	X – X – X X X X X 183	X – X X X X – – – 184	X – X X X X X – – 185	X – X X X X – X – 186	X – X X X X X X – 187	X – X X X X – – X 188	X – X X X X X – X 189	X – X X X X – X X 190	X – X X X X X X X 191
– X X – X – – – – 192	– X X – X – X – – 193	– X X – X – – X – 194	– X X – X – X X – 195	– X X – X – – – X 196	– X X – X – X – X 197	– X X – X – – X X 198	– X X – X – X X X 199	– X X X X – – – – 200	– X X X X – X – – 201	– X X X X – – X – 202	– X X X X – X X – 203	– X X X X – – – X 204	– X X X X – X – X 205	– X X X X – – X X 206	– X X X X – X X X 207
– X X – X X – – – 208	– X X – X X X – – 209	– X X – X X – X – 210	– X X – X X X X – 211	– X X – X X – – X 212	– X X – X X X – X 213	– X X – X X – X X 214	– X X – X X X X X 215	– X X X X X – – – 216	– X X X X X X – – 217	– X X X X X – X – 218	– X X X X X X X – 219	– X X X X X – – X 220	– X X X X X X – X 221	– X X X X X – X X 222	– X X X X X X X X 223
X X X – X – – – – 224	X X X – X – X – – 225	X X X – X – – X – 226	X X X – X – X X – 227	X X X – X – – – X 228	X X X – X – X – X 229	X X X – X – – X X 230	X X X – X – X X X 231	X X X X X – – – – 232	X X X X X – X – – 233	X X X X X – – X – 234	X X X X X – X X – 235	X X X X X – – – X 236	X X X X X – X – X 237	X X X X X – – X X 238	X X X X X – X X X 239
X X X – X X – – – 240	X X X – X X X – – 241	X X X – X X – X – 242	X X X – X X X X – 243	X X X – X X – – X 244	X X X – X X X – X 245	X X X – X X – X X 246	X X X – X X X X X 247	X X X X X X – – – 248	X X X X X X X – – 249	X X X X X X – X – 250	X X X X X X X X – 251	X X X X X X – – X 252	X X X X X X X – X 253	X X X X X X – X X 254	X X X X X X X X X 255

Table A.1: ACIS Grade Description